Technische Universität München
TUM School of Natural Sciences

Paving the way for PeVatron studies with the MAGIC Telescopes: Performance evaluation using observations of the Crab Nebula at large zenith angles

Juliane Ursula van Scherpenberg

Vollständiger Abdruck der von der TUM School of Natural Sciences der Technischen Universität München zur Erlangung einer **Doktorin der Naturwissenschaften (Dr. rer. nat.)** genehmigten Dissertation.

Vorsitz: Prof. Dr. Andreas Weiler

Prüfende der Dissertation:

1. Prof. Dr. Susanne Mertens
2. Prof. Dr. Elisa Resconi

Die Dissertation wurde am 16.04.2025 bei der Technischen Universität München eingereicht und durch die TUM School of Natural Sciences am 22.05.2025 angenommen.

Abstract

In this thesis, I present the first detailed study of the performance of the MAGIC Telescopes during observations at large zenith angles. These observations provide a better sensitivity of the instrument to gamma-ray emission with energies of tens of TeV and enable the extension of the observable energy range up to ∼ 100 TeV. Studying gamma-ray emitting sources in this energy range with the good angular resolution and precision in the energy estimation that Imaging Atmospheric Cherenkov Telescopes (IACTs) can provide is crucial for understanding the origin of Galactic Cosmic Rays (CRs).

From CRs studies, the existence of sources inside the Milky Way Galaxy, that are capable of accelerating atomic nuclei to energies of at least a few PeV, is expected. These sources of unknown nature are referred to as *PeVatrons*. In the interactions with their environment the accelerated nuclei produce gamma rays with energies of tens of TeV to several PeV, the detection of which allows to identify the location of their production site. Recent observations from air shower arrays have identified sky regions exhibiting emission beyond 100 TeV. Their limited capability of spatially resolving the details of the emission, however, in most cases does not allow to firmly identify the nature of the underlying astrophysical object. The Crab Nebula is exceptional in this regard. It is a well-studied source across the electromagnetic spectrum and was recently detected at energies beyond 1 PeV. It is the brightest persistent source in the gamma-ray sky and is used to calibrate gamma-ray telescopes and to characterize their performance.

For this thesis, I have analyzed a large set of data taken on the Crab Nebula with MAGIC at zenith angles between 50° and 80°. Using these data, as well as Monte Carlo (MC) simulations, I have studied the quantities that characterize the performance of the MAGIC Telescopes. I have evaluated their dependence on the zenith angle, the azimuth direction, and energy and have identified new systematic effects which only become apparent at large zenith angles. I have evaluated the differential flux sensitivity of MAGIC for large and very-large zenith angle observations up to 70 TeV in estimated energy and reconstructed the Crab Nebula spectral energy distribution (SED) up to 100 TeV. My study shows that the performance of the MAGIC Telescopes is stable up to zenith distance (Zd) 75° and identifies the separation of gamma-ray signal events from the hadronic background as the main limitation of the performance. An evaluation of the flux variability further shows the stability of the observations over time and provides a sensitivity to potential intrinsic flux variations of the Crab Nebula. The results presented in this thesis demonstrate the promising potential of MAGIC to contribute to the identification of Galactic PeVatrons and serve as a valuable reference for the planning of future observations of PeVatron candidate sources.

Zusammenfassung

In dieser Dissertation präsentiere ich die erste detaillierte Untersuchung der Leistungsfähigkeit der MAGIC-Teleskope während Beobachtungen bei großen Zenitwinkeln. Diese Beobachtungen ermöglichen eine höhere Empfindlichkeit des Instruments für Gammastrahlung mit Energien von einigen Dutzend TeV und erlauben die Erweiterung des beobachtbaren Energiebereichs bis zu $\sim 100\,\mathrm{TeV}$. Die Untersuchung von Gammastrahlenquellen in diesem Energiebereich mit der hohen Winkelauflösung und der präzisen Energieabschätzung, die bodengebundene Cherenkov-Teleskope bieten, ist von entscheidender Bedeutung für das Verständnis des Ursprungs der galaktischen kosmischen Strahlung.

Die Forschung zu kosmischer Strahlung legt die Existenz von Quellen innerhalb der Milchstraße nahe, die in der Lage sind, Atomkerne auf Energien von mindestens einigen PeV zu beschleunigen. Diese Quellen unbekannter Natur werden als *PeVatrons* bezeichnet. In Wechselwirkungen mit ihrer Umgebung erzeugen die beschleunigten Kerne Gammastrahlen mit Energien von einigen Dutzend TeV bis hin zu PeV. Deren Detektion ermöglicht die Lokalisierung der Produktionsstätten dieser hochenergetischen Strahlung. Jüngste Beobachtungen mit Luftschauer-Detektoren haben Himmelsregionen mit Emissionen oberhalb von 100 TeV identifiziert. Aufgrund ihrer begrenzten Fähigkeit, die Emissionsregionen räumlich aufzulösen, ist es jedoch in den meisten Fällen nicht möglich, die Natur der zugrunde liegenden astrophysikalischen Objekte eindeutig zu bestimmen. Eine Ausnahme stellt der Krebsnebel dar. Er ist eine gut untersuchte Quelle über das gesamte elektromagnetische Spektrum hinweg und wurde kürzlich bei Energien über 1 PeV detektiert. Als die hellste beständige Quelle am Gammastrahlenhimmel dient er sowohl zur Kalibrierung von Gammastrahlenteleskopen als auch zur Charakterisierung ihrer Leistung.

Im Rahmen dieser Arbeit habe ich einen umfangreichen Datensatz von Beobachtungen des Krebsnebels mit MAGIC bei Zenitwinkeln zwischen 50° und 80° analysiert. Basierend auf diesen Daten sowie auf MC-Simulationen habe ich die Leistungscharakteristika der MAGIC-Teleskope untersucht. Ich habe deren Abhängigkeit von Zenitwinkel, Azimutrichtung und Energie evaluiert und dabei neue systematische Effekte identifiziert, die erst bei großen Zenitwinkeln sichtbar werden. Zudem habe ich die differentielle Fluss-Sensitivität von MAGIC für Beobachtungen bei großen und sehr großen Zenitwinkeln bis zu einer geschätzten Energie von 70 TeV bestimmt und das Energiespektrum des Krebsnebels bis zu 100 TeV rekonstruiert. Meine Untersuchung zeigt, dass die Leistungsfähigkeit der MAGIC-Teleskope bis zu einem Zenitwinkel von 75° stabil bleibt, wobei die Unterscheidung von Gammastrahlen-Signalen vom hadronischen Untergrund die Hauptbegrenzung der Leistungsfähigkeit darstellt. Eine Analyse der Flussvariabilität bestätigt zudem die Stabilität der Beobachtungen über die Zeit hinweg und liefert eine Abschätzung der Sensitivität für mögliche intrinsische Fluktuationen des Krebsnebel-Flusses.

Die in dieser Dissertation präsentierten Ergebnisse demonstrieren das vielversprechende

Potenzial von MAGIC zur Identifikation galaktischer PeVatrons und liefern eine wertvolle Referenz für die Planung zukünftiger Beobachtungen von PeVatron-Kandidaten.

Contents

List of Figures

List of Tables

List of Acronyms

ADC	analog-to-digital conversion	52
AGN	Active Galactic Nucleus	2
AMC	active mirror control	51
C.U.	Crab Unit	70
CD	contact discontinuity	
CMB	cosmic microwave background	6
COG	center of gravity	56
CR	Cosmic Ray	iii
CTAO	Cherenkov Telescope Array Observatory	3
DAQ	data acquisition	52
DRS4	Domino Ring Sampler version 4	52
DSA	diffusive shock acceleration	7
DT	discriminator threshold	52
EAS	Extensive Air Shower	44
FOV	field-of-view	2
GC	Galactic Center	12
GRB	Gamma-ray Burst	15
GWTS	Galactic wind termination shock	
HAWC	High-altitude Water Cherenkov Observatory	11
HE	high-energy ($50\,\mathrm{MeV} < \mathrm{E} < 50\,\mathrm{GeV}$)	1
HGPS	H.E.S.S. Galactic Plane Survey	114
HPD	hybrid photo detector	53
HST	Hubble Space Telescope	20
IACT	Imaging Atmospheric Cherenkov Telescope	iii
IC	Inverse Compton	14
IPRC	individual pixel-rate control	52
IRF	instrument response function	66
ISM	interstellar medium	2

JWST	James Webb Space Telescope	20
KM2A	Square-Kilometer Array	46
LC	light curve	62
LHAASO	Large High Altitude Air Shower Observatory	11
LIDAR	light detection and ranging	53
LoNS	light of the night sky	37
LUT	Look-Up-Table	51
LZA	large zenith angle	65
MAGIC	Major Atmospheric Gamma-ray Imaging Cherenkov	49
MARS	MAGIC Analysis and Reconstruction Software	49
MC	Monte Carlo	iii
MHD	magnetohydrodynamic	18
MSE	Mean Squared Error	59
OSA	On-site Analysis	58
phe	photo-electron	56
PMT	Photomultiplier Tube	37
PSF	point-spread-function	52
PW	Pulsar Wind	14
PWN	Pulsar Wind Nebula	11
RA	right ascension	55
RF	Random Forest	59
RMS	root-mean-squared	40
ROC	Receiver Operating Characteristic	77
RS	Reverse Shock	15
SED	spectral energy distribution	iii
SFR	star-forming region	10
SN	Supernova	10
SNR	Supernova Remnant	2
SSC	Synchrotron Self Compton	15
TS	Termination Shock	14
UHE	ultra-high-energy ($E > 100\,\mathrm{TeV}$)	11

VCSEL vertical cavity surface emitting laser 51

VHE very-high-energy ($50\,\mathrm{GeV} < \mathrm{E} < 100\,\mathrm{TeV}$) 1

VLZA very large zenith angle 54

WCDA Water Cherenkov Detector Array 46

Zd zenith distance iii

Chapter 1

Introduction

In 1912, one man setting out to study ionizing radiation, which was believed to originate from Earth, ended up taking measurements that lay the basis for an entirely new field of research: astroparticle physics. Viktor Hess had launched several balloon flights in order to study the nature of this mysterious radiation previously discovered in laboratory experiments on the ground. He expected the number of ionizing particles to decrease as his balloons were ascending, instead he found the opposite behavior. With higher altitudes, the signal rates increased, which finally led him to conclude that this radiation must reach the Earth's atmosphere from outer space. These experiments are today referred to as the discovery of Cosmic Rays (CRs).

This cosmic radiation has been studied in increasing detail ever since its discovery. We have come to understand that the radiation Viktor Hess was detecting was comprised of secondary particles produced in the interactions of highly energetic atomic nuclei with the Earth's atmosphere. Thanks to a variety of instruments studying CRs over the last decades, we have detected them across a large energy range and have measured their energy-dependent flux and composition. The vast majority of astrophysical particles reaching the Earth are charged particles, $\sim 90\%$ of which are protons. Since charged particles are deflected by magnetic fields, CRs measured at Earth can not be traced back to their source of origin. Even now, more than 100 years after the discovery of CRs, their origin is not well understood. Basic considerations have led to the consensus that the cosmic rays we detect up to energies of a few PeV, the so-called *knee* of the cosmic ray energy spectrum, are accelerated in sources within the Galaxy, whereas extragalactic sources are assumed to be responsible for acceleration to higher energies. Which exact sources and physical mechanisms therein produce highly energetic CRs is, however, unknown to this day. A much smaller fraction of cosmic radiation consists of gamma rays and neutrinos. What the latter lack in number density, they make up in the importance of understanding the origin of their charged counterparts. In contrast to charged particles, cosmic neutrinos and gamma rays travel in straight lines to the observer and are produced in the interactions of CRs with each other or the ambient medium. Finding their sources and understanding the processes and environment in which they are produced can provide important insights into the mechanisms that accelerate CRs to the observed energies. Figure 1.1 illustrates the interplay of these different cosmic messengers in the field of astroparticle physics.

The extremely small cross-section of neutrinos allows them to propagate through space nearly unabsorbed but, at the same time, poses a large challenge in their detection. Until now, only two sources of astrophysical neutrinos have been identified with acceptably high significance: TXS 0506+056 [115, 116] and NGC 1068 [114]. Large-scale diffuse neutrino emission has been detected from the Galactic Plane of the Milky Way Galaxy [113]. Gamma rays are easier to detect, either by satellite-borne experiments or ground-based telescopes, and numerous sources of gamma rays have been detected. The latest catalog of the Large Area Telescope onboard the Fermi Gamma-ray Space Telescope (Fermi-LAT), which is most sensitive to high-energy ($50\,\mathrm{MeV} < \mathrm{E} < 50\,\mathrm{GeV}$) (HE) gamma rays and can detect emission up to 300 GeV, contains close to 7200 sources [40]. The TeVCat catalog containing very-high-energy ($50\,\mathrm{GeV} < \mathrm{E} < 100\,\mathrm{TeV}$) (VHE) gamma-ray emitting sources currently has

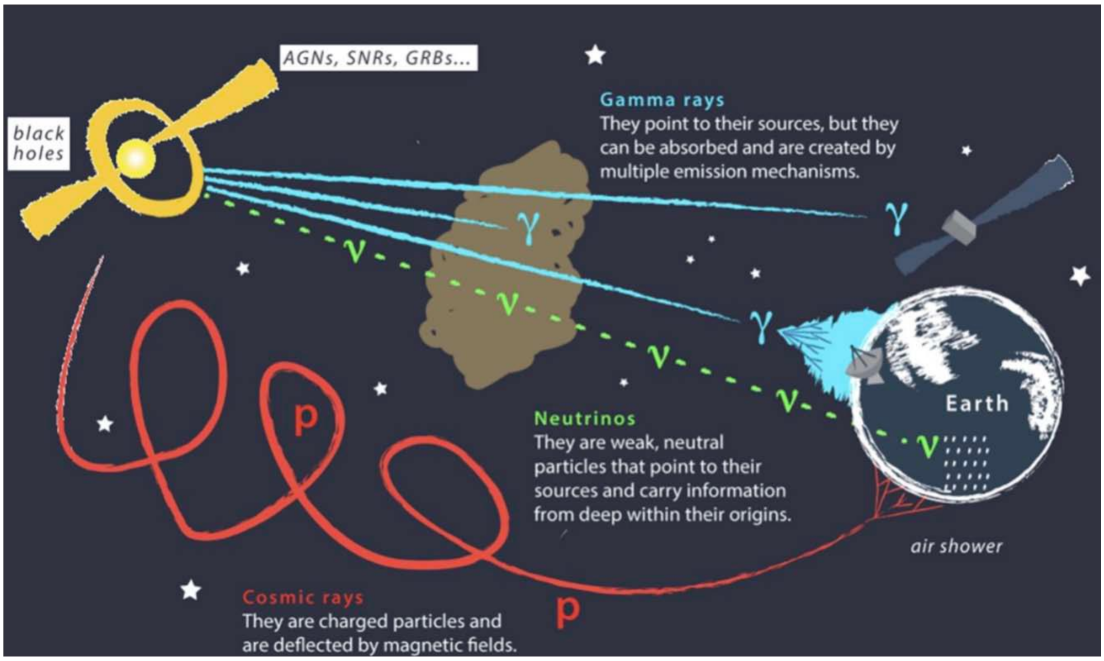

Figure 1.1: A sketch illustrating the field of astroparticle physics. Credit: Juan Antonio Aguilar and Jamie Yang, IceCube/WIPAC

over 300 entries [183]. The majority of the sources listed in TeVCat have been discovered by the second generation of Imaging Atmospheric Cherenkov Telescopes (IACTs), the MAGIC, H.E.S.S., and VERITAS telescopes. IACTs are ground-based detectors which indirectly observe gamma rays via the Cherenkov radiation emitted by secondary charged particles, that are produced in the interactions of gamma rays with the atmosphere. Satellites, such as Fermi-LAT can scan the entire sky within a timescale of hours due to their large field-of-views (FOVs) providing a large potential for the discovery of new sources. IACTs can only perform pointed observations but, on the other hand, possess a better angular resolution. The observation of VHE gamma rays from various sources within and outside the Milky Way has proven that efficient particle acceleration can take place, for example, in the relativistic jets of Active Galactic Nuclei (AGN) or in the shock fronts produced by fast-expanding material interacting with the interstellar medium (ISM).

However, one long-standing assumption still remains to be proven: the acceleration of CRs to energies around the *knee* at $\sim 3\,\mathrm{PeV}$ in Supernova Remnant (SNR) shocks. While HE and VHE gamma rays have been detected from these types of sources, their energies fail to reach the numbers necessary to explain the presence of PeV cosmic rays.

The search for sources capable of accelerating CRs to the knee, so-called *PeVatrons*, has been boosted in recent years by the advent of gamma-ray air shower observatories, such as HAWC and LHAASO, which are more sensitive to energies of several tens to hundreds of TeV. Linking gamma-ray signals at these energies to hadronic processes in their source of origin would prove the existence of PeV CRs. This effort is, however, not straightforward since gamma rays can be equally produced via leptonic emission mechanisms, in which case, they still provide important insight into the processes in astrophysical sources but do not explain the origin of the hadronic CRs. It is, therefore, of utmost interest to study the regions in the Galaxy emitting gamma rays around $\sim 100\,\mathrm{TeV}$ in the greatest possible detail. Measurements with high energy resolution are essential to distinguish between leptonic and hadronic emission mechanisms. Additionally, resolving the energy-dependent morphology of this emission will help identify its exact localization and, thereby, the nature of its source of origin. In this context, the field of VHE gamma-ray astronomy is confronted with a trade-off between a great capability of detecting the highest energetic emission with air shower arrays and the better energy and angular resolution that IACTs can provide. The next generation of IACTs, which are currently being built as part of the Cherenkov Telescope Array Observatory (CTAO), will improve the situation by distributing a large number of telescopes of different sizes over large areas in the Northern and Southern hemispheres. There is, however, another way to mitigate this contrast and enable currently operating IACTs to detect gamma rays up to 100 TeV. The MAGIC collaboration has shown this by observing the Crab Nebula, the brightest persistent gamma-ray source in the sky, close to the horizon at zenith angles up to 80° [140]. These observations provide the opportunity for comprehensive studies of PeVatron candidates before CTAO becomes fully operational and at a much lower cost.

Large zenith angle observations of the Crab Nebula with the MAGIC Telescopes are the main subject of this thesis. In this work, I present a detailed study of the MAGIC Telescopes' performance during observations at zenith angles between 50° and 80°. This study provides the first complete assessment of the functioning of the system in this zenith angle range. It lays the groundwork for future studies of PeVatron candidates, as it provides a reference that can be used to estimate the detection capabilities of MAGIC for the study of the highest energetic gamma-ray emission. The thorough evaluation of all aspects of the telescopes' performance will allow future observers to build solid science cases for their proposed observations.

The thesis is structured as follows:

- **Chapter 2** gives more details on the subject of PeVatrons, which source classes are considered to be PeVatron candidates, and how gamma-ray observations can help to identify them. It also gives a detailed description of the Crab Nebula, the first source unequivocally identified to accelerate particles to PeV energies, and the source that I analyzed in this thesis.
- **Chapter 3** gives an overview of gamma-ray astronomy, introducing gamma-ray production mechanisms and the techniques and current instruments of direct and indirect gamma-ray detections.
- **Chapter 4** gives a description of the MAGIC Telescopes. The hardware of the system is presented, and the data analysis software is explained.
- **Chapter 5** presents the main result of this thesis, the detailed study of the performance of the MAGIC Telescopes during observations at large zenith angles. I summarize the most important findings at the end of this chapter and provide an outlook into possible improvements and potential science cases.
- **Chapter 6** concludes this thesis with a summary of the previous chapters.

Chapter 2

The search for PeVatrons

2.1 The unknown origin of cosmic rays

Cosmic Rays (CRs) have been studied in great detail with space-based and ground-based experiments. They have been measured across twelve orders of magnitude in energy from 10^9 to 10^{20} eV, and their composition has been characterized. CRs are ionized nuclei, around 90% of them are protons, 9% alpha particles, the rest are heavier nuclei, and a small fraction are electrons and gamma rays [188]. Their energies are comparable to or much higher than their mass, meaning that they move at relativistic velocities [89]. Figure 2.1 shows the differential energy spectrum of CRs above 10 TeV as a function of energy per nucleus. The overall spectrum of cosmic rays follows a power law of the form $F(E) \sim E^{-\alpha}$, with α the spectral index. In log-log plots, power laws become straight lines and α their slope. The CR spectrum exhibits several features that correspond to changes in the slope which become more clearly visible when the flux is multiplied with a factor of $E^{2.6}$ as it was done in Figure 2.1. These features are referred to as the *Knee*, the *second Knee*, and the *Ankle*. A cut-off is observed at $\sim 50\,\mathrm{EeV}$. The origin of these changes in the spectral index is not entirely understood, but they are generally attributed to changes in the source population of CRs. Which sources exactly are responsible for the production of CRs and which processes accelerate them to the observed energies are the two major open questions in astroparticle physics. Since CRs are electrically charged, they do not travel on direct paths from their acceleration site to Earth but are deflected by intergalactic magnetic fields. This makes it challenging to identify their place of origin from CR observations alone. However, with basic considerations, some well-motivated assumptions can be made. The condition that the Larmor radius $r_\mathrm{L} = E/ZeB$ of a particle with charge Ze and energy E in a source with an average magnetic field strength B has to be smaller than the size R of the source puts an upper limit to the energy of particles contained in certain source types: $E < Ze\,B\,R$. The implications of this simple condition were summarized by Hillas in a classic plot [111], a recent version of which is shown in Figure 2.2. By placing types of sources in a diagram of magnetic field strength versus size and comparing them with Larmor radii, he gave a simple overview of which source can be responsible for the acceleration of the highest energetic cosmic rays beyond the ankle and which sources are capable of accelerating and containing lower energetic CRs [89]. In addition to the capability of different types of sources to accelerate CRs to different energy ranges, their diffusion properties give another clue to their place of origin. In a commonly used framework, the *leaky box model*, the escape of the CRs from the Galaxy is assumed to be a statistical process, where the CRs have a finite probability of escaping the "box" dependent on their interactions with the Galactic magnetic field [154]. The mean residence time of CRs in the Galaxy decreases with increasing energy, as higher-energy particles experience faster diffusion and have a greater probability of escaping. CRs produced within the Galaxy with energies below the knee are confined in the Galaxy long enough to account for the measured fluxes, whereas higher energetic particles escape faster. To explain the measurements, contributions from sources outside the Galaxy need to be considered. These considerations on the types of source capable of

CR acceleration and on the confinement of CRs in the Galaxy have led to the accepted interpretation of the features in the CR spectrum: at energies below the knee at $\sim 3\,\mathrm{PeV}$, CRs are assumed to originate from sources within our Galaxy, while extragalactic sources are made responsible for acceleration to energies above the ankle at $\sim 4\,\mathrm{EeV}$. The area between the knee and the ankle is likely a transition between these two source populations, with the second knee corresponding to a change analogous to the knee but for heavier nuclei. The cut-off at the highest energies is consistent with predictions of the so-called GZK effect, the inelastic scattering of CRs with the cosmic microwave background [188].

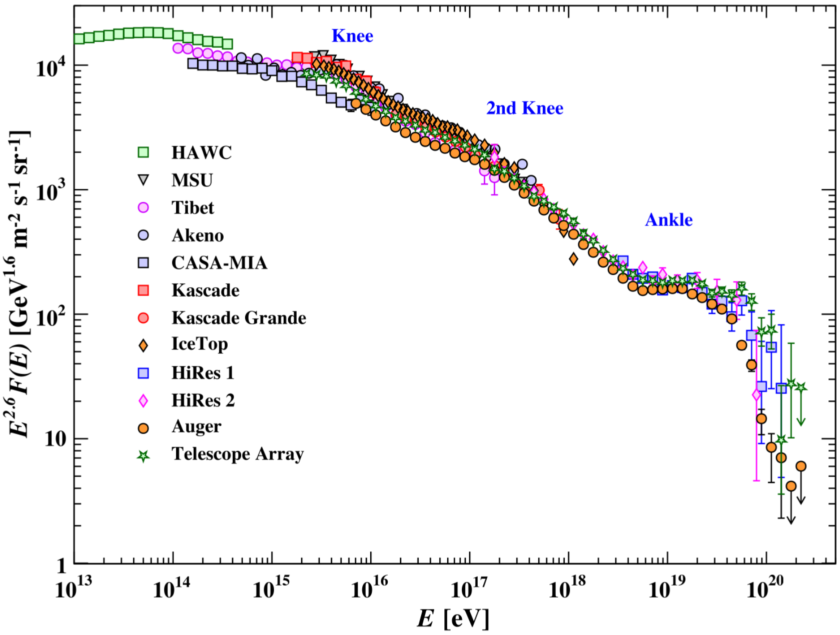

Figure 2.1: The differential all-particle energy spectrum of cosmic rays above 10 TeV. The flux along the y-axis is multiplied by a factor of $E^{2.6}$, which helps in identifying slight changes in the slope of the spectrum. These features are indicated as the *Knee*, the *2nd Knee*, and the *Ankle* and are generally attributed to changes in the source population of CRs. Taken from [188].

2.2 The need for Galactic PeVatrons

The assumption that CRs up to the *knee* of the spectrum originate from sources within the Galaxy requires the existence of Galactic particle accelerators reaching energies of at least $\sim 10^{15}\,\mathrm{eV}$. These sources that are accelerating charged particles up to at least PeV energies are called PeVatrons. The search for PeVatrons has lately received increasing attention, and several extensive review articles have been published in recent years, for example [68, 76, 48, 88], from which I summarize the most relevant aspects in the following sections. A particle is most efficiently accelerated by injecting it into a region filled with a uniform electric field $\mathcal{E}$. After crossing a distance L, the particle will have the energy $E_{\max} = ZeL\mathcal{E}$. The surroundings of cosmic particle accelerators are generally assumed to be filled with highly-conductive plasma. The equilibrium condition of such plasma requires an electric field $\mathcal{E}$ that locally balances the Lorentz force given by the magnetic field $\mathcal{B}$ and the plasma local velocity U: $\mathcal{E} = (U) \times \mathcal{B}$. The substitution of $\mathcal{E}$ then recovers the aforementioned Hillas criterion:

$$E_{max} = Ze\,L\,U\,B \approx 0.3Z \left(\frac{L}{\mathrm{pc}}\right) \left(\frac{U}{1000\,\mathrm{km\,s^{-1}}}\right) \left(\frac{B}{\mathrm{\mu G}}\right) \mathrm{TeV}, \tag{2.1}$$

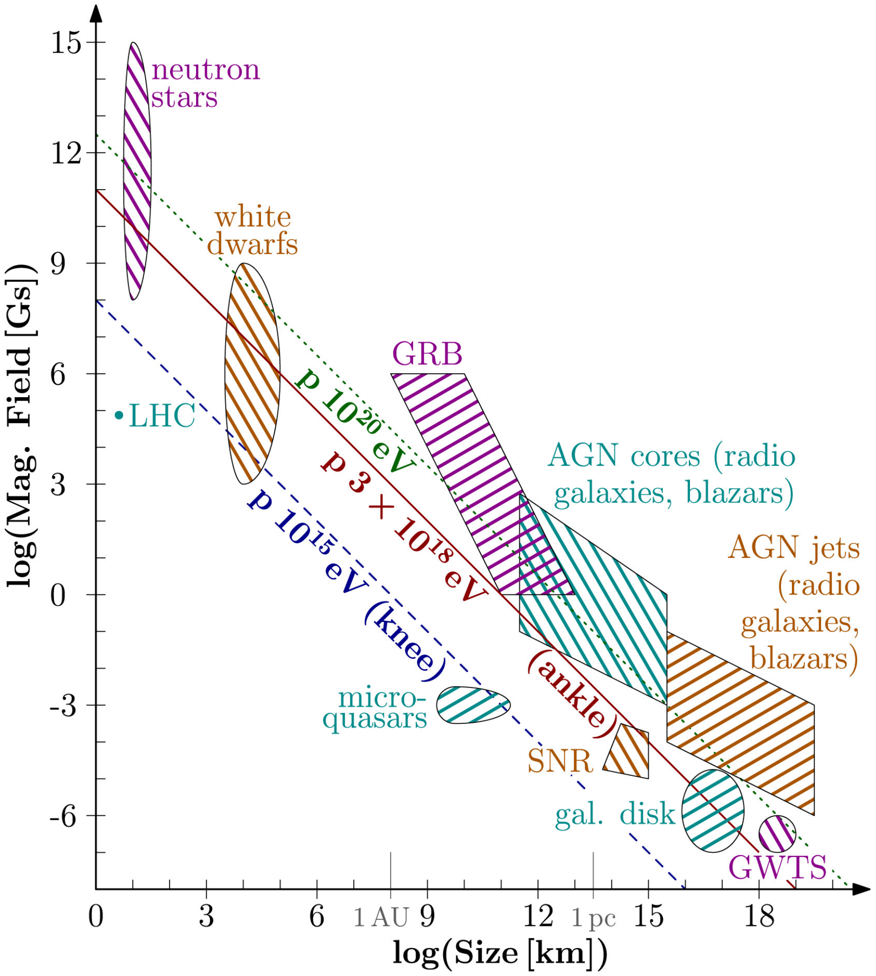

Figure 2.2: The classical Hillas plot with up-to-date data (see [44] for references) on various source classes. Larmor radii for protons at the knee (blue dashed line), the ankle (red solid line), and the cut-off at 10^{20} EeV (green dotted line) are indicated. Taken from [44].

where typical orders of magnitude have been inserted for the source size, plasma shock velocity, and the interstellar magnetic field within the Galaxy [76, 88, 48]. This shows that acceleration up to PeV energies is indeed possible within typical source parameters, given that the magnetic field is locally enhanced by several orders of magnitude. The latter has, in fact, been shown to be possible in the presence of strong shocks, as described in more detail in the following section. Equation 2.1 is a theoretical value under perfect acceleration conditions. In reality, gains in particle energy are always competing with energy losses or are limited by the lifetime of the accelerator. The latter is the major limitation for the acceleration of hadrons, as they do not suffer from losses through radiative processes as much as electrons (see Section 3.1).

2.3 Acceleration of Cosmic Rays

A simple, commonly invoked model of cosmic ray acceleration is *diffusive shock acceleration (DSA)*, or first-order Fermi (Fermi-I) acceleration. It is the advancement of second-order Fermi (Fermi-II) acceleration, proposed by Enrico Fermi in 1949 [82], who showed that particles that are colliding with stochastically-distributed, magnetized plasma clouds moving at an average velocity v gain a fraction of energy which is proportional to v^2 (hence Fermi-II, or second-order Fermi acceleration).

In the following, I give a short explanation of the DSA process, following the explanation in [161]. Astrophysical shocks form when plasma waves propagate at speeds faster than the speed of sound, which for a monoatomic ideal gas is given by $c_s = \sqrt{5P/3\rho}$, where P is the pressure and ρ the density. The thickness of the shock can typically be assumed to be infinitely thin compared to the relevant length scales in the gas on either side of it. The shock is assumed to be *collisionless*, signifying that the mean free path of particles crossing the shock is longer than the length scale of the shock, and they do not collide with the gas during the acceleration process. For a strong non-relativistic shock, propagating at a speed U much larger than c_s ($\mathcal{M} = U/c_2 \gg 1$), the relation between the plasma velocities and pressure on either side of the shock are given by

$$\frac{v_2}{v_1} = \frac{1}{4} \quad \text{and} \quad \frac{\rho_2}{\rho_1} = 4, \tag{2.2}$$

where variables with subscript 1 refer to the unshocked medium upstream of the shock, and subscript 2 refers to the shock medium downstream of the shock. In the rest frame of the shock, the upstream material moves toward the shock with velocity $v_1 = U$ and flows out of the shock with $v_2 = U/4$ in the downstream region. Viewed from the rest frame of either side of the shock, the respective other side moves with a velocity $v \equiv |v_2 - v_1| = 3U/4$ toward the shock. A fast particle with momentum $p_x = E/c$ crossing the shock front and colliding with the medium on the other side will be accelerated to an energy $E' = E + p_x v$ and, therefore

$$\frac{\Delta E}{E} = \frac{v}{c}. \tag{2.3}$$

This is true for both crossing from downstream to upstream and vice-versa, such that particles gain energy whenever they cross the shock front: the collision with the other side is always head-on, in contrast to the stochastic process of Fermi-II acceleration. The proportionality to the first order in v gives this process the name of Fermi-I or first-order Fermi acceleration.

The spectrum of particles that are accelerated through multiple crossings of the shock is determined from the energy gain and the escape probability. After having crossed the shock j times, each time gaining a factor $\beta = 1 + v/c$ in energy, a particle of original energy E_0 has been accelerated to the energy $E = E_0 \beta^j$. If the probability of a particle to remain in the shock region is given by $\mathcal{P}$, after j crossings out of N_0 particles, $N = N_0 \mathcal{P}^j$ remain in the acceleration region. It follows

$$\frac{N}{N_0} = \left(\frac{E}{E_0}\right)^{\log \mathcal{P} / \log \beta} \tag{2.4}$$

and therefore the spectrum of the particles following a power-law distribution:

$$n(E) \propto E^{\log \mathcal{P} / \log \beta - 1} \propto E^{-k} dE, \tag{2.5}$$

with $k = 1 - \log \mathcal{P} / \log \beta$ the spectral index.

The flux of particles that cross the shock with relativistic velocities is $F = nc/4$, and downstream of the shock they are advected with a bulk velocity of $U/4$. The fraction of particles lost per unit time is therefore $\frac{nU/4}{nc/4} = U/c$ and $\mathcal{P} = 1 - U/c$. Since the shock is assumed to be non-relativistic, i.e. $U \ll c$, it follows

$$\log \mathcal{P} = \log(1 - U/c) \approx -\frac{U}{c}. \tag{2.6}$$

Accounting for the fact that particles cross the shock at an angle with respect to the shock normal and integrating over all possible directions results in an average energy gain of

$$\beta = 1 + \frac{4}{3}\frac{v}{c} = 1 + \frac{U}{c}. \tag{2.7}$$

Analogous to Equation 2.6 $\log \beta \approx U/c$. This results in the spectral index

$$k = 1 - \frac{\log \mathcal{P}}{\log \beta} \approx 2. \tag{2.8}$$

DSA provides a simple model for particle acceleration in astrophysical shocks, which results in the power-law spectrum of accelerated particles and a spectral index roughly in line with what is to be expected from the measured CR spectrum at Earth.

Several assumptions are made in the described scenario. The back-reaction of the particle on the shock is neglected (*test-particle limit*), no magnetic field instabilities are assumed, and radiative losses are not taken into account. All of these factors are mutually dependent and have an effect on shock dynamics. The correct description of these effects, summarized under the term non-linear DSA, is the subject of active research and studied in numerical approaches. See [48] for a review.

2.4 The current status of PeVatron studies

2.4.1 The Supernova Remnant Paradigm

When a massive star explodes, the ejected material moves at velocities of the order of 10,000 $\mathrm{km\,s^{-1}}$ into the ISM. Since this exceeds the typical sound speed within the ISM by orders of magnitude, a shock front is formed between the extending ejecta material and the surrounding medium. The resulting structure is called a Supernova Remnant (SNR). In the first $\sim 200\,\mathrm{yr}$ of the SNR evolution, the shock expands freely into the ISM (*free expansion phase* or *ejecta-dominated phase*). It accumulates more and more matter, increasing the total mass of the outward-moving material and decreasing the shock speed. When the mass of the accumulated material becomes comparable to the ejecta mass, the SNR enters the so-called *Sedov-Taylor phase*. Here, the shock velocity decreases while the total energy of the system is contained as long as radiative losses are negligible. This phase is also called the *adiabatic phase*. Once the shock speed decreases such that the temperature in the shocked gas drops below $\approx 10^7\,\mathrm{K}$, electrons and ions start to recombine and further cool the gas by optical line emission. This phase is called the *radiative phase* of the SNR. Once the shock velocity has decreased to the level of the typical turbulence within the ISM, the SNR dissolves and has reached the end of its lifetime. For an extensive reference on the physics and evolution of SNRs, I refer the reader to [182].

Gamma rays are produced in the early phases of the SNR evolution due to particle acceleration via DSA in the SNR shock. The H.E.S.S. collaboration was able to resolve a shell-like structure of the emission at TeV energies in several young SNRs, providing proof that efficient particle acceleration takes place at the SNR shock (e.g., [99, 7, 97]). A clear hadronic signature in the gamma-ray emission has been found at GeV energies by Fermi-LAT from the SNRs IC 443 and W44 through observations of the characteristic pion-bump [9] (see Section 3.1.3). At higher energies, it is still unclear whether the observed emission originates from accelerated leptons, hadrons, or a mix of both. The answer to this question is of great interest since SNRs play an important role in the context of the origin of Galactic CRs. They are believed to produce the bulk of the CRs measured at Earth and to be capable of accelerating CRs to energies beyond PeV. They have been the most popular types of sources considered to be responsible for the acceleration of cosmic rays within the Galaxy since 1930s, when Baade and Zwicky first proposed this scenario [39]. There is well-motivated reasoning as well as circumstantial evidence for this assumption [68, 48]:

- The energetics of supernovae match the measured energy density of CRs on Earth. It would be sufficient if 1-10% of the energy released in supernova explosions is converted into energy of CRs.

- Acceleration of particles via DSA at SNR shock fronts produces a particle energy spectrum compatible with the CR spectrum measured at Earth.

- It has been shown theoretically that magnetic field enhancements of the order of 100 µG at SNR shock fronts are feasible and can provide the necessary strengths of magnetic fields for acceleration up to PeV energies. This is further supported by X-ray observations of SNR shells that show evidence for an enhancement of the local magnetic fields several orders of magnitude above the typical value in the ISM.

- Gamma rays have been observed from SNRs. The Fermi-LAT collaboration has unambiguously identified signals of neutral pion decay from SNRs, which proves the existence of highly energetic protons in this source [9]. Multi-TeV gamma-ray emission has been observed as well from SNRs, partly even resolving the shell-like structure of the emission, providing evidence for the efficient acceleration of particles at the SNR shock front.

While this list justifies the focus of the community on SNRs in the search for PeVatrons, there is still no proof that these sources are capable of accelerating CRs up to PeV-energies and beyond. So far, no measurements of emission from SNRs have shown evidence for the acceleration of particles to these energies.

A possible explanation for this is the potentially short duration in which SNRs act as PeVatrons. The shock velocity needs to be high enough to enable the acceleration to PeV-energies, which is only the case at the end of the free expansion/the beginning of the Sedov-Taylor phase of SNRs, referring to an age of the order of 100 years [87, 68]. The magnetic field enhancement at SNR shocks is primarily assumed to be due to so-called non-resonant streaming instabilities, often referred to as Bell instability [46]. This enhancement, however, can only reach the values necessary for PeV acceleration when shock velocities and/or densities are extraordinarily high. These two conditions compete with each other, since high densities of the surrounding medium naturally decrease the shock front velocities. Therefore, only very rare cases of SNRs might be actually capable of being PeVatrons, reducing the rate of Galactic SNR PeVatrons to a few percent of the Galactic supernova rate. Combined with the short duration of the PeVatrons phase, this results in only one SNR PeVatron being active for the order of ~ 1 century every 10^4 years. This could prevent us from ever proving in real time that SNRs are PeVatrons [69]. Gamma-ray emission induced by interactions of PeV protons might, therefore, not be directly observable from the known SNRs but could be detected from nearby molecular clouds, in which the escaped CRs interact and create highly energetic gamma-ray emission for timescales of the order of 10^4 years [87]. The difficulties in providing an enhanced magnetic field in the shock could be partly mitigated by providing a more precise description of the medium into which the SNR is expanding. Typically, a constant magnetic field is assumed, but Supernovae (SNe) often occur in dynamic environments such as star-forming regions (SFRs) (see Section 2.4.2), where the magnetic field can be much more dynamic. In addition, the canonical SNR scenario also suffers from other shortcomings. The measured gamma-ray spectra of SNRs in the TeV range, which should mimic the spectrum of accelerated particles, seem steeper than the expected $\sim E^{-2}$. The diffusion of cosmic rays within the Galaxy has been estimated to cause a spectral steepening of the article spectrum which is injected into the ISM of 0.3-0.6. The measured spectral index of 2.7 at Earth would, therefore, correlate to an induced spectrum of $\sim E^{-2.1}$ to $\sim E^{-2.4}$, steeper than expected. In the CR composition, the isotopic abundance of ^{22}Ne/^{20}Ne is larger than what is measured in the solar wind. This is difficult to explain within the SNR framework and scenarios where at least part of the CRs are accelerated in other types of sources that are being increasingly discussed in the context of PeVatrons.

2.4.1.1 The Supernova Remnant G106+2.7 - a promising PeVatron candidate

In recent years, the SNR G106+2.7 has received increased attention from the community. G106+2.7 has an interesting comet-like shape with two bright regions, dubbed the "head" and the "tail" region, exhibiting emission from radio to gamma rays. Close to the head region, a Pulsar Wind Nebula (PWN) is located, called the "Boomerang" nebula, with the pulsar PSR J2229+6114 off center of the nebula. This complex morphology and the vicinity of the PWN make it hard to distinguish between a hadronic or leptonic origin of the emission. The air shower arrays Tibet-ASγ, High-altitude Water Cherenkov Observatory (HAWC), and Large High Altitude Air Shower Observatory (LHAASO) [175, 18, 59] have all detected emission above tens of TeV from this region which - if hadronic - points to protons of the energy of at least 500 TeV, making it a PeVatron candidate. However, due to their limited angular resolution, they could not determine whether the emission originates from the head or tail region. MAGIC observed the region with unprecedented angular resolution up to 20 TeV [139]. The study showed that the most energetic emission observed by the air shower arrays most likely originates from the tail region, and evidence for the acceleration of hadrons in this emission region was found. While the particles responsible for the emission in the head region might be a mixture of leptons accelerated in the PWN and protons accelerated in the SNR shock, the tail region is best described by a purely hadronic model, in which CR have escaped the SNR and illuminate nearby molecular clouds [139]. To unambiguously identify G106+2.7 as a hadronic PeVatron, further observations with high angular resolution need to be carried out beyond tens of TeV.

2.4.2 Star-forming regions

SFRs are areas in space typically within dense molecular clouds that exhibit favorable conditions to produce new stars. Most stars are formed in star clusters and produce stellar associations. OB associations consist of bright and massive O- and B-type stars which exhibit powerful stellar winds. These winds and supernovae in these stellar clusters are likely sources of CRs. The interactions of multiple stellar winds and of supernova ejecta with surrounding gas can lead to multiple shocks capable of efficiently accelerating CRs [55].

2.4.2.1 The star-forming region Cygnus X

The Cygnus X region is a large SFR located 1.4 kpc from Earth and a size of $\sim 200\,\mathrm{pc}$. It contains the Cyg OB2 association. The largely extended region has been studied by multiple wide-FOV gamma-ray instruments which found emission from HE gamma rays detected by Fermi-LAT [8, 35] to VHE gamma-rays detected by HAWC [3] and up to ultra-high-energy ($E > 100\,\mathrm{TeV}$) gamma rays detected by LHAASO [131]. The cosmic ray density profile can be inferred from the gamma-ray emission measurements. A radial profile decreasing with $1/r$ could be explained by a continuous injection of CRs accelerated in the shocks of stellar winds of the massive stars in the system [55, 15]. A constant profile would point to a burst-like injection from a supernova explosion. While the study of [15] clearly pointed to a $1/r$ profile of the CR density, [3] could not clearly distinguish between the two cases. The observations by LHAASO also favored a $1/r$ profile of the CR density and from the detection of PeV photons from the region, they conclude that a powerful PeVatron should sit at the center of the system for which they see CygOB2 to be a powerful candidate. The extension of the gamma-ray emission observed by the mentioned instruments spans several degrees and is larger than the FOVs of current IACTs. Since Cygnus X is a very complex region, not only containing CygOB2 but several other sources such as the microquasar Cygnus X3 and the SNR γ-Cygni, observations with the high angular resolutions that IACTs are essential to fully understand the sources of gamma-ray emission in Cygnus X.

2.4.3 The Galactic center

The vicinity of the Galactic Center (GC) contains various sources that are capable of accelerating charged particles and is filled with regions of molecular gas, which provide a rich target for these particles to interact and create gamma rays. Thus, to properly understand the nature of the emission in this complex region, observations across a broad energy range with high angular resolution are needed, as well as a precise knowledge of the gas distribution. The H.E.S.S. collaboration has performed several detailed studies in the VHE gamma-ray band of the GC region, favored by the location of their telescopes in the southern hemisphere, which provides good conditions for the observation of this sky region. In 2016, they claimed the presence of a PeVatron in the GC [98]. This claim was, on the one hand, based on the radial profile of the CR density, which indicated freshly injected CRs into the region. On the other hand, their measured gamma-ray spectrum showed no cut-off and was consistent with particle spectra extending to PeV energies. The signal was extracted from an incomplete annulus (*Pacman region*) around Sgr A*. For MAGIC, the observational conditions are less favorable since the GC is only observable under zenith angles $>58°$, which, on the other hand, provides a higher sensitivity at TeV energies (the performance of MAGIC at large zenith angles is one of the main subjects of this thesis and studied in great detail in Chapter 5). Results of $\sim 100\,\mathrm{h}$ of observations of the GC with MAGIC did not reveal clear evidence for the presence of particles up to PeV energies since the measured spectrum favored a break around 17 TeV [138]. These results from MAGIC match a second, more detailed study by the H.E.S.S. collaboration from 2018, using advanced analysis techniques to model the complex region. In this publication the definition of the signal region was also adjusted with respect to the 2016 study, which led to a increase in the estimated flux of $\sim 80\%$ over a wide energy range. Recent results from the HAWC collaboration [19] are in line with the original PeVatron claim by the H.E.S.S. collaboration, as they detect emission up to 114 TeV from a point source at the GC. Due to the limited angular resolution of HAWC, the emission region is less confined and overlaps with the positions of Sgr A* and another point source identified by H.E.S.S., the Arc (HESS J1746-285). The LHAASO collaboration presented multiple sources with gamma-ray emission extending to 100 TeV and beyond in their recent first catalog of gamma-ray sources [58]. The GC is, however, not part of this catalog. While this region certainly remains of interest in the context of cosmic ray acceleration, the non-detection by LHAASO and the curved spectra measured by MAGIC and the 2018 H.E.S.S. publication suggest that the PeVatron scenario needs further investigation.

2.4.4 Pulsar Wind Nebulae

2.4.4.1 Pulsars

Pulsars are created during core-collapse supernovae at the end of massive stars' (> 8 solar masses) lives. During these explosions, the outer layers of the stars are expelled, forming the SNR, while a dense inner core collapses gravitationally onto itself. Its mass typically ranges from 1-3 solar masses with a size of the order of $\sim 10\,\mathrm{km}$ in diameter. The angular momentum and magnetic flux of the progenitor star are conserved, resulting in rotational periods P from milliseconds to seconds and magnetic field strengths B between 10^8 and 10^{11} T for the remaining neutron star [94]. Neutron stars are the densest stellar objects known so far and create the strongest known magnetic fields in the universe.

Baade and Zwicky first postulated the existence of neutron stars in 1934 [39]. Woltjer suggested in 1964 that these neutron stars could exhibit magnetic fields up to 10^{12} T [186] and Pacini postulated pulsed electromagnetic radiation from neutron stars in 1967 [156]. Almost simultaneously, Jocelyn Bell discovered the first radio pulsar using observations performed with the Mullard Radio Astronomy Observatory [109].

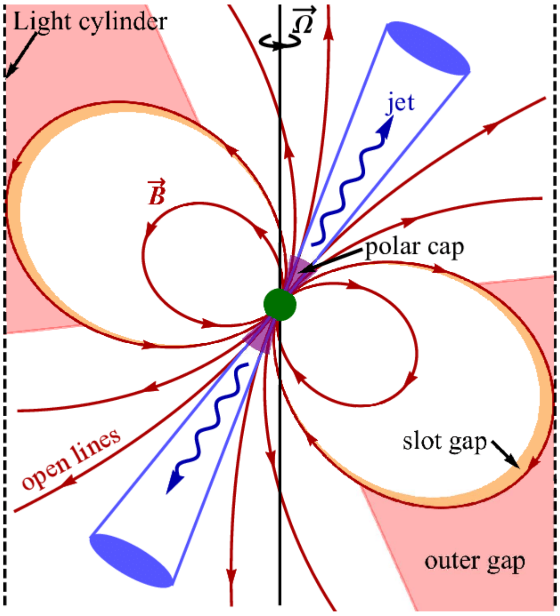

Figure 2.3: A schematic of a pulsar's magnetosphere, highlighting the regions where particle acceleration has traditionally been believed to take place. Taken from [92] under `https://creativecommons.org/licenses/by/4.0/`

A sketch of the magnetic field structure of a pulsar can be seen in Figure 2.3. The polar axis of the magnetic field can be inclined with respect to the rotational axis of the neutron star. The magnetic field lines are closed and co-rotating with the neutron star up to the light cylinder at a radius $R_{LC} = c/\Omega$, where $\Omega = 2\pi/P$ is the angular velocity of the star. Beyond the light cylinder, the rotational velocity would exceed the speed of light c; hence the magnetic field lines cannot co-rotate anymore and spiral outward.
The free charges inside the neutron star rotating through the strong poloidal magnetic field create an electric field at the surface of the star that can overcome the gravitational pull of the object, extracting electrons from its surface. These extracted electrons fill the space surrounding the neutron star and form a plasma magnetosphere that is essentially perfectly conductive, where the electromagnetic interactions greatly dominate over other types of forces. Goldreich and Julian proved that, at the equilibrium, the space charge density ρ_{GJ} of the magnetosphere is given by [91]:

$$\rho_{GJ} = \frac{-\vec{\Omega}\cdot\vec{B}}{2\pi c}\frac{1}{1-\left(\frac{\Omega r}{c}\sin\theta\right)^2}, \tag{2.9}$$

where $\vec{\Omega}$ is the angular velocity, $\vec{B}$ the magnetic field, r and θ polar coordinates and c the speed of light. The electric field resulting from ρ_{GJ} and the Lorentz force on the electrons balance each other such that no particle acceleration is possible. However, if the net charge density is different than the Goldreich-Julian density, an electric field component parallel to the magnetic field appears. The latter is not screened by the Lorentz force and can accelerate electrons to (ultra)relativistic energies along the magnetic field lines. The electrons emit curvature radiation as gamma rays when traveling along the bent field lines. Subsequent pair-production via interactions of the gamma rays with the strong magnetic field (close to the star) or lower energetic X-rays (at larger distances) increase the charge density, bringing it closer to ρ_{GJ}. This poses a limit to the maximum potential drop that is available to particle acceleration in the pulsar magnetosphere. These processes of acceleration, radiation, and cascading are interlinked, affecting the geometry of the acceleration sites ranging from small

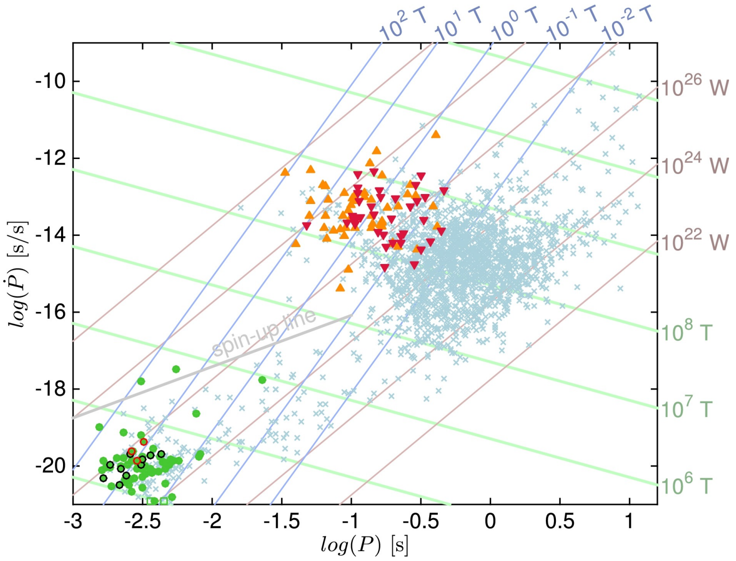

Figure 2.4: Gamma-ray and radio pulsar population shown as a distribution in period (P) and period time derivative ($\dot{P}$). Orange, red and green marked pulsars show gamma-ray emission. Pulsar marked in light blue have only been detected in radio. Figure taken from [94].

gaps to large regions. These feedback processes also limit the gamma-ray luminosity. In energetic pulsars, acceleration is efficient but also leads to high pair multiplicities resulting in efficient screening and small regions available for acceleration. In these cases, the fraction of the pulsar's rotational energy transferred to gamma-ray luminosity is lower than in less energetic pulsars, where lower pair multiplicities allow accelerations in larger regions resulting in more efficient particle acceleration and radiation [94].

As shown in Figure 2.4, from most of the over 2400 pulsars that have been discovered to date, only radio emission has been detected. Around 300 of these have also been detected in gamma rays by Fermi-LAT. Only 3 pulsars have been published in VHE gamma rays by IACTs: The Geminga pulsar, the Vela pulsar, and the Crab pulsar.

Several zones have been proposed as possible acceleration and emission sites depending on the observed wavelength of pulsed radiation detected from pulsars: The polar cap, the slot gap, and the outer gap as indicated in Figure 2.3. Gamma-ray observations of pulsars have been crucial in evaluating these models. The polar cap, the first zone to be proposed to be an acceleration site [71, 163], was abandoned as such following the successful detection of the Crab pulsar at energies above few tens of GeV by MAGIC [29, 26], VERITAS [181] and Fermi-LAT [1, 2]. Other models, including the slot gap and outer gap models, as well as scenarios based on equatorial current sheets or striped winds, are still compatible with observations and remain under current investigation. A deeper understanding of known gamma-ray pulsars and the detection of new ones are necessary to resolve the question of which scenarios or combinations thereof best describe the structure of the pulsar's magnetosphere and particle acceleration sites therein.

2.4.4.2 Pulsar Wind Nebulae

PWNe are a subclass of SNRs (Section 2.4.1) in which a central pulsar is powering the emission, which is then dominated by non-thermal processes. The dominating processes are Synchrotron and Inverse Compton (IC) emission by electrons and positrons (see Section 3.1) that originate from the pulsar magnetosphere and are accelerated to relativistic energies in the system. The electrons and positrons stream outward from the pulsar in a highly magnetized cold (i.e. dark and non-emitting) Pulsar Wind (PW). In the interaction with the more slowly outward-moving ejecta of the SN, a Termination Shock (TS) is formed.

The PW flow becomes disordered, and the leptons are re-accelerated to relativistic energies. Synchrotron and IC emission is produced. Contrary to classical SNRs, PWNe have a stronger emitting central region compared to the emission produced in the limbs of the system in the SNR shell. Figure 2.5 shows a sketch of the radial structure of such a system.

Gamma rays are produced in PWNe via IC emission. The highly relativistic electrons and positrons transfer much of their energy to photons from various photon fields present in the nebula. The most dominant contribution comes from the synchrotron photon field, produced by the same electron population that then up-scatters these photons to gamma-ray energies via IC. The detailed study of the synchrotron emission in relation to the IC emission provides great potential to constrain the number of electrons and the strength of the magnetic field that are present in the nebula (see Synchrotron Self Compton (SSC) in Section 3.1.2).

Around 100 PWNe have been identified in our Galaxy [153]. They undergo an interesting and complex evolution that has only recently gotten more attention in modeling. After the initial phase in which the PWN expands freely in the SN ejecta material ("Free expansion phase"), in the second, so-called "Reverberation Phase", the outer boundary of the PWN hits the Reverse Shock (RS) of the SNR. For less energetic PWN, the nebula will be strongly compressed to a small volume, while for energetic systems, the compression by the RS will lead to an increase in the internal pressure of the PWN until it becomes comparable to the external pressure and a new steady, subsonic expansion is beginning. In late stages, the central pulsars, themselves having a high kick velocity of 100-500 km/s, leave the system and create cometary-shaped, bowshock nebulae in their direct interaction with the ISM. For a detailed study of the modeling of the reverberation phase of PWN, refer to [41, 43, 42] and to [153] for a review on PWNe evolution. They are remarkable laboratories for studying plasma dynamics, energy conversion processes, and particle acceleration up to PeV energies. Their bright emission across the entire electromagnetic spectrum and their vicinity to Earth allows detailed and comprehensive studies of these sources, providing valuable insight into similar astrophysical processes occurring, for example, in Gamma-ray Bursts (GRBs) or AGN. Pulsars are difficult to study directly unless pulsed emission is observed, but since they provide the seed energy, magnetic field, and particle population for their surrounding PWN, studies of the latter can bring new insights into the properties of rotating neutron stars.

Most of our current understanding of PWNe is based on observations of the Crab Nebula. It stands out among the PWN population due to the extraordinarily high spin-down power of its pulsar. This, together with its proximity to Earth (~ 2 kpc) and young age (~ 1000 years), makes it the brightest persistent, non-thermal object in the sky in most wavelengths, particularly in gamma-rays, and by that, the best-observed object of its class and probably the best-studied astrophysical source outside the Solar System. Hence, more details on the evolution, particle acceleration, and emission mechanism of PWNe will be given in the following sections about the Crab Pulsar and Nebula.

2.5 The Crab Nebula - a PeVatron

The Crab Nebula is the remnant of a core-collapse supernova explosion that was recorded in 1054 by Chinese Astronomers. Shortly after its detection by John Bevis in 1731, it became the first object in Charles Messiers Catalogue of Nebulae and Star Clusters. It has since become the best-studied astronomical object outside the Solar System. It belongs to the class of Pulsar Wind Nebulae (PWNe), also known as filled-center SNRs, as they are the remnants of stellar explosions and contain a pulsar at their center which is actively transporting energy into the system thereby creating a second nebula in the center of the SN ejecta. The Crab Nebula has long been identified as an extraordinary particle accelerator capable of transforming a large fraction of its energy into the kinetic energy of particles

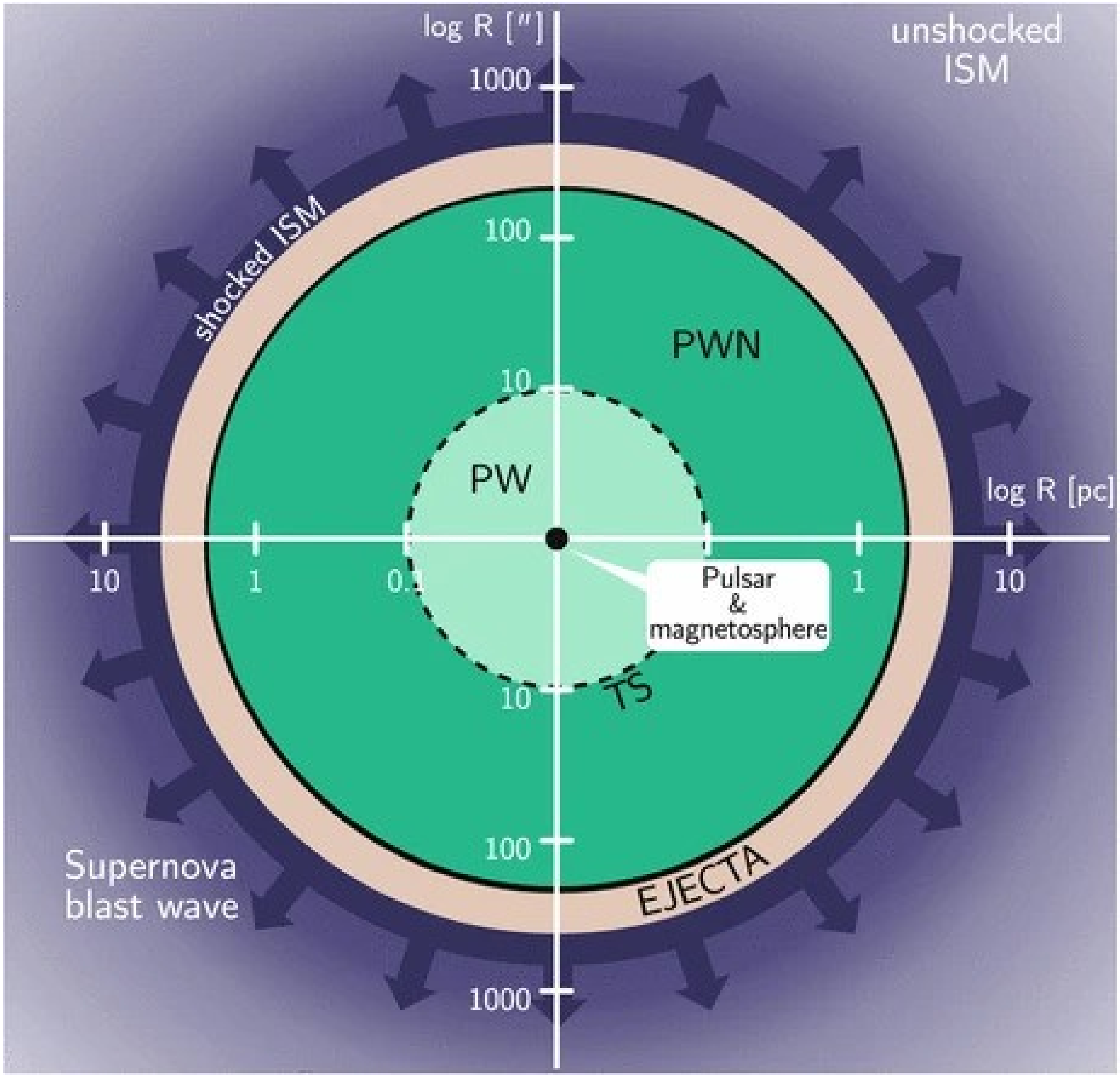

Figure 2.5: A sketch of the structure of PWN/SNR system, taken from [77]. Radial distances are expressed in logarithmic scale in parsec along the x-axis and arcseconds along the y-axis. In the center, the cold, highly magnetized PW is freely expanding until the TS. The leptonic plasma of the PWN is confined between the TS and the contact discontinuity with the ejecta material of the SN. The ejecta are freely expanding outward until the forward shock that is formed with the ISM.

with extremely high energies. Since the detection by LHAASO of PeV gamma-ray emission, the Crab Nebula has been undoubtedly proven to be a PeVatron. This source is a unique laboratory, the study of which can provide valuable insight into the role that PWNe play in the context of CR acceleration. In this section, I will give an introduction to the current state of knowledge on the Crab Pulsar and Nebula with a special emphasis on the importance of its gamma-ray emission in the understanding of its nature.

2.5.1 The Crab Pulsar

The first evidence for a pulsating radio source in the Crab Nebula was presented in 1968 by Staelin and Reifenstein based on observations with the National Radio Astronomy Observatory in Green Bank, West Virginia [172]. Shortly after, optical pulsations from the same source with a period of $\sim 33\,\mathrm{ms}$ were discovered [65, 148] as well as pulsed X-ray emission [85] and first evidence for pulsed gamma-ray signals [179]. The Crab Pulsar was the first pulsar firmly associated with a known SNR, providing proof that pulsars are, in fact, rotating neutron stars that are formed during explosions of massive stars.

Since its initial discovery, the Crab Pulsar has been studied in detail across all wavelengths of the electromagnetic spectrum by numerous instruments. It rotates with a period P of $33.7\,\mathrm{ms}$ which is slowing down at a rate of $\dot{P} = 4.2 \cdot 10^{-13}\,\mathrm{s\,s^{-1}}$ [171]. The corresponding loss of rotational energy is $\dot{E} \approx 5 \cdot 10^{38}\,\mathrm{erg\,s^{-1}}$, most of which is injected into its surroundings in the form of a highly magnetized pulsar wind expanding at relativistic speed. Only $\sim 1\%$ of the spin-down power is converted into electromagnetic radiation. This emission has been detected from the MHz radio band up to TeV energies.

The broadband pulsed emission of the Crab Pulsar up to HE gamma-rays is attributed to synchro-curvature radiation. Various models describing necessary particle acceleration for the observed spectra predicted cut-offs in the SED at different energies. The polar cap model, which was the preferred model at that time, could be ruled out by MAGIC observations of pulsed emission above 25 GeV in 2008 [30], pointing to emission regions further out in the magnetosphere. Subsequent observations by MAGIC and VERITAS detecting pulsed emission beyond 400 GeV and complemented by the detection of the P2 pulse at TeV energies [32], more and more pointed to a second component present in the emission. The Fermi-LAT collaboration could firmly identify a spectral break in the gamma-ray emission between 1–10 GeV, consistent with the one expected from curvature emission [1]. The spectrum of both pulses P1 and P2 can be fit with a smooth power law from $\sim 10\,\mathrm{GeV}$ to $\sim 1.5\,\mathrm{TeV}$, strongly suggesting that a single mechanism is responsible for the emission in this energy range. Since the gamma-ray emission at the highest energies can not be explained by synchro-curvature radiation, IC is the most probable emission mechanism of the second component. The process responsible for the particle acceleration necessary to produce this emission is still under debate. Possible scenarios are a two-stage cascade process [32], the acceleration in the equatorial current sheet [103], the striped-wind scenario [147], or the magneto-centrifugal scenario [155].

2.5.2 The Crab Nebula

Distance measurements

Measuring the distance of the Crab Nebula from Earth has proven difficult over the decades of studying it, owing to a variety of methods to estimate the distance, all of which have some difficulties and partially large uncertainties. Virginia Trimble provided an overview in 1973 of the various methods available at the time and concluded that the most probable distance of the nebula is around 2kpc [176]. This value has been confirmed since (e.g., [120]) and is the nominal value still cited today.

Broadband Emission

Already in the 1960s, it was widely accepted that the continuous emission observed from the central region of the Crab Nebula in radio and optical wavelengths was caused by synchrotron radiation of highly energetic electrons in the nebula. This was first proposed by Shklovsky and soon after confirmed by polarization measurements of optical and radio emission [169]. In 1963, X-ray emission was discovered from the central region of the nebula [50]. Its origin was unclear at first, with [64] proposing it to be thermal emission from a central neutron star, the existence of which was still speculative at that time. Shklovsky and Woltjer proposed a unified emission scenario from radio to X-rays based on synchrotron radiation [170, 187] which was confirmed by the observation of X-ray polarization in 1972 [150]. At the time of its discovery, it was clear that the X-ray emission would play an important factor in understanding the Crab Nebula since the power radiated in X-rays was found to be at the same level as in the optical and much larger compared to the radio band. There was also a clear consensus on the fact that the electrons responsible for the observed X-ray emission could not be relics of the supernova explosion. Their cooling timescales were too short, and an additional flow of energy and particles from the nebula's center had to be present to explain the X-ray emission, e.g., [164]. Pacini proposed a neutron star as this central source [156].

In 1967, gamma-rays up to 560 keV were observed from the Crab Nebula[104] smoothly connecting to the previous hard X-ray observations. Suggesting again that the entire observed spectrum is produced by synchrotron emission. This study showed that electrons with energies up to 10^{14} eV had to be present in the nebula and gave an estimate of the total energy that had to be injected into the nebula in the form of relativistic electrons of $E = 5 \cdot 10^{49}$ erg. The source of this injected energy became evident with the discovery of the Crab Pulsar in 1968.

This discovery and the subsequent learnings about pulsar dynamics sparked many efforts to model the magnetic field and particle outflow from the pulsar and the resulting electromagnetic emission in the nebula. Until today, the modeling is based on the assumption that beyond the TS, the pulsar flow is well described by magnetohydrodynamics (MHD). The energy injected into the pulsar wind per unit time by the central pulsar is described with the following equation

$$\dot{E} = \kappa \, \dot{N}_{GJ} \, m_e \, \Gamma_w \, c^2 \, (1 + \frac{m_i}{\kappa m_e}) \, (1 + \sigma), \tag{2.10}$$

$\dot{N}_{GJ}$ is the Goldreich-Julian charge density (see 2.4.4.1) and is well constrained by the pulsars rotational period and its magnetic field. Lesser known parameters, which can be constrained by observations of the nebular emission, are

- κ, the pair multiplicity, giving the number of pairs created in the pulsar's magnetosphere by one electron extract from its surface.
- Γ_w, the pulsar wind Lorentz factor,
- $\sigma = \frac{B^2}{4\pi n_\pm m_e c^2 \Gamma^2}$ the ratio between the Poynting flux and the kinetic energy of the pairs in the wind, the so-called magnetization.

The original MHD-models proposed since the 1970s [158, 122, 123, 79] could account for the magnetic field strength, the synchrotron luminosity and the observed reduction of the size of the emission region with increasing frequency by assuming a wind magnetization $\sigma \approx 3 \cdot 10^{-3}$, a wind Lorentz factor $\Gamma_w \approx 3 \cdot 10^6$, and an injection rate of particles in the nebula $\dot{N} \approx 10^{38}\,\mathrm{s}^{-1}$ [31]. By introducing an additional electron population to the electrons from the pulsar wind ("wind electrons") to account for the radio emission ("radio electrons"), the broad-band observed synchrotron emission from radio up to HE gamma-rays could be well reproduced. The advent of VHE gamma-ray astronomy and the discovery and spectral measurements of emission up to tens of TeV from the Crab Nebula by Whipple [184, 178], CANGAROO [174] and HEGRA [13] in the 1990s unveiled an additional previously predicted emission component: IC emission of that same electron population on the synchrotron, far-infrared or CMB photon fields [72, 11, 36, 37, 73].

The most recent and complete phenomenological modeling of the Crab Nebula's broadband SED has been provided by [78]. The model describes the emission from two electron populations (radio and wind electrons) and dusty plasma in a radially dependent magnetic field and is fitted to a large number of spectral and extension measurements from radio to VHE gamma-rays, see Figure 2.6.

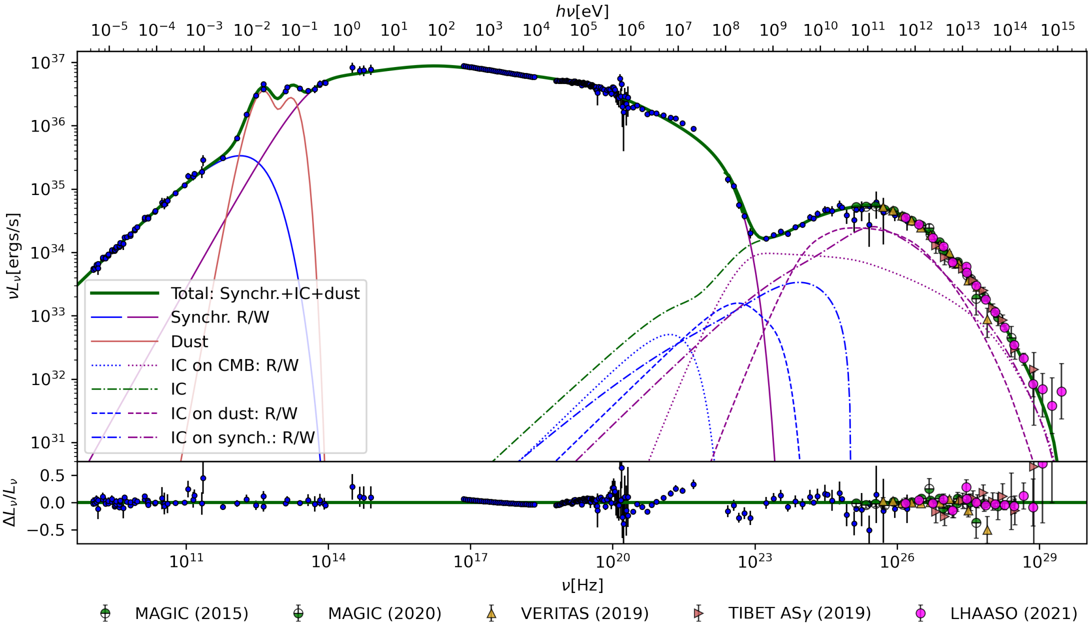

Figure 2.6: The broadband SED of the Crab Nebula. The figure was taken from [78], which gives details on the data sets presented here. The spectrum is modeled with a population of radio and wind electrons producing synchrotron radiation and IC emission via scattering of the same electron on the cosmic microwave background, dust radiation fields, and the synchrotron component.

Morphology

In 1921, Lampland described the object as having a complex structure of ovate shape with "thread-like filaments, giving it a peculiar frayed or raveled aspect along its border", with these filamentary structures being less pronounced in its much brighter diffuse appearing center [129]. The Crab Nebula was described as a filament structure that only emits lines and an amorphous central region that exhibited continuous emission. Scargle disestablished the term amorphous since it was clear that the center also showed fine structures.

The optical continuous emission was measured to come from a region of around $2'$ in diameter, 2-3 times smaller than the size of the radio emitting region [49].

The observations that lead to the discovery of X-ray emission from the nebula, exploited a lunar occultation of the nebula to obtain estimates of the angular size of the X-ray emitting region [50]. The total angular width of the X-ray source was estimated to be $1'$, less than half of the optical size, pointing to electrons being accelerated in the central region. These observations were followed up by [151], who showed an idealized circle-shaped source with a diameter of $100''$. It was confirmed that the X-ray and optical sources have the same emission region, the former having a smaller extension.

In 2000, Chandra observed a jet-torus structure, clearly showing deviations from spherical symmetry, which prompted efforts in 2D modeling (see Figure 2.7). The results of these efforts showed that the TS has a very oblate shape, being much closer to the pulsar surface near the poles. This aspect is important to explain the formation of the observed jets. These models provided a new lower limit for $\sigma = 10^{-2}$, an order of magnitude larger than the value previously derived by 1D models.

Most recently, the James Webb Space Telescope resolved the infrared emission of the nebula with unprecedented precision. Figure 2.8 shows the filamentary structure of the dust emitting regions and the synchrotron radiation in the infrared band in white. At the center fine ripples around the central pulsars are visible and larger white bands further away reveal structures of the magnetic field in the nebula. With recent advances in computation power, the first 3D models of the nebula became feasible and showed efficient mixing in the pulsar wind. These models showed that a more uniform magnetic field in the nebula is possible while maintaining the jet-torus structure in the inner nebula. In these models, σ can be as large as $\mathcal{O}(1)$, three orders of magnitude larger than the original estimates.

The extension of the gamma-ray emitting region was studied by the HEGRA collaboration in 2000 when they quoted an upper limit of the source extension of $1.5'$ at a medium energy of 2 TeV. In 2020, the H.E.S.S. collaboration presented a result of $\sim 60''$ for energies above 700 GeV [100]. A more recent H.E.S.S. study from 2024 shows an extension of $\sim 1.7'$ at a few TeV decreasing to $\sim 82''$ above 10 TeV [12]. These results are consistent with the assumption that the IC and synchrotron emission originate from the same electron population and that the higher the energies of the electrons, the stronger they are confined to the center of the nebula.

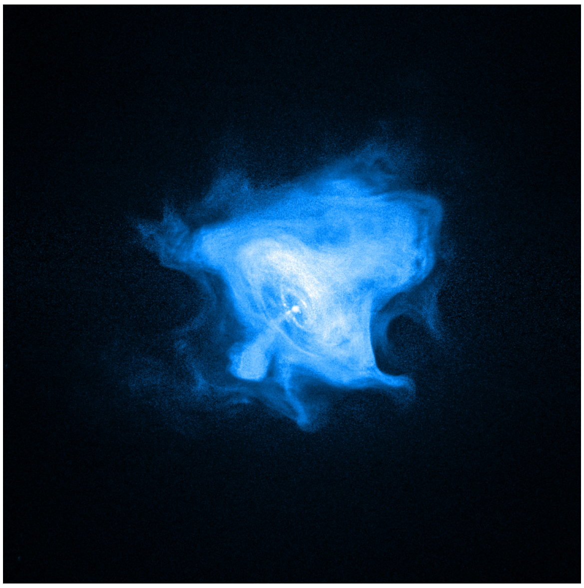

Figure 2.7: The Crab Nebula observed in X-rays by the Chandra satellite. It shows a clear jet-torus structure. The inner ring and the bright central region are also clearly visible.

Activity in the nebula and gamma-ray flares

Lampland discovered structural changes in the Crab Nebula by comparing photographic plates taken between 1913 and 1921 [129]. Further studies of structural changes were carried out by Baade and Münch. All of these observations were summarized and interpreted in a review by Scargle 1969 [164], who described the variable features as wisps.

The imaging capabilities with the unprecedented angular resolution provided by the Hubble Space Telescope in optical, the Chandra observatory in X-ray, and long-baseline observations

Figure 2.8: The Crab Nebula as seen by the James Webb Space Telescope. Colored lines show the dusty filaments of the Nebula. The white areas represent the synchrotron radiation. The central pulsar is visible as small bright dot, and in ring-like structures around it the wisps are revealed. Larger structures of the synchrotron radiation reveal more information on the magnetic field geometry in the nebula. Credits: NASA, ESA, CSA, STScI, Tea Temim (Princeton University) (Image); Joseph DePasquale (STScI) (Image processing)

in radio wavelengths at the end of the 1990s showed moving wisps and structures in the inner nebula across multiple wavebands. Detailed studies identified numerous structures such as more wisps, knots, and other brightness variations [108, 107, 47] from radio to X-rays pointing to their association with each other and suggesting that they are manifestations of the termination shock of the pulsar wind. More recent studies demonstrated that the wisps' time evolution varies between wavebands, suggesting that particle acceleration at different energies takes place at different places [167]. In [152], it was shown that more energetic electrons, responsible for the X-ray emission, are likely accelerated in narrow equatorial regions of the TS, whereas lower energies might originate from broader regions or might even be accelerated homogeneously across the TS.

Observations of large gamma-ray flares by the AGILE and Fermi satellites in 2010 came as a huge surprise to the community [53]. While global flux variations in the hundreds of MeV range on the order of 10% of the average flux were expected, the flux increase of a factor of a few (even 30 in the most extreme case of the April 2011 flare) within hour-timescales was astonishing. Until now, close to 20 flares have been detected with a frequency of ~ 1.5 per year. Multiple scenarios have been proposed to explain the origin of the gamma-ray flares, none of which are widely accepted. Based on the rapid variability timescales, the emitting region must be small, on the order of 10^{-4} pc, roughly 10,000 times smaller than the size of the entire gamma-ray emitting region. The fact that the flaring emission extends to GeV energies, well beyond the synchrotron burn-off limit (see Section 3.1.1), means that either MHD conditions can not be valid in the emitting region or that the emission must be strongly Doppler boosted. Magnetic reconnection models have been most successful in reproducing the variability timing and spectral properties of observed flares (e.g., [60]). Several regions in the nebula are possible to be sites of these reconnection events, some of which are associated with known optical or X-ray features, such as the inner ring [45, 54, 136], the inner knot [125], or the base of the jets [135]. Simultaneous multi-wavelength observations have been achieved for several flares, but until now, no correlated signals have been found. It can be expected that the variability observed in HE gamma-rays will also translate to fluctuations at the high end of the VHE range, given that the same electrons should be responsible for both emissions. Observations of such variability at the far end of the IC component could give valuable insight into the underlying electron population and the magnetic field strength in the flare-emitting regions. Pointing instruments such as IACTs are more sensitive than wide field-of-view air shower arrays to short-term flux variability. It can be crucial in gaining more insight into the origin of the gamma-ray flares to increase the observable energy range of IACTs to around 100 TeV and beyond. This can be achieved by observations at very large zenith angles (see Chapter 5), where I also perform a study of the flux variability of the nebula and the sensitivity of MAGIC towards potential flares in the VHE regime.

Open questions

The current state of knowledge of the Crab Nebula, open questions, and the importance of gamma-ray observations in answering them have been summarized in a recent review by Amato and Olmi [31], from which the contents of this paragraph are mostly cited.

One important issue in the understanding of the nebula is the so-called “sigma problem”: From studies of the pulsar magnetosphere, we know that σ should be of the order of 10^4 up to the TS, however for particle acceleration to take place efficiently the magnetic energy has to be converted such that at the shock σ is not larger than $\mathcal{O}(1)$. Several scenarios have been proposed to explain this conversion of energy. One plausible explanation is the existence of a magnetically striped wind region, the extent of which depends on the angle between the rotational and magnetic axis of the pulsar. In this region, current sheets form between field lines of alternating polarity, providing an ideal environment for magnetic reconnection, which can transfer energy efficiently from the magnetic field to the plasma [67]. The efficiency of this process depends on the number of pairs in the wind flow and, therefore, on κ.

Efficient DSA, the most commonly invoked particle acceleration process, can only occur if the magnetization is below $\sim 10^{-3}$, which can be achieved in small sectors in the striped-wind scenario. Still, it is unclear if that fraction is enough to explain the observed emission. Driven magnetic reconnection at the TS has been proposed as an alternative acceleration mechanism but seems unrealizable given the large numbers for κ and σ that it requires. The IC component predominantly depends on the number of particles in the wind and can provide a clear measurement of κ. Indirectly, it gives strong constraints on the magnetic field strength in the nebula (see Section 3.1.2). In fact, [78] show that the strongest constraints on the magnetic field strength in the nebula come from VHE gamma-ray data. They model radial dependence of the magnetic field strength downstream from the termination shock as a power law $B(r) = B_0(\frac{r}{r_s})^{-\alpha}$. While their best-fit synchrotron spectra are degenerate with respect to the parameter α, the VHE component is highly dependent on it. VHE observations can, therefore, provide strong constraints not only on the strength but on the radial extent of the magnetic field. They show, however, that due to large statistical uncertainties and significant differences between measurements, different values of α are produced, dependent on the choice of data sets. It is, therefore, crucial to provide more precise measurements of the IC component of the Crab Nebula's SED.

2.6 The importance of gamma-ray observations

That gamma-ray emission beyond 100 TeV is indisputable evidence for hadrons of PeV energies has long been a commonly used statement. However, recent works have shown that in spite of the suppression of IC emission due to the Klein-Nishina effect, also extremely energetic electrons can produce gamma-rays of tens or even hundred TeV. It is still true that $\sim$ 100 TeV gamma rays are a sign of the presence of extremely energetic particles, but the distinction between leptonic and hadronic populations remains difficult even at the highest energies. In fact, the first unequivocally detected Galactic PeVatron turns out to be likely purely leptonic: the Crab Nebula. Previous measurements of the Crab Nebula spectrum up to $\sim$ 100 TeV did not undoubtedly classify the source as a PeVatron since assuming the emission to be leptonic would not result in PeV energies of the underlying particles. The detection of gamma rays of more than 1 PeV from the Crab Nebula by LHAASO has, however, proven the capability of the source to accelerate particles to PeV-energies [132], while still not resolving the question of the nature of the responsible particles. Hadronic emission from the Crab Nebula is theoretically possible. Ion-cyclotron emission has been proposed as a particle acceleration mechanism, which would mean the presence of ions in the nebula. This can only be probed by neutrino or gamma-ray emission. The gamma-ray emission induced by ion interactions is expected to only dominate at energies far beyond 100–150 TeV, where the IC process is suppressed by the Klein-Nishina effect. Therefore, the recent observations by the LHAASO collaboration can give insight into whether ions play a substantial role in the nebula. Many of these PeVatron candidates in the LHAASO catalog have pulsars in their vicinity, giving more importance to the understanding of particle acceleration from pulsars and PWNe and whether they are purely leptonic sources or could also account for at least a fraction of the CRs. It is worth to continue studying the Crab Nebula in great detail to shed more light on the role of PWNe in the context of CR acceleration. Studies with more precise spectral resolutions than air shower arrays could additionally help in disentangling leptonic from hadronic emission processes and thereby help to identify the hadronic PeVatrons that are needed to explain the knee of the CR spectrum.

Notably, only one of the specific sources, G106+2.7, mentioned in this chapter is associated with a SNR. Given the limitations to the SNR paradigm (Section 2.4.1), this may not be surprising. In fact, some LHAASO PeVatron candidates might be associated with stellar clusters, although the limited angular resolution of air shower arrays poses a large uncertainty on this statement. It is important to follow up on these discoveries with IACTs, which have a significantly better angular resolution, although not yet as sensitive to the highest energies. They might be able to give more insight into the precise sites of emission and energy-dependent morphology and help identify the specific processes that are responsible for the observed emission.

While considerable progress has been made in the search for Galactic PeVatrons, the fundamental questions of which mechanisms drive the acceleration and which types of sources are responsible remain unanswered. Next-generation instruments such as CTAO will give important new insights, but already with existing instruments, valuable information has been gained and can still be gained by improving the sensitivities at the highest energies. Understanding how MAGIC as a currently operating IACT can contribute to this endeavor was the main motivation for the detailed study of its performance during large zenith angle observations, which enable higher-energy observations. The results of the study are presented in Chapter 5.

Chapter 3

Gamma-ray Astronomy

3.1 Production mechanisms of gamma rays

Astrophysical gamma rays are generally produced by the interactions of relativistic electrons or protons with partially ionized gas or plasma, with photons of a radiation field, or with a pervading magnetic field. The following sections summarize the production mechanisms of gamma rays that are most relevant to the scope of this thesis.

3.1.1 Synchrotron Radiation

In the presence of magnetic fields, charged particles spiral around the magnetic field lines and lose energy which is radiated in the form of photons, so-called synchrotron radiation. The power emitted by a charged particle of mass m is proportional to m^{-2}, which means that lighter particles lose energy much faster and produce more synchrotron radiation than heavier particles. Synchrotron radiation is primarily observed from electrons and does not play a large role in the energy losses of protons. The energy loss rate via synchrotron radiation of electrons is given by [51]

$$\frac{dE}{dt} = -\frac{4}{3}\sigma_T \, c \, U_B \, \gamma_e^2 \left(\frac{v_e}{c}\right)^2 \propto E^2 B^2, \tag{3.1}$$

where σ_T is the Thomson cross-section, $U_B = B^2/2\mu_0$ the magnetic field's energy density, v_e the electron's velocity, and $\gamma_e = E/m_e c^2$ its Lorentz factor. The expression has been averaged over random pitch angles ϕ, the angles between the electron velocity vector and the orientation of the magnetic field. The angular frequency of synchrotron radiation produced by an electron is $\omega_{syn} = \gamma_e^2 \omega_B$, with $\omega_B = eB/m_e$, the classical cyclotron frequency. The observed synchrotron frequency is then

$$\nu_{\text{syn}} = \frac{\omega_{\text{syn}}}{2\pi} = \frac{1}{2\pi}\left(\frac{E}{m_e c^2}\right)^2 \frac{eB}{m} \sin\phi \propto E^2 B \tag{3.2}$$

The total power spectrum of the emitted synchrotron radiation of one electron is then given by

$$P(\nu) \propto F(x) = x \int_x^\infty K_{5/3}(z)\, \mathrm{d}z, \tag{3.3}$$

where $K_{5/3}$ the modified Bessel function of order 5/3. F(x) can be approximated with $F(x) \approx 1.85 \cdot x^{1/3} \exp(-x)$. F(x) peaks at $x \approx 1$ and steeply falls off at higher frequencies roughly independent of the underlying particle spectrum [14]. $x = \nu_c/\nu_0$, where the critical frequency $\nu_c = \frac{3}{2}\nu_{\text{syn}}$ is defined as the frequency where the spectrum decreases rapidly. This peak-like structure of the spectrum is very characteristic of synchrotron radiation and can be observed in a variety of sources, such as AGN and PWNe.

The number of electrons in astrophysical sources typically is a power law distribution over wide ranges in energy of the form

$$n_e(E)dE \propto E^p dE, \tag{3.4}$$

where p is the spectral index. The power radiated by electrons from a unit volume of energy E in the frequency interval dE is then given by

$$j(E)dE = -(dE/dt) \cdot n(E)dE \propto E^2 B^2 E^p dE = B^2 E^{p+2} dE \tag{3.5}$$

The power of synchrotron photons of frequency ν in the $d\nu$ must be the same as Equation 3.5 and therefore with the relation from Equation 3.2 and assuming B=const. it follows

$$j(\nu) = j(E)\frac{dE}{d\nu} \propto B^2 \left(\frac{\nu}{B}\right)^{\frac{p+2}{2}} B^{-1/2}\nu^{-1/2} = B^{\frac{1-p}{2}}\nu^{\frac{1+p}{2}}. \tag{3.6}$$

A particle spectrum with spectral index p will therefore emit synchrotron radiation following a power law with spectral index $\alpha = (1+p)/2$ scaling with the magnetic field strength as $B^{\frac{1-p}{2}}$. The shape of the synchrotron spectrum of a population of electrons in a source is therefore mainly determined by the shape of the electron spectrum, which can then be determined from the observed spectral index α of the synchrotron radiation as $p = 2\alpha - 1$. The maximum energy of synchrotron photons emitted by electrons which are accelerated in astrophysical shocks, is given by the balance of energy gains of the electrons through the acceleration process and energy losses due to synchrotron radiation. The characteristic lifetime τ of an electron with energy E during which it loses a substantial amount of energy via synchrotron radiation is given by [51]

$$\tau = -\frac{E}{dE/dt} \propto \frac{E}{E^2B^2} \propto \frac{1}{EB^2} \tag{3.7}$$

For a magnetic field of $B = 50\,\mathrm{mG}$ and for an electron that is emitting synchrotron photons in the X-ray band, this results in a characteristic lifetime of the order of a few years. Electrons emitting synchrotron radiation in gamma-ray bad ($\sim 50\,\mathrm{MeV}$) have a lifetime of a few days. This means that continuous synchrotron radiation can not extend to energies far beyond tens of MeV or at most $\sim 100\,\mathrm{MeV}$ [51]. This limit is often referred to as the *Synchrotron Burn-Off limit.*

3.1.2 Inverse Compton Scattering

Relativistic electrons colliding with photons of ambient low-energy radiation fields undergo Inverse Compton (IC) scattering, in which they transfer energy to the photons. The increase of energy of the scattered photon can be determined by transforming the system into the electron rest frame and applying the case of standard Compton scattering. The energy of the scattered photon for a head-on collision in this reference system is then given by

$$h\nu_s = \frac{h\nu}{1+\frac{h\nu}{mc^2}}, \tag{3.8}$$

where ν is the incident frequency of the photon before scattering. In each transformation of the laboratory frame to the electron restframe, the photon energy gains an additional factor of $\left(\frac{1+\beta}{1-\beta}\right)^{1/2}$, with $\beta = v_e/c \approx 1$, the electron velocity. This results in an overall increase in the photon energy of

$$h\nu_s \approx 4\gamma_e^2 h\nu \left(1 + \frac{4\gamma_e h\nu}{mc^2}\right)^{-1} \approx 4\gamma_e^2 h\nu, \tag{3.9}$$

where in the second identity $4\gamma h\nu \ll mc^2$ has been assumed, which is satisfied in most applications. Not all collisions in a real source will be head-on, thereby reducing the energy gain of photons. For an isotropic distribution of incoming photons, the average scattered energy gain is one-third of Equation 3.9 [51]. Due to the γ^2 dependency of the energy gain, large photon energies can be achieved. Through multiple scattering with energetic electrons, photons in the radio band can be up-scattered to X-rays and gamma-rays.

The cross-section of IC scattering σ_{IC} depends on the product of the energies in units of the electron rest mass $m_e c^2$ of the interacting electron and photon $k = \epsilon_e \epsilon_\gamma$. In non-relativistic scenarios, where $k \ll 1$, σ_{IC} approaches the Thomson cross-section $\sigma_T = (8\pi/3) r_e^2 = 6.65 \cdot 10^{-29}\,\mathrm{m}^2$, with r_e, the classical electron radius. At larger energies, quantum effects become important and the electron recoil needs to be taken into account, the scattering process becomes inelastic. σ_{IC} is then given by the Klein-Nishina cross-section, which for large energies, $k \gg 1$ can be approximated with

$$\sigma_{IC} \approx \frac{3}{8} \frac{\sigma_T}{k} [\ln(2k) + 1]. \tag{3.10}$$

σ_{IC} in Equation 3.10 is smaller than σ_T and decreases for high energies roughly as $1/k$. IC scattering becomes inefficient at high energies, leading to a strong softening of the observed photon spectrum [14].

Lower energetic electrons only give a small fraction of their energy to the photon in each scattering process. They scatter multiple times until they have lost all of their energy, resulting in longer cooling time scales. Highly energetic electrons transfer almost their entire kinetic energy to the photon in a single scattering process. On the one hand, this results in faster cooling with increasing electron energy, and on the other hand, this means that the resulting photon energy reflects the energy of the electron almost one-to-one. The observation of gamma rays at 1 PeV therefore shows the existence of electrons of the same energy in the respective source.

The energy loss rate of electrons via IC scattering is given by

$$\frac{dE}{dt} = -\frac{4}{3} \sigma_T \, c \, U_{ph} \, \gamma_e^2 \left(\frac{v_e}{c} \right)^2, \tag{3.11}$$

with U_{ph} the energy density of the photons. Equation 3.9 and Equation 3.11 have the same dependencies on energy as for Synchrotron radiation (Equations 3.2 and 3.1) and assuming a monoenergetic photon field the same conclusion follows, that an electron population with a power law index p, will produce an IC gamma-ray spectrum with a spectral index $\alpha = (p+1)/2$. The latter is only valid for the Thomson regime. In the Klein-Nishina regime, the spectrum becomes steeper with $\alpha \sim p + 1$.

Synchrotron Self Compton

If the energy density of the synchrotron photon field produced by electrons in an astrophysical source is sufficiently large, the same electrons will undergo IC scattering with these synchrotron photons. This process is called *Synchrotron Self Compton (SSC)*. The energies in the source are then subject to energy losses via Synchrotron and IC processes, the rates of which are given by Equation 3.1 and Equation 3.11 and are of the same form. The only difference is the energy density with which the electrons interact.

$$\frac{(dE/dt)_{IC}}{(dE/dt)_{Syn}} = \frac{U_{ph}}{U_B}, \tag{3.12}$$

and the relative energy losses of electrons through each process depend only on the relative energy densities of the photon fields and the magnetic field [51]. In the case of SSC, the assumption of a monoenergetic photon field is clearly not justified, and the resulting IC becomes more complicated. A recent analytical study of IC spectra generated by up-scattering a power law distribution of target photons can be found in [124].

The multi-wavelength study of SSC spectra can provide insight into the number of particles that are producing the emission and into the strength of the magnetic field. The IC almost solely depends on the number of electrons in the source, which indirectly can provide strong constraints on the magnetic field. If the magnetic field is assumed too weak, the number of particles has to be increased in order to reproduce the synchrotron spectrum. This, in turn, will lead to an overestimation of the IC flux.

3.1.3 Proton collisions

The major channel of gamma-ray production from protons is the decay of neutral pions π^0, which are produced in inelastic collisions between the protons and ambient gas if the proton energy in the rest frame exceeds $E = 2m_\pi c^2(1+m_\pi/4m_p) \approx 280\,\mathrm{MeV}$. π^0 decay immediately into two gamma rays with a mean lifetime of the π^0 being only $t_{\pi^0} = 8.4{\cdot}10^{-17}\,\mathrm{s}$. The gamma-ray spectrum of π^0 shows a distinctive feature independent of the energy distribution of the parent protons, the so-called pion bump at $E_\gamma = m_\pi c^2/2 \simeq 67.5\,\mathrm{MeV}$. The observation of this pronounced shoulder in the observed gamma-ray spectrum from a source is clear evidence of the presence of protons. At high energies ($> 1\,\mathrm{GeV}$), the cooling times of protons due to collisions are almost independent of energy, and the shape of the initial spectrum does not change. Gamma-ray spectra from these processes reproduce the shape of the proton spectrum, providing valuable insight into the proton population in the source and, by extension, the proton acceleration processes. Roughly 1/10 of the proton energy is transferred to gamma rays. A proton particle spectrum extending to energies beyond PeV would therefore produce a gamma-ray spectrum extending beyond 100 TeV.

Gamma-ray emission from proton collisions is only observable if the accelerated protons are located or enter a region with a large enough gas density. Without sufficient collision partners, the protons will not produce the necessary numbers of π^0 to produce bright gamma-ray emission. This condition is usually satisfied directly in the acceleration region, or in molecular clouds, which CRs that have escaped from the acceleration sight might enter and produce observable gamma-ray emission.

In the proton-gas interactions, charged pions are also produced with equal probabilities, the decays of which produce neutrinos. Detections of neutrinos from astrophysical sources provide the second unequivocal proof for the presence of energetic protons.

3.2 Direct Detection of gamma rays

For gamma-ray energies up to $\sim 30\,\mathrm{MeV}$, the primary interaction process is Compton scattering (see Section 3.1.2). The *COMPTEL* instrument onboard the *Compton Gamma-ray Observatory (CGRO)* [1] operated between 1991 and 2000. It consisted of two detector arrays. In the upper one, a liquid scintillator, gamma-rays underwent Compton scattering and continued to the lower detector consisting of a sodium-iodine (NaI) scintillator, where they were completely absorbed. The original incoming direction was estimated from the location of both interactions and the measured energy deposited in each detector [166]. Above $\sim 30\,\mathrm{MeV}$ up to energies of $\sim 100\,\mathrm{GeV}$, gamma rays are predominantly detected via pair production (see Section 3.3.1.2). The current most important mission using this detection technique is the *Large Area Telescope* (LAT) onboard the *Fermi* Gamma-ray Space Telescope[2]. The *Fermi*-LAT consists of three main detector modules: The anticoincidence detector, the pair converter and tracker systems, and the calorimeter. Schematics of the detection principle and the detector modules are shown in Figure 3.1. The anti-coincidence scintillator is the outermost layer directly underneath the thermal blanket and serves as a veto for charged cosmic rays. The electrically neutral gamma rays pass through without producing a signal and enter the pair conversion and tracker module. This module is arranged in 4 x 4 towers, each consisting of 18 layers of silicon strip detectors. The first 16 layers are covered with tungsten, providing the target material for the creation of electron-positron

---

[1] `https://heasarc.gsfc.nasa.gov/docs/cgro/comptel/`

[2] `https://fermi.gsfc.nasa.gov/`

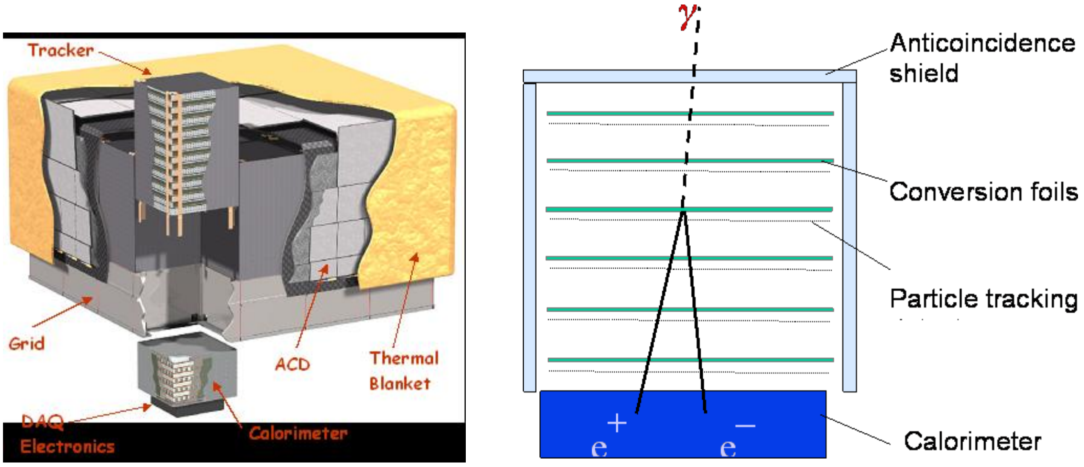

Figure 3.1: Left: Illustration of the LATs detector components. Right: Schematic of the gamma-ray detection principle via pair production. Both taken from [83].

pairs in the presence of a nucleus. The trajectory of the produced lepton pairs, from which the original direction can be reconstructed, is recorded in the silicon trackers. Underneath the trackers in each tower, a calorimeter measures the total energy contained in the produced secondaries [38]. Direct detection of gamma rays is mainly limited by their intrinsically low fluxes with increasing energy. Beyond $\sim 100\,\mathrm{GeV}$, the limited size of satellite instruments does not provide sufficient statistics. Ground-based instruments become necessary, which can only indirectly detect gamma rays.

3.3 Indirect Detection of gamma rays

The size of the effective detector area necessary to observe very-high-energy ($50\,\mathrm{GeV} < \mathrm{E} < 100\,\mathrm{TeV}$) (VHE) gamma rays is too large to be realized in space-based instruments. Therefore, telescopes have to be built on the ground to detect them. This is only possible via indirect measurements since gamma rays, as well as cosmic rays, interact with nuclei in the upper atmosphere, creating *extensive air showers*. In this section, I describe the basic principles of extensive air showers and how they can be detected and used to infer the properties of the incident particle.

3.3.1 Electromagnetic Air showers

The two relevant processes in extensive air showers induced by leptons or photons are *Bremsstrahlung* and *pair production*. In the former, an electron or positron emits a photon while interacting with the Coulomb field of an atmospheric nucleus. The latter describes the process of photons producing an electron-positron pair in the presence of the Coulomb field of a nucleus. Ionization losses of electrons cause air showers to die out when the energy of individual electrons falls below a *critical energy* E_c. It is defined as the energy at which an electron's energy loss over one radiation length through Bremsstrahlung is equal to its energy loss from ionization. The *radiation length* generally refers to the average distance after which an electron has $1/e$ of its initial energy. For an electron in the atmosphere $E_c \approx 87\,\mathrm{MeV}$.

3.3.1.1 Bremsstrahlung

The amount of matter X traversed by a particle, the so-called slant depth, is given in units of g/cm^2. It is often expressed in units of radiation lengths

$$t = X/X_0, \tag{3.13}$$

where X_0 is the characteristic radiation length of electrons. X_0 for Bremsstrahlung was calculated and tabulated by [177] and is given as follows for the case of complete screening. *Screening* denotes the effect of atomic electrons screening the nuclear Coulomb field and becomes complete at the particle energies that are present in extensive air showers [95].

$$\frac{1}{X_0} = 4\alpha r_e^2 \frac{N_A}{A} \left[Z^2 (L_{rad} - f(Z)) + Z L'_{rad} \right], \tag{3.14}$$

where $\alpha = (1/137)$ is the fine-structure constant, r_e the classical electron radius and N_A the Avogadro Number; L_{rad}, $f(Z)$ and L'_{rad} are corrections to the Coulomb field due to screening. In air $X_0 \approx 37\,\mathrm{g\,cm^{-2}}$. The probability for an electron of energy E to undergo Bremsstrahlung in traversing dt is [160]

$$\phi_{br}(y)dy = \left[1 + (1-y)^2 - (1-y)\left(\frac{2}{3} - 2b\right) \right] \frac{dy}{y}, \tag{3.15}$$

where y is the fraction of the electron energy carried away by the photon.
From, Equation 3.14 and 3.15 then follows the energy loss rate

$$\frac{dE}{dt} = \frac{1}{X_0}\frac{dE}{dX} = -\frac{1}{X_0}\int_0^1 Ey\,\phi_{br}(y)\,dy = -\frac{E}{X_0}\,(1+b). \tag{3.16}$$

The parameter $b \equiv [18\ln(183/Z^{\frac{1}{3}})]^{-1} \approx 0.0122$ in air. It is, therefore, negligible and the energy loss of a particle via Bremsstrahlung as a function of traveling distance through a medium can be given as

$$\frac{dE}{dX} = -\frac{E}{X_0}, \tag{3.17}$$

3.3.1.2 Pair production

If the photon energy exceeds the pair creation threshold of 1022 keV, it can produce an electron-positron pair. The differential cross section for pair production with $E = xk$ the energy of the electron or positron and the photon energy k is given by [95, 177]

$$\frac{d\sigma_{pair}}{dx} = \frac{A}{X_0 N_A}\left[1 - \frac{4}{3}\,x\,(1-x)\right] \tag{3.18}$$

with X_0 the radiation length for Bremsstrahlung given by the expression in Equation 3.14. The total pair cross-section is therefore

$$\sigma_{pair,tot} = \int_0^1 \left(\frac{d\sigma_{pair}}{dx}\right) dx = \frac{7}{9}\frac{A}{X_0 N_A}, \tag{3.19}$$

which in air corresponds to $\sigma_{pair,air} \approx 500\,\mathrm{mb}$. It follows that the radiation lengths for bremsstrahlung and pair production are almost the same. They are related as

$$X_{0,pair} = \frac{9}{7} X_{0,brems} \tag{3.20}$$

3.3.1.3 Coulomb Scattering

Coulomb scattering of electrons in the atmosphere is responsible for the lateral spread of air showers.[3]

$$\langle\theta^2_{scatt}\rangle dt = \frac{4\pi}{\alpha}\left(\frac{m_e^2c^4}{p^2\beta^2c^2}\right)dt \tag{3.21}$$

gives the mean square scattering angle $\langle\theta^2_{scatt}\rangle$ of an electron in an infinitesimal layer of a medium of thickness dt expressed in units of radiation length (see Equation 3.13) [95].

3.3.1.4 Electromagnetic Cascades

In a simplified one-dimensional picture called the *Heitler Splitting Model* [106], ignoring all processes other than Bremsstrahlung and pair production, one can assume that during each interaction process, the energy of the parent particle is equally split between the newly created particles. A primary photon of energy E_0 having traversed an air column of thickness corresponding to its radiation length X_0 will create an $e^\pm$ pair, each particle carrying energy $E_0/2$. We then assume again that each of these leptons undergoes Bremsstrahlung after having penetrated a column corresponding to its radiation length, splitting its energy equally between the outgoing scattered electron or positron and the radiated photon. After t radiation lengths, the combined number of particles in the shower will be $N = 2^t$. Each particle carries the energy $E_t = E_0/2^t$. The shower maximum X_{max} is reached when E_t is equal to the critical energy E_c. The number of particles at the shower maximum is therefore

$$N(X_{max}) = \frac{E_0}{E_c} \tag{3.22}$$

and

$$X_{max} = X_0\frac{\ln(E_0/E_c)}{\ln 2} \tag{3.23}$$

Typically, in this picture, it is also assumed that after the shower maximum, the number of particles in the shower is exponentially absorbed according to

$$N(X) \simeq N(X_{max})\exp\left(-\lambda_{abs}\frac{X - X_{max}}{X_0}\right), \tag{3.24}$$

with λ_{abs} the particle absorption length in the shower. Despite the crude approximations and assumptions, Heitler's model provides a good description of the general longitudinal behavior of an electromagnetic air shower, which is shown in Figure 3.2. The lateral distribution of particles in an electromagnetic cascade is defined by the Moliere Radius

$$R_m = \frac{E_{\rm scatt}}{E_c}X_0 \simeq 9.5\,{\rm g\,cm^{-2}}, \tag{3.25}$$

where $E_{\rm scatt} \simeq 21\,{\rm MeV}$ is the scattering energy [95]. It is mostly independent of the energy of the primary particle. At sea level $R_m \approx 79\,{\rm m}$. More precisely, the shower development is described by solutions to the coupled cascade equations, which calculate the particle flux as functions of energy and slant depth in the atmosphere for both $e^\pm$ and photons. Detailed analytical calculations of these equations have been carried out. See [149] for an extensive review of electromagnetic cascade theory. The analytical function that is still commonly used today is named after Nishimura, Kamata and Greisen [119, 93]. The *NKG function* yields analytical expressions of longitudinal, latitudinal, and angular distributions of particles in an air shower, as well as their energy spectra as a function of slant depth.

---

[3] Pair production and Bremsstrahlung also yield an angular spread with respect to the parent particle, which is negligible compared to the spread caused by Coulomb scattering.

It can be shown that, when ionization losses and Coulomb scattering are ignored and complete screening is assumed, the cascade equations have solutions of the form

$$n_e(E,t)dE = a1\left(\frac{E_0}{E}\right)^s \frac{dE}{E}e^{-\mu t} \quad (3.26) \qquad n_\gamma(E,t)dE = b1\left(\frac{E_0}{E}\right)^s \frac{dE}{E}e^{-\mu t} \quad (3.27)$$

When solving for the parameters $a1, b1, s, \mu$, one finds that s is related to the rate of growth and decay of the number of particles in the shower. For $s = 1$, the rate is zero, which corresponds to the shower maximum. For $s < 1$, the number of particles in the shower is growing and decreasing for $s > 1$. The parameter s is referred to as the *shower age* and is illustrated in Figure 3.2 [95].

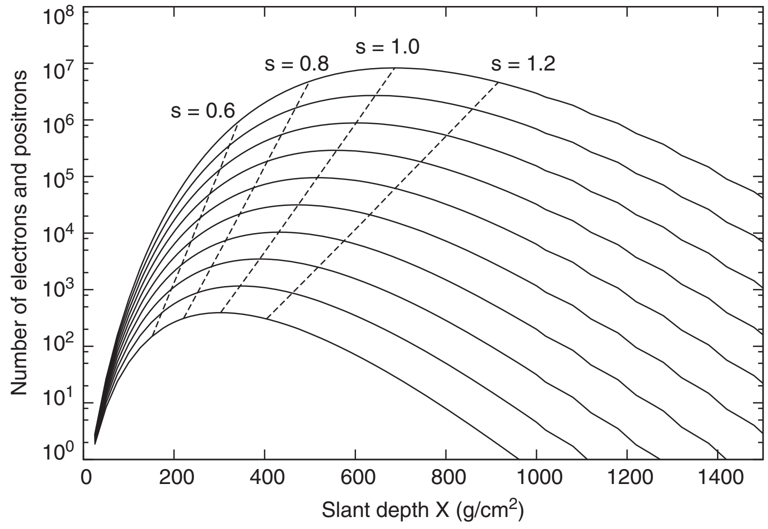

Figure 3.2: Shower size as a function of slant depth for energies between 316 GeV (lowest curve) to 10^7 GeV (highest curve). The dashed lines trace the number of particles in each shower for specific shower ages s (see Section 3.3.1.4). Taken from [89].

3.3.2 Hadronic Air showers

The electromagnetic air showers described in the previous section make up only a small fraction of all the extensive air showers created in the atmosphere. The vast majority are hadron-induced showers. Primary hadrons undergo inelastic scattering with nuclei in the atmosphere, creating secondary highly energetic nucleons and nuclei and, among others, kaons, pions, muons, and neutrinos. Each of these secondary particles undergoes various interactions and decay processes, leading to a much more complex development than electromagnetic cascades. A simplified model based on the Heitler model described above was introduced by Matthews [143, 142]. This *Heitler-Matthews splitting model* imagines the atmosphere in layers of thickness $\lambda_I \ln 2$, analogous to the length after which an electron radiates a single photon in the electromagnetic case (see Equation 3.23). λ_I denotes the interaction length of strongly interacting particles. After transversing one layer, hadrons interact and produce $N_{charged}$ charged pions, and $N_{neutral} = 0.5N_{charged}$ neutral pions. The latter decay immediately into two photons, initiating electromagnetic cascades as described in the previous section. The charged pions continue transversing through the atmosphere, interacting after each layer until their critical energy E_c is reached, at which their interaction length exceeds their decay length. The energy is split equally between the two charged pions and the neutral pion in each reaction. Therefore, $1/3$ of the energy goes into an electromagnetic shower induced by the decay of π^0 into two gamma rays. The rest goes into hadronic shower components via charged pion interactions. After crossing n layers in the atmosphere, the energy in the electromagnetic and hadronic components are

$$E_{had} = \left(\frac{2}{3}\right)^n E_0 \tag{3.28}$$

$$E_{em} = \left(1 - \frac{2}{3}\right)^n E_0. \tag{3.29}$$

The energy per charged pion is therefore $E_{\pi^{\pm}} = E_0/(\frac{3}{2}N_{charged})^n$.
To estimate the depth of the shower maximum for a proton-induced shower X^p_{max}, one can, as a first approximation, only consider the first point of interaction and evaluate the shower maximum of the electromagnetic shower initiated at that point. Each of the $0.5N_{charged}$ neutral pions will create two gamma rays, each of which will initiate an electromagnetic shower of energy $E_0/(3N_{charged})$ The first point of interaction is given by $X_{first} = \lambda_I \ln 2$. With Equation 3.23, that leads to

$$X^p_{max} = X_{first} + \frac{X_0}{\ln 2} \ln E_0/(3N_{charged}E_{c,e}) \tag{3.30}$$

This approximation underestimates X^p_{max} since it neglects the contributions from subsequent generations of subshowers. But it shows the correct dependency of X_{max} with the primary energy when compared to detailed simulations.

3.3.3 Description of the Atmosphere

The mean interaction lengths of charged particles and photons do not depend on the respective medium they are penetrating, only on the amount of matter they are passing through. It is, therefore, useful to express the path of a particle through the atmosphere by the airmass. It is defined as the integral over the atmosphere's density profile along the traveled path length s. For a given height h and zenith angle θ, s is given by

$$s(\theta) = \frac{h}{\cos\theta}. \tag{3.31}$$

Typically the airmass σ is given in terms of the relative airmass, defined by the ratio of airmass along $s(\theta)$ to the vertical airmass at sea level:

$$X = \frac{\sigma(\theta)}{\sigma(0)} \tag{3.32}$$

Per definition, the relative airmass in the vertical direction for an observer at sea level is then equal to 1.
When approximating the atmosphere as being plane parallel (i.e., neglecting the Earth's curvature) and assuming a constant density ρ, the relative airmass is given by

$$X(\theta) = \frac{1}{cos(\theta)} \tag{3.33}$$

Figure 3.3 shows Equation 3.33 in the zenith angle range [50°, 80°], which is relevant for the scope of this thesis. At 60° the airmass is doubled with respect to the vertical direction and quickly increases with larger zenith angles. At 70° it increases by a factor of three and at 75° almost by a factor of 4. At 80° the airmass is along the line of sight is almost six times larger compared to the vertical direction.
Equation 3.31 is only accurate up to zenith angles $\lesssim 70°$ and goes to infinity for $\theta = 90°$. For very large zenith angles, the Earth's curvature needs to be taken into account, and s

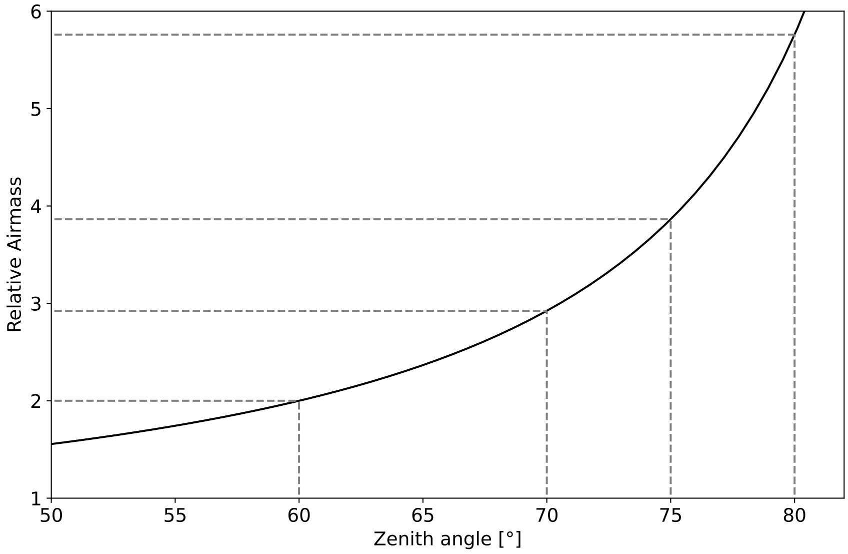

Figure 3.3: The relative airmass for zenith angles between 50° and 80° under the flat Earth assumption. Dashed lines help to visualize the airmass values at zenith angles 60°, 70°, 75°, and 80°.

becomes $R_E = 6371\,\mathrm{km}$ being the Earth's radius,

$$s(\theta) = \sqrt{(R_E + h)^2 - R_E^2 \sin^2(\theta)} - R_E \cos\theta \tag{3.34}$$

and

$$X = \frac{s}{h} = \frac{R_E}{h}\sqrt{\cos^2\theta + 2\frac{h}{R_E} + \left(\frac{h}{R_E}\right)^2} - \frac{R_E}{h}\cos\theta. \tag{3.35}$$

For a standard isothermal exponential atmosphere, the density profile of the atmosphere is given by

$$\rho(h) = \rho(h = 0)\, e^{-(h/h_s)}, \tag{3.36}$$

with the constant scale height $h_s = (kT/Mg)$, where k is the Boltzmann constant, T the temperature, M the molecular weight and g the gravitational acceleration and $h = h(\theta)$ given by Equation 3.31 or Equation 3.34, respectively.
The airmass is given as

$$X(\theta) = \int_s^\infty \rho(h(\theta))\, dh \tag{3.37}$$

The exact solution to calculating the corresponding column density for inclined trajectories is given by the *Chapman integral* [61] for which several approximate solutions have been developed. Figure 3.4 shows the relative airmass for the flat Earth approximation as well as additional, more precise approximations for zenith angles above 70°.
For $\theta = 90^\circ$, the relative airmass is around 40, meaning a particle reaching an observer from the horizon crosses 40 times the amount of atmosphere compared to a vertical particle trajectory.

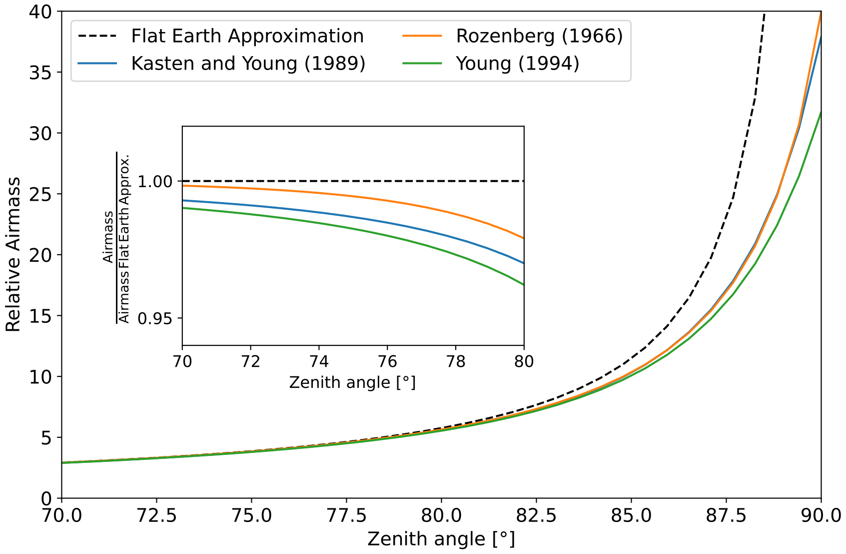

Figure 3.4: The relative airmass for zenith angles between 70° and 90°. The values under the flat Earth assumption are shown as a black dashed line. They go to infinity at 90°. The colored lines show approximations developed by [121] (blue), [162] (orange), [189] (green). The inlay shows the relative deviation of each of these solutions to the flat Earth approximation. Up to 80° they deviate less than 5%.

3.3.4 Cherenkov light

Cherenkov light is produced by charged particles moving in a dielectric medium at a speed exceeding the group velocity of light in that medium. The particle polarizes the medium, resulting in a dipole field along the axis of its motion. Usually, the wavelets radiated from the different parts of the particle track interfere destructively, such that the dipole field is zero at a larger distance and no electromagnetic radiation is present. If the particle's velocity v exceeds the speed of light, then the dipole radiation will interfere constructively under a certain emission angle θ_c from the particle track. A plane wave of light emission is formed, which produces, due to the azimuthal symmetry of the process, a light cone with a semi-opening angle θ_c and the particle track as its central axis. The basic geometry of this process is illustrated in Figure 3.5. From this sketch it becomes clear that the angle θ_c under which coherent emission takes place can be written as

$$\cos\theta_c = \frac{1}{\beta n}, \tag{3.38}$$

with $\beta = v/c$, and n the refractive index of the medium. The maximum angle $\theta_{c,max}$ under which Cherenkov light emission can occur is given by $\beta = 1$, therefore

$$\theta_{c,max} = \arccos(1/n). \tag{3.39}$$

Since v has to be larger than c/n, the threshold velocity below which no Cherenkov radiation is produced is given by

$$\beta_{th} = (1/n), \tag{3.40}$$

which translates to a minimum energy of a charged particle with restmass m_0

$$E_{th} = \frac{m_0 c^2}{\sqrt{1 - \frac{1}{n^2}}}. \tag{3.41}$$

From $|\cos\theta_c| \leq 1$ follows that, for Cherenkov radiation to occur, $n > 1$ has to be fulfilled,

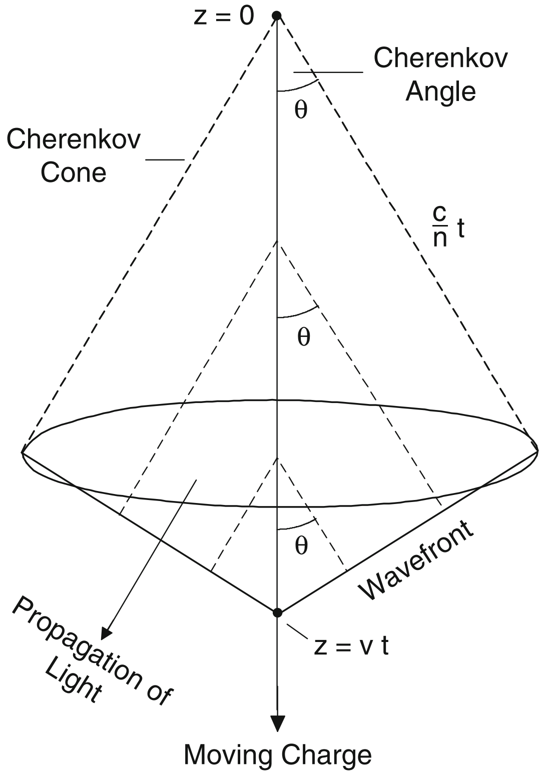

Figure 3.5: Geometrical sketch of the Cherenkov radiation of a charged particle traveling through a dielectric medium of refractive index n a larger speed v than the light group velocity in that medium c/n. The particle propagates along the z-axis, the Cherenkov angle is shown as θ, the direction of the Cherenkov photons is indicated, as well as the position of the wavefront at time t. Taken from [95].

implying that it is predominantly produced in the optical part of the electromagnetic spectrum.

While Cherenkov radiation had been observed before as a bluish glow in transparent substances near radioactive sources, the first systematic study and explanation attempts were due to Cherenkov in 1934 [62]. In 1937, Frank and Tamm provided a mathematical description of the process. This classical derivation differed negligibly from the later provided quantum-mechanical descriptions. The Frank-Tamm formula for the energy loss dE of a charged particle due to Cherenkov radiation per unit path length dl in units $[\mathrm{eV\,cm^{-1}}]$ is as follows:

$$\left(\frac{dE}{dl}\right)_{Ch} = 4\pi\left(\frac{ze^2}{c}\right)\int_{\beta n>1}\left(1-\frac{1}{\beta^2 n^2}\right)\cdot\omega d\omega, \tag{3.42}$$

where ze is the charge of the particle, and ω the angular frequency of the emitted radiation. From Equation 3.42, the number of photons N_{ph} emitted along a path of length l in a wavelength range (λ_1, λ_2) can be obtained.

$$N_{ph} = 2\pi z^2\alpha l\left(\frac{1}{\lambda_1}-\frac{1}{\lambda_2}\right)\cdot\left(1-\frac{1}{\beta^2 n^2}\right) = 2\pi z^2\alpha l\left(\frac{1}{\lambda_1}-\frac{1}{\lambda_2}\right)\cdot\sin^2\theta_c, \tag{3.43}$$

with the fine-structure constant $\alpha = e^2/\hbar c = 1/137$. Table 3.1 lists numerical values for some of the described quantities for electrons and muons in air and water.

3.3.4.1 Cherenkov light from extensive air showers

Cherenkov light is produced in the atmosphere by the charged particles propagating in extensive air showers. It can be detected with Imaging Atmospheric Cherenkov Telescopes (IACTs). Its geometric properties enable a reconstruction of the basic shower properties and,

Table 3.1: Numerical values for the maximum Cherenkov angle, the energy threshold for Cherenkov radiation, and the number of emitted Cherenkov photons per unit path length for electrons and muons in air and water.

	Air (sea level)		Water	
n	1.00029		1.33	
$\theta_{c,max}[^{\circ}]$	1.4		41	
$dN/dl_{\lambda\in(400nm,500nm)}[\mathrm{cm}^{-1}]$	0.3		250	
Particle	e^{-}	μ	e^{-}	μ
$E_{th}[\mathrm{MeV}]$	21	4400	0.26	53

therefore, provide a way to estimate the type, energy, and incoming direction of the primary particle. For this purpose, it is important to understand the effect of the atmosphere on the propagation of Cherenkov photons from their point of production to the telescope.

Since the Cherenkov angle varies with the refraction index, which in turn depends on the density of air, it changes with height from around 0.2° at 30 km up to 1.5° at sea level. This results in an annulus of high Cherenkov photon density on the ground at typically $\sim 150\,\mathrm{m}$, where the difference in emission angle compensates for the difference in travel distance from the point of emission to the ground [74]. This effect is illustrated in Figure 3.6. At the beginning of the shower, electrons travel mostly parallel to the shower axis, but as the shower progresses, multiple scattering can lead to larger transverse momenta, further contributing to an increased angle between the emitted Cherenkov photons and the shower axis. A detailed parametrization of the angular distribution of Cherenkov photons in air showers as a function of height and shower age has been derived by [33]. On the ground, the photon density from an air shower is almost constant between the impact point of the shower axis and the light annulus. After the steep increase in density at the annulus, it decreases fast at larger distances, as shown in Figure 3.7.

The interplay between varying Cherenkov emission angles and travel distances to the ground also leads to an inversion of the arrival time of the photons with respect to the shower age. Photons created early in the shower are produced at greater heights, resulting in longer travel distances than photons produced later and closer to the ground. Inside the annulus, this creates a time reversal, where later-produced photons arrive before earlier ones. Outside the ring, this order reverses: the combined production delay and travel time of photons from lower altitudes exceed the direct travel time of photons from higher altitudes. Figure 3.8 shows the arrival time delay of photons produced at different heights as a function of lateral distance for a vertical shower. One can see that the signal duration of a vertical shower recorded by an IACT will last between 2–5 ns inside of the ring and will rapidly increase at larger distances from the shower axis.

3.3.5 The Imaging Atmospheric Cherenkov Technique

The Cherenkov light emitted by the charged particles in extensive air showers can be exploited in the *Imaging Atmospheric Cherenkov Technique* by IACTs. A detailed historical overview of the beginning of ground-based gamma-ray astronomy is given in [145], some aspects of which are summarized here. The groundwork for this was laid in 1953 by Galbraith and Jelley who, after being made aware of a possible contribution from Cherenkov radiations in the light of the night sky (LoNS), set up a rudimentary experiment consisting of a 25cm diameter parabolic mirror with a single Photomultiplier Tube (PMT) in its focus. They detected short light pulses, many of which were coincident in time with signals from air showers detected by adjacent Geiger-Müller counters [90]. In the following decades, several

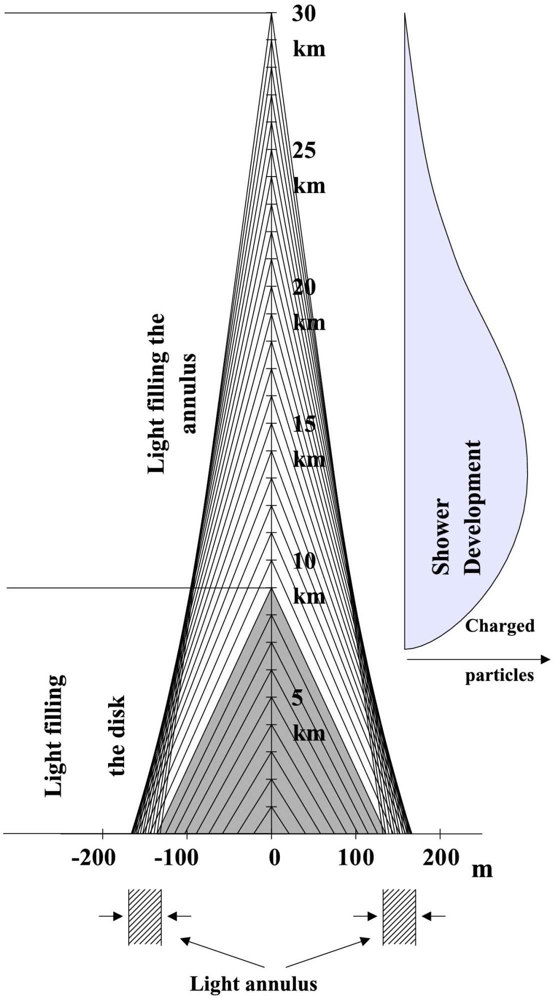

Figure 3.6: Illustration of the Cherenkov ring formation on the ground for a vertical shower. Taken from [74].

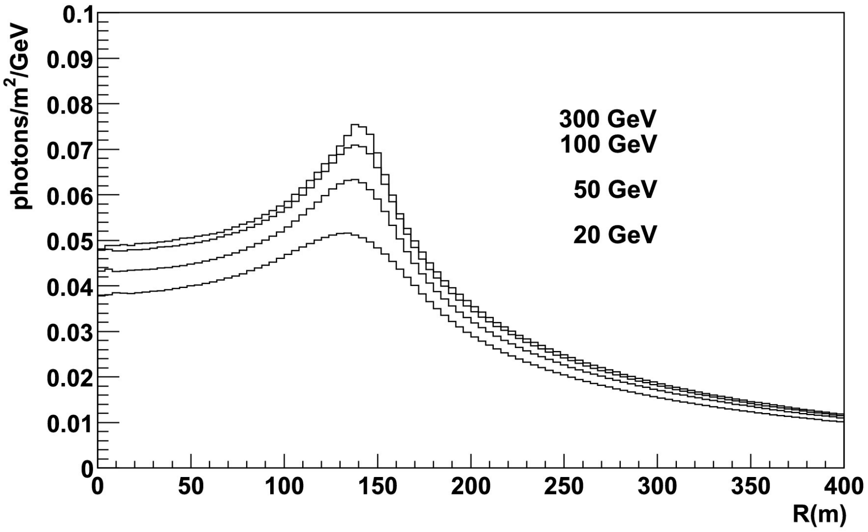

Figure 3.7: Cherenkov photon density distribution on the ground for vertical showers of different energies as a function of radial distance from the shower axis. Taken from [74].

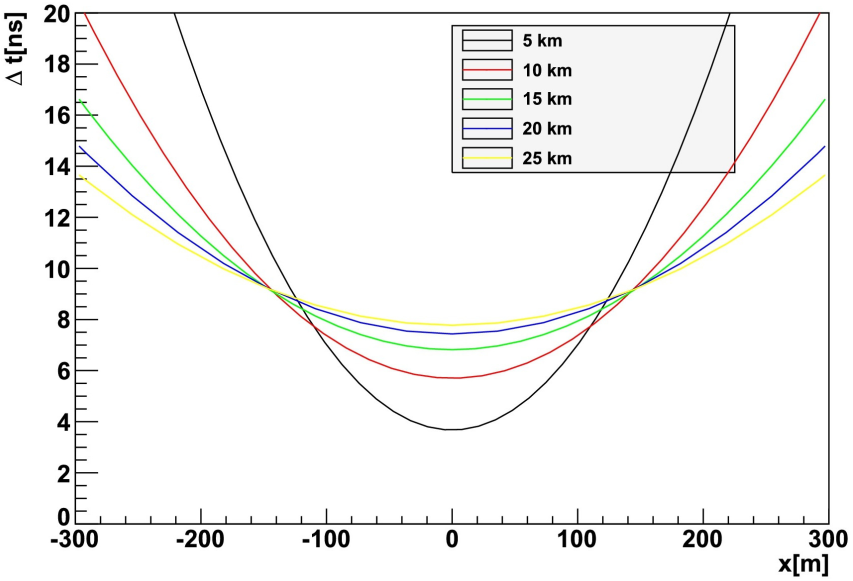

Figure 3.8: Arrival time delay of photons produced at different heights as a function of lateral distance from the shower axis.

groups across the globe operated telescopes trying to detect gamma-ray signals from various astrophysical sources via Cherenkov radiation without success. These first telescopes all relied on counting excess events - the difference in recorded pulses from the on-source region to an off-source region. The Whipple Telescope was the first to install an imaging camera consisting of 37 pixels, which could record the images of the air showers. In 1985, Hillas proposed a way of parameterizing these images, and inferring the characteristics of single events from these parameters. This was the next major step in the development of the detection technique and led to the first detection of a significant gamma-ray signal from the Crab Nebula from the Whipple collaboration in 1989 [184]. The HEGRA collaboration operated five IACTs between 1992 and 2002, demonstrating the advantages of operating multiple telescopes in stereo mode in terms of stronger background suppression and improved angular and energy resolution. With the success of these telescope systems, VHE gamma-ray astronomy using IACTs was firmly established. The current generation of Cherenkov Telescopes, most notably the VERITAS, H.E.S.S., and MAGIC Telescopes, all share the common well-established basic telescope setup, operation, and interpretation of the data.

3.3.5.1 The Basic Principle of IACTs

IACTs are equipped with large mirror surfaces to collect sufficient Cherenkov photons, sensitive cameras with light sensors capable of detecting single photons, and ultra-fast readout systems that can resolve the short nanosecond-scale signals. Their mirrors reflect light arriving under the same angle into the same point in the camera. Light traveling along the line-of-sight of the telescope's pointing direction is reflected directly into the camera center. Larger light incident angles are recorded at larger distances from the camera center. Since the Cherenkov angle changes along the shower axis, photons emitted from different regions of the shower are reflected to different parts of the camera, creating an image of the shower shape in the atmosphere. Figure 3.9 illustrates this procedure. The images recorded in the cameras of IACTs, thanks to the well-defined geometrical properties of air shower development and Cherenkov light emission, carry enough information to distinguish between gamma-ray and hadron-induced showers and to reconstruct the incoming direction and energy of the primary particle.

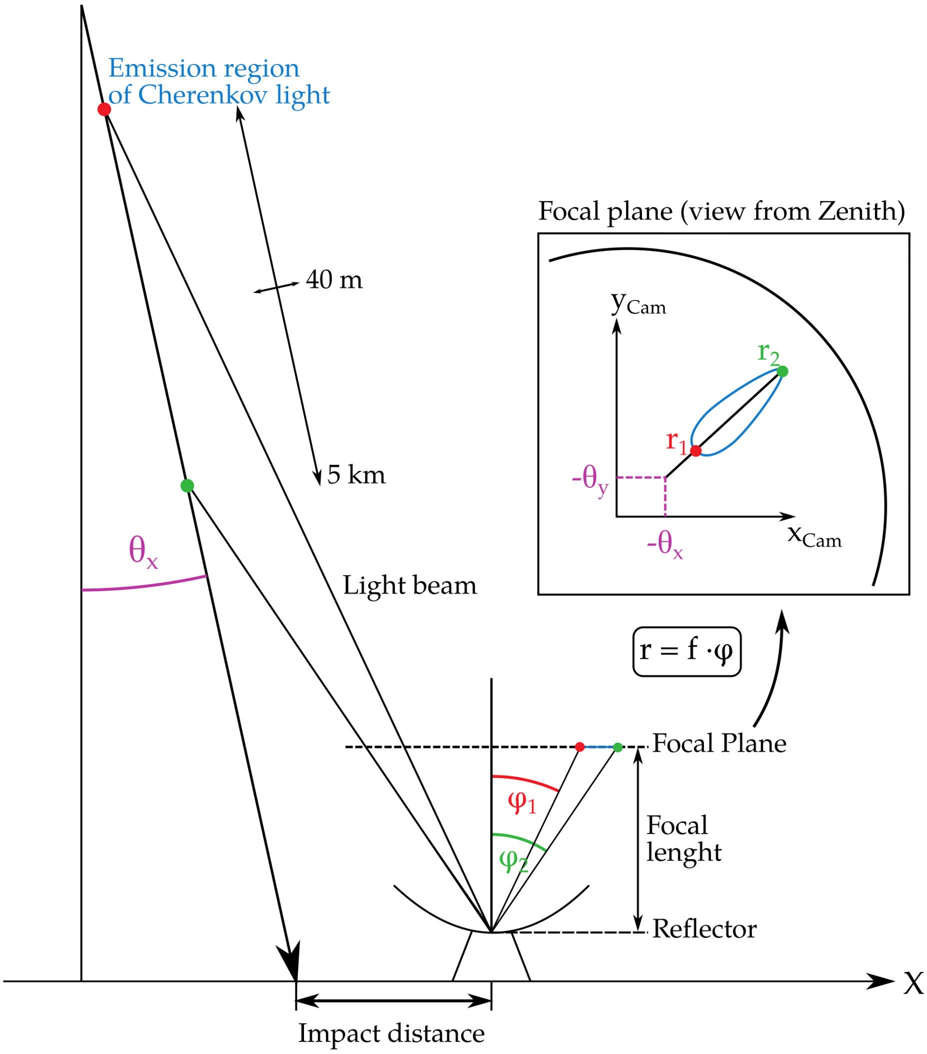

Figure 3.9: Mapping of the shower into the camera in the telescope's focal plane. Incident angles are converted to distance from the camera center. Taken from [173].

Image parameterization

As mentioned above, Hillas was the first to propose a parameterization of the recorded camera images [110]. By evaluating the distribution of recorded photons across the camera, he defined the image axis as the signal-weighted least-squares fit through the pixels containing signal. The *width* and *length* parameters were defined as the root-mean-squared (RMS) of the signal perpendicular and along this axis, respectively. These *Hillas parameters* are still used in current experiments and have been refined and extended since. Section 4.2.2 gives more details on the image parameterization procedure used for the analysis of data from the MAGIC Telescopes.

Gamma/Hadron Separation

The distinction between gamma-ray and hadron-induced air showers is made based on the shape of the recorded camera image. In hadronic air showers, the charged particles are produced with higher transverse momenta, which leads to an overall more broad and scattered shape compared to purely electromagnetic showers (see Figure 3.10). Images of gamma-ray-induced showers usually have a well-defined elliptical shape, whereas hadronic images are more chaotic. This leads to differences in the distribution of values of the Hillas parameters, which are used during data analysis to select the gamma-ray signal. This procedure is described in more detail in Section 4.2.4.4.

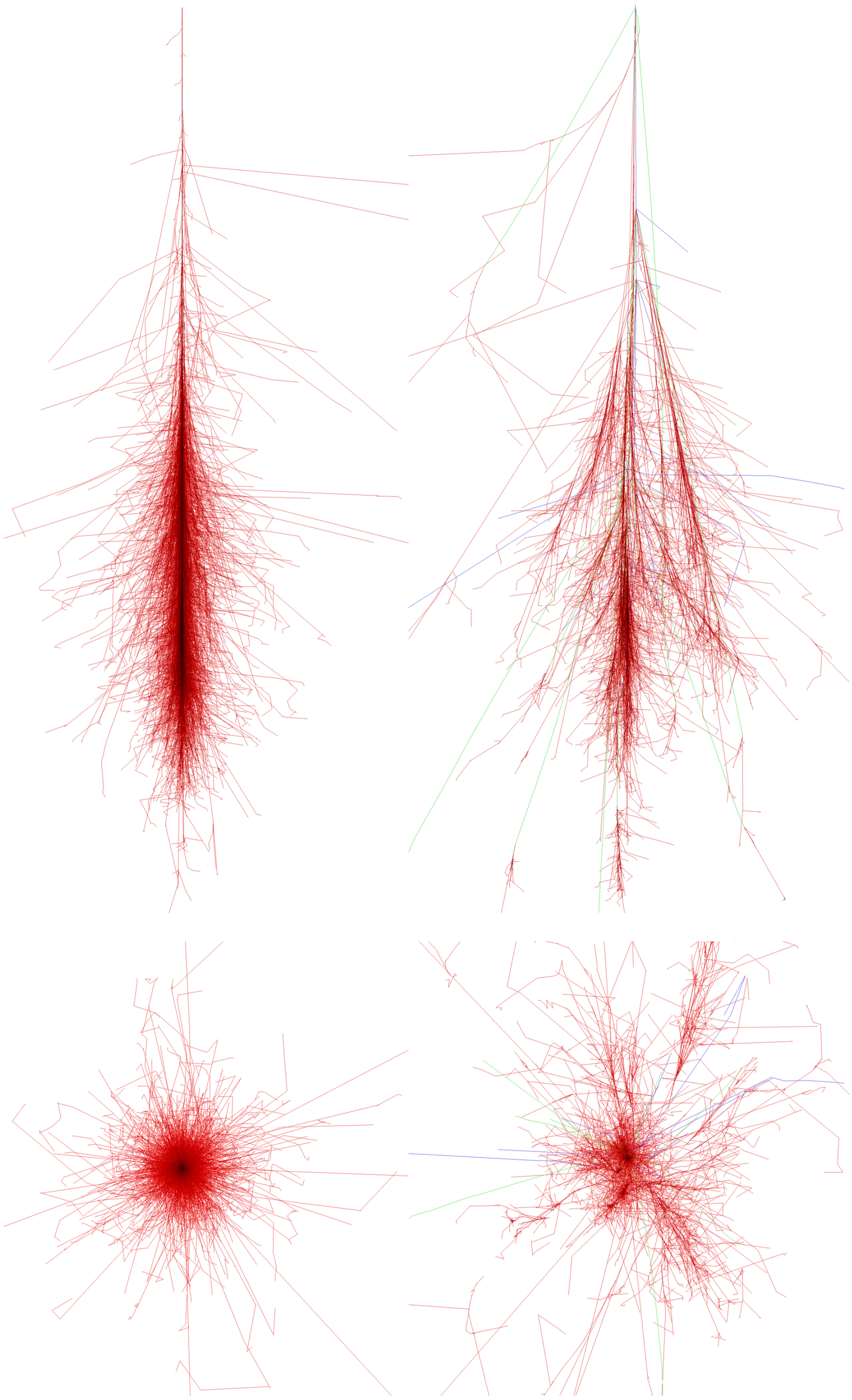

Figure 3.10: Simulated air showers induced by a 100 GeV photon (left) and proton (right), respectively. Red lines show trajectories of electrons and positrons, green lines show muons, blue line show hadrons. The top depicts the longitudinal development and the bottom the lateral spread. [80, 81]

Energy estimation

The number of particles in the extensive air shower and, therefore, the number of emitted Cherenkov photons is directly related to the energy of the primary particle. The number of detected photons, together with other parameters such as the distance of the shower axis to the telescope (*Impact* parameter) or the height of the shower maximum, can be used to get a good estimate of the primary energy. Further details on this procedure are given in Section 4.2.4.3.

Direction reconstruction

From purely geometrical considerations, a single telescope can only determine the orientation of the shower axis in a plane; the precise arrival direction is underdetermined. To accurately reconstruct the arrival direction, the Impact parameter also needs to be determined. This can be significantly improved when several telescopes operate together in stereoscopic mode. They see the shower from different directions, each spanning a plane containing the shower axis. The Impact point is then defined by the intersection of these planes, and the accurate arrival direction can be determined from the transformation into a joined camera coordinate system as shown in Figure 3.11. The DISP-method provides a possibility to estimate the source position with higher accuracy for a single telescope and is further improved in its stereo application. More details on the implementation of this procedure is given in Section 4.2.4.2.

3.3.5.2 Considerations concerning large zenith angle observations

With increasing zenith angle, the path length and the air mass between the first point of interaction of the primary particle and the ground increases (see Figure 3.4). This has several consequences for air shower development and observation. Inclined showers develop in the upper layers of the atmosphere where the air density is lower. This leads to an increase in the length of the showers as they develop over larger distances. Up to $\sim 80^\circ$ their lateral extension increases just slightly as the Moliere radius (Equation 3.25) increases with lower air density. Only beyond 80° deflection effects from the Earth's magnetic field cause a strong additional lateral spread [96]. In principle, the shower object in the atmosphere therefore becomes larger with increasing zenith angle. This does, however, not translate into larger images recorded by IACTs. The extensive air shower develops at larger distances, which means that the produced Cherenkov light needs to transverse more atmosphere before it reaches the telescopes. This leads to an attenuation of the Cherenkov photons, especially in the UV range, due to Rayleigh scattering and absorption. Figure 3.12 shows the Cherenkov spectra reaching the MAGIC Telescopes from extensive air showers for a small (15°) and a very large (75°) zenith angle. One can clearly see the suppression of small wavelengths for the large zenith angle and, therefore, a shift of the peak of the spectrum towards the blue. On the one hand, this contributes to an increase of the energy threshold of IACTs with increasing zenith angle since only bright showers that are induced by higher energetic primaries will produce enough Cherenkov radiation to trigger the telescopes. On the other hand, the dimmer tails of the shower might not be recorded by the camera, and the image will mostly reflect the light that has been emitted around the bright shower maximum. This means that the observed shower object is smaller than in reality. The large distance of 50–100 km between the shower maximum and the telescopes additionally strongly decreases the angular size of the shower, finally resulting in a strong decrease of the geometrical sizes of the shower images with increasing zenith angles (see Section 5.2.3.2). The larger distance of the air showers from the telescopes, due to simple geometric considerations, leads to an increase in the area illuminated by the Cherenkov light pool on the ground. On the one hand, this translates into a lower Cherenkov photon density, which again contributes to an

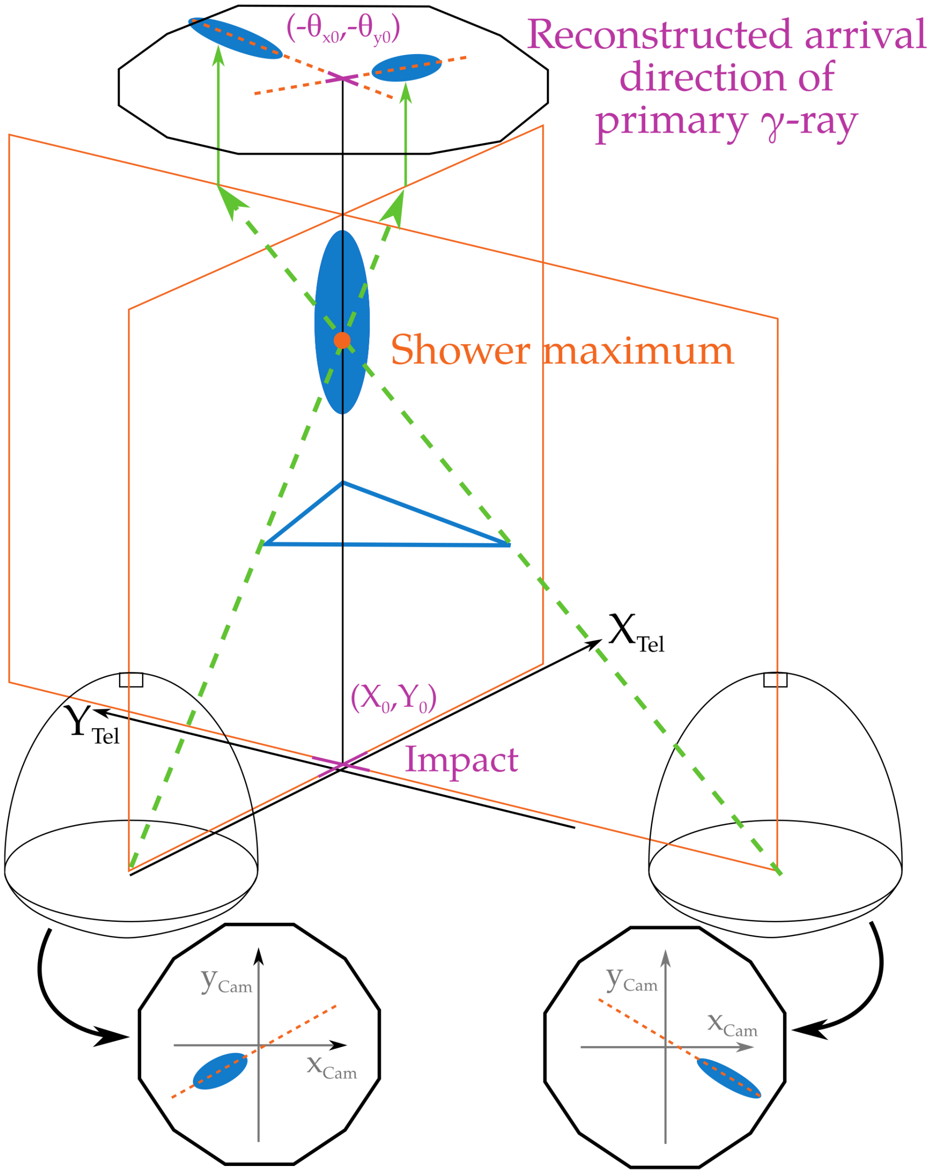

Figure 3.11: Illustration of the primary arrival direction reconstruction using two IACTs. Each telescope spans a plane based on the recorded image containing the shower axis. The Impact point on the ground is given by the intersect of the planes and the arrival direction can be inferred from the transformation into a joined camera coordinate system. Taken from [173].

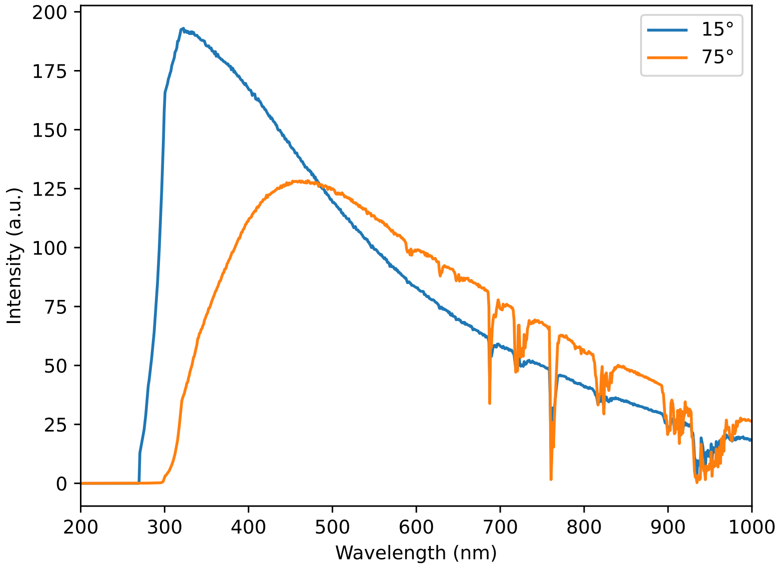

Figure 3.12: Spectra of Cherenkov radiation produced from air showers reaching the MAGIC Telescopes camera. The data has been obtained from Monte Carlo simulations; for more details, see [102]. Spectra for zenith angles 15° and 75° are shown. The shift in the peak of the spectrum for higher zenith angles due to higher absorption of UV photons is clearly visible. The spectrum at 75° is scaled up for better visibility, the y-scale does not reflect the actual total absorption. The data for this plot were obtained from CORSIKA simulations and were provided by Alexander Hahn.

increase in the energy threshold. On the other hand, this produces a dramatic increase in the effective area of IACTs, increasing the sensitivity at the highest energies (see Chapter 5). Another interesting effect of observations at large zenith angles is a shift of the average position of the shower image with respect to the source position in the camera. Since the Extensive Air Shower (EAS) develop in the upper atmosphere in a region of lower air density, the Cherenkov angle is smaller for these showers. As described in Section 3.3.5.1 and shown in Figure 3.9, the incident angle of the Cherenkov light translates into the distance from the source position in the camera coordinate system. Images from EAS at large zenith angles tend to be more concentrated towards the source position compared to images recorded during lower zenith angle observations. Figure 3.13 shows the distributions for different zenith angle ranges of the *Dist* parameter of the shower image obtained from MC simulations. The *Dist* parameter denotes the distance between the *COG* of the shower image and the source position (see Section 4.2.2). With increasing zenith angle, the distributions move to smaller values as the showers are reconstructed closer to the source position in the camera.

3.3.6 Air shower detectors

The particles produced in extensive air showers can also directly be detected by distributing particle detectors over a large area on the ground. This setup can be used to study both cosmic rays and gamma rays. The detectors are usually either large water tanks equipped with Photomultiplier Tubes (PMTs), that detect the Cherenkov light emitted by charged particles entering the tank, or scintillator detectors that record the signals from charged particles. Air shower detectors are wide field-of-view observatories, meaning that they can observe a large portion of the sky at any given time and can scan a large portion of the entire observable sky in 24 hours due to the Earth's rotation. Since they are also not restricted to dark observing conditions and not influenced by weather, they have a duty cycle of more than 90%, contrary to IACTs, which typically have duty cycles of $\sim 10\%$. However, compared

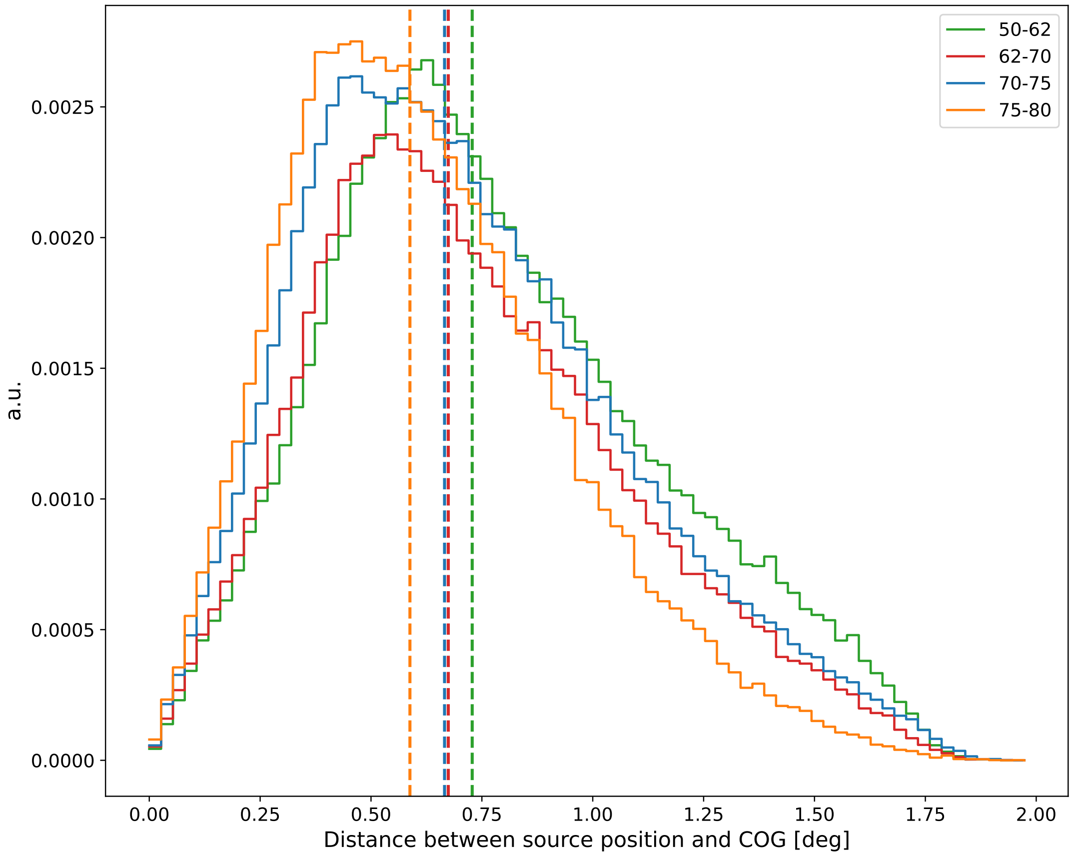

Figure 3.13: Distributions of the *Dist* parameter of the shower image in MAGIC camera coordinates obtained from MC simulations. The dashed lines show the medians of the respective distribution. With increasing zenith angle, the distributions shrink because most of the shower development occurs in the outer layers of the atmosphere, where the air density is low, and Cherenkov light emission angles are correspondingly lower. Therefore, the showers are imaged closer to the source position in the camera.

to IACTs, air shower arrays generally have a worse angular resolution and energy resolution due to higher inaccuracies in the reconstruction of the EAS properties.

The High-altitude Water Cherenkov Observatory (HAWC) [4] is a cosmic ray and gamma-ray detector located at 4100 m a.s.l. near Puebla, Mexico. It consists of 300 water Cherenkov tanks of 7.3 m diameter and 4 m height, packed densely in an area of about 22000 m^2 and equipped with 4 PMTs each [20]. By recording the amplitude and timing of recorded signals from one EAS, it is possible to estimate the position of the shower core and the arrival direction. Gamma-ray signals are distinguished from hadronic signals by evaluating the morphological differences in the recorded footprints of the air showers. The HAWC observatory has been fully operating since 2015. Through recent advances in the air shower reconstruction algorithms, the observatory's performance was significantly improved. HAWC achieves an angular resolution of less than 0.2° for energies above 40 TeV, and the effective area reaches the physical area of the array above ~ 100 TeV. The best sensitivity of less than 10% of the Crab Nebula flux for Crab-like point sources is reached between 2 TeV and 50 TeV for zenith angles below 30° [20]. The HAWC collaboration has provided catalogs of VHE gamma-ray sources that were detected by the observatory. The third and most recent catalog, 3HWC, is based on 1523 days of observation data. It contains 65 sources that have been detected above several TeV at a significance of more than 5σ [17]. Figure 3.14 shows

---

[4] `https://www.hawc-observatory.org/`

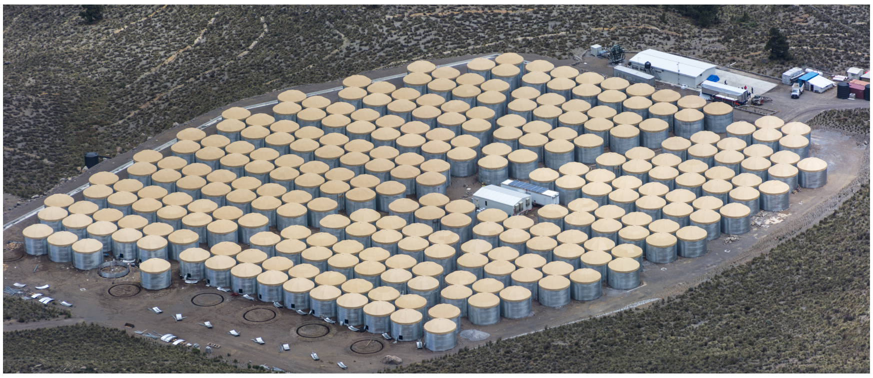

Figure 3.14: Aerial view of the HAWC observatory. Credit:Jordanagoodman `https://creativecommons.org/licenses/by-sa/4.0/`

an aerial view of the HAWC observatory.

Since 2019, the Large High Altitude Air Shower Observatory (LHAASO) has been operational. LHAASO is a multi-component cosmic ray and gamma-ray observatory located at 4100m a.s.l. in the Sichuan Province, China. It is designed to study cosmic rays between 1 TeV and 100 PeV and simultaneously act as a gamma-ray detector in the energy range between 100 GeV and 1 PeV. The three components of the LHAASO are the Square-Kilometer Array (KM2A), the Water Cherenkov Detector Array (WCDA), and the wide-field-of-view air Cherenkov/Fluorescence telescopes (WFCTA). The latter are used for cosmic ray studies [137]. KM2A is designed to perform cosmic ray studies and gamma-ray observations above $\sim$ 30 TeV. The array was fully completed in July 2021 [57]. It consists of a total of $\sim$ 5200 scintillator detectors distributed over a circular area of 1.3 km^2, which record the signals of electromagnetic particles in the air shower. Overlapping with the scintillator array, 1188 water Cherenkov tanks are deployed underground as muon detectors. The muon detectors add up to more than 40,000 m^2 of active muon surface. A high number of muons present in the hadronic particle cascades compared to electromagnetic showers is a clear way of identifying the hadronic background. The large active muon surface of KM2A allows for an exceptionally strong suppression of hadronic background with only a fraction of 10^{-5} to 10^{-4} of hadrons surviving selection criteria for energies above $\sim$ 100 TeV. The angular resolution is better than 0.2° and the effective area close to 1 km^2 for energies above $\sim$ 100 TeV [57]. The WCDA covers a total area of 78,000 m^2 and is divided into 3 separate arrays. The arrays are large water pools of 4.4 m depth, separated by black plastic curtains into a total of 3120 water Cherenkov detectors (WCDs) of 5 m $\times$ 5 m each [137]. The WCDA is designed to observe gamma rays between 100 GeV and 30 TeV and has been fully operational since 2021 [58]. A detailed illustration of the detector layout of LHAASO is shown in Figure 3.15.

Air shower arrays play an important role in uncovering the gamma-ray universe at the highest energies and unveiling the connections of gamma-ray emission to cosmic ray acceleration sites. Their high duty cycles, large effective areas, and large field-of-views provide an advantage when it comes to detecting the low fluxes of the highest gamma-ray energies ($>$100 TeV) and sources that have large spatial extensions. Especially concerning the search for galactic PeVatrons (Section 2.4), observatories such as HAWC and LHAASO have notably changed the picture in recent years. The 3HWC catalog contains 25 sources, the spectra of which have been measured to energies larger than 100 TeV [17], making them promising PeVatrons candidates. The LHAASO collaboration recently published their first catalog of gamma-ray sources [58], listing 43 sources with emission beyond 100 TeV out of a total of 90 sources. These catalogs provide important information that can be used for more detailed studies of these sources by IACTs, which can help shed more light on the properties of these sources with higher precision in energy and spatial resolution.

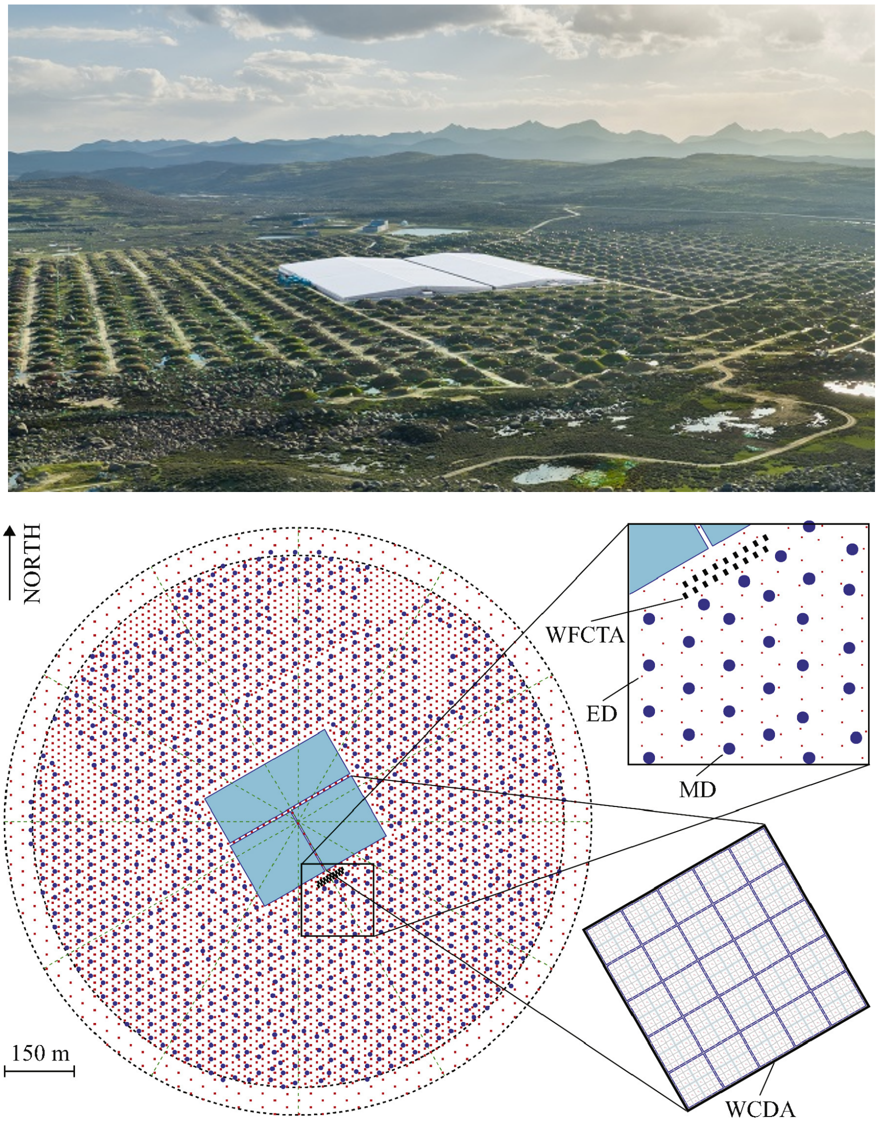

Figure 3.15: Top: Aerial view of the LHAASO observatory [133]. Bottom: Detailed detector layout: Scintillator detectors (ED, red dots) and muon detectors (MD, blue dots) are space throughout the large circular area. The WCDA is located at the center of the circle, the WFCTA next to it (black rectangles). Taken from [56].

Chapter 4

The MAGIC Telescopes

The Major Atmospheric Gamma-ray Imaging Cherenkov telescopes consist of two IACTs located at 2200 m a.s.l. at the Roque de los Muchachos Observatory on the Canary Island of La Palma in Spain (28°N, 18°W). They are positioned at 85 m distance from each other. The system is usually operated in stereoscopic mode, which triggers only events that are recorded simultaneously in both telescopes. The recorded data is processed with the MAGIC Analysis and Reconstruction Software (MARS), which converts the raw data into physically meaningful outputs through several analysis steps. Figure 4.1 shows the two MAGIC telescopes along with the counting house from which they are operated. An overview of the most important hardware installations in the telescope system and a summary of the data analysis chain is given in this chapter.

4.1 The telescope system

With a mirror diameter of 17 m and a total weight of less than 70 t per telescope, the system was specifically designed to enable a low energy threshold and a fast rotation speed, the latter of which is particularly important for the observations of short-lived transient events, such as GRBs. The two telescopes, MAGIC-I and MAGIC-II, started to operate in 2004 and 2009, respectively. The design of MAGIC-II was almost identical to MAGIC-I, with some improvements, specifically in the camera design and readout system. In 2011-2012, the system underwent a major upgrade to unify and further improve its performance. The MAGIC-I camera was replaced to match the design of MAGIC-II, and the read-out system was upgraded [27]. The following sections give an overview of the various hardware and subsystems installed in the telescopes which can be seen in Figure 4.2.

4.1.1 Structure and Drive

The main dish is mounted on a steel understructure and consists of carbon-fiber tubes to optimize its weight. An aluminum arch holds the camera at a focal length of 17 m from the dish. The drive system is described in detail in [52]. It is an alt-azimuth mount with two motors controlling the azimuth movement of the telescope on a circular rail. A third motor is responsible for the movement in elevation. Inaccuracies in the tracking due to mechanical deformations of the telescope structure are monitored by comparing the camera position against the known position of bright stars and corrected by applying a pointing model based on these measurements. With this, a tracking accuracy of $1.3'$ is achieved. To reposition between sources during standard observations, the movement speed of the telescopes is set to $4^\circ\,\mathrm{s}^{-1}$. In case of a GRB-alert, the telescopes reposition with $7^\circ\,\mathrm{s}^{-1}$ [6].

4.1.2 Reflector and Active Mirror Control

The reflector of each telescope is mounted on the main dish of the telescope structure. It measures 17 m in diameter, corresponding to an active mirror surface of $\sim 240\,\mathrm{m}^2$. Each mirror is divided into more than 240 individual panels of $1\,\mathrm{m}^2$ in size. In the original design

Figure 4.1: Overview of the MAGIC Telescopes site. MAGIC-I on the left, MAGIC-II on the right. The counting house is in the middle of the two telescopes. On top of the counting house, the LIDAR is mounted inside the white dome. Credit: Alicia Lopez-Oramas

of MAGIC-I, 4 mirrors of 50 cm × 50 cm size were mounted on each of these panels. For the construction of MAGIC-II, this additional subdivision was no longer necessary since it became possible to produce single mirrors of 1 m^2. The overall reflective surface has a focal length of 17 m and is designed to have a parabolic shape in order to maintain the temporal features of the recorded Cherenkov light flashes. To achieve this, the individual mirror panels are produced with spherical shapes of varying curvature radii ranging from 33.9 m at the center to 36.4 m at the edge of the reflector. Several mirror designs have been installed on the telescopes over the years. They all share an inner honeycomb aluminum structure which is very rigid but light-weight at the same time. The small mirror panels originally installed in MAGIC-I, as well as the original central mirror panels of MAGIC-II are aluminum diamond-milled mirrors: Aluminum plates are glued to the front and back of the honeycomb structure. The front plate is first pre-milled to a radius of 35 m and then shaped to the desired final curvature radius with the precise diamond-milling technique. The outer edge of the MAGIC-II reflector originally consisted of glass mirrors designed by Media Lario Technologies (MLT) together with scientists at the Italian National Institute for Astrophysics (INAF). Here, two thin glass sheets are glued to each side of the honeycomb structure and bent to the desired curvature with the so-called cold slumping technique. The concave side of the mirror is then coated with aluminum via e-beam deposition. In both mirror designs, the reflective aluminum is coated with a thin quartz layer to protect it from environmental influences. Despite this protective coating, the mirrors degrade over time due to the constant exposure to weather and environment. In regular mirror exchanges, heavily degraded mirrors are exchanged for new ones. Since 2019, a new design by MLT has been installed in these exchanges. These back-coated glass mirrors follow the glass mirror design by MLT and INAF, but instead of directly coating the top glass sheet with aluminum, an additional ultra-thin (400 µm) glass sheet is coated with aluminum and is then glued to the glass-honeycomb sandwich, the glass layer facing upward. This way, the aluminum is

protected by the thin glass layer, which makes it much more robust and, in principle, provides the possibility to clean the mirrors in case they become too dirty.
Due to the limited rigidity of the lightweight carbon fiber structure, the reflector deforms depending on the pointing direction of the telescopes. This is mitigated by the active mirror control (AMC). Actuators installed at the back of each panel can move the mirrors in any direction. The actuators are calibrated to ensure that each single mirror focuses to the center of the MAGIC camera. The corresponding positions, binned in azimuth and zenith, are saved in Look-Up-Tables (LUTs). The AMC software adjusts the individual mirror positions during observations for each pointing position based on these LUTs.

Figure 4.2: A photo of MAGIC-II. The carbon fiber structure of the main dish of MAGIC-I is seen as a reflection in the mirror. The MAGIC-II camera rests on a support beam close to the camera access tower on the left. In the center of the reflector, two mirror panels are missing. Here, several auxiliary systems are installed, such as the calibration box, the starguider camera, and the SBIG camera. See text for further information. Credit: Maximilian Linhoff

4.1.3 Camera

Since 2012, both MAGIC telescopes share a common camera design. Each camera is located in the focal plane at 17 m distance from the reflector. 1039 one inch (25.4 mm) PMTs are installed in the camera and arranged in a circular shape. The PMTs have a 0.1° FOV, resulting in a total FOV of 3.5° for the entire camera. The circular PMTs are equipped with hexagonal Winston cones, concentrating the light on the detector and thereby reducing gaps between the individual light sensors. The PMTs of type Hamamatsu R10408 can detect single photons with a peak quantum efficiency of 32% at a wavelength of 350 nm. Each pixel is equipped with a high-voltage power supply, a preamplifier, and a vertical cavity surface emitting laser (VCSEL). The VCSELs creates an analog optical signal from the electrical signal that is produced by the photons interacting with the photo-cathode of the PMTs. The optical signals are then transmitted via optical fibers to the counting-house, where the readout electronics are located. The average pulse width of the measured signals is 2.5 ns (FWHM). The single pixels are combined in clusters of 7 for easier installation and maintenance [27]. A spectralon plate can be moved in front of the camera to evaluate the reflected image of bright stars. This is necessary to assess the point-spread-function (PSF) of the telescope (see Section 4.1.5.5).

4.1.4 Trigger and read-out

In the read-out electronics the optical signals from the camera are converted back to analog electrical signals on the receiver boards. A Level 0 (L0) trigger criterium is applied, requiring single pixels to exceed a preset discriminator threshold (DT). The DTs are calibrated for each pixel channel to ensure a stable trigger rate. They are further adjusted online via the individual pixel-rate control in case of variable light conditions, e.g., due to stars in the FOV. Domino Ring Sampler version 4 (DRS4) chips consisting of 1024 capacitors forming a ring buffer serve as analog memory, which is read out and digitized when a trigger is received. The duration of the read-out signal is defined by the sampling speed of the DRS4 and the number of capacitors that are read out around the expected signal arrival time. The former is set to 1.64 GHz. 50 capacitor signals - in the analysis also referred to as *time slices* - are read out, resulting in a duration of the recorded signal of $\sim 30\,\mathrm{ns}$. The charges in the capacitors are read out sequentially by analog-to-digital conversion (ADC) converters with a dead time of $\sim 27\,\mu\mathrm{s}$, which is negligible compared to the usual trigger rate of 100–300 Hz. As mentioned, a first trigger criterium (L0) based on a simple DT is applied to each pixel. Signals passing these criteria serve as input to the Level 1 (L1) trigger, which is applied to the camera of each telescope: the inner 547 pixels of the camera from the trigger region and are divided into 19 macrocells, containing 36 pixels each (see Figure 4.3). For standard observations, the trigger logic looks for 3 neighboring pixels (3NN) that temporarily coincide. 2NN, 4NN, and 5NN logics are also implemented but only applied in specific use cases. When the L1 trigger criterium is met in a macrocell of a single telescope camera it is propagated to the final trigger level (L3, stereo trigger). The stereo trigger is passed only if both telescopes report an L1 signal event within 180 ns to allow for the light time of flight. The L1 signals are artificially stretched to 100 ns duration and adjusted according to the zenith and azimuth orientation of the telescopes to adjust for differences in the arrival time of the Cherenkov light from the air shower. When the L3 trigger is passed, each telescope read-out system receives the signal to store the event. The data acquisition software applies a calibration (see Section 4.1.5.1) to the ADC converters and combines the signal from all channels to build one event, which it writes to disk. For more detailed information on the read-out and trigger system, refer to [27] and references therein.

4.1.5 Calibration and Monitoring

4.1.5.1 Calibration

A calibration box equipped with a pulsed laser of 355 nm wavelength is installed at the center of each telescope dish at 17 m distance from the camera. The laser uniformly illuminates the camera with light pulses lasting $\sim 1\,\mathrm{ns}$, similar to the duration of the signals from air showers. This system is used to perform flatfielding, i.e., adjusting the HV of each individual PMT to compensate for the varying gains between sensors. The calibration box is used further to determine the conversion factor between ADC counts and photo-electrons by recording a calibration run before the observation of each source. In addition, the light pulses from the calibration laser are used to calibrate the analog arrival times in the DRS4 channels, which vary due to differences in propagation times from the camera to the chip. During observations, the laser is constantly firing at 25 Hz to monitor the gain in the read-out channels. For more detailed information, refer to [27] and references therein.

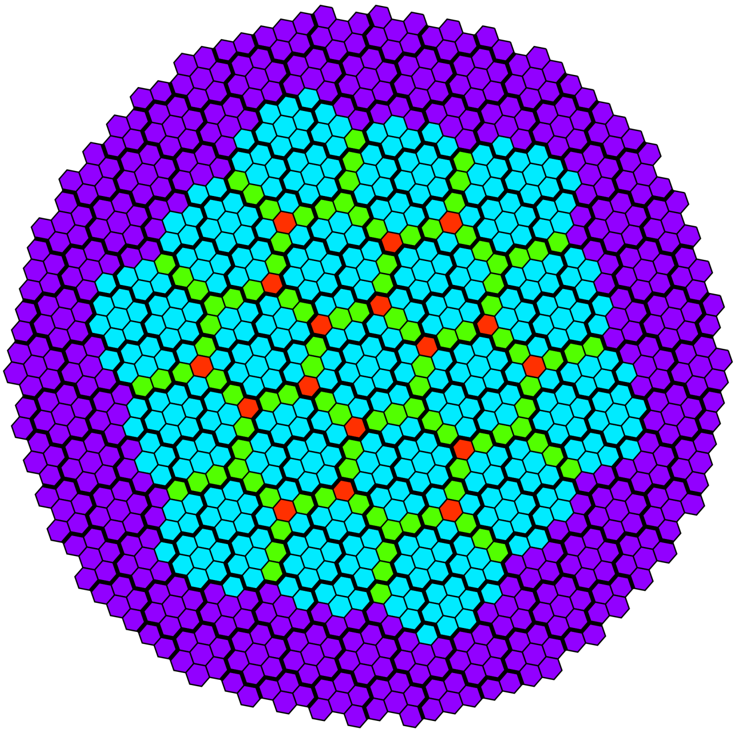

Figure 4.3: The trigger region of the MAGIC camera. The cyan pixels show the 19 macrocells of the L1 trigger. Green pixels belong to two, red pixels to three macrocells. The pixel cluster containing 7 pixels each are shown by thick black lines.

4.1.5.2 LIDAR

Varying atmospheric conditions change the amount of absorption of Cherenkov light from EAS and can affect the quality of their reconstruction. It is, therefore, necessary to monitor the atmospheric transmission during observations. In MAGIC, this task is performed by a light detection and ranging (LIDAR) system [86]. It consists of a laser operating at 532 nm, a 60 cm mirror and an hybrid photo detector (HPD). It is located on the roof of the MAGIC counting house inside a protective dome. The laser shoots short light pulses into the atmosphere, and backscattered light is collected by the mirror and focused onto the HPD. Clouds and aerosol backscatter light stronger compared to the usual Rayleigh scattering of a clear atmosphere. The travel distance of the photons can be inferred from the timing information. By applying an atmospheric model, the height of clouds and the amount of absorption can be estimated. This information can be used to correct the estimated energy of an air shower and the effective area of the telescope system [165]. The LIDAR can cover distances of up to 30 km from the telescopes. While this is sufficient for standard observations, it does not cover the distances at which EAS develop when observed at zenith angles larger than $\gtrsim 70°$. For the data taken between 70° and 80°, which I analyzed for this thesis, the LIDAR was partly still operating and used to discard nights of obvious bad weather, but additional methods based on images taken with the SBIG camera (see Section 4.1.5.5) and the star-guider camera (see Section 4.1.5.4) were used to evaluate the transmission of the complete atmosphere in the telescopes pointing directions.

4.1.5.3 Pyrometer

A radiation pyrometer is mounted close to the west access tower of the MAGIC-I telescope. This instrument measures the sky temperature. When clouds are present, they reflect the Earth's thermal radiation, which increases the sky's temperature. Via an empirical function, the parameter *cloudiness* is computed, which gives an estimate on the cloud coverage [185]. While the LIDAR is much more precise when assessing the presence of clouds in the field of view, in times when it is unavailable the pyrometer provides a good alternative to estimate the data quality.

4.1.5.4 Starguider camera

Each of the two MAGIC telescopes is equipped with a starguider camera. This CCD camera is mounted at the center of the dish and is aligned with the telescope's optical axis. Its FOV contains the MAGIC PMT camera and part of the sky behind it. Six LEDs arranged in a ring around the main camera provide a reference to find the camera center. By measuring the positions of stars with respect to the camera center and comparing them to their catalogued positions, the mispointing of the telescope with respect to the desired pointing position can be estimated. The number of stars recognized by the starguider cameras can also be used as an additional measure for the weather conditions in cases where the LIDAR is unavailable. Depending on the atmospheric transmission, the amount of stars that the starguider cameras can identify varies and by applying a lower cut on this number, data taken with bad transmission can be discarded.

4.1.5.5 SBIG camera

Next to the starguider camera, another CCD camera (SBIG camera) is installed at each telescope. The SBIG cameras are generally used to monitor the PSF of the telescope system. At the beginning of each night of observations, the telescopes are pointed to a bright star and a white reflective plate is moved in front of each PMT-camera. The SBIG camera takes an image of the star's reflection on the reflective plate. By evaluating the extension of the image, the ability of the main mirror to focus a point-like source into the camera center is evaluated, and the PSF is calculated.

To monitor the atmospheric transmission during observations beyond Zd 70°, a method was developed and implemented to measure the observed magnitude of a bright star close to the gamma-ray source of interest with the SBIG camera. The camera is equipped with a filter wheel containing four filters: red, blue, green, and luminance. To assess the atmospheric transmission, images are taken with 90 s exposure cycling through the red ($\lambda_{\mathrm{mean}} = 640\,\mathrm{nm}$), green ($\lambda_{\mathrm{mean}} = 530\,\mathrm{nm}$), and blue ($\lambda_{\mathrm{mean}} = 450\,\mathrm{nm}$) filters. An automatic procedure performs plate solving and aperture photometry to measure the magnitude of bright stars in the images. The atmospheric transmission is obtained by comparing the measured magnitude with the magnitude at airmass zero, which has been obtained by previous calibration measurements. This procedure provides the atmospheric transmission for very large zenith angle (VLZA) observations with a systematic uncertainty of $\lesssim 10\%$ [112, 140, 146].

4.1.6 Pointing strategy

Off-source observations need to be performed to estimate the background in the signal region. These Off-data need to be taken under the same conditions as the on-source data to reduce systematic effects. This can be done by observing a sky field that moves along the same track in the sky as the source of interest and does not contain a known gamma-ray source. However, this requires stable observing conditions and additional observation time. The so-called *wobble* mode [84] is more efficient. In wobble mode, the source is located at an offset from the camera center. The Off-data is taken from the reflected region opposite the center. The background is measured under the same conditions as the signal region. By switching back and forth (*wobbling*) between these positions, potential systematic differences between the camera regions can be canceled out. More regions in the camera than just the reflected source region can be defined as off-regions (*simultaneous background)*. They should not overlap, however, which limits the allowed size of simultaneous off regions. The source

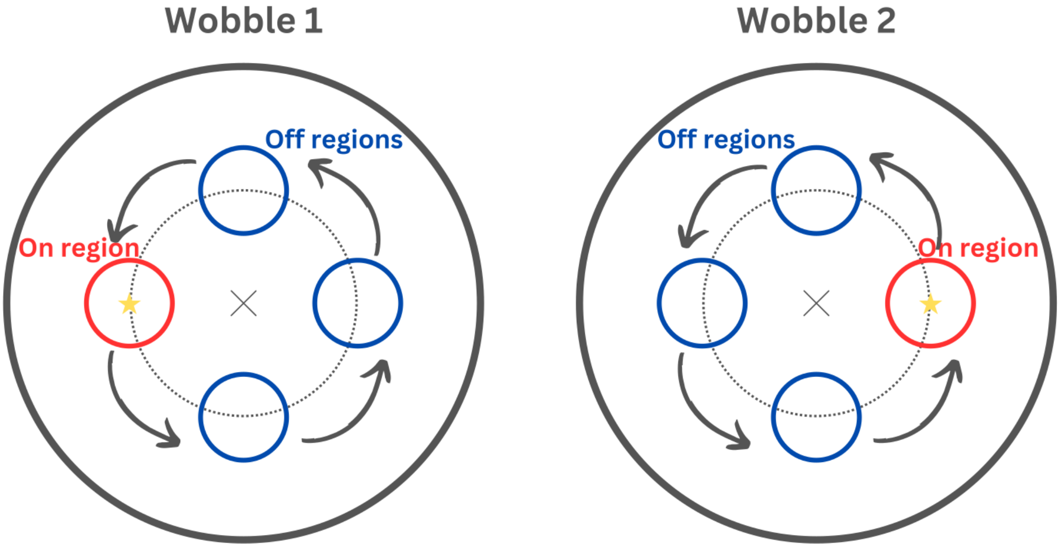

Figure 4.4: Illustration of the pointing strategy in wobble mode. One wobble pair is shown using 3 simultaneous Off regions. The On and Off regions are always located at a fixed offset from the camera center (black cross). The camera center moves from one side of the source (yellow star) to the other when switching between wobbles. The camera center is pointed to a fixed position in right ascension and declination, and source and off regions rotate around it due to the telescope's Alt-Azimuth mount.

and off positions will rotate around the camera center because the camera center is pointed to a fixed position in equatorial sky coordinates, whereas the telescope is moving in Alt-Azimuth coordinates. Figure 4.4 illustrates the wobbling procedure with three simultaneous background regions. The wobble method reduces systematic effects and provides Off-data without any additional observation time. In MAGIC, two standard wobble pairs are defined. They are located at 0.4° angular distance from the camera center and rotated by $0°/180°$ and $90°/270°$ with respect to the right ascension axis. The wobble offset and angles can be adjusted depending on the source morphology or the presence of bright stars in the FOV. The latter is the case for observations of the Crab Nebula. To avoid the bright star Zeta Tauri contaminating the signal region, Crab observations are carried out with only one wobble pair at 0.4° offset and angles 35° and 215°.

4.2 Data Analysis

The analysis of MAGIC data relies on the MAGIC Analysis and Reconstruction Software (MARS) [190]. MARS is a framework that consists of multiple executable programs and several macros that perform data reduction, event characterization, and high-level data production, such as skymaps, SEDs, signal significance estimation, and more. On top of the observation data, simulated data are needed for the estimation of some quantities. These MC simulations are air showers generated with the CORSIKA code [105] and are further processed with the standard MAGIC simulation package [141]. The following sections summarize the analysis pipeline through which raw data is processed step by step to finally output physics results.

4.2.1 Signal extraction

The raw data contain the single waveforms for each pixel in the recorded event. These signals need to be calibrated, their arrival time extracted, and the ADC counts converted in the number of photo-electrons (phe) that hit the PMT. This process is performed by the MARS executable `sorcerer`. The program finds the baseline from the pedestal run, which is taken at the beginning of each night of observations, and subtracts it from the waveform. After this, a sliding window algorithm looks for the 5 consecutive slices containing the highest sum of charges. The arrival time of the event is calculated from the count-weighted average of the arrival time of each of these slices [21]. The F-factor method is used to find the conversion from ADC counts to phe [144]. After applying this conversion factor, each pixel is assigned an arrival time and charge, and the recorded event can be treated in the form of a camera image.

4.2.2 Image cleaning and parameterization

The pixels containing the signal from an EAS are extracted, while the pixels only containing noise from the LoNS are discarded. The resulting cleaned shower images are then parameterized by computing the Hillas parameters (see Section 3.3.5.1). These steps are performed by the MARS executable `star`, which also determines the pointing position of the telescopes by applying pointing corrections from the starguider (see Section 4.1.5.4) to the position reported by the drive. The image cleaning is done in two consecutive steps [168, 24]. First, the core pixels of the shower are identified by finding groups with a minimum number of neighboring pixels N_{pixel} exceeding a threshold value of $Q_{\text{core}} = N_{\text{pixel}} \times Q_1$. The charge threshold value $Q_1 = m_{\text{NN}} \times Lv_1$ is the product of an NN-multiplier m_{NN} and the cleaning level Lv_1, which varies according to the level of noise from the LoNS. Observations taken under moonlight require a higher cleaning level than data taken in dark conditions. To avoid single bright pixels dominating a group, the charge of each pixel is clipped at a value $Q_{\text{clip}} = c \times Q_1$ before summing it with neighboring pixels. Furthermore, all signals within a group need to arrive within a certain time window t_{core}. In the second cleaning step, boundary pixels are identified. Each pixel neighboring a core pixel passing a second charge threshold Q_2 and arriving within 1.5 ns of the respective core pixel survives this cleaning step. All data analyzed for this thesis were taken under dark conditions with a 3NN trigger pattern. The relevant parameters of the cleaning procedure are summarized in Table 4.1. Values for different trigger patterns and light conditions can be found in [28] and [16].

Table 4.1: Image cleaning parameters

N_{pixel}	m_{NN}	Lv_1[phe]	Q_1[phe]	c	Q_2[phe]	t_{core}[ns]
2	1.8	6	10.8	2.2	3.5	0.9
3	1.3	6	7.8	1.05	3.5	0.7
4	1.0	6	6.0	1.05	3.5	1.1

The cleaned images are then parameterized. The list of original Hillas parameters [110] was based on calculating the momenta of the image in the camera plane and using the second-order momenta to represent the image as an ellipse. These were later extended further. A partial list of image parameters used in the MAGIC data analysis is given below.

- *size*: the total number of photo-electrons in the shower image.
- *length*: the length of the major axis of the ellipse.
- *width*: the length of the minor axis of the ellipse.
- *center of gravity (COG)*: the coordinates in the camera plane of the weighted mean signal.

- *alpha*: the angle between the major axis of the ellipse and the line connecting the *COG* and the nominal source position.
- *dist*: the distance between the nominal source position and the *COG* in the camera.
- *Conc-N*: the fraction of the signal contained in the N brightest pixels. A measure for the compactness of the shower.
- *leakeage1/2*: the fraction of signal in the outmost (1)/ two outmost (2) rings of the camera with respect to the image *size*. An estimate of how much the image would extend beyond the camera.
- *asym*: the distance between the brightest pixel and the *COG*. A measure for the asymmetry of the shower.
- *Number of Islands*: counting the number of isolated groups of pixels in the cleaned image. A high number of islands indicates a hadronic shower.
- *M3long*: the third momentum of the image along the major axis of the ellipse.
- *time gradient*: the slope of a first-order polynomial fitted to the arrival times along the major axis. A measure for the time development of the shower.
- *time-rms*: the RMS of the arrival times of the image.

The image cleaning and the calculation of above listed parameters are done for each telescope individually and the information is stored in separated files for M1 and M2. The MARS program called `superstar` combines the data into a common file. While preserving the individual telescope parameters, it additionally utilizes them to construct a three-dimensional picture of the shower. The main resulting stereo parameters are the following:

- *Shower axis direction*: the incoming direction of the primary particle. It is obtained by intersecting the major axes of both camera images in a common camera frame (see Section 3.3.5.1). A more precise estimation of the source position can be achieved with the *DISP*-method, described in Section 4.2.4.2.
- *Impact parameter*: the location of the shower impact on the ground with respect to the telescope position. It is defined as the perpendicular distance between the shower axis and the telescope pointing position. The impact parameter is calculated with respect to each telescope position.
- *Height of shower maximum (MaxHeight)*: a powerful parameter for the estimation of the energy of the primary particle since more energetic showers penetrate deeper into the atmosphere. It is defined as the intersection point of the shower axis and the lines connecting the telescopes with the position of the images COG in the sky. In practice, this three-dimensional problem is difficult to solve precisely, and `MaxHeight` is estimated as the height at which the perimeter of the triangle connecting these three lines is minimized (see Figure 3.11).
- *Cherenkov radius*: the radius of the Cherenkov light pool (Section 3.3.4.1) created by a single electron with a critical energy $E_\mathrm{c} = 86\,\mathrm{MeV}$ at the height of the shower maximum traveling in the direction of the air shower. The radius is measured in the plane perpendicular to the shower axis.

- *Cherenkov density*: the photon density in the light pool created by a single electron with critical energy $E_\mathrm{c} = 86\,\mathrm{MeV}$ at the height of the shower maximum traveling in the direction of the air shower. The density is measured in the plane perpendicular to the shower axis.
- *CosBSangle*: the cosine of the angle between the *shower axis* and the geomagnetic field. The component of the geomagnetic force normal to the shower axis acts on the tracks of positively and negatively charged particles diluting the shower and decreasing the *size* [66].

The reconstruction of stereo parameters performs well when the angle between the two major axes of the images in the common camera plane is large. If both telescopes see the air shower from roughly the same direction, the images are more aligned and the precision of the stereo parameter estimation suffers. This occurs especially at large zenith angles, were the effective baseline between the telescopes varies strongly depending on the azimuth of their pointing direction.

4.2.3 Data selection

Up to this level, the data analysis is done automatically by On-site Analysis. Analyzers working with data taken with standard settings under dark conditions can download the files produced by `superstar` and start directly with the data selection described in this section. For the analysis presented in this thesis, I started at this level. The quality of the acquired data needs to be evaluated in terms of the conditions under which they were taken. It can occur that certain hardware was failing at the time the data was taken, in which case these data need to be discarded. Especially the transmission of the atmosphere during observations can have a large systematic effect on the data. It is mostly affected by high air humidity, clouds, or the presence of dust in the atmosphere. The latter is specifically the case when sand from the Sahara desert is blown towards the Canary Island, enriching the atmosphere with a high concentration of sand and dust particles. Data taken under suboptimal weather conditions need to be identified and discarded or corrected. To get a general overview of the data quality, the shifters performing the observations keep a log every night, noting down weather conditions and hardware failures. Obvious problems with the data can be quickly identified by checking these *runbooks*.

A finer selection is done with the program `quate`. It can apply selections on a number of parameters and select time slices in which the quality cut conditions are met. In the standard analysis, the data is selected based on the atmospheric transmission values at 9 km altitude $T_{9\mathrm{km}}$ obtained with the LIDAR (Section 4.1.5.2). Data with $T_{9\mathrm{km}} < 0.5$ are discarded, while data with transmission values between 0.5 and 0.9 can be kept but need to be corrected and additional systematic uncertainties need to be accounted for. Data with $T_{9\mathrm{km}} > 0.9$ do not need to be corrected [165]. At times, when the LIDAR was not available, the measurements from the pyrometer (see Section 4.1.5.3) can be used instead to judge the transmission. `quate` also allows the selection of data based on the number of recognized stars in the starguider cameras (Section 4.1.5.4) and the zenith corrected L3 event rate. These are usually less precise but might become necessary when the LIDAR or the pyrometer are unavailable or no valid options. This was the case for the analysis of the data taken at zenith angles above 70° presented in this thesis. The details on the data selection in this case are given in Section 5.2.1.

4.2.4 Event charcterization

A recorded air shower event is characterized by its incoming direction and its energy. Furthermore, it is classified as a signal or background event based on the identification of the primary particle as a gamma ray or hadron. All of these quantities are estimated with a Random Forest (RF) algorithm, the basic functionality of which is introduced below, followed by more details on the implementation for the specific parameter estimations. The training of the RFs is done in MARS by the program `coach`. It is provided a gamma-ray MC sample for training and, in the case of gamma-hadron classification, a set of Off data which do not contain any significant gamma-ray signal. Once the RFs are trained, they are applied to the data to be analyzed and to another test gamma-ray MC sample by the program `melibea`. In this process, also the data selection performed in the previous step with `quate` is applied, and only events passing the selection cuts are written into the `melibea` output files.

4.2.4.1 Random Forests

RFs are a type of machine learning algorithm. They identify patterns and make predictions on quantities based on predefined parameters in the input data. By providing a training data set, a model f is built based on the chosen input parameters x and the desired outcome y such that $f(x) = y$. In reality, the model can never be perfect and will not provide an ideal description of the above relation. It is limited by how well the input parameters x correlate with the outcome variable y and by additional noise that is present in the training data. Machine learning algorithms find the model which minimizes the Mean Squared Error defined as

$$MSE = (Bias(f))^2 + (Variance(f))^2 + \sigma^2.$$

This entails a trade-off between minimizing the bias and minimizing the variance. The bias decreases with the number of provided training samples, as a wider variety in the input data enables the algorithm to better generalize to unseen data and makes oversimplification less likely. However, the variance increases with the number of training samples because the algorithm will eventually pick up on the noise in the data - an effect called "overfitting."
RFs are machine learning algorithms based on decision trees. Each tree is provided with a subsample of the input data, produced by *Bagging (Bootstrap Aggregation)* and a random sub-choice of input variables. At every node, it will find the optimal split value of the chosen parameter which makes the two created subsamples the most different. In the case of a *regression* algorithm, this is done by finding the split that provides the largest variance reduction. In the case of a *classification* algorithm, this optimal threshold value is determined by finding the maximum information gain, meaning the split that provides the purest child leaves. Individual decision trees are highly sensitive to the training data and might give high variances. In the RFs approach, this procedure is done in parallel for multiple trees of varying subsamples of input data and parameters, making the algorithm less sensitive to the training data and reducing the correlation between individual trees in the forest.

4.2.4.2 Estimation of the incoming direction with DISP Random Forest

The reconstruction of the incoming direction of the primary particle can be estimated based on the geometrical considerations described in Section 3.3.5.1 and Section 4.2.2. More precise results can be achieved with the DISP method. It was originally developed to improve the direction reconstruction for a single IACT [130]. For stereo observations, the results from the two single telescopes are combined. The source position is expected to lie on the major axis at a certain distance from the COG. This **D**istance between the **I**mage centroid and the **S**ource **P**osition (DISP) can be estimated based on size, length and width of the camera image. A RF regression algorithm is trained with a set of gamma-ray MC simulations, for which the true incoming direction is known. The input parameters used for the training are *Size, Width, Length, TimeGradient, Impact, MaxHeight, and Zenith.*

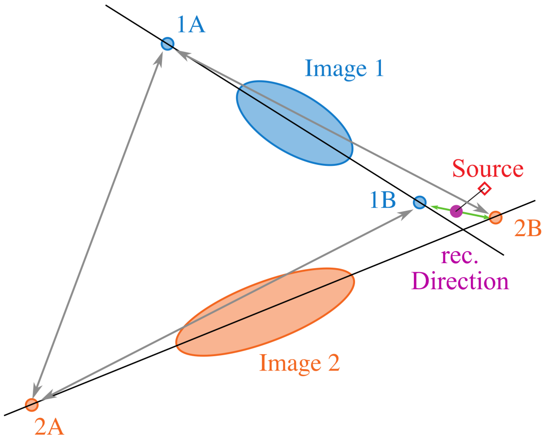

Figure 4.5: Illustration of the stereo DISP method. The RF regression algorithm finds two possible source positions (1A/B and 2A/B) for each camera image along their major axes (black solid lines). All four distances between the points are calculated (double-sided arrows). The reconstructed source position is the weighted average (purple dot) of the shortest distance (green arrow). Finally, the angular distance θ to the actual expected source position (red diamond) is calculated. Image taken from [173].

To find the final reconstructed source position, the results from the two camera images are compared, as shown in Figure 4.5. For each camera image, two possible source positions (A/B) are identified at the estimated distance at each end of the ellipse. The final result is found by comparing the distances between all four pairs of estimated source positions from both camera images. The mean of the smallest distance weighted by the number of pixels in each image is the final reconstructed position. If the smallest distance exceeds the minimum value of 0.22°, the event is discarded [28]. The angular distance θ between the reconstructed source position and the expected source position based on the telescope pointing direction is calculated and later used for signal extraction cuts (see Section 4.2.5). The reconstructed shower axes, as seen from both telescopes, are now no longer the major axis of the ellipse but the line connecting the respective COG with the reconstructed source position. Therefore, the geometrical stereo parameters *MaxHeight*, *Impact*, *Cherenkov radius and density* are recalculated based on the DISP reconstruction.

4.2.4.3 Energy Estimation

The stereo energy estimation algorithm used for this analysis is described in detail in [117, 118]. The application of the new RF for the stereo energy reconstruction led to a significant improvement in the precision of the energy estimation compared to the previous method, which was based on LUTs. Especially at large zenith angles, the improvement was remarkable. The RF improves the energy resolution by more than a factor of two compared to the LUT method. As in the DISP-RF, the energy is estimated via a regression algorithm based on the MC simulations of gamma rays. The input parameters are *Size, Width, Length, TimeGradient, Leakage*, and *zenith angle*. Additionally, geometrical parameters previously estimated with the DISP RF are given as input, namely *Impact, MaxHeight, CosBAngle, Cherenkov radius and density*. The procedure is nested: first, the DISP RF is trained and applied to the data. Using the DISP estimated parameters as input variables, the stereo energy RF is trained.

4.2.4.4 Gamma-Hadron Classification

The RF that identifies events as hadrons or gamma rays is a classification algorithm [22]. As training data, it receives a set of MC simulated gamma-rays and a sample of Off-data, which consists of observational data that does not contain gamma-ray signal and is therefore purely hadronic.[1] It is generally important that for the Off-data, a data sample, separate from the observation data containing the gamma-ray source of interest, is used. This Off-sample will contain shower images across the entire camera region, as will the observation data. However, the Off-sample only contains hadronic showers, whereas the observation data will contain hadronic shower images from the background as well as electromagnetic shower images that belong to the signal region. All data are initially in one single node, which is subsequently split into multiple generations of child nodes. The optimal value of an input parameter to split nodes into two succeeding nodes is found by evaluating the Gini-index Q_{Gini} in each child node.

$$Q_{\text{Gini}} = 4\frac{N_\gamma}{N}\frac{N_{\text{h}}}{N} \tag{4.1}$$

The quality of the split is judged by the average of the Gini-indices of each node Q_{split}. The optimal cut value minimizes Q_{split}. For each split, a set of three input parameters is randomly chosen. The parameter for which the optimal cut gives the lowest Gini-index is chosen for that split. The splitting continues until the number of events in a node is below 5 or the node contains only events of one type. Gamma-ray events in the final nodes are assigned a value of 0, and hadron events have a value of 1. The final nodes will be assigned the parameter *hadronness*, defined as the average of its events. When the RF is applied to data, each event is classified into one of these final nodes, based on the values of its parameters, and assigned a *hadronness*. In the standard analysis, the RF consists of 100 trees. The event is fed to each of these trees and its final hadronness value is the average of assigned values from each of these trees. The *hadronness* parameter is later used to extract signal events over the hadronic background (see Section 4.2.5).

4.2.5 High-level analysis

After the application of the RFs to the data, all parameters that are necessary to perform the high-level analysis have been reconstructed. Several programs exist in MARS to extract the signal significance, gamma-ray flux, and sky maps from the data provided by `melibea`.

4.2.5.1 Signal significance

The signal significance is evaluated from the number of excess events in the signal region over the background. The distribution of events in the camera is binned in terms of the squared angular distance θ^2 from the source position. The signal is expected to peak at small θ^2 values while the background is homogeneously distributed across the camera. The program `odie` creates two histograms which are both plotted in the θ^2-plot. The ON histogram contains the distribution of events with respect to the actual source position. The OFF histogram sums the events with respect to the background positions. The OFF histogram is normalized to the number of Off positions to account for the difference in exposure time. It is further normalized to the ON histogram if it differs more than one standard deviation from the ON histogram in a pre-defined normalization region far away from the source position. The PSF of the MAGIC telescopes is well described by a double 2D-Gaussian, which means that point-like sources are reconstructed into a circular shape in the camera. A cut in θ^2 is applied based on the extension of the PSF. It defines the circular signal region in which

---

[1] These data can either be observations of regions in the sky that do not contain a known gamma-ray source, or they are observations of a potential source that did not yield any significant signal.

the number of On and Off events N_{on} and N_{off} are used to calculate the significance of the signal. The formula to evaluate the significance was developed by Li & Ma [134] based on the assumption that the number of events in the signal region $N_{\text{on}} = N_{\text{S}} + \alpha \cdot N_{\text{off}}$. With N_{S}, the number of signal events and α accounting for differences in observational times between the On and Off measurements. N_{S} is the (unknown) number of true signal events. The estimated number of signal events is given by the excess in the signal region $N_{\text{excess}} = N_{\text{on}} - N_{\text{off}}$. The significance S is then given by equation 17 in [134]:

$$S = \sqrt{2}\left\{N_{\text{on}} \ln\left[\frac{1+\alpha}{\alpha} \cdot \frac{N_{\text{on}}}{N_{\text{on}} + N_{\text{off}}}\right] + N_{\text{off}} \ln\left[(1+\alpha) \cdot \frac{N_{\text{off}}}{N_{\text{on}} + N_{\text{off}}}\right]\right\}^{1/2} \tag{4.2}$$

4.2.5.2 Flux estimation

The gamma-ray flux F of a source in a certain energy bin ΔE is given by the number of events in that bin reaching the telescopes per unit area and unit time.

$$F(\Delta E) = \frac{N_{\text{excess}}(\Delta E)}{A_{\text{eff}}(\Delta E) \cdot t_{\text{eff}}} \tag{4.3}$$

N_{excess} is given by the θ^2-plot for each energy bin. The area covered by the Cherenkov light pool of an air shower defines the collection area of the instrument. The effective collection area A_{eff} also takes the limited trigger efficiency and further analysis cuts into account. A_{eff} is estimated from MC data, which have undergone the same application of RFs and the same analysis cuts as the observation data. It is defined as the fraction of all simulated events that survive the cuts, multiplied by the size of the light pool, which is given by the maximum simulated *impact* parameter.

$$A_{\text{eff}}(E) = \frac{N_{\text{final}}}{N_{\text{sim}}} \times \pi r^2_{\text{impact}} \tag{4.4}$$

A_{eff} is largely energy and zenith dependent. More details on these relations are given in Section 5.1.3. The effective time is the total elapsed observation time t_{elapsed} of the data set corrected for possible gaps between data runs and the dead time t_{d} of the read-out, which is 27 µs in the case of MAGIC. Since the arrival times of events follow Poissonian statistics, the distribution of time differences between individual events follows the exponential function

$$\frac{\mathrm{d}N}{\mathrm{d}t} = N_0 \lambda e^{-\lambda t}, \tag{4.5}$$

where N_0 is the number of triggered events and λ the true rate of events. λ is estimated by fitting Equation 4.5 to the data and the effective observation time is then given by

$$t_{\text{eff}} = t_{\text{elapsed}}/(1 + \lambda t_{\text{d}}). \tag{4.6}$$

The differential energy flux is calculated by assuming a spectral shape of the underlying emission and weighting the events in each energy bin accordingly. It is then given by

$$\frac{\mathrm{d}F}{\mathrm{d}E} = \frac{\mathrm{d}^3 N_{\text{excess}}(E)}{\mathrm{d}E\,\mathrm{d}A_{\text{eff}}(E)\,\mathrm{d}t_{\text{eff}}} \tag{4.7}$$

The SED gives the energy output of the source per logarithmic bin. It is obtained by multiplying Equation 4.7 with E^2. The flux points are placed inside the energy bins according to [128]. If the significance of the signal in an energy bin does not exceed 2σ, an upper limit is computed instead, according to the method described in [159]. Light curves show the evolution of integral flux over time. Above a given energy, the differential flux is integrated over the desired time span. All the described quantities and distributions are computed with the MARS program `flute`, which receives as input the test MC sample and the observation data output by `melibea`. `flute` is run separately for each analysis period, zenith angle bin, and, in specific cases, azimuth sample. The program `foam` combines data from multiple `flute` outputs into one common data set, estimating the total exposure and flux.

4.2.5.3 Spectral Deconvolution

For the measured excess events, only the reconstructed energy is known. Since the energy estimation method has a limited resolution, events of a certain true energy might be reconstructed into neighboring energy bins. This effect needs to be corrected by unfolding procedures when reconstructing the spectrum of a source. Different unfolding methods that are used in MAGIC are described in [23]. The migration matrix $\mathcal{M}_{ij}$ is the central quantity in unfolding. It describes the fraction of events in the true energy bin j, that are reconstructed into the estimated energy bin i. The measured spectrum $\vec{g}$ is therefore given by the multiplication of $\mathcal{M}_{ij}$ with the true spectrum $\vec{f}$,

$$\vec{g} = \mathcal{M} \cdot \vec{f}, \tag{4.8}$$

and the true spectrum can in principle be found by inverting the matrix

$$\vec{f} = \mathcal{M}^{-1} \cdot \vec{g} \tag{4.9}$$

Often, $\mathcal{M}_{ij}$ is not invertible and the solution can be estimated by minimizing the least-squares expression

$$\chi_0^2 = (\vec{g} - \mathcal{M} \cdot \vec{f})^T \; \mathcal{V}[\vec{g}] \; (\vec{g} - \mathcal{M} \cdot \vec{f}), \tag{4.10}$$

where $\mathcal{V}[\vec{g}]$ is the covariance matrix of $\vec{g}$.
The minimization often produces large fluctuations and uncertainties, requiring an additional regularization term that imposes constraints on $\vec{f}$. Equation 4.10 then becomes

$$\chi^2 = \frac{w}{2}\chi_0^2 + Reg(\vec{f}) \tag{4.11}$$

The weight parameter w is introduced to control the strength of the regularization. Three different methods of regularization are implemented in MARS [23]. If the true spectrum of the source is somewhat known, for example by previous measurements, the *forward folding* procedure can be applied. Here the assumed true spectrum is simply modified with the instrument response and fitted to the data. In MAGIC, the forward folding is used to cross-check the results of the other unfolding methods and to obtain the spectral parameters. The flux points presented in this thesis are computed with the unfolding procedure described above.

Chapter 5

The Performance of the MAGIC Telescopes at large and very large zenith angles

At the beginning of IACT observations, data were typically not taken at zenith angles beyond $\sim 30°$ to minimize atmospheric effects and obtain high-quality shower images. Towards the end of the last century, efforts began to increase the observation range up to larger zenith angles of $\sim 60°$ aiming to exploit the increase in the effective collection area but at the same time acknowledging the challenges accompanying the observations such as smaller image sizes [126]. Observations beyond at zenith angles larger than 60° remain rare to this day, with exceptions such as, for example, [10, 127] from the H.E.S.S. collaboration, or [34] from the VERITAS collaboration. Today, standard observations with the MAGIC telescopes are performed between 5° and 60° Zd. This range has been increased up to 70° to enable studies of sources that are only observable in this range, such as the GC (see Section 2.4.3, [138]). This also allows the maximization of observation time for given sources or is used to access a better sensitivity at higher energies. In 2014, an effort was started to test the limitations of observations at large zenith angles and the observation range was extended up to 80° Zd. These observations uncovered the highest energies ever observed with MAGIC accessing the emission from the Crab Nebula up to 100 TeV [140]. Extending the observable energy range to these energies is important for the searches of Galactic Pevatrons (see Section 2.6).

In this thesis, I will refer to the zenith distance range between 50° and 60° as *large zenith angles (LZA)*. I will refer to zenith angles above 60° as *very large zenith angles (VLZA)* [1].

The MAGIC collaboration has provided extensive studies of the telescope system's performance throughout its existence. Detailed studies of several aspects of the data acquisition and analysis were performed during the first years of operation of MAGIC I, as well as a complete evaluation of the stereoscopic performance of the system when MAGIC II began operating. The most recent reference is the performance study published in 2016, after the major upgrade of the system [28] (see Section 4.1). All of these studies provide details on the energy threshold, the instrument response function, and its flux sensitivity. However, only up to a zenith angle of 50°, not covering the above-mentioned range between 50° and 80°. In [140], a set of data taken in the zenith angle range [70°,80°] was published, showing the capability of these types of observations to observe energies up to 100 TeV but not providing a detailed evaluation of the performance. To complete this picture, I have performed a study of the MAGIC telescopes' performance during point-source observations performed between 50° and 80° Zd. It follows the general procedure of previous performance studies while taking special care of effects that arise at these large zenith angles due to the increased airmass along the line of sight.

The first section of this chapter provides a description of the quantities that characterize the

---

[1] Due to the zenith ranges in which the MC simulations are produced in MAGIC, a distinction in the analysis is actually done at 62°. In the description of the results presented in this chapter, I will, therefore, sometimes refer to the data subsamples above 62° as VLZA.

performance of the instrument and summarizes their values up to 50° as presented in [28]. The subsequent sections describe my study of the performance at zenith angles above 50°. In Section 5.4, I compare the MAGIC performance at large zenith angles with MAGIC at lower zenith angles and other existing and future instruments. Finally, I summarize the results in Section 5.5 and discuss their implications for future observations and improvements in Section 5.6.

5.1 Quantities to evaluate the performance

This section introduces the parameters that quantify the performance of the telescope system. They are mostly calculated from MC simulated data, for which the true properties of the event are known and the quality of the reconstruction can be thoroughly evaluated. For each quantity that is described here, I give its values for observations below 50° Zd which have been determined in [28]. These help in the understanding of the relevant parameters and their dependencies on observational settings. They also provide a baseline for comparison with my results for larger zenith angles that are shown in Section 5.2.

5.1.1 Energy threshold

The energy threshold is defined as the peak energy of the differential rate of events. It is customary to apply weights to the distribution of MCs, such that it follows a power law distribution with a spectral index of -2.6. The peak of the energy-binned histogram of MC events defines the energy threshold. The precise value can either simply be the bin with the maximum number of entries, given it is sufficiently narrow, or estimated by fitting a distribution to the histogram. The maximum value of the fit is taken as the energy threshold. The threshold is evaluated at three stages of the data analysis by evaluating the number of events

- passing the trigger criteria (*Trigger threshold*),
- additionally being successfully reconstructed with the DISP method (Section 4.2.4.2) and having a *Size* larger than 50 (*Reconstruction threshold*),
- additionally passing signal extraction cuts of $hadronness < 0.5$ and $\theta^2 < 0.03°$ (*Signal extraction threshold*).

The here-mentioned cuts for the signal extraction refer to the analysis of point sources. In the treatment of extended sources, their values need to be adjusted. Figure 5.1 shows the energy threshold as a function of the zenith angle that was published in [28]. The threshold increases with zenith angles since the shower maximum region moves to larger distances from the telescope, and the Cherenkov light from less energetic events suffers increased absorption in the atmosphere and the dilution of the photon density caused by the increased spread of the light pool over a larger area. The threshold also increases with each analysis stage since low-energy events are more difficult to reconstruct and differentiate from the hadronic background. It was found in [28] that the energy threshold follows the empirical function

$$E_{\text{threshold}} = 74 \times \cos(Zd)^{-2.3}\,\text{GeV} \tag{5.1}$$

5.1.2 The Instrument Response Function

The instrument response function (IRF) is used to estimate the number of expected signal events from a source of a given flux or vice-versa to estimate the intrinsic flux of a source, given the number of events that have been detected with a given instrument.

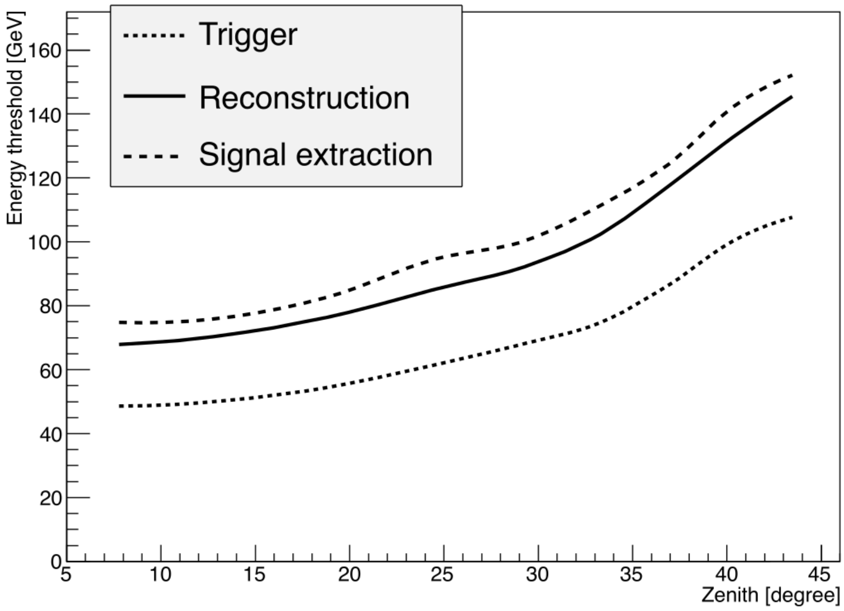

Figure 5.1: The energy threshold as a function of zenith angle up to 45°. The threshold rises with increasing zenith angles due to greater absorption in the atmosphere and lower photon density across the larger Cherenkov light pool. The threshold rises with each stage of the analysis, where especially low energy events are removed due to their inferior reconstruction. Figure taken from [28].

$$N(E)\mathrm{d}E = t_{\mathrm{obs}} \int_{E_{\mathrm{true}}} R(E|E_{\mathrm{true}}) \times \phi(E_{\mathrm{true}}), \tag{5.2}$$

where t_{obs} is the observation time, $\phi(E_{\mathrm{true}})$ the assumed source flux and $R(E|E_{\mathrm{true}})$ the instrument response. In gamma-ray astronomy $(E|E_{\mathrm{true}})$ is generally described as the product of three independent functions:

$$R(E|E_{\mathrm{true}}) = A_{\mathrm{eff}}(E_{\mathrm{true}}) \times PSF(E_{\mathrm{true}}) \times E_{\mathrm{disp}}(E|E_{\mathrm{true}}). \tag{5.3}$$

Here, $A_{\mathrm{eff}}(E_{\mathrm{true}})$ is the effective collection area of the instrument, $PSF(E_{\mathrm{true}}$ its PSF a measure for the angular resolution, and $E_{\mathrm{disp}}(E|E_{\mathrm{true}})$ the energy dispersion or energy resolution. These quantities are described in more detail in the following sections.

5.1.3 Effective collection area

The effective collection area A_{eff} is part of the IRF. It quantifies the geometrical area on the ground where events can be triggered by the telescope system, folded with the efficiency of all applied trigger and cut criteria (see Section 4.2.5.2). It is calculated via Equation 4.4. Analogous to the energy threshold it can be evaluated at several stages of the data analysis. For the estimation of the source flux, the effective area is calculated after applying the same signal extraction cuts to the MCs as chosen for the source data.

For MAGIC the effective area is mainly defined by the geometrical size of the Cherenkov light pool [28]. Consequently, A_{eff} strongly depends on the zenith angle of the observation. At larger zenith angles, EAS develop at greater distances from the telescopes. Due to the conical nature of the emitted Cherenkov light, it illuminates a larger area on the ground. Figure 5.2 illustrates this effect. A_{eff} also depends on the energy of the primary particle. The Cherenkov light density must be high enough to produce a trigger; therefore, only energetic EAS produce a signal. Below the energy threshold, the effective area is small and increases quickly with energy until it saturates at a certain value. As the zenith angle increases, the

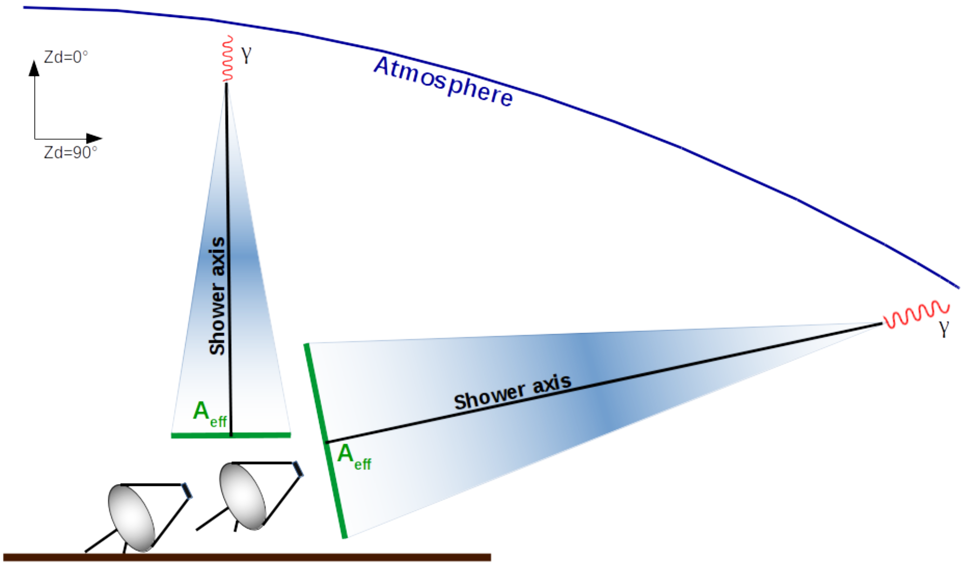

Figure 5.2: A sketch to illustrate the increase in the area illuminated by the Cherenkov light pool at large zenith angles.

energy at which the increase occurs shifts to higher values, and the saturation level becomes greater. This behavior can be clearly seen in Figure 5.3, which shows the effective area for low and medium zenith angles [28].

5.1.4 Angular resolution

The angular resolution is the second component of the IRF. It can be quantified in two ways [28]: as the standard deviation Θ_{Gauss} of a two-dimensional Gaussian function fitted to the distribution of the reconstructed direction of gamma-ray events or by calculating the 68% containment radius Θ_{68} of the reconstructed events. Assuming radial symmetry, fitting a 2D-Gaussian to the distribution of reconstructed source coordinates in the camera coordinate system is the same as fitting an exponential function to the histogram of the squared angular distance θ^2 from the nominal source position. Note that while both numbers give well-motivated measures of the angular resolution, they are intrinsically different. For a 2D-Gaussian distribution, Θ_{Gauss} contains only 39% of the events and will therefore typically be smaller than Θ_{68}. This becomes visible in Figure 5.4, which shows the angular resolution for low and medium zenith angles. The angular resolution improves with energy and reaches the best value of 0.04° at TeV energies.

The PSF is the probability density function, quantifying the likelihood of an event being reconstructed to different coordinates than its true arrival direction. The shape of the signal events in a θ^2 histogram defines the PSF, which describes the camera image of a point-like source at an infinite distance. Up to typical cut values, the θ^2 distribution is generally well described by a two-dimensional Gaussian. The tails of the distribution are, however, better accounted for by a 2D double Gaussian function [28] or a King function [70]. The angular resolution depends on the size of the gamma-ray images. Larger images that are

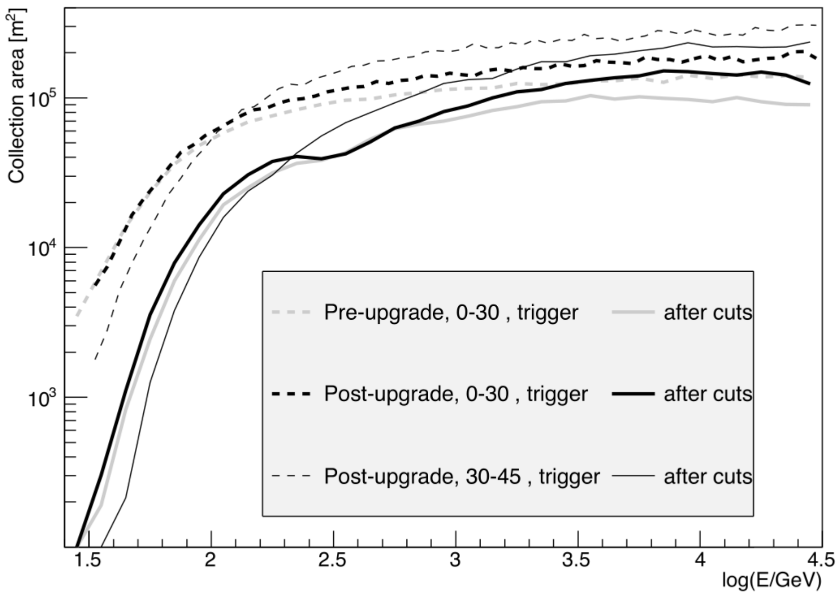

Figure 5.3: The effective area as a function of energy. The dashed lines correspond to the effective area at trigger level, solid lines after all cuts have been applied. Thick lines correspond to the zenith range $[0°,30°]$ and thin lines to the medium zenith angles $[30°,45°]$. The gray lines show the effective area before the hardware upgrade. Figure taken from [28].

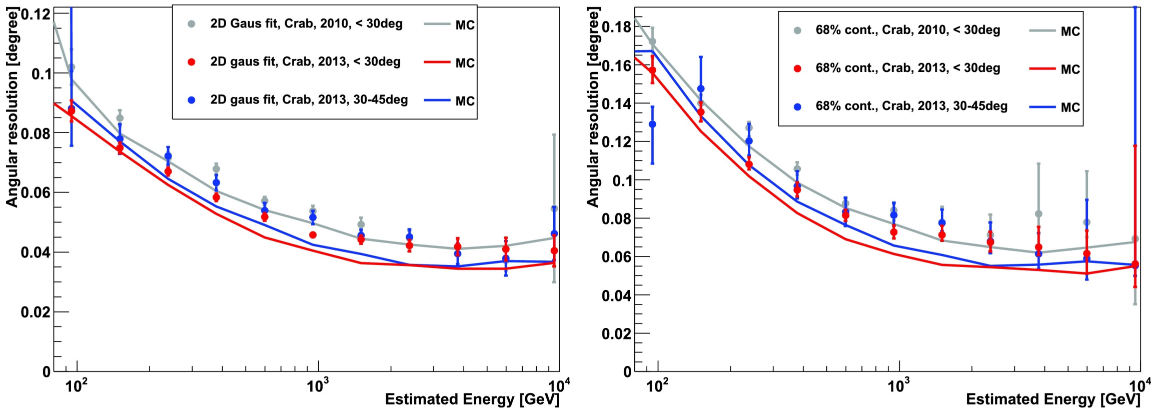

Figure 5.4: The angular resolution of MAGIC as a function of energy. The left panel shows the resolution obtained from the fit of 2D Gaussian to the distribution of reconstructed event coordinates, and the right plot shows the values obtained from calculating the 68% containment radius of the events. Two zenith ranges are shown, $[0°,30°]$ (red) and $[30°,45°]$ (blue). Data points show the values obtained from observation data of the Crab Nebula, while solid lines show the values obtained from MCs. The grey points and the grey line show the angular pre-upgrade resolution. The resolution improves with larger energies due to the more precise reconstruction of large shower images. Figure taken from [28].

spread across many pixels provide a better basis for the stereo reconstruction of the arrival direction. Therefore, the angular resolution worsens at lower energies, where air showers and their corresponding images are small, and at larger zenith angles, where EAS develop at large distances from the telescopes, also resulting in small images.

5.1.5 Energy resolution and energy bias

Another important feature of the IRF is the energy dispersion. As mentioned in Section 4.2.5.3, the energy of gamma-ray events is reconstructed with limited precision. The migration of events to neighboring energy bins is quantified by the energy resolution. At the low and high ends of the detectable energy range, the reconstruction might be biased. At low energies, only showers that happen to appear unusually bright for their energy are triggered and will be falsely reconstructed as more energetic events. At the high-energy end, large showers are not fully contained in the camera, hence their recorded camera image is smaller than the actual size of the EAS. This causes the algorithm to falsely assign smaller energies to these showers. The energy range in which the MCs are produced that are used to train the energy estimator can also bias the reconstruction. Since the algorithm can, at most, reconstruct the simulated range, the energy migration is asymmetric towards the edges, introducing a systematic over- or underestimation. It is, therefore, important to produce the simulations across a sufficiently large energy range. The energy resolution and bias are estimated from MCs for which the true energy of the event is known. For each event in a given energy bin the value

$$\Delta E = \frac{E_{\text{est}} - E_{\text{true}}}{E_{\text{true}}} \tag{5.4}$$

is calculated, where E_{true} is the true simulated energy of the MC event and E_{est} its reconstructed energy. The resulting distribution is fitted with a Gaussian. Its mean denotes the energy bias, and its standard deviation is the energy resolution.
Figure 5.5 shows the energy resolution and bias for low and medium zenith angles from [28]. It shows the large positive bias close to the energy threshold, which quickly reduces to fluctuations around zero for higher energies. The resolution is around 23% for low and high energies and takes its best value of 15% around 500 GeV.

5.1.6 Flux sensitivity

The flux sensitivity quantifies the capability of the telescope system to detect sources. It is defined as the minimum gamma-ray flux from a point source that is detected with a significance of $\geq 5\sigma$ in 50 h of observations. In this context, the significance is calculated as

$$S = \frac{N_{\text{excess}}}{\sqrt{N_{\text{bkg}}}}, \tag{5.5}$$

with N_{excess} the number of excess events and N_{bkg} the number of background events. To ensure the validity of a Gaussian treatment of the event distribution and to limit effects from systematic differences between On and Off distributions, additional requirements are that $N_{\text{excess}} > 10$ and $N_{\text{excess}} > 0.05 N_{\text{bkg}}$ [28]. It is calculated from observations of the Crab Nebula. The data set is split into a train and test sample. The train sample is used to optimize the cuts. The sensitivity is calculated in each energy bin for a range of *hadronness* and θ^2 cuts. Their values correspond to a range of gamma-ray efficiencies calculated from MC data. The final sensitivity is calculated by applying the combination of cuts that is giving the best sensitivity to the test sample in the respective energy bin. It is customary in gamma-ray astronomy to give the sensitivity in Crab Units (C.U.). A sensitivity of 10% C.U. means that the telescopes can detect a source with an intrinsic flux of 10% of the Crab

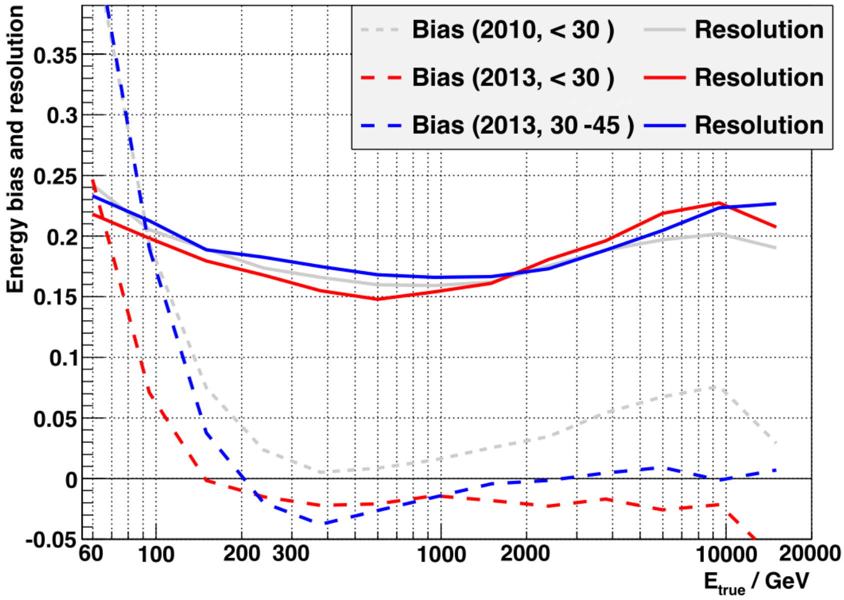

Figure 5.5: The energy resolution (solid lines) and energy bias (dashed lines) for the two zenith ranges [0°,30°] (red) and [30°,45°] (blue). The grey lines show the pre-upgrade resolution and bias. Figure taken from [28].

Nebula's flux in 50 h. Evaluating the sensitivity in narrow energy bins (typically 5 bins per decade in energy) ensures that the estimation is valid independently of the spectral shape of the source of interest.

Figure 5.6 shows the differential sensitivity of MAGIC for low and medium zenith angles. At low energies, observations at low zenith angles achieve a sensitivity of <10% C.U.. The optimal sensitivity of the system is reached in the energy range between 500 GeV and a few TeV. At larger energies, observations at larger zenith angles outperform low zenith observations.

5.2 The performance at large zenith angles

5.2.1 Data Set

I evaluated the performance of the MAGIC Telescope system in four zenith bins above 50°: [50°-62°], [62°-70°], [70°-75°], [75°-80°]. These bins correspond to the ranges in which the standard MAGIC MC simulations are produced.

The system of two telescopes is not symmetric in azimuth. The effective baseline between the two telescopes depends on the zenith and azimuth angle of the observation. Close to 0° Zd, the baseline stays almost constant at the nominal distance of 85 m between the telescopes across all azimuth angles. But the greater the zenith distance becomes, the more pronounced the difference in projected baselines along the line of sight. MAGIC-I is located in the northeast direction of MAGIC-II. The projected baseline reaches its minimum at the azimuth angle corresponding to this northeast orientation. Perpendicular to that, the baseline is maximal. Figure 5.7 shows an aerial view of the MAGIC telescopes, indicating the aligned and perpendicular azimuth directions. In Figure 5.8, the effective baseline between the telescopes as a function of azimuth angle is shown for observations at different zenith angles.

To investigate the effect of large differences in the baseline, I split the datasets above 70° for which the difference is most extreme into two subsets based on the azimuth direction.

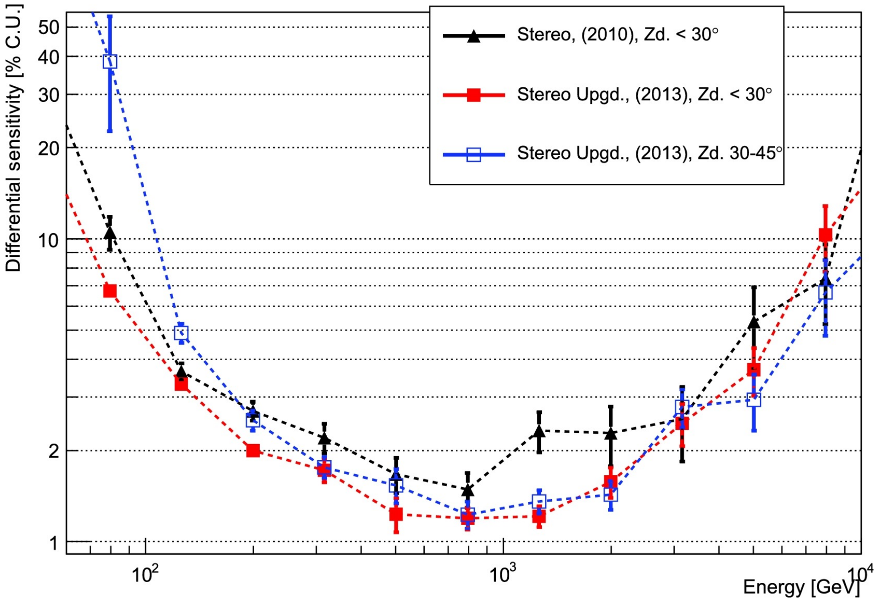

Figure 5.6: The differential sensitivity of MAGIC. It gives the minimal flux in C.U. of a point-like source that can be detected with 5σ significance after $50\,\mathrm{h}$ of observations. The sensitivity for two zenith ranges $[0°,30°]$ (red) and $[30°,45°]$ (blue) are shown, as well as pre-upgrade sensitivity (black). Figure taken from [28].

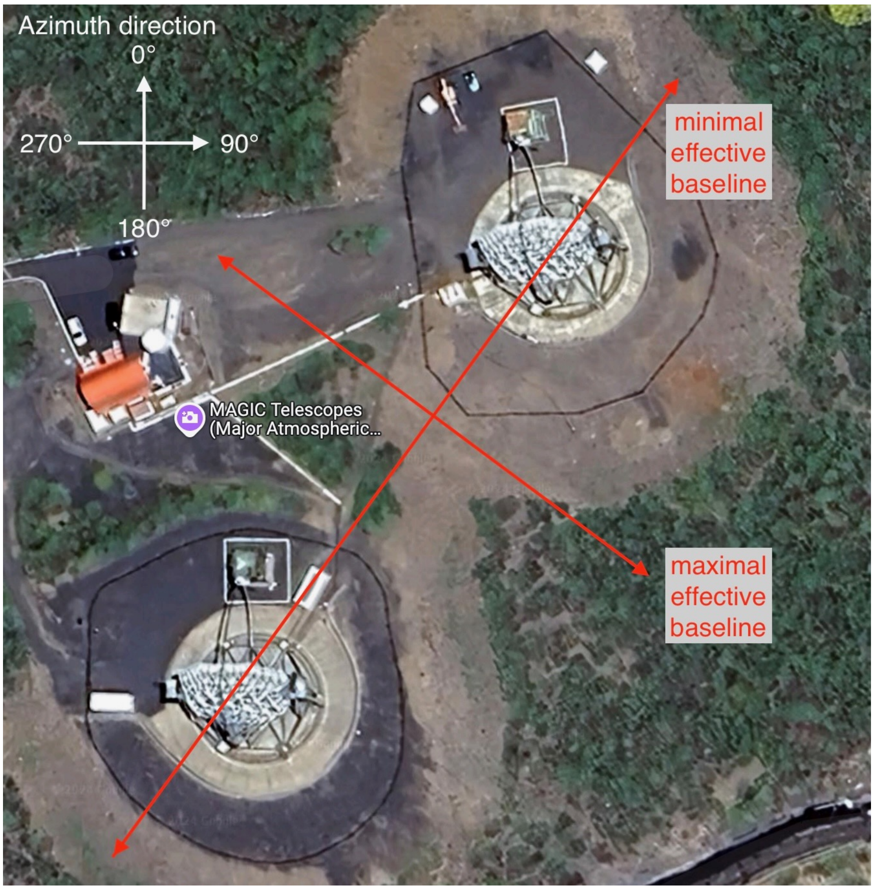

Figure 5.7: A satellite image of the two MAGIC Telescopes, taken during the day, when both telescopes are in park position pointing north corresponding to $0°$ in azimuth. The pointing directions in which the effective baseline between the telescopes are at minimum and at maximum are shown as red arrows.

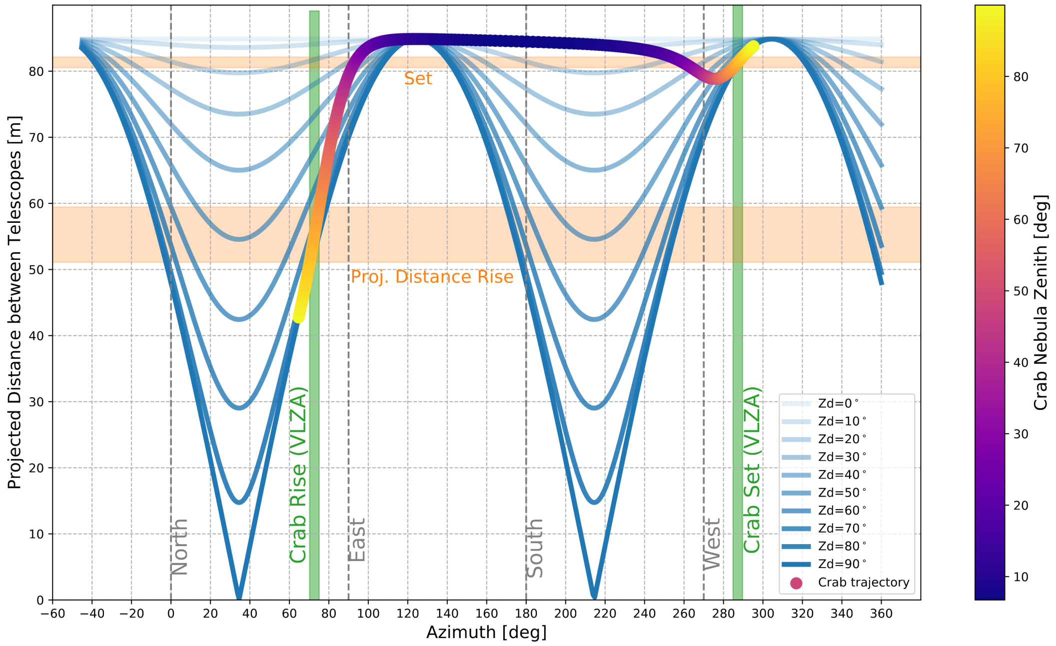

Figure 5.8: The effective baseline between the telescopes as a function of the azimuth pointing direction. The blue shaded lines show the baseline azimuth dependence for various zenith angles between 0° and 90°. The baselines vary stronger for larger zenith angles, reaching the most extreme range of [0m,85m] for 90°. The trajectory of the Crab Nebula is overlayed, the colorbar showing its zenith angle. Green-shaded regions show the azimuth range, and orange-shaded regions show the range of projected baselines for Crab observations above 70°.

Zenith range []	50-62	62-70	70-75	75-80
E_{max} [TeV]	80	80	500	500
MaxImpact [km]	0.7	1	1.6	2

Table 5.1: Maximal simulated values of energy and *Impact* for the different MC samples.

The azimuth bins were selected to match the direction of the Crab Nebula during these observations. At these zenith angles, the Crab Nebula is observed in the azimuth direction of $\sim 70°$ from September to November (*Rise* direction) and at Az $\sim 285°$ from December to April (*Set* direction). I tested two separate approaches of matching the azimuth in the MCs to the *Rise* and *Set* directions of the Crab Nebula. The first approach, which I refer to in the subsequent text and figures as the *standard azimuth splitting*, follows the procedure adopted in [140] by selecting bins of 70° width centered around the two azimuth directions of the Crab. In a second approach which I call *baseline azimuth splitting*, I focused on the projected baseline of the telescopes in these two azimuth bins of the Crab Nebula (see Figure 5.8), which are around 50 m to 60 m (*Rise*) and 80 m to 82 m (*Set*). The MCs were selected in azimuth bins for which the effective baseline differs at most 10 m from the Crab Nebula setup, resulting in five narrow azimuth bins for the *Rise* MCs and two broader bins for the *Set* MCs. The two sets of azimuth selections are visualized in Figure 5.9 and Figure 5.10. In the following sections, I will describe the differences between these two approaches regarding the presented results. The performance quantities for the different zenith bins can only be determined up to the maximum energies up to which the different sets of MCs are simulated. These values are summarized in Table 5.1.

The results shown in the subsections 5.2.2.1 to 5.2.2.5 were produced with MC data of the hardware stable period ST.03.07, which covers the periods of May 2016 to July 2017 and

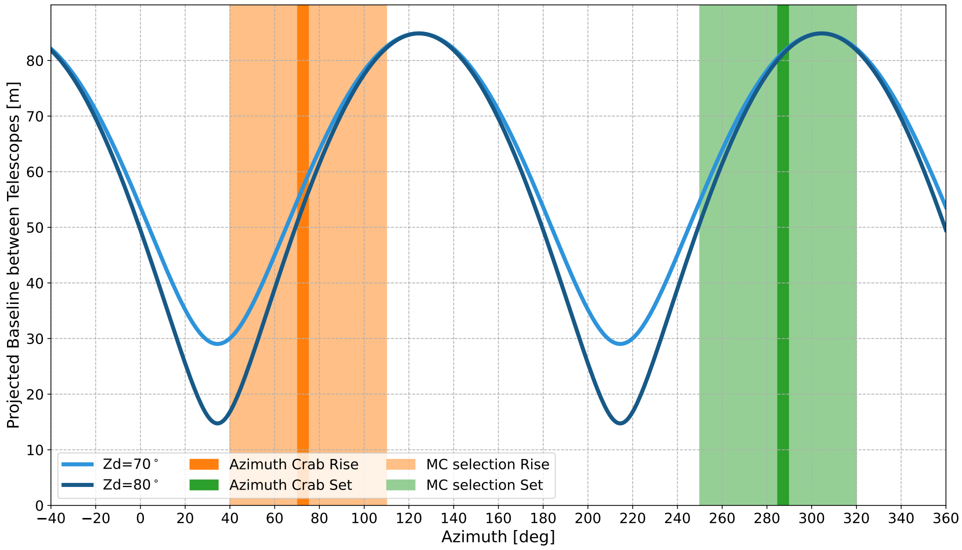

Figure 5.9: Visualization of the selected azimuth ranges for the *standard azimuth splitting* of the MCs. The blue lines show the variation of the projected baseline between the telescopes for the zenith angles 70° and 80°. The dark-shaded stripes show the azimuth ranges of the Crab Nebula in this zenith range for the Rise (orange) and Set (green) directions. The light-shaded regions show the corresponding ranges in azimuth into which the MCs sets were split.

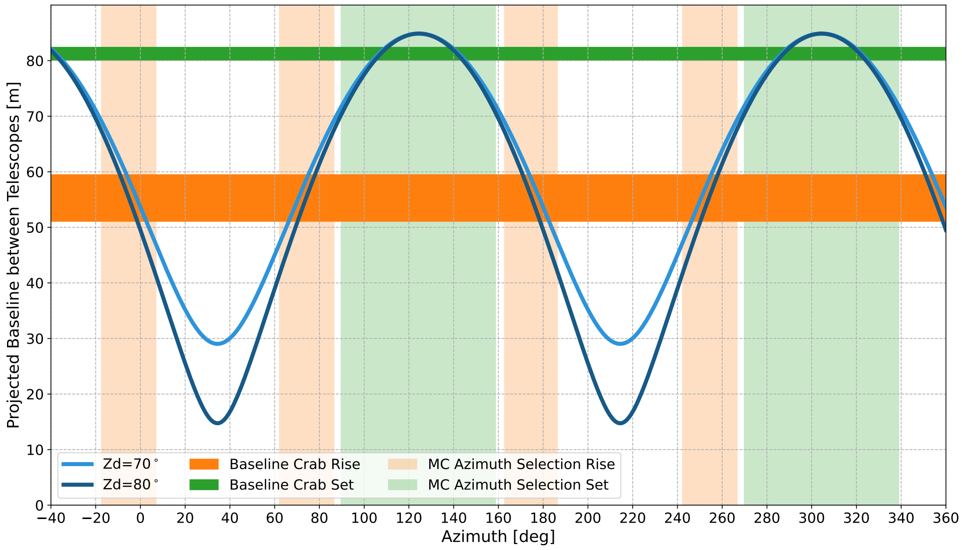

Figure 5.10: Visualization of the selected azimuth ranges for the *baseline azimuth splitting* of the MCs. The blue lines show the variation of the projected baseline between the telescopes for the zenith angles 70° and 80°. The dark-shaded stripes show the baseline ranges of the Crab Nebula in this zenith range for the Rise (orange) and Set (green) directions. The light-shaded regions show the corresponding ranges in azimuth into which the MCs sets were split. They were chosen in such a way that the baselines differ at most $10\,\mathrm{m}$ from the Crab Nebula baselines.

November 2017 to June 2018. I chose the period ST.03.07 for the performance study since it contains the largest amount of Crab Nebula data taken at VLZA and additionally has a solid availability of Off data taken across all zenith and azimuth ranges. It is, therefore, the most complete data set to study the performance of the MAGIC Telescopes above 50° with the best possible precision. For the flux sensitivity and the spectra and light curves of the Crab Nebula presented in the remaining parts of this section, I used all the Crab Nebula data that I analyzed to achieve maximal statistics. In the zenith angle range between 50° and 70°, this also includes data from the period ST.03.06 (November 2014 - April 2016), and between 70° and 80°, this covers all data taken between December 2014 and March 2020 across five analysis periods.
All data were taken under dark conditions; no moonlight was present. To the dataset below 70°, I applied the standard quality selection cuts, removing data taken with atmospheric transmission values at a 9 km distance from the telescopes below 0.8, as measured by the LIDAR (see Section 4.1.5.2). As mentioned in Section 4.1.5.2, the LIDAR does not reach the distances at which EAS occur that are observed under zenith angles larger than 70° and is therefore not sufficient to select unfavorable observation conditions. I adopted the quality selection procedure developed in [157], in which the nights of low atmospheric transmission are deselected based on the number of stars recognized in the starguider cameras (Section 4.1.5.4), and the L3 Trigger rates (Section 4.1.4). These cuts have to be identified for each subset in zenith and azimuth as well as for each wobble position, as the number of stars in the field of view of the starguider camera changes between wobbles. A detailed table showing the applied selection cuts is given in Table A.1. Additionally, I applied a global lower cut of 0.6 on the LIDAR transmission at 12 km distance to remove data of obviously bad quality. Table 5.2 summarizes the Crab Nebula data set, which I analyzed, and gives the available observation time in hours before and after applying the quality selection cuts. For the periods apart from ST.03.07, almost no dedicated Off observations were performed. For data taken in ST.03.06, I resorted to using a small sample of Crab Nebula data. In the periods ST.03.10 and the following, observations were performed on sources different from the Crab Nebula at zenith angles between 70° and 80°, and I used these data to train the RFs for these periods. For the rest of the analysis, I followed the standard procedure described in Section 4.2.

5.2.2 Results of the performance study

In the following sections, I report on my efforts to characterize the performance of MAGIC during point-source observations at large zenith angles. I present the results of these efforts regarding the performance quantities described in Section 5.1.

5.2.2.1 Gamma/Hadron Separation

As described in Section 4.2.4.4, the classification of events into gamma-like signal and hadronic background events is done by a RF algorithm, which is trained on a sample of MC simulated gamma-ray data and observation data without gamma-ray signal. In order to achieve a reliable classification, the distribution in zenith angle and ideally also in azimuth angle and effective baseline should match between MC and Off data and be similar to the actual observation data which is to be analyzed. Furthermore MCs and Off data need to match the hardware-stable period in which the observation data was taken. Observations qualify as Off data if either they have been specifically taken on source-free regions in the sky or were gamma-ray observations that did not yield a detection of gamma-ray signal, which is often the case for follow-up observations on GRBs or flaring AGN. In the case of the present data set, the availability of Off data is quite scarce because few GRB or AGN observations are performed at these large zenith angles. They mostly require a low energy

Table 5.2: Summary of the analyzed Crab Nebula data before/after quality cuts. Total times refer to the respective sum of observation time after cuts. The table shows into which subsamples the entire data sample has been split for the analysis, since hardware stable periods, zenith angles, and - above 70° - azimuth angles need to be treated separately.

Zenith range [deg]		**ST.03.06** 11/2014 - 04/2016	**ST.03.07** 04/2016 - 08/2017; 11/2017 - 06/2018	**ST.03.10** 06/2018 - 10/2018	**ST.03.11** 11/2018 - 09/2019	**ST.03.12** 09/2019 - 02/2020	**Total after cuts**
50 - 62		25.1/23.9h	4.9/4.1h	-	-	-	**28h**
62 - 70		19.9/18.1h	10.4/9.9h	-	-	-	**28h**
70 - 75	Rise	-	9.2/7.6h	5.7/5.3h	2.3/2.3h	9.4/7.8h	**23h**
	Set	8.1/7.7h	23.8/19.6h	-	6.3/6.3h	4.6/4h	**37.6h**
75 - 80	Rise	-	8.2/5.9h	6.2/5.9h	2.6/2.6h	6.5/4.9h	**19.3h**
	Set	8.7/7.8h	25.7/20.8h	-	6.3/6.1h	3.6/3h	**37.7h**
Total after cuts		**57.5h**	**67.9h**	**11.2h**	**17.3h**	**19.7h**	**173.6h**

threshold and are therefore favorably performed at lower zenith angles. For the periods ST.03.06 and ST.03.07, a few dedicated Off observations on Dark Patches were performed in the in the [70°, 80°] range, though not covering the entire zenith and both (i.e., *Rise* and *Set*) azimuth ranges. For later periods, no dedicated Off data were taken. For the data set between 50° and 70°, some Off data is available from follow-up observations, which, however, poorly matches the azimuth direction of the Crab Nebula. To train the RF in the zenith angle range where no real Off data was available, I used a small subset of source data from the Crab Nebula and, in later periods, from two other sources for the RF training. Given the extremely low gamma-ray event rate expected at these zenith angles and the corresponding energy range, even though it is not ideal, this is an acceptable procedure.

Figure 5.11, Figure 5.12, and Figure 5.13 show the available Off data in each respective zenith and azimuth bin together with the distribution of Crab Nebula data and the MC selection as a function of zenith, azimuth and projected baseline for the period ST.03.07, which I used primarily for the here-described performance study.

Figure 5.14 visualizes the gamma-hadron classification. The cumulative distributions of assigned *hadronness* values after applying the RF are shown for the Crab Nebula data and MCs. Gamma-ray events are assigned low *hadronness* values, which leads to the very fast increase of the MC distribution. The Crab Nebula data consists of a vast majority of hadronic background events since no additional cuts to select any signal have been applied. The dotted (dashed-dotted) lines show the fraction of background events that would survive a cut-value chosen in such a way that 85% (95%) of gamma-ray MCs survive it. Figure 5.14 compares the results of two RFs, one trained with the *standard azimuth splitting* MC sample and one with the *baseline azimuth splitting* sample. Both RFs were trained with the combined real- and source-off data sets. The two methods show no noticeable difference, apart from the 75°-80° Rise case, where the baseline splitting shows a slightly higher fraction of surviving background events for the 95% efficiency cut. Since the data set between 70° and 80° in the period ST.03.07 contains dedicated Off observations, as well as data taken on another source, namely the Dragonfly Nebula, I could compare the results of the gamma-hadron

classification for both extreme cases of using only real-Off data and using only source-Off data. The results are shown in Figure 5.15 for the *standard azimuth splitting.* There is no considerable difference between the two cases, the same is true for the baseline azimuth splitting.
For all data subsets above 70°, around 10% of the background events survive when selecting 95% of the simulated signal events.
Figure 5.16 shows the quality of gamma-hadron separation for various energies in the form of Receiver Operating Characteristic curves. Curves closer to the top left corner of the respective plot show a better classification, i.e., a higher rate of correctly identifying gamma-ray events (true positive rate) with a lower rate of wrongly identifying hadronic events as gamma rays (false positive rate). One would expect the separation to improve with energy as the shower images become larger and their different properties more obvious. The opposite behavior is, however, evident for the [62°, 70°] bin and even more prominent for the [75°, 80°] sample. This is due to the somewhat counterintuitive nature of the dependencies between trigger efficiency, energy, impact parameter, and image size at large zenith angles, which is explained in more detail in Section 5.2.3.2.
Overall, it has become clear that the quality of gamma-hadron separation decreases considerably at VLZA. An increasingly low rate of signal gamma-ray events at the energies of interest compete with a high rate of background events that survive signal extraction cuts on the *hadronness* parameter. The gamma-hadron classification provides the largest room for improvements to increase the performance at very large zenith angles. In future observations at large and very large zenith angles, special care should furthermore be taken to ensure enough dedicated *Off* observations to cover not only the zenith angle range of the source of interest but also the azimuth range and effective telescope baseline.

5.2.2.2 Energy threshold

I evaluated the energy threshold of observations taken above 50° by producing histograms binned in energy of MC events, weighted to follow a power law with spectral index of −2.6, as described in Section 5.1.1. I produced these histograms in 8 bins of equal size in cos(Zd) which are shown in Figure 5.17. Since, especially for the largest zenith angles, the distribution becomes very broad with long tails to higher energies, I decided to fit the histograms with a Landau distribution (see Equation 5.6) to find a consistent value for the peak of the histogram[2]. The location parameter μ of the fitted Landau function defines the energy threshold.

$$p(x,\mu,\sigma) = \frac{1}{\pi\sigma}\int_0^\infty e^{-t}\cos\left(t\left(\frac{x-\mu}{\sigma}\right)+\frac{2t}{\pi}\log\left(\frac{t}{\sigma}\right)\right)\mathrm{d}t \tag{5.6}$$

The resulting energy thresholds as a function of the zenith angle for the three different analysis stages described in Section 5.1.1 are shown in Figure 5.18. As can be seen in this figure, the empirical formula found in [28] is not a good match to the values above $\sim 60°$. I have fitted a function of the same form to the data points at the *Trigger* stage, resulting in a fit of

$$E_{\mathrm{threshold}} = (54 \pm 2) \times \cos(\mathrm{Zd})^{-2.93\pm0.02}\,\mathrm{GeV} \tag{5.7}$$

The energy threshold increases with the zenith angle, most dramatically above 60°. The exponentially increasing airmass above 60° Zd translates to the fast increase in energy threshold as Cherenkov light from smaller airshowers induced by less energetic gamma rays is more strongly absorbed (see Section 3.3.5.2). At the largest zenith angles, the differential

---

[2] I used the python package `pylandau`: `https://github.com/SiLab-Bonn/pylandau`

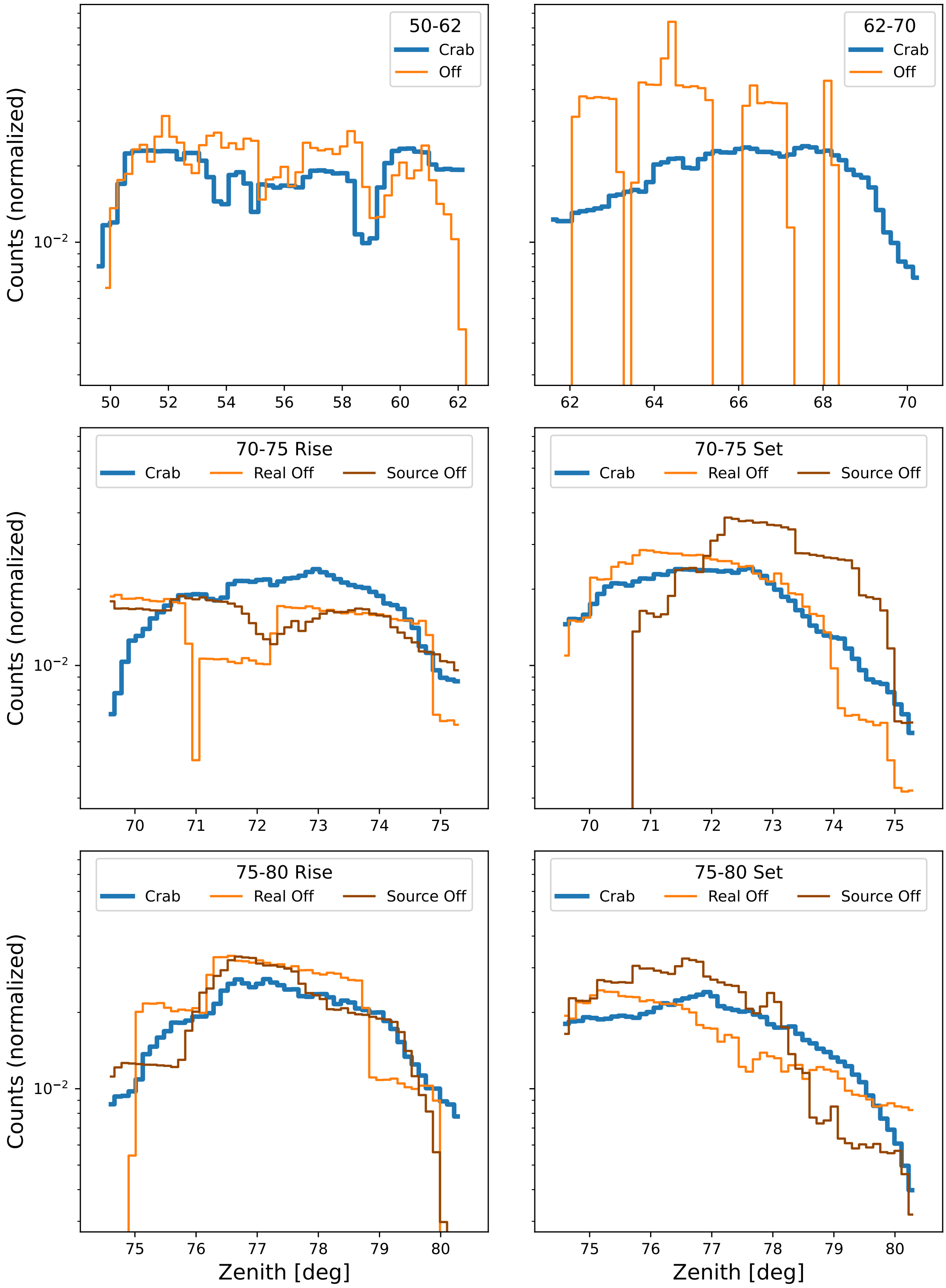

Figure 5.11: Zenith distributions of available Crab Nebula and corresponding Off data for the period ST.03.07. For the two zenith bins $[50°, 62°]$ and $[62°, 70°]$ (top two panels), no distinction is made between "real" and "source" Off data since all Off data are "real" in the sense of not containing any gamma-ray signal. For all data subsets, the Off data cover most of the zenith range quite well.

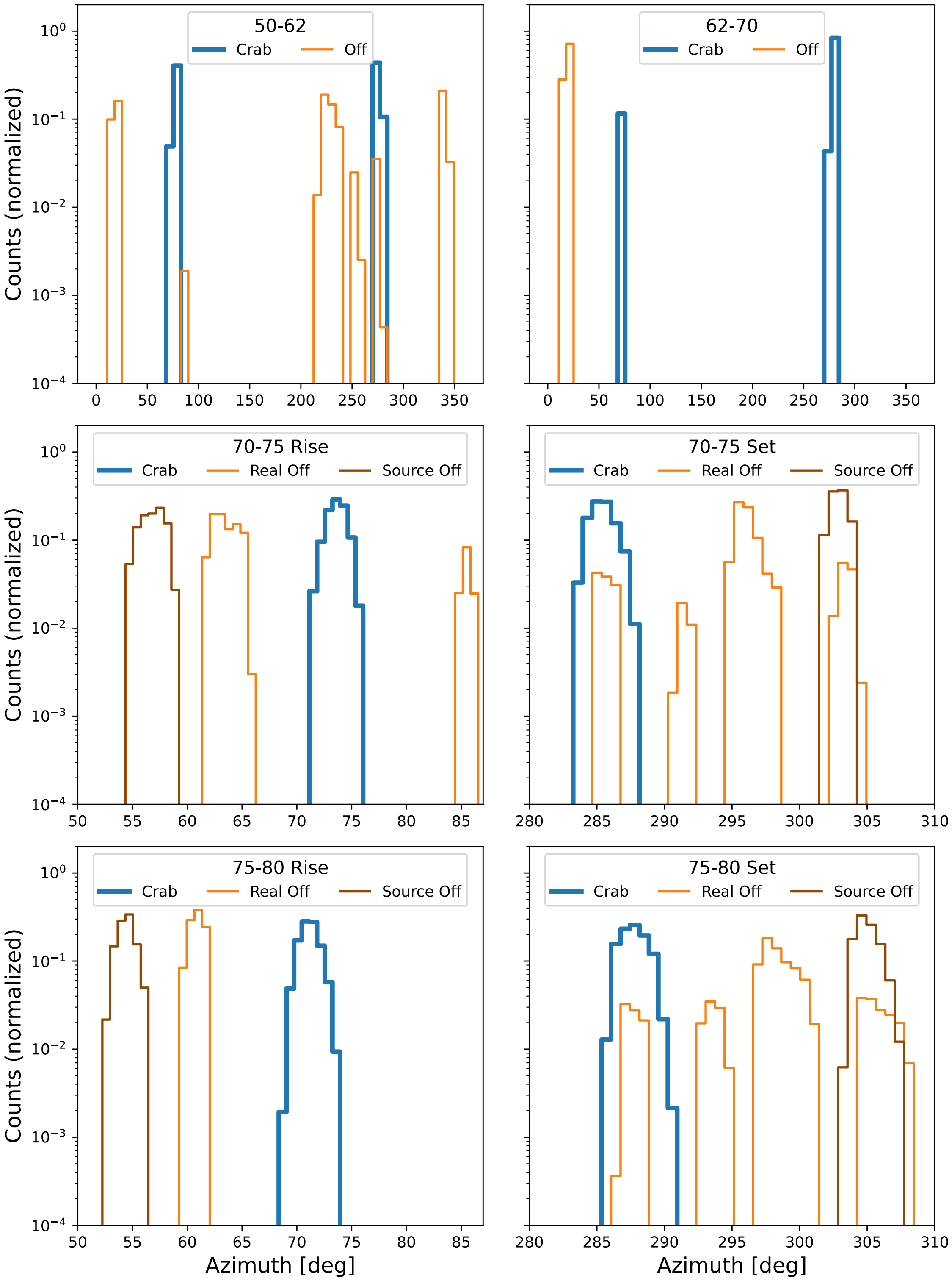

Figure 5.12: Same as for Figure 5.11, but showing the distribution in Azimuth. Especially for the zenith bin [62°, 70°], and the *Rise* samples, the Off data does not match the Crab Nebula data very well.

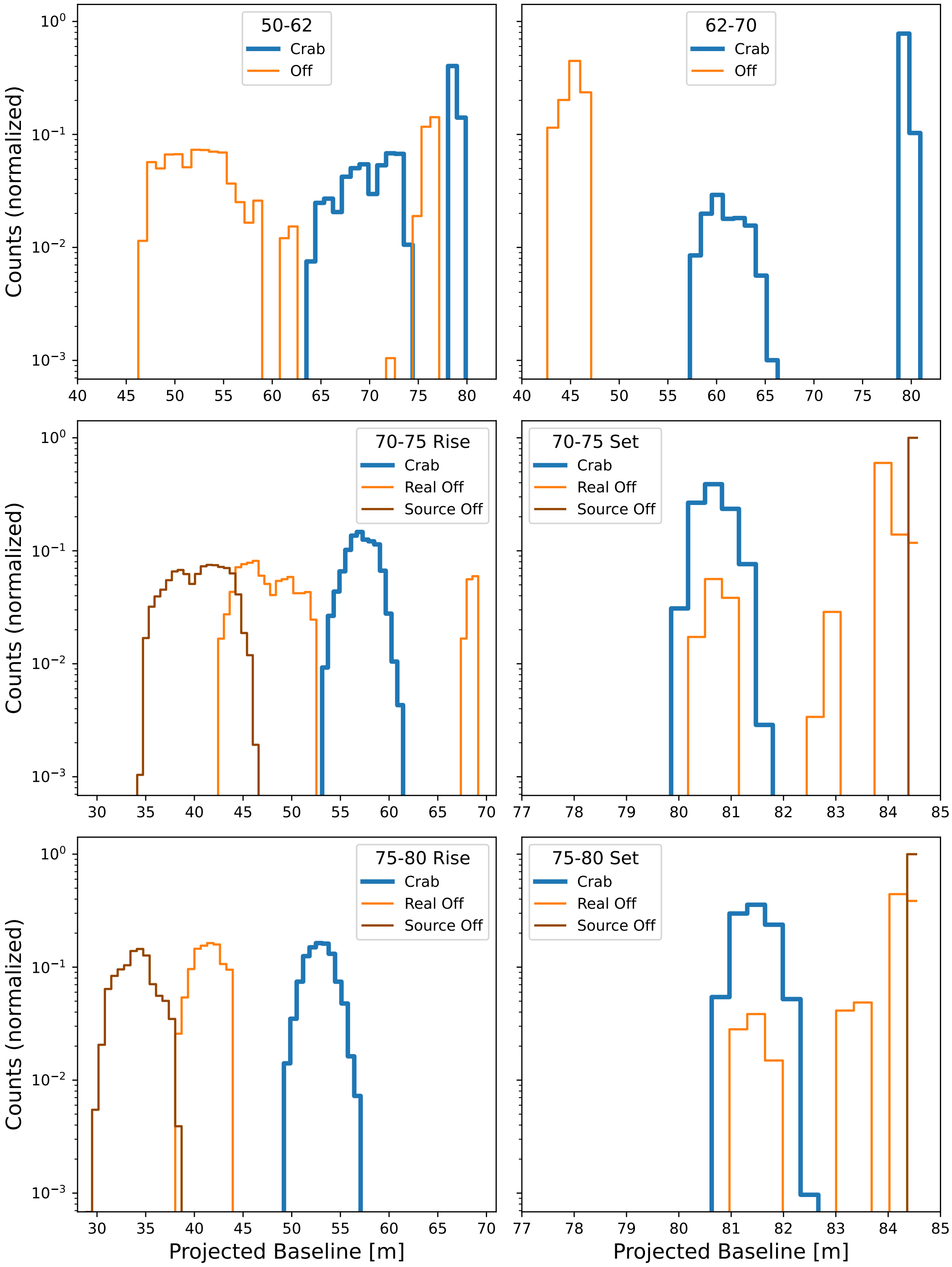

Figure 5.13: Same as for Figure 5.11 and Figure 5.12, but showing the distribution in projected baseline. Since the baseline is strongly connected to the azimuth angle the situation is similar: for the zenith bin $[62°, 70°]$, and the *Rise* samples, the Off data does not match the Crab Nebula data very well.

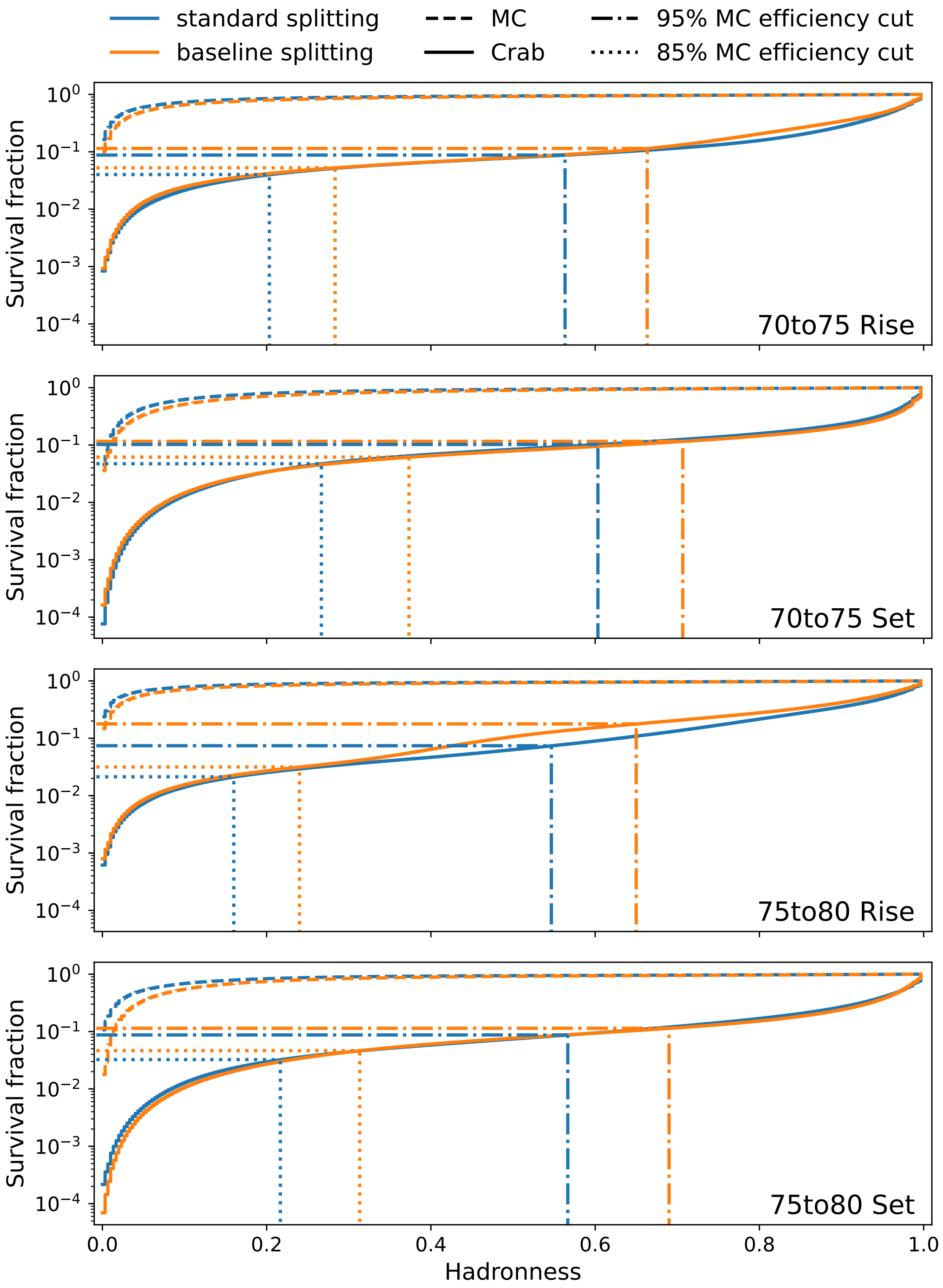

Figure 5.14: Cumulative Hadronness distributions for MCs (dashed lines) and Crab Nebula data (solid lines). The blue lines correspond to the *standard azimuth splitting*, and the orange lines to the *baseline azimuth splitting*. The dashed-dotted and dotted lines visualize the cut values at which 95% and 85% of the MC survive, respectively. The vertical lines show at which *hadronness* value those efficiencies are reached, and the horizontal lines show which fraction of the background would survive this cut.

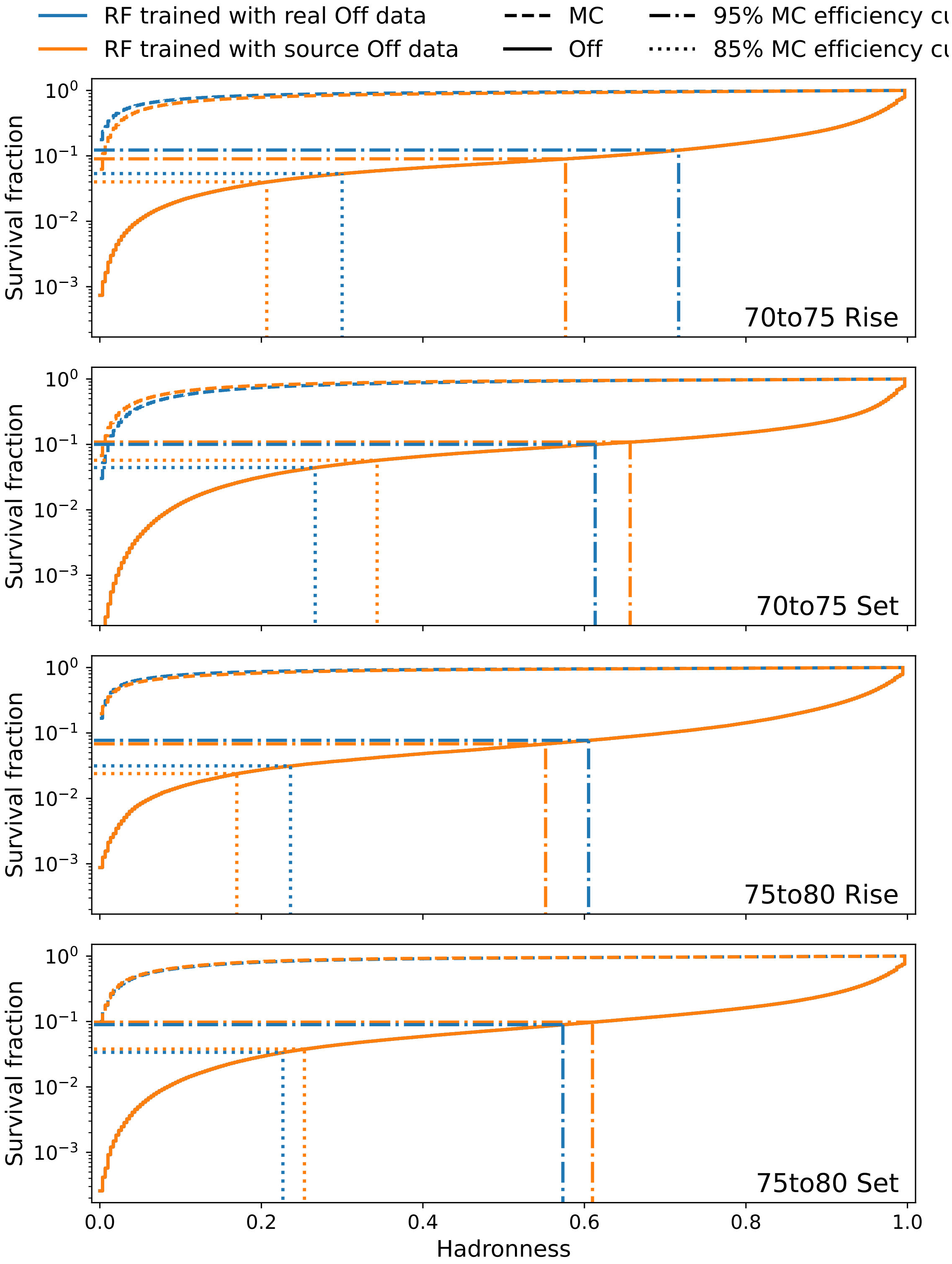

Figure 5.15: Cumulative Hadronness distributions for MCs (dashed lines) and Off data (solid lines) for the case of *standard azimuth splitting*. The blue lines correspond to the RF trained with "real" Off data, and the orange lines to the RF trained with "source" Off data (see text for more information). Note that the RF can not be applied to the data set it was trained with, which is why the actual Off sample plotted here is the real Off for the "source" Off trained RF (orange) and vice-versa. The dashed-dotted and dotted lines visualize the cut values at which 95% and 85% of the MC survive, respectively. The vertical lines show at which *hadronness* value those efficiencies are reached, and the horizontal lines show which fraction of the background would survive this cut.

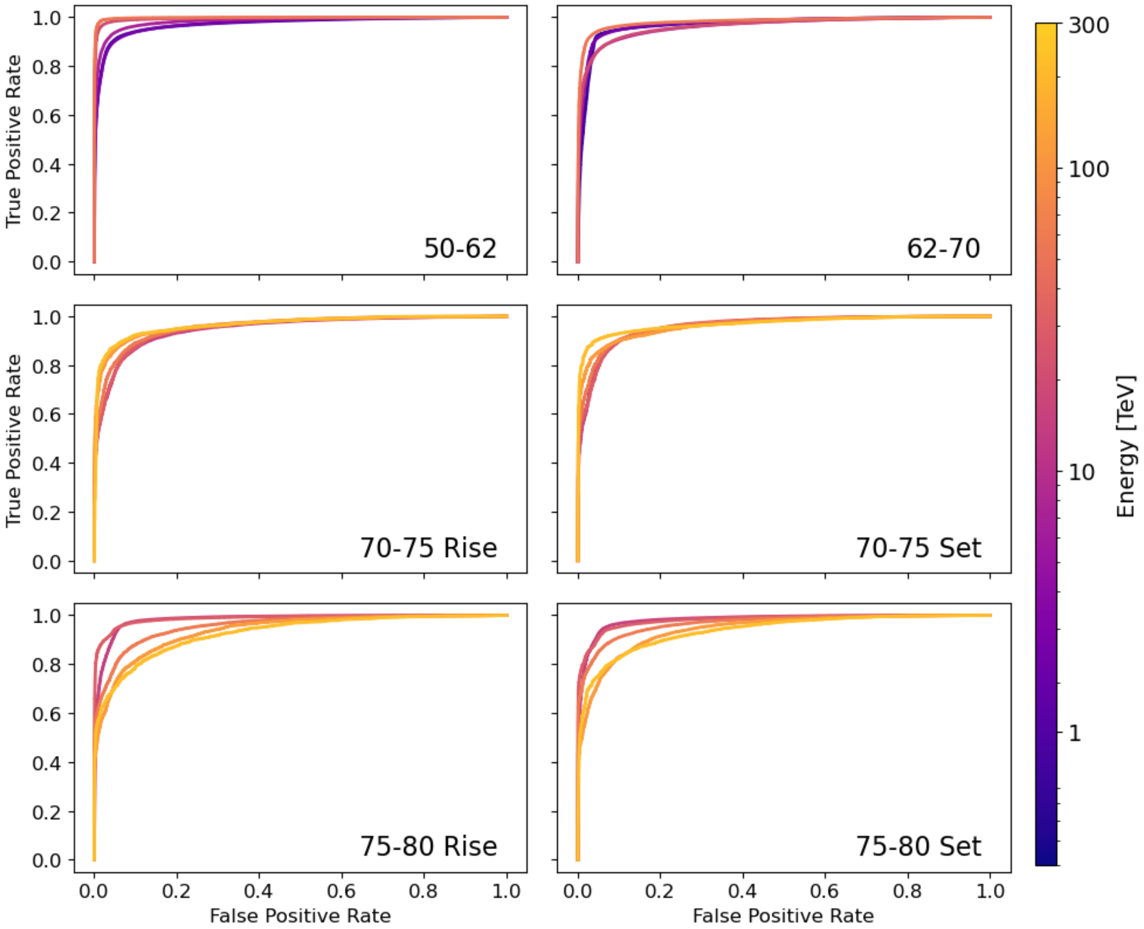

Figure 5.16: Receiver Operating Characteristic curves for the gamma-hadron classification algorithm at various energies for all zenith angle subsamples. The classification performs better at lower zenith angles. The two subsets between 50° and 70° shown in the two top panels cover the same energy range. With higher energies the gamma-hadron separation improves in the $[50^\circ, 62^\circ]$ bin while it worsens in the $[62^\circ, 70^\circ]$ bin. A similar behavior can be seen for the samples above 70° where the separation power increases with energy for the $[70^\circ, 75^\circ]$ bin, while it decreases in the largest zenith angle bin. Overall the gamma-hadron separation is notably worse above 70°.

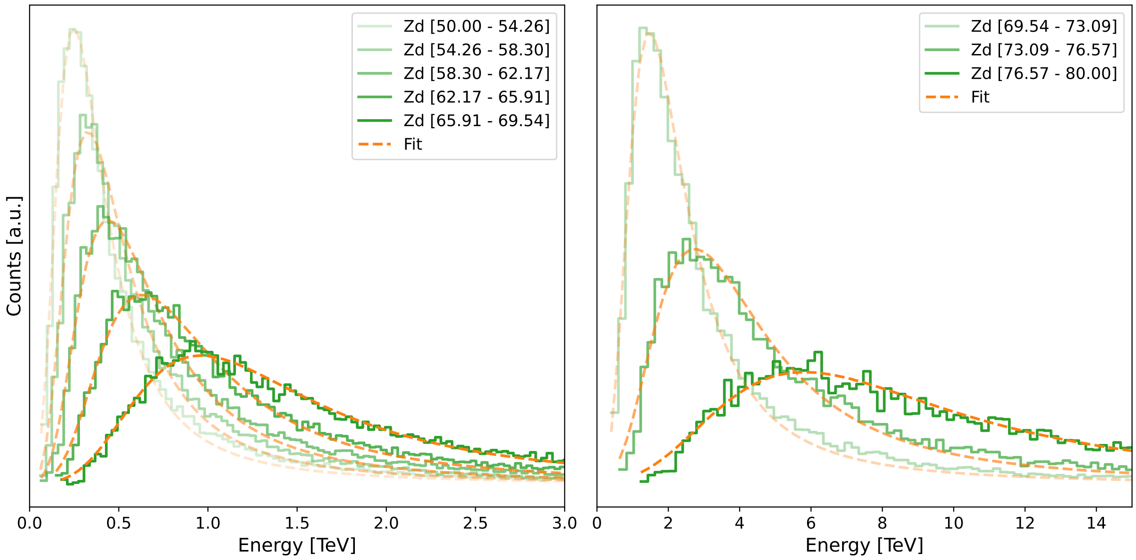

Figure 5.17: Histograms binned in simulated energies of MC events that have passed the trigger criteria of the data analysis for different zenith angle bins in the ranges $[50°,70°]$ (left) and $[70°,80°]$ (right).

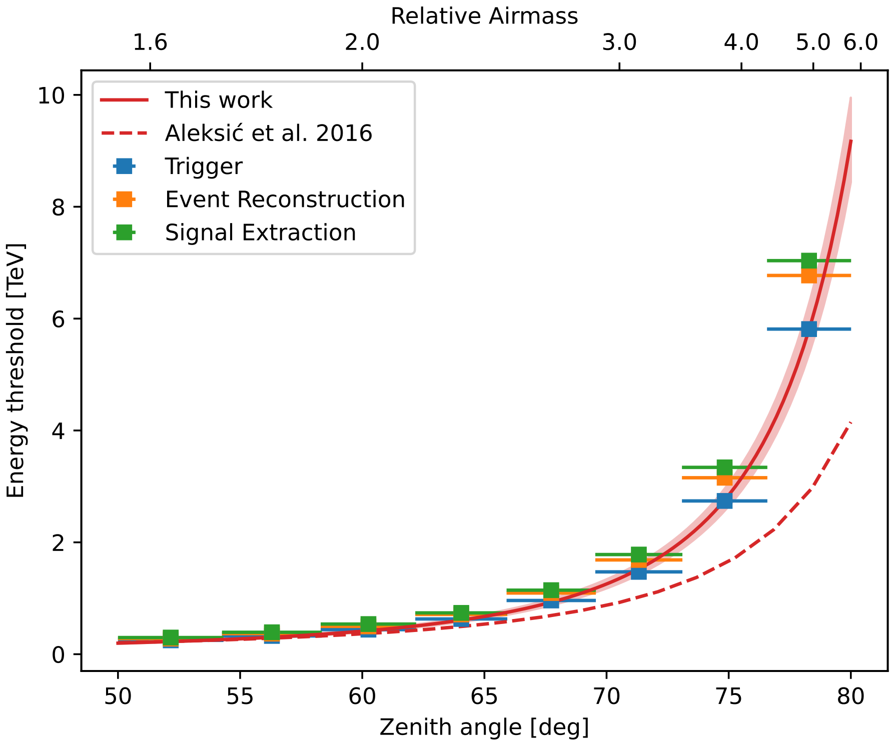

Figure 5.18: The energy threshold as a function of zenith angle above $50°$ (bottom axis) and relative airmass (according to Equation 3.33, top axis). The thresholds are shown for the three different stages of data analysis as described in Section 5.1.1. The dashed red line indicates the empirical function found in [28], and the solid red line is the updated fit to the data given in Equation 5.7.

rate distribution becomes broad and extends to lower energies than the threshold (see Figure 5.17). It is, therefore, possible to achieve meaningful results also for energies below the threshold.

For each additional stage in the analysis, the energy threshold increases slightly. The increase between the *Trigger* and the *Signal Extraction* level is around 20% of the value at the *Trigger* stage. In Figure 5.18 error bars on the values of the energy thresholds were omitted for better visibility. I have quantified the error on the energy threshold value determined from the Landau fit to the histograms in two ways. First, by taking the scale parameter σ of the fitted Landau function, which gives a measure of the width of the distribution, as symmetric errors around the fitted energy threshold. Second, by estimating asymmetric errors calculating the containment of 34% of the events below and above the energy threshold. In the first case, the size of the error is around 35% of the threshold value; in the second case, it is $\sim 70\%$ for the lower bound and even around 100% for the upper bound. These values do not change between analysis stages. Therefore, compared to the spread of the energies of surviving simulated events around the determined threshold value, the slight shift at each analysis stage is negligible, and the threshold can be assumed to be constant throughout the entire data analysis pipeline.

Furthermore, within the described uncertainties, I found no considerable difference between the evolution of the energy threshold for *standard azimuth splitting* and the *baseline azimuth splitting*.

5.2.2.3 Effective collection area

I evaluated the effective collection area according to Equation 4.4. The results are shown in Figure 5.19. As for the lower zenith angles shown in Figure 5.3, the effective area steeply increases close to the respective energy thresholds and starts to saturate towards the highest reachable energies. With larger zenith angles, the increase moves to higher energies due to the higher energy threshold but overtakes, the lower zenith angles at a few TeV, reaching maximum values of more than $2\,\mathrm{km}^2$ or even more than $4\,\mathrm{km}^2$ in the case of the largest zenith angle bin. The same signal extraction cuts as for the energy threshold have been applied here (see Section 5.1.1). I have compared the results for the effective area for both the standard azimuth splitting and the baseline azimuth splitting, as well as the Rise and Set sample, without finding substantial differences.

5.2.2.4 Energy resolution and bias

According to the method described in Section 5.1.5, I evaluated the energy resolution and bias for observations above 50°.

The resulting values are shown in Figure 5.20 for the [50°, 70°] range and the standard azimuth splitting sample at above 70°. As for lower zenith angles, the strong bias towards the edges of the observed energy range can be seen, while it stays close to zero for energies between $\sim 2\,\mathrm{TeV}$ and few tens of TeV for below 70°, and between 10 and 100 TeV above 70°. In the same energy ranges, the resolution is always around or below 20% and even reaches $\sim 10\%$ around 20 TeV for the zenith bin [62°,70°]. A comparison of the energy resolution and bias above 70° between the *standard azimuth splitting* and the *baseline azimuth splitting* is shown in Figure 5.21. The energy resolution is around 10% worse for the *baseline azimuth splitting* compared to the *standard azimuth splitting*. The bias shows a similar behavior in both cases. For the *baseline azimuth splitting*, a pronounced difference is visible between the Rise and Set samples in the largest zenith bin [75°, 80°]. The Rise sample is showing a $\sim$ 5–10% better resolution and bias below $\sim 100\,\mathrm{TeV}$.

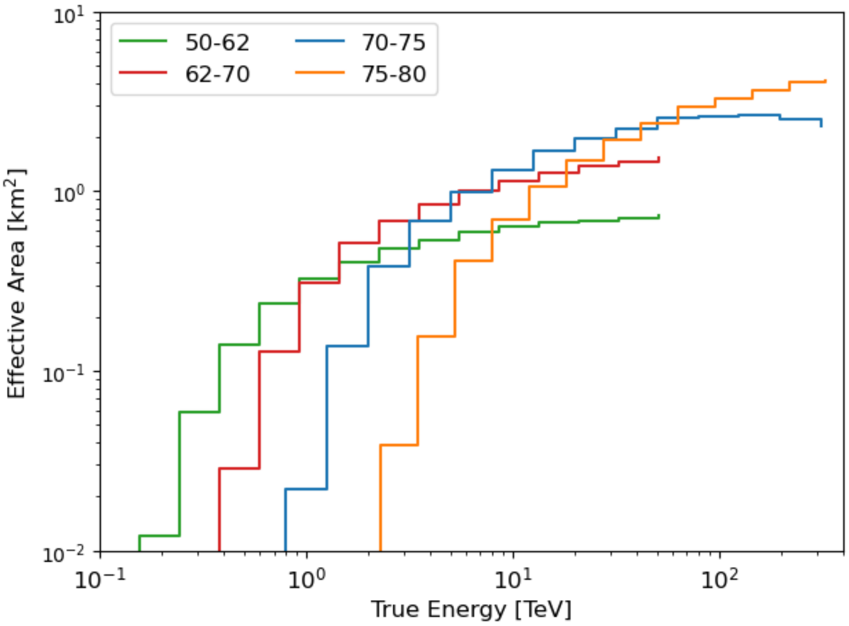

Figure 5.19: The effective collection area for the four zenith bins above 50°. For $[50^{\circ}$,$62^{\circ}]$ the maximum effective area of$\sim 0.7\,\mathrm{km}^2$ and for $[62^{\circ}$,$70^{\circ}] \sim 1.5\,\mathrm{km}^2$ is reached at several tens of TeV. At these energies the effective area of observations above 70° overtake the data below 70° and reach maximum values of $\sim 2.3\,\mathrm{km}^2$ ($[70^{\circ}$,$75^{\circ}]$) and even $\sim 4\,\mathrm{km}^2$ ($[75^{\circ}$,$80^{\circ}]$).

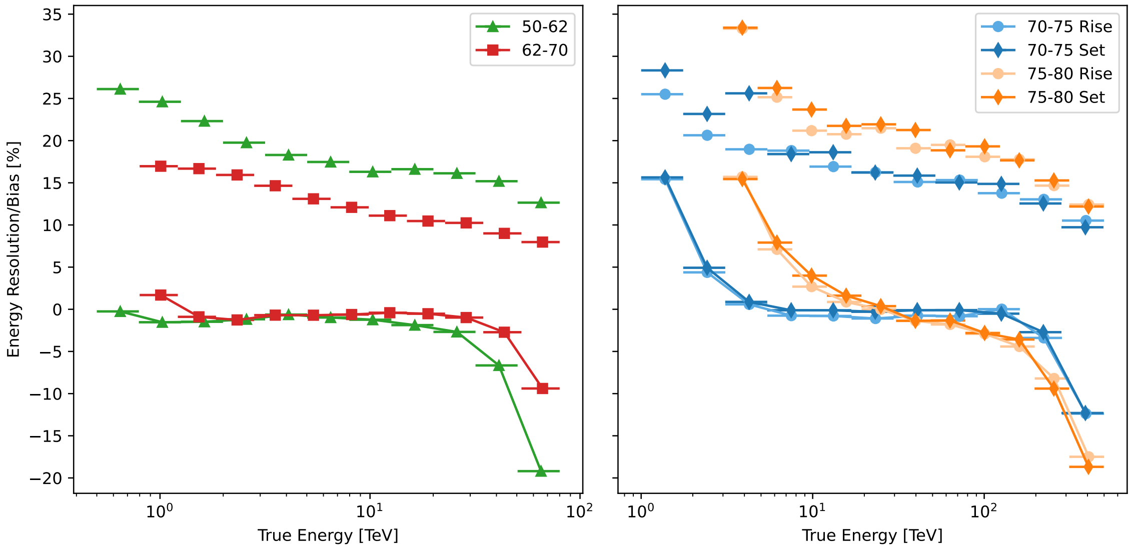

Figure 5.20: The energy resolution (separate data points) and energy bias (data points connected with a line) for the four zenith bins above 50°. The right panel shows the results for the standard azimuth splitting. The bias shows the expected behavior towards the edges of the simulated energy range and varies around zero in the center. The resolution is around or below 20% in the central energy range.

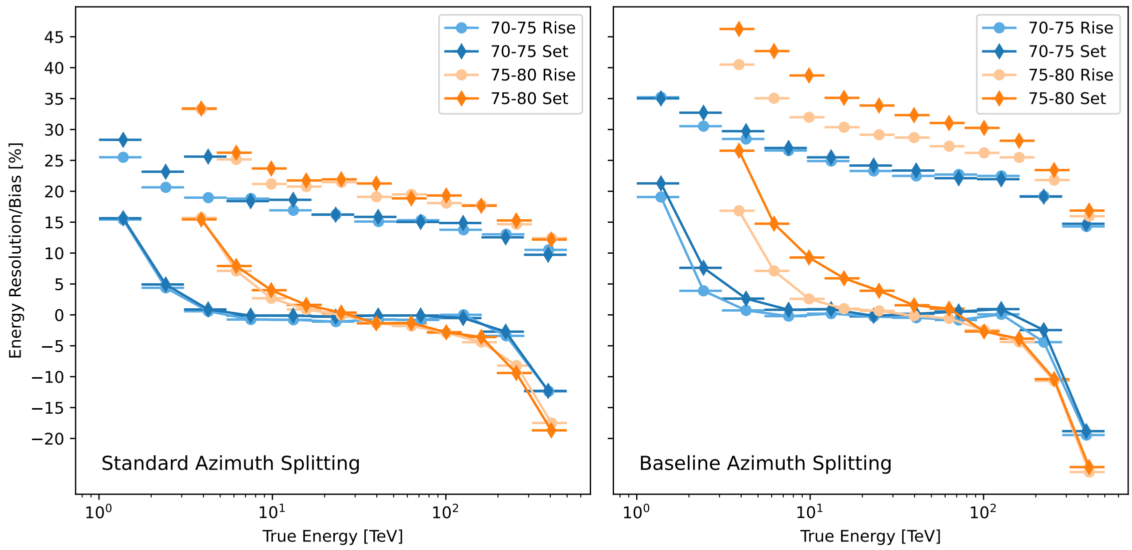

Figure 5.21: The energy resolution (separate data points) and energy bias (data points connected with a line) for standard azimuth splitting (left) and baseline azimuth splitting (right). The *baseline azimuth splitting* shows around 10% worse energy resolution compared to the *standard azimuth splitting*.

5.2.2.5 Angular resolution

I have evaluated the angular resolution at zenith angles between 50° and 70° in the same way as described in Section 5.1.4 by both fitting an exponential function to the θ^2-distributions of reconstructed events as well as by calculating the 68% containment radius of the reconstructed events. I evaluated the angular resolution in all four zenith bins described in Section 5.2.1. The exponential fits to the θ^2-distribution in each energy bin for each zenith bin are shown in Section A.2.

The resulting values of the angular resolution above 50° are shown in Figure 5.22 for both the *standard azimuth splitting* and *baseline azimuth splitting*. A similar behavior to Figure 5.4 can be seen. The angular resolution improves with increasing energy for all zenith bins. As expected, the values for Θ_{Gauss} are lower than for Θ_{68}. The best resolution of less than 0.06° at several tens of TeV is achieved in the [62°, 70°] zenith bin. Above 70° a clear difference is visible between the two zenith angle bins, with the [70°, 75°] outperforming the [75°, 80°] by $\sim 25\%$. The *baseline azimuth splitting* shows a worse angular resolution by around 0.02°. By comparison of the θ^2-histograms that are shown in Section A.2 for each energy bin for each data subsample, it becomes clear that the *baseline azimuth splitting* shows a much more accurate fit of the 2D-Gaussian to the histogram, while the *standard azimuth splitting* exhibits large tales in the upper half of the range in which the histogram is fitted. The values shown in Figure 5.22 for the *standard azimuth splitting* might, therefore, be underestimating the actual angular resolution, while the values shown for the *baseline azimuth splitting* are an accurate representation of the data.

The Rise samples consistently show a slightly better angular resolution than the Set samples above 70°. While this difference is within the systematic uncertainties (see Section 5.2.4), it is worth discussing since one would expect the opposite behavior. For the Rise sample, the effective baseline between the telescopes is lower than for the Set sample, which decreases the stereo effect of the observation. The direction reconstruction profits from the two telescopes observing an air shower from different directions and overlaying their respective camera images. The more aligned the telescopes are, the more aligned the recorded images and the stereo reconstruction is expected to deteriorate. A possible explanation for the here observed opposite behavior is that at VLZA, the geometrical parameters of the showers play a minor role in the reconstruction since the shower images become much smaller (see Section 5.2.3). In fact, the most important parameter in the training of the Disp RF (Section 4.2.4.2) is the Time Gradient. Possibly, this parameter is determined with less precision or conflicting values between the two telescopes for the Set direction, while it performs well in the Rise direction.

5.2.2.6 Flux sensitivity

I calculated the differential flux sensitivity as described in Section 5.1.6. In order to compute the sensitivity, I used observation data taken on the Crab Nebula. A summary of this data set can be found in Table 5.2. For the sensitivity in the zenith angle range between 50° and 70°, I used Crab Nebula data taken between November 2014 and April 2018. To determine the sensitivity above 70° up to 80°, I used the complete available data set taken in this zenith angle range between December 2014 and March 2020. Consequently, I used all the MCs corresponding to the hardware-stable periods of the data sets to determine the *Hadronness* and θ^2 efficiency cuts. The resulting differential sensitivity curves are shown in Figure 5.23, the precise values are listed in Section A.5.

The maximum energy of each sensitivity curve shown is defined by the maximum energy at which a positive rate of gamma-ray events is found in the respective data sets. It should be kept in mind that these sensitivities are calculated as a function of estimated energy. With a proper unfolding (see Section 4.2.5.3) of the data accounting for the energy dispersion the detectable energy range might increase to higher energies. As would be expected, at the lowest energies, observations at lower zenith angles outperform VLZA observations reaching less than 10% and even less than 5% of the Crab Nebula flux for the range [50°, 62°]. The sensitivity this data set starts to increase above 10% C.U. at a few TeV where the [62°, 70°] set quickly approaches the values of the [70°, 75°] sensitivity. The fluctuations above 10 TeV are due to a lack of statistics in the data sets at those energies. Up to its maximum energy around 40 TeV the [50°, 62°] observations perform slightly better than the [62°, 70°] and [70°, 75°] data sets. At energies beyond ~ 50 TeV observations in the zenith range [70°, 75°] provide a sensitivity of slightly more than 100% of the Crab Nebula flux. The zenith bin [75°, 80°] shows a much worse sensitivity compared to all other evaluated zenith ranges, resulting from the overall worse performance shown consistently in the previous sections. I have evaluated the sensitivity also separately for the *Rise* and *Set* samples. The calculations suffer from the loss of statistics due to the splitting of the data set and show no difference within the uncertainties. The sensitivities evaluated for the *standard azimuth splitting* and *baseline azimuth splitting* also match within uncertainties.

5.2.2.7 Spectral energy distribution

I have studied the spectral energy distribution obtained from the data summarized in Table 5.2. For each period, zenith, and azimuth subset, the differential flux was estimated with `flute` and then combined with `foam` (see Section 4.2.5.2). A minimum *Size*-cut of 50 was applied. Following [28] energy-dependent *hadronness* and θ^2-cuts were applied with high gamma-ray efficiency of 90% and 75% respectively to minimize systematic uncertainties. As a first sanity check of the analysis, I compared the measured number of excess events obtained from `foam` with the expectation. Assuming the best-fit Crab Nebula SED from [28] and multiplying it with the effective area and observation time of the dataset gives the expected number of excess counts in estimated energy. Multiplying these predictions with the energy migration matrix provides the expected counts in terms of true energy. The result is shown in Figure 5.24 for each zenith angle bin. The measured excess matches well with the prediction up to the energy bin at 100 TeV. Here, the expected number of counts

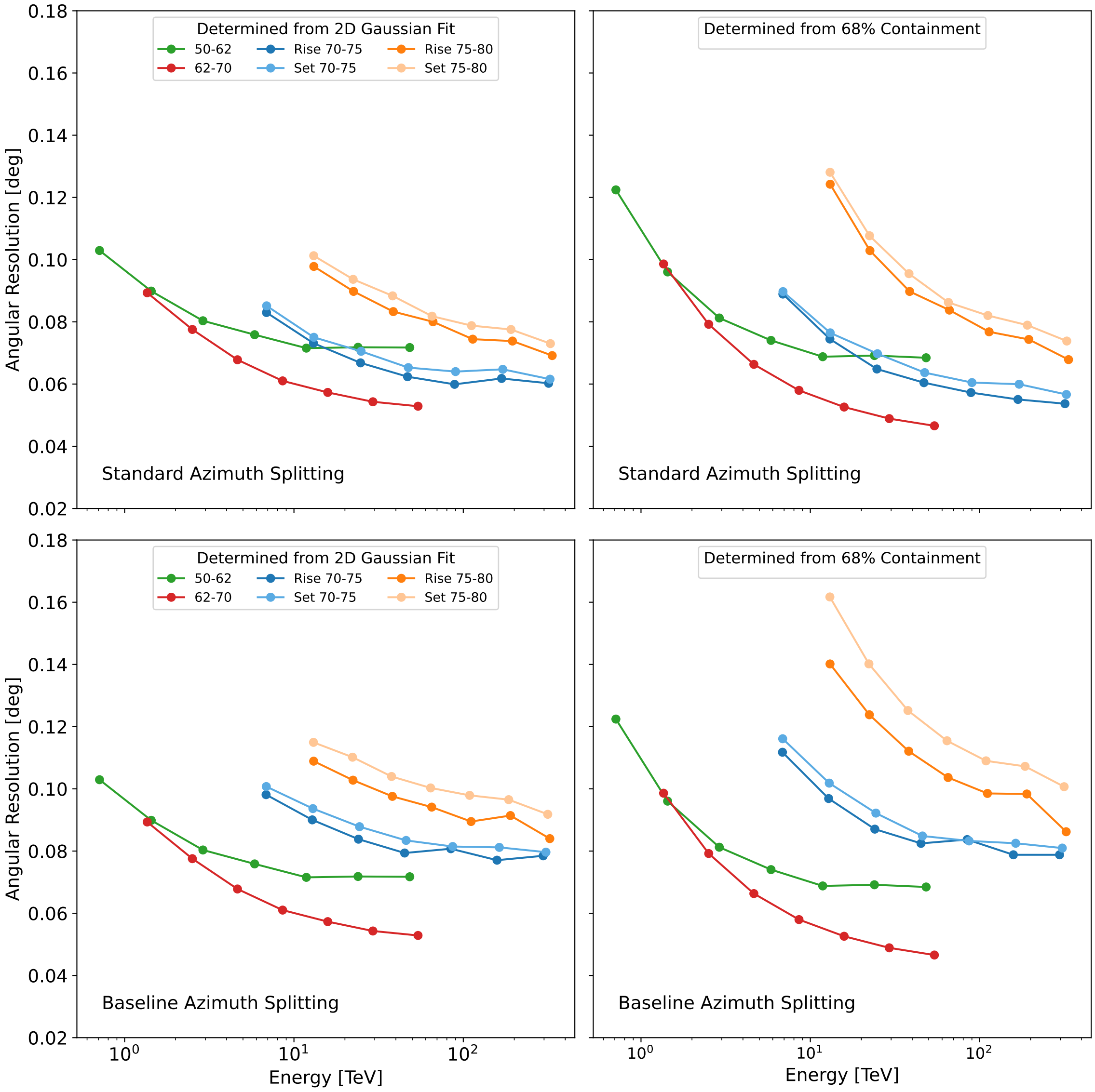

Figure 5.22: The angular resolution for zenith angles above 50°. Left: Values obtained from the standard deviation of a 2D-Gaussian fitted to the distribution of reconstructed source directions. Right: Values obtained by determining the radius containing 68% of the reconstructed events. Per definition the values in the left plot are expected to be smaller than in the right plot (see Section 5.1.4).

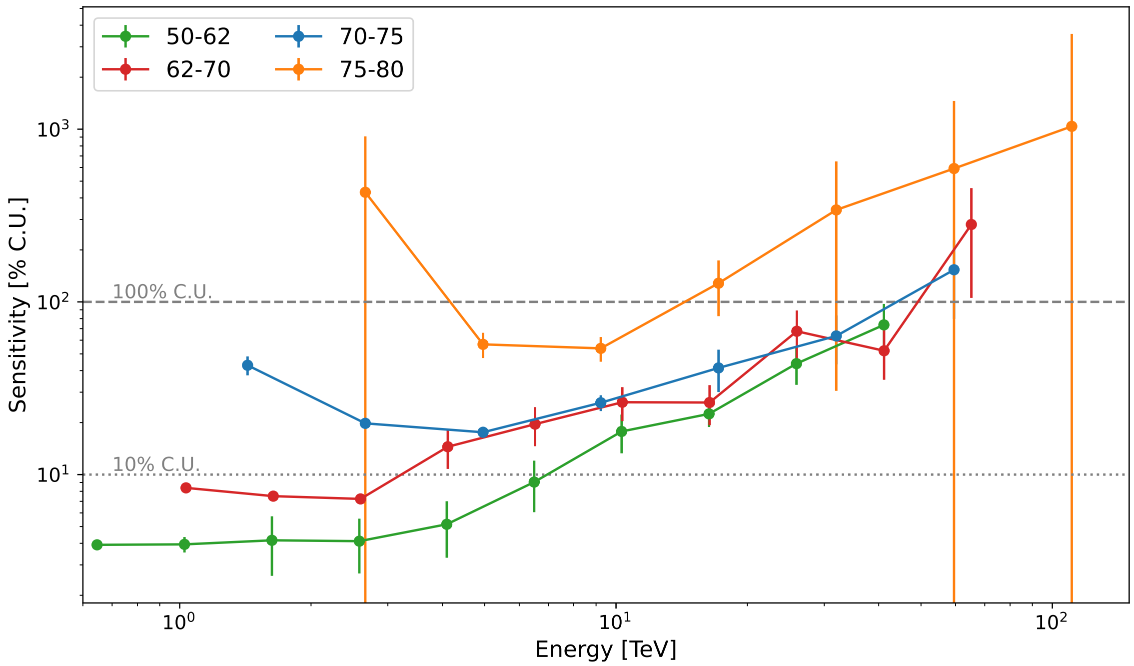

Figure 5.23: The 50 h differential flux sensitivity of MAGIC in terms of estimated energy for observations at zenith angles larger than 50° in percent of the Crab Nebula flux. For a detailed discussion, refer to the text.

is below 10, and even small statistical fluctuations can lead to no measured excess at these energies and beyond.

Comparisons between the SEDs (before unfolding) of different zenith angles, as well as the Rise and Set sample of the data above 70° are shown in Figure 5.25 and Figure 5.26. The flux estimation is consistent between these data samples within statistical uncertainties, showing the stability of the performance across the wide zenith range presented here. In these plots, it again becomes clear that the data taken at the highest zenith angles in the range [75°,80°] does not contribute positively to the flux estimation at the highest energies. It is less sensitive compared to the [70°,75°] while adding more noise and stronger fluctuations at lower energies. For this reason, I have discarded this zenith bin in the last step to produce the final unfolded SED. Figure 5.27 shows the unfolded spectrum obtained with data taken in the zenith angle range [50°,75°], the data points are listed in Table 5.3. Based on previous measurements, the fitted spectral energy estimation was assumed to have the log-parabola shape

$$\mathrm{d}N/\mathrm{d}E = f_0 \cdot \left(\frac{E}{10\,\mathrm{TeV}}\right)^{-\alpha-\beta\log_{10}(E/10\,\mathrm{TeV})} \mathrm{cm}^{-2}\,\mathrm{s}^{-1}\,\mathrm{TeV}^{-1} \tag{5.8}$$

The shaded region represents the SED with statistical uncertainties obtained from the forward folding procedure. Flux points were obtained by the Tikhonov and Schmelling unfolding methods (see Section 4.2.5.3). For comparison, best-fit SEDs from previous MAGIC publications are shown. Considering the statistical and systematic uncertainties (Section 5.2.4), the spectrum I have obtained in this analysis is in good agreement with previous measurements. Its best-fit spectral parameters are $f_0 = 4.91 \pm 0.18 \cdot 10^{-14}$, $\alpha = -2.92 \pm 0.04$, $\beta = -0.13 \pm 0.10$, with $\chi^2/Ndf = 1/4$.

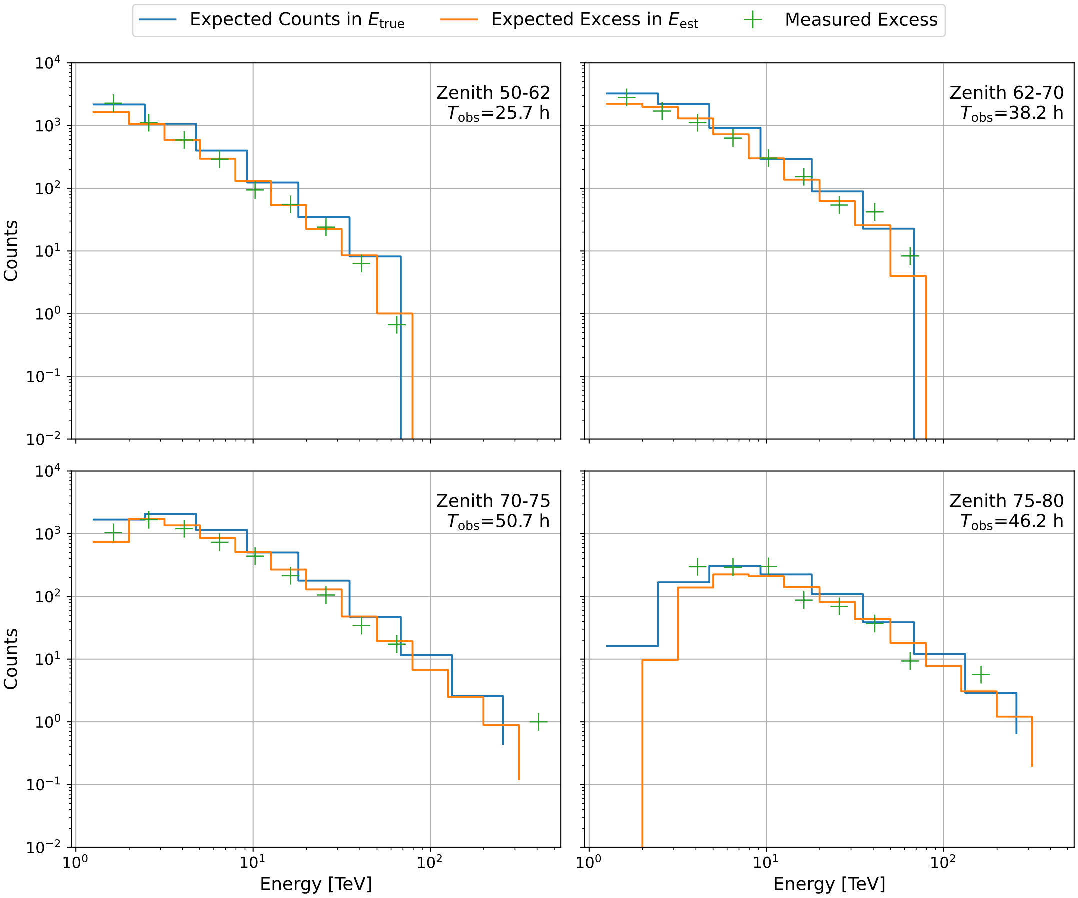

Figure 5.24: The measured number of excess events in each zenith angle bin of the Crab Nebula data set compared with the expected number of counts. The best-fit SED from [28] has been assumed. Observation times are the total effective times in the respective subsample, and the effective area has been calculated with `flute`. The measured number of excess events is given without error bars because the program `foam` does not provide them.

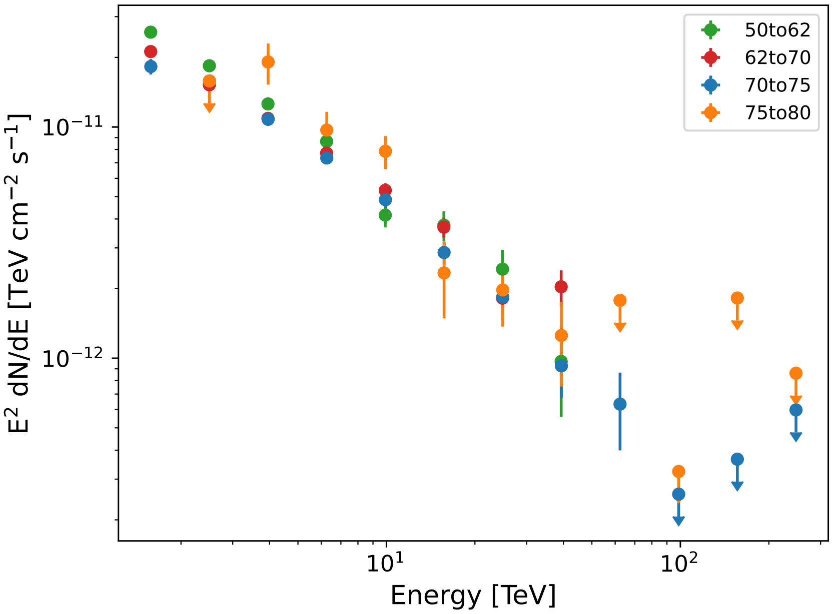

Figure 5.25: Comparison of SEDs before the unfolding of different zenith angles. Upper limits are drawn whenever the significance of a data point is below 2σ.

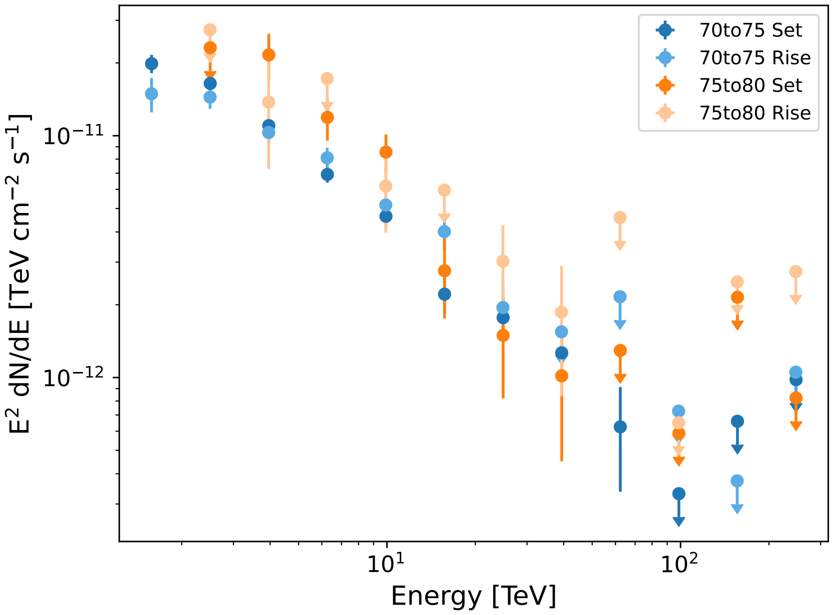

Figure 5.26: Comparison of SEDs before the unfolding of the Rise and Set samples. Upper limits are drawn whenever the significance of a data point is below 2σ.

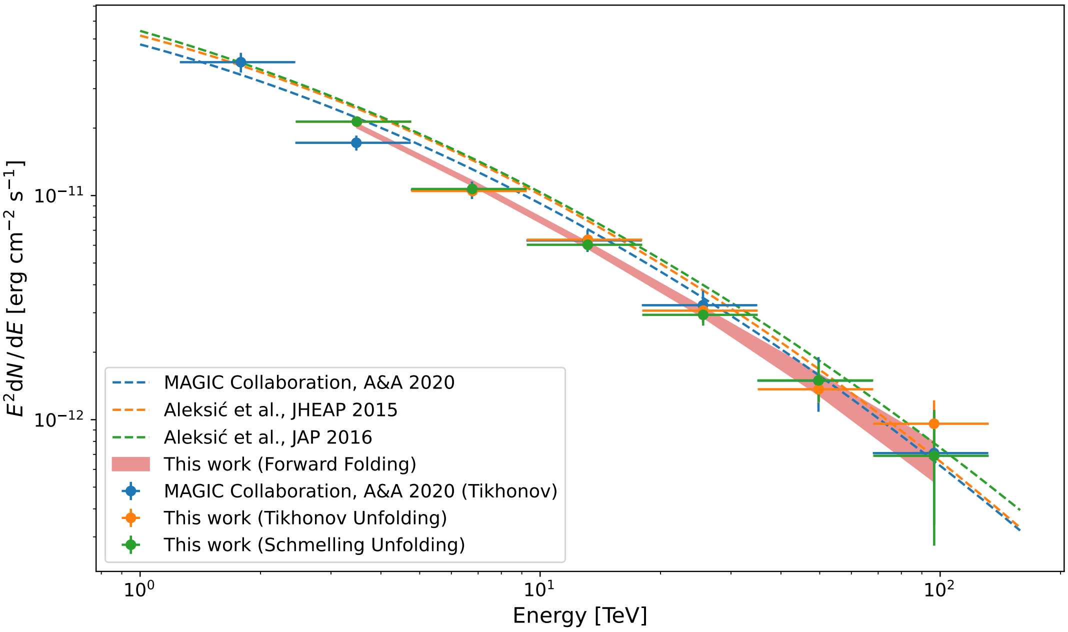

Figure 5.27: Unfolded SED of the analyzed data set between $50°$ and $75°$ Zd. Orange and green data points show the flux points obtained with the Tikhonov and Schmelling Unfolding algorithms, respectively. The red band shows the best-fit spectrum with statistical uncertainties from the Forward Folding procedure. Dashed lines show best-fit spectra from previous MAGIC publications, and blue data points show the flux point from the first publication by MAGIC using VLZA data only. Within statistical uncertainties, all spectra and flux points are consistent.

Table 5.3: The values of the unfolded Crab Nebula SED obtained from data analyzed in the zenith angle range [50°, 75°]. The column "Energy Range" gives the width of the energy bin, and the second column gives the value of the data point. The Flux values are given together with their uncertainties in the last column.

Bin	Energy Range [TeV]	Energy [TeV]	$E^2\,\mathrm{d}N/\mathrm{d}E$ $[\mathrm{erg\,cm^{-2}\,s^{-1}}]$
1	2.45 - 4.76	3.48	$(2.14 \pm 0.05) \times 10^{-11}$
2	4.76 - 9.26	6.77	$(1.07 \pm 0.04) \times 10^{-11}$
3	9.26 - 18.00	13.16	$(6.03 \pm 0.34) \times 10^{-12}$
4	18.00 - 35.00	25.56	$(2.94 \pm 0.31) \times 10^{-12}$
5	35.00 - 68.04	49.70	$(1.50 \pm 0.30) \times 10^{-12}$
6	68.04 -132.28	96.63	$(0.69 \pm 0.42) \times 10^{-12}$

5.2.3 Specific aspects of very large zenith angle observations

5.2.3.1 Distance between Air shower and telescopes

As mentioned before, the increase in path length through the atmosphere along the line of sight with increasing zenith angle causes air showers to develop at larger distances from the telescopes. This behavior is shown in Figure 5.28 for MC events. The altitude above ground of the shower maximum is determined as described in Section 3.3.5.1. The distribution of the shower maximum height for different energies and zenith angles are shown in Figure A.11. The height is converted into the distance from the telescope and into the relative airmass via Equations 3.34 and 3.35. Below 62°, the distance of the shower maximum is below $\sim 30\,\mathrm{km}$ for most events, while at the largest zenith angles, showers develop up to 90 km away from the telescopes corresponding to a relative airmass of more than 5.

5.2.3.2 Geometrical sizes of shower images

At low zenith angles, the main factor that determines the geometrical size of a shower image in the MAGIC camera is the energy of the event. The larger the primary energy, the more particles are produced in the airshower, resulting in a longer and wider shape of the shower. This is shown in Figures 5.29 and 5.30, where the distribution of the *Length* and *Width* Hillas parameters are shown in selected energy ranges for different zenith angles. Within one zenith angle bin the images become longer and wider with increasing energy which translates to a larger number of pixels being illuminated in the camera. The same behavior is also valid at large zenith angles; however, a simple relation of "the higher the energy, the larger the image" is not applicable due to an interplay of dependencies of the trigger efficiency between zenith angle, impact parameter, and energy. These dependencies are shown in Figure 5.31. Each row represents one zenith angle bin, given in the top right of each panel, increasing in value from top to bottom. Each column shows a range of impact parameters, increasing to the right. Each individual panel shows distributions of the number of pixels per event. Differently colored histograms refer to different energy ranges, the values of which are given in the color bars. Each histogram has been normalized to the total number of events in the respective zenith angle and impact parameter bin. Within the same impact parameter range, the average number of pixels for events of the same energies decreases with the zenith angle. This is due to the fact that at large zenith angles, showers develop at greater distances from the telescopes due to the increased airmass and, therefore, appear smaller. For the same reason, image sizes also decrease with increasing impact parameters corresponding to larger distances of the shower from the telescopes. Noteworthy is the change in energy composition of the events dependent on the impact parameter. At low impacts, low energy events make up the majority of triggered events, they are not bright enough to be detected at the large

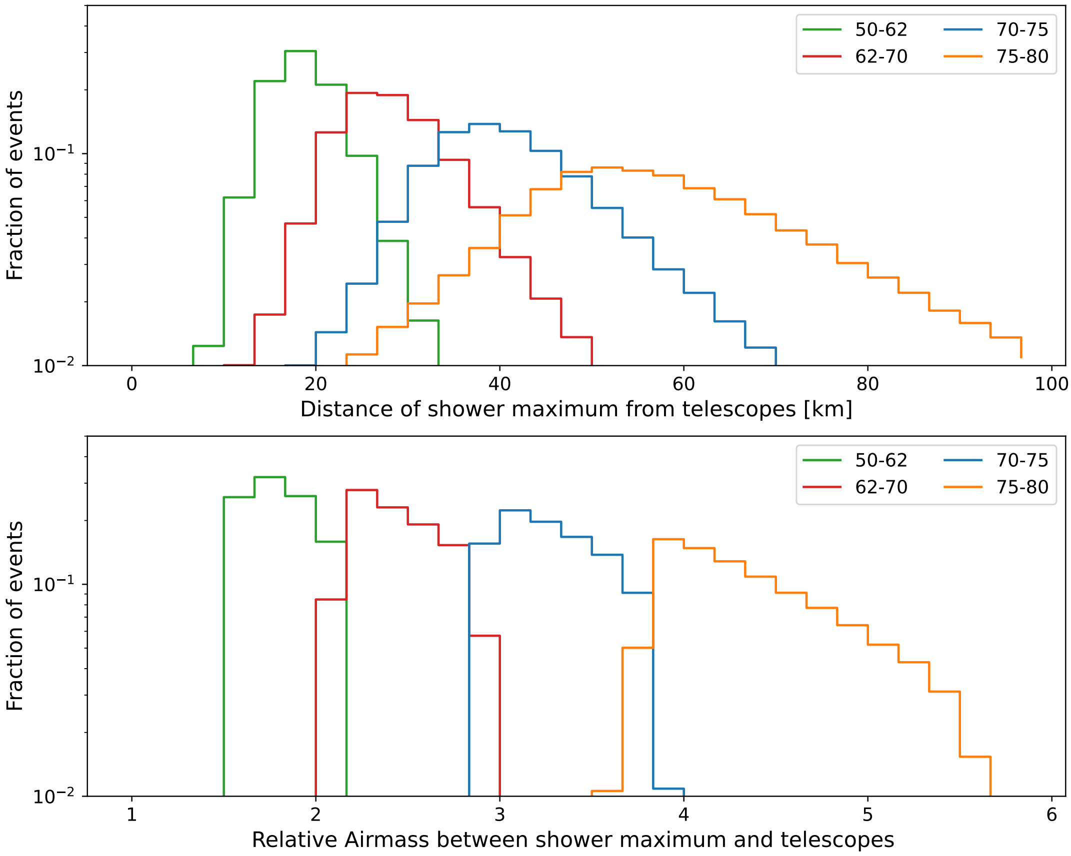

Figure 5.28: The event distributions in terms of distance (top panel) and airmass (bottom panel) between the shower maximum and the telescopes for the four analyzed zenith angle bins.

distance corresponding to large impact parameters. At the largest impact distances, the most energetic events dominate the population. Events with energies beyond tens of TeV are primarily detected at at zenith angles above 70° and impact distances larger than 1 km. Their shower images, however, become increasingly smaller, with a majority of the events containing only around 10 or fewer pixels. This poses a challenge for the reconstruction of the image parameters described in Section 3.3.5.1. This can cause a strong decrease in the capacity of correctly identifying gamma-like and hadron-like events at large energies for VLZA as shown in Figure 5.16.

5.2.3.3 Background Asymmetry

Above 70°, the airmass changes considerably within a zenith angle range of a few degrees (see Figure 3.4), which also translates to a larger noise from the LoNS. Since the MAGIC camera has a diameter of 3.5° this can lead to a considerable difference in the trigger efficiency between the top and the bottom of the camera at large zenith angles. Due to the increased noise levels at larger zenith angles, fewer events will pass the trigger criteria and image cleaning, leading to a lower event rate in the top half of the camera. I have estimated this effect by comparing the event counts in these two regions using Off data, for which a homogenous event count rate would be expected if a constant airmass is assumed across the entire FOV. Figure 5.32 shows the normalized event counts for the top and bottom half of the MAGIC-I camera as a function of the reconstructed y-position of the events in camera coordinates. As expected the event counts for the top half of the camera are systematically lower than in the bottom half of the camera. The bottom panel of Figure 5.32 shows the

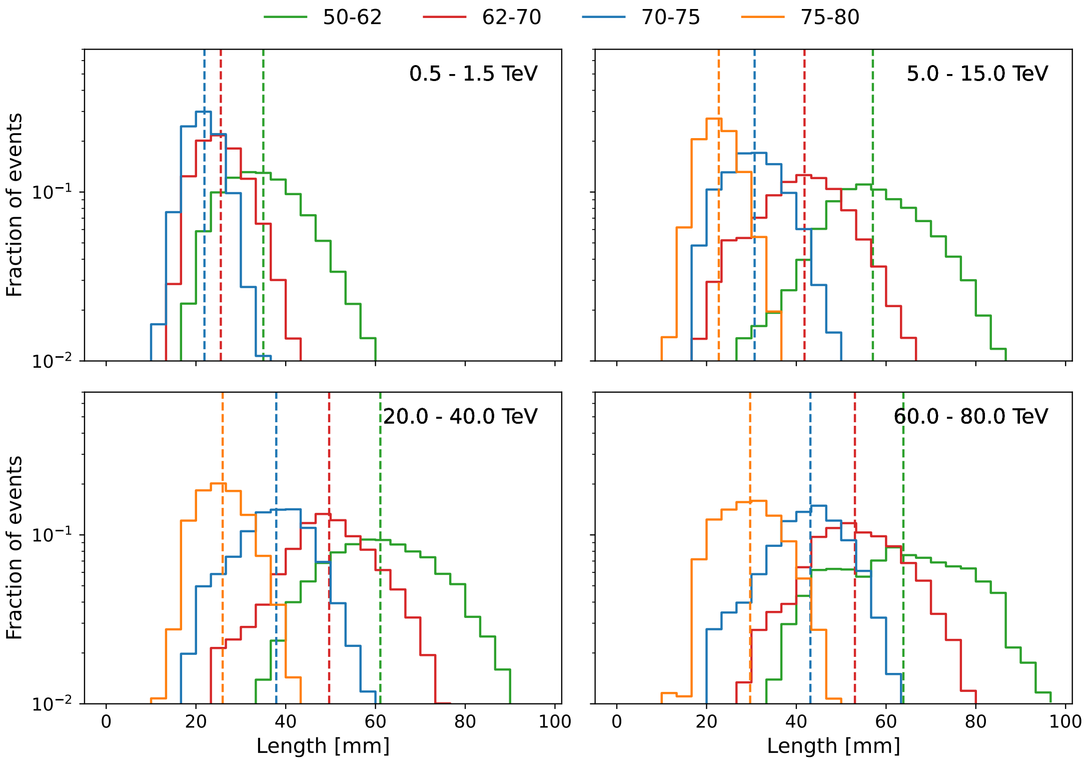

Figure 5.29: The size of the *Length* parameter in the camera plane in units of mm ($30\,\mathrm{mm} \approx 0.1°$) in selected energy bins for different zenith angles. By comparing the distributions within one zenith angle bin, the figure shows that with increasing energy, shower images become longer. The dashed vertical lines show the medians of the respective distributions to help guide the eye. Comparing showers of the same energy between zenith angles shows clearly that images at larger zenith angles are shorter compared to lower zenith angles, as the showers at large zenith angles develop at greater distances.

relative difference. It is more pronounced for the largest zenith angle bin [75°, 80°] and increases with the distance from the camera center. At the standard wobble distance of 0.4° it is still below 5% for both zenith bins, however for large wobble offsets, which are commonly used in the study of extended gamma-ray sources, the difference becomes more substantial and already reaches 10% at an offset of 0.6° for the [75°, 80°] range. Similar data for the zenith range below 70° have been omitted here for better visibility. The background asymmetry at these zenith angles is below 1%.

5.2.3.4 Effects of atmospheric refraction

The effect of light refraction in the atmosphere starts to become noticeable above zenith angles of $\sim 60°$. Figure 5.33 shows the coordinates in the MAGIC camera of true simulated MC events and the reconstructed position. MCs used for point-source analysis are simulated in a ring with the standard wobble offset of 0.4°, which is shown in orange in the figure. Each blue dot represents the reconstructed position of an event. The simulated rings are reconstructed nicely with a certain spread around the original position. However, especially above 70°, it becomes evident that the events in the top half of the camera are systematically reconstructed to lower Y-coordinates, producing a reconstructed ring that is slightly squished with respect to the original one. Figure 5.34 shows this effect in polar camera coordinates. The rotational angle ϕ represents the angular position of the reconstructed coordinates along the ring, 0° being the positive X-axis. I calculated the mean reconstructed angular distance from the camera center $R_{\text{reco,mean}}$ in bins of ϕ for several small bins in $\cos(Zd)$. Figure 5.34

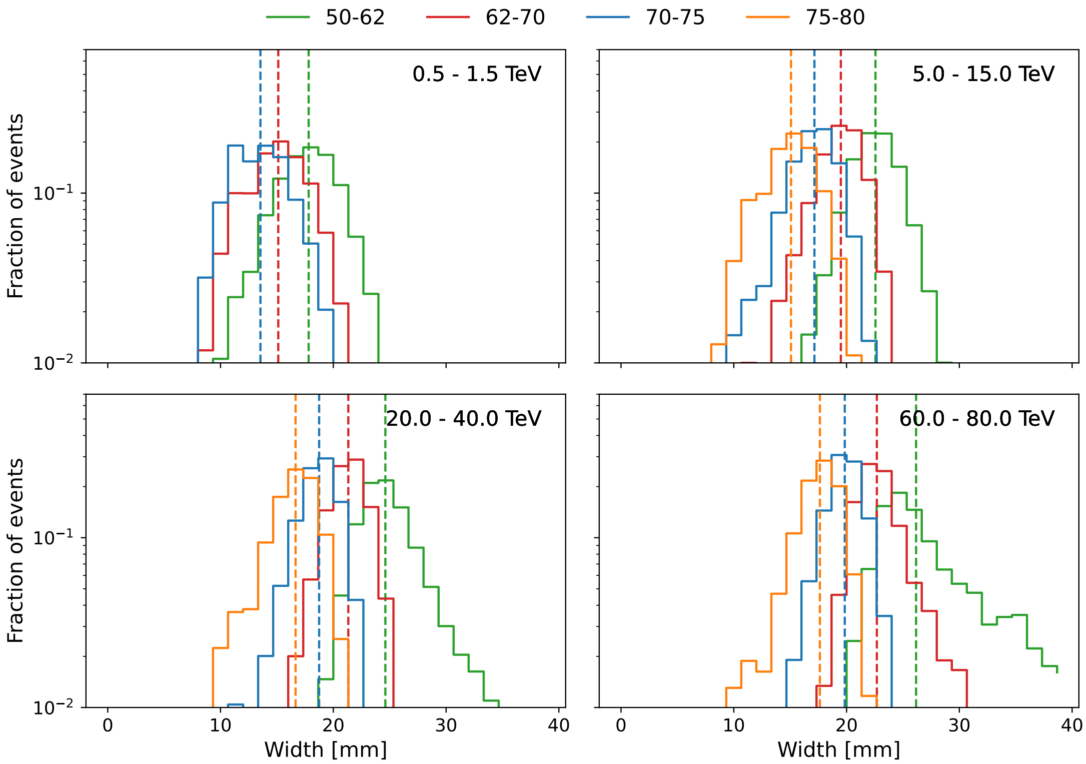

Figure 5.30: The size of the *Width* parameter in the camera plane in units of mm ($30\,\mathrm{mm} \approx 0.1^\circ$) in selected energy bins for different zenith angles. By comparing the distributions within one zenith angle bin, the figure shows that with increasing energy, shower images become wider. The dashed vertical lines show the medians of the respective distributions to help guide the eye. Comparing showers of the same energy between zenith angles shows clearly that images at larger zenith angles are narrower compared to lower zenith angles, as the showers at large zenith angles develop at greater distances.

shows the deviation of $R_{\mathrm{reco,mean}}$ from the true simulated value of 0.4°. The plot clearly shows the growing deviations from the nominal value with increasing zenith angle for the top half of the camera ($\phi \in [0^\circ, 180^\circ]$). Already at zenith angles $\sim 60^\circ$, the deviations become noticeably larger than the fluctuations around 0 for smaller zenith angles.
This effect is due to the stronger atmospheric refraction with larger zenith angles. Since the camera image is flipped with respect to reality, events in the top half originate from larger zenith angles than in the bottom half. Due to refraction, the light path emitted by the corresponding air showers is bent and seems to arrive from slightly lower zenith angles resulting in a lower reconstructed Y-coordinate in the camera. Figure 5.35 shows the refraction effect as function of airmass (see Section 3.3.3). In a small slice around X=0, I evaluated the deviation of $R_{\mathrm{reco,mean}}$ from the true value for the top half and the bottom half of the camera separately. While the bottom half, corresponding to lower zenith angles, stays roughly constant, the top half shows a clear dependence on the airmass. This roughly linear dependence corresponds with the expectation of the effect being due to atmospheric refraction.
This effect causes an additional systematic uncertainty on the angular resolution which is discussed in Section 5.2.4

5.2.4 Systematic uncertainties

A detailed study of the systematic uncertainties on the energy scale and the collection efficiency (i.e., the flux normalization) has been performed in [25, 28]. Many of the there

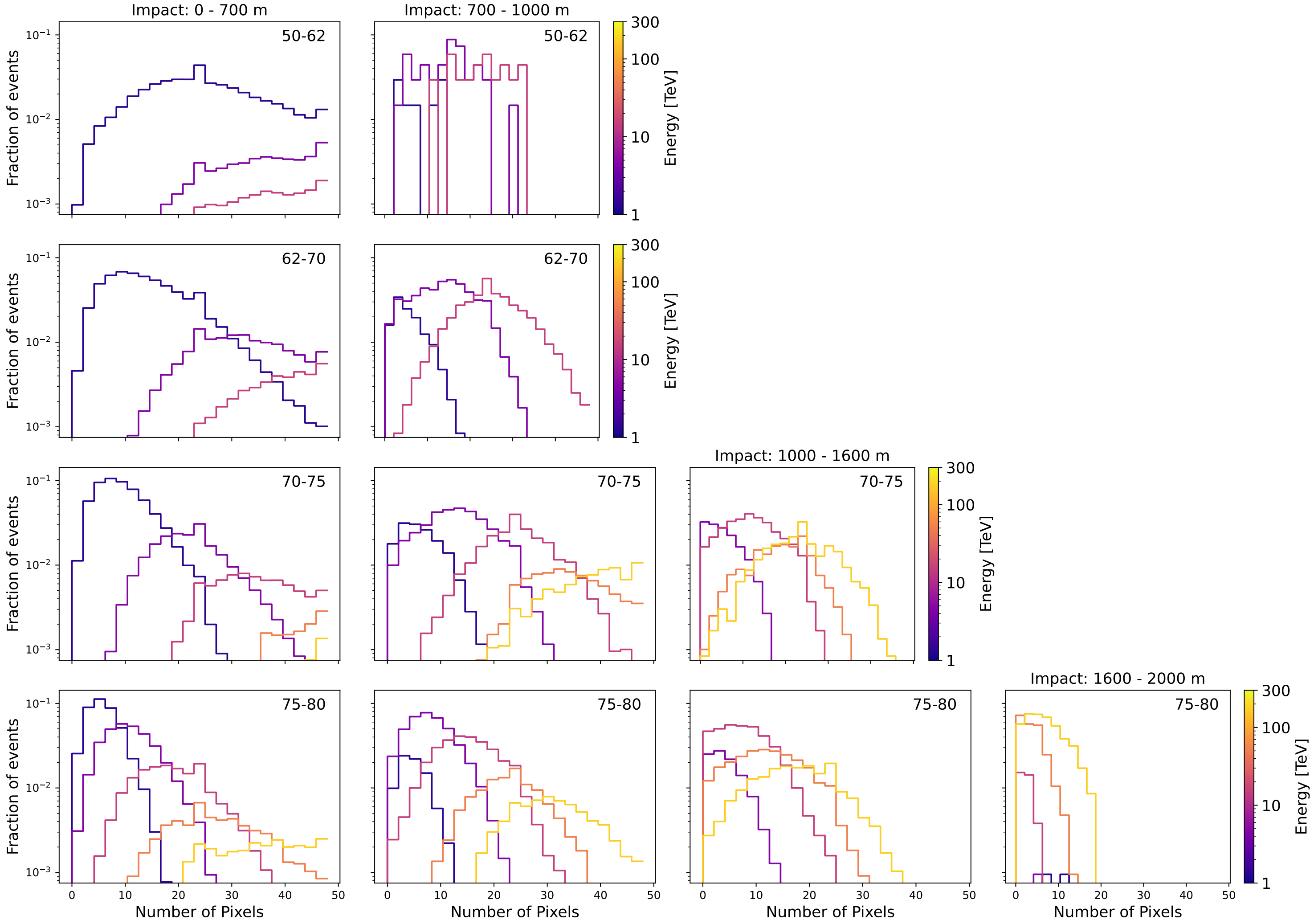

Figure 5.31: Evolution of shower image sizes in terms of zenith angle, impact parameter, and energy. Each plot shows a histogram of the number of pixels of individual shower images for various energies in the range 1-300 TeV. Each row represents one zenith bin, noted in the top right corner of each plot. Each column represents a range of Impact parameters given above the topmost plot. The histograms are normalized to the total number of events in that respective zenith and impact bin. Image sizes increase with energy but decrease with larger zenith angles and larger impact parameters.

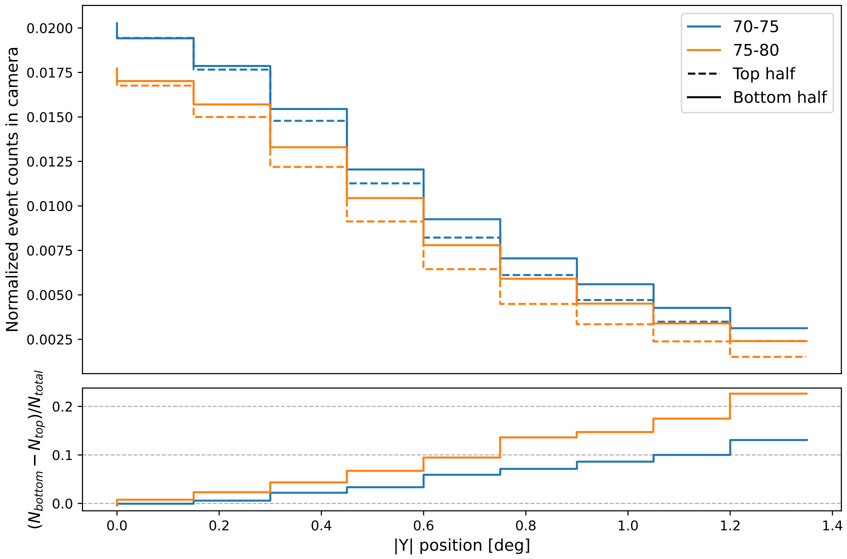

Figure 5.32: The differences in event counts between the top and bottom half of the camera obtained from Off data. The top panel shows the event counts for the two camera halves, respectively, as a function of vertical distance from the camera center for the two zenith bins above 70°. The relative difference between the two camera halves is shown in the bottom panel. The difference becomes more pronounced for higher zenith angles and larger distances from the camera center. Up to the standard wobble distance of 0.4° it stays below 5%.

described quantities do not depend on the zenith angle of the observation and can be applied unchanged to the observations at LZA and VLZA. I will here only give an overview of the factors that differ from the cited values at large zenith angles. Most of these specific factors have been estimated already in [140]. I will summarize these findings and extend them by estimating the effects of the background asymmetry and atmospheric refraction described in the previous section.

5.2.4.1 Atmospheric transmission

The atmosphere has to be considered part of the detector for the estimation of systematic uncertainties of IACTs. Limited knowledge of atmospheric transmission has a direct consequence on the energy and effective area estimation, most dramatically at low energies [28]. An overestimation of the transmission leads to the assumption that more light is to be expected from an air shower of a given energy than is actually arriving at the telescopes. At the lowest energies, this means that showers that are assumed to be detected, in reality, do not pass trigger criteria, image cleaning, or analysis cuts. The effective collection area is then smaller than assumed, which translates to an underestimation of the flux. The overestimation of light associated with gamma rays of certain energy furthermore leads to a bias in the energy estimation, migrating events to smaller energies. It is therefore important to have a good understanding of the overall light throughput of the telescope system, starting from the atmospheric transmission to the mirror reflectivity and the light collection efficiency of the PMTs. The latter two have been estimated in [25]. The precision of the measurement of the atmospheric transmission has been estimated to be 4-10% for zenith angles up to 60° [86, 165] and 10% above 70° [140].

5.2.4.2 Pointing accuracy

The deformation of the telescope structure due to the gravitational load during observations is largely compensated by the AMC and the starguider monitoring (see Section 4.1.5.4). The

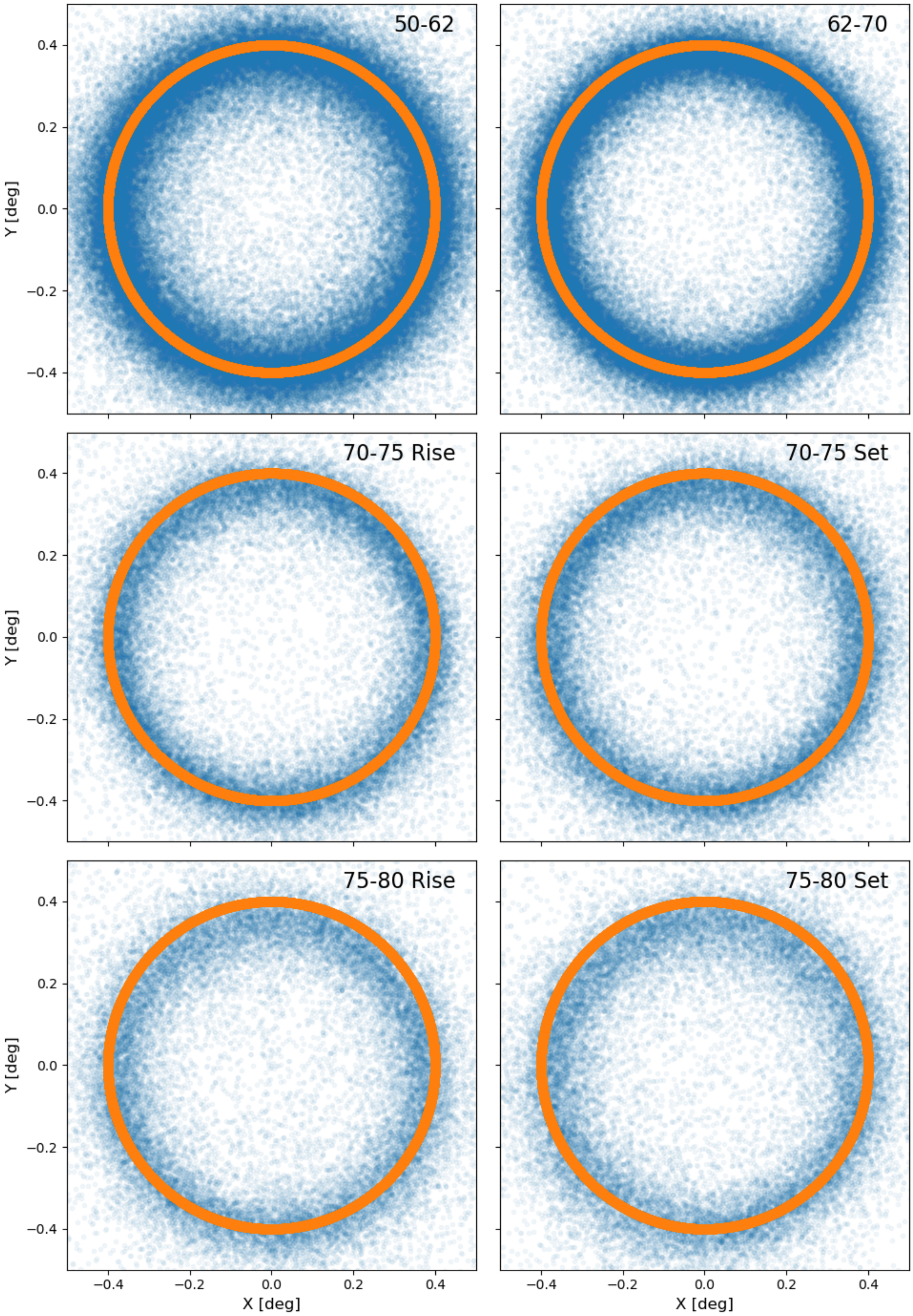

Figure 5.33: The true simulated (orange) and reconstructed (blue) event positions in camera coordinates. Above $62°$, but especially above $70°$, the systematic underestimation of the Y-coordinate for events in the top half of the camera becomes visible.

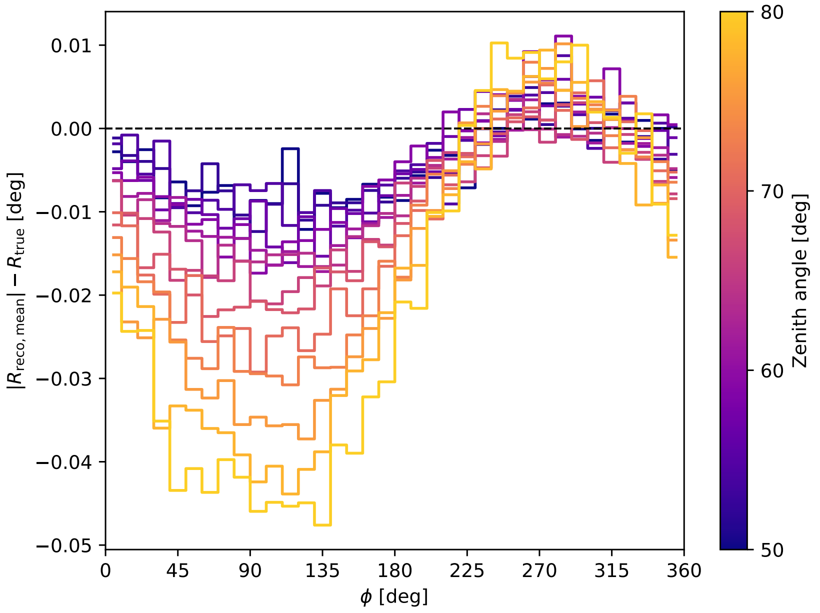

Figure 5.34: The effect of the squished ring reconstruction in polar camera coordinates. The difference between the reconstructed angular distance from the camera and the true simulated distance is drawn along the y-axis as a function of the rotational angle ϕ for several zenith angles. A clear increase with the zenith angle in the systematic reconstruction to lower radii in the top half of the camera is visible.

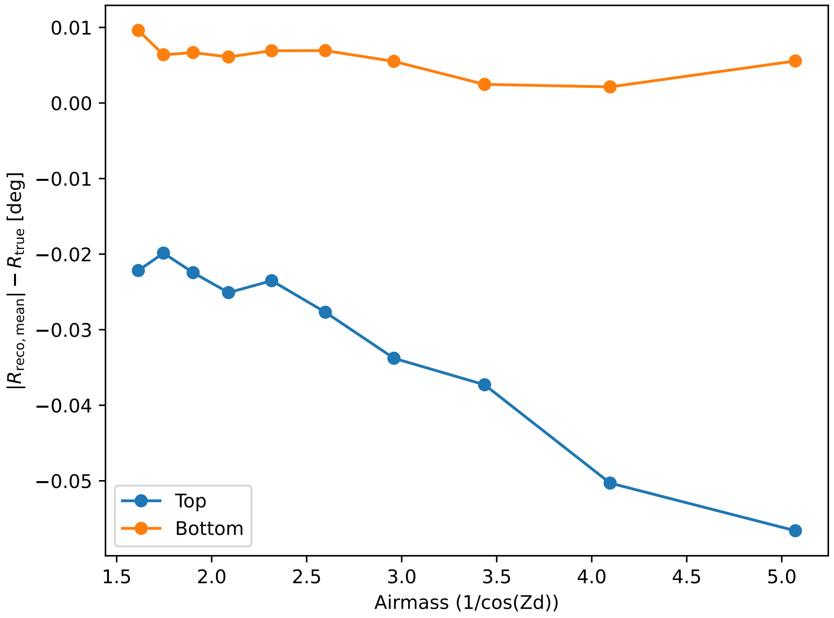

Figure 5.35: The effect of the squished ring reconstruction as a function of airmass. The difference between the reconstructed angular distance from the camera and the true simulated distance is shown as a function of airmass for the top and the bottom of the camera corresponding to lower and larger zenith angles, respectively (images in the camera are flipped with respect to reality). $R_{\text{reco, mean}}$ for the curves was found by fitting a Gaussian distribution to the reconstructed coordinates in a slice of width 0.2° around X=0 for positive and negative Y-coordinates separately.

residual mispointing has been estimated both in [28] and [140]. For low and medium zenith angles, an accuracy of 0.02° was found, while a larger value of 0.04° was found at VLZA. The PSF at VLZA has a total extension of around 0.16°, resulting in a negligible effect of pointing inaccuracy.

5.2.4.3 Background Subtraction

An inhomogeneous acceptance in the camera FOV can lead to fluctuations in the number of estimated background events, potentially strongly influencing the flux and spectral index estimation of a weak source. Background asymmetries can be mitigated by using the wobble method, which alternates the signal and background regions, and by re-normalizing θ^2 histograms in the off-source region. In [28], the systematic uncertainty on the background estimation has been estimated to be $\sim 1\%$. In Section 5.2.3.3, I have shown that fluctuations up to 5% in the background counts are possible. Also here, wobbling will reduce this effect substantially, but to be safe, an additional $\sim 1\%$ uncertainty should be considered. Added in quadrature to the previously estimated value, this results in a total uncertainty on the background estimations of 1.4%.

For weak sources, depending on the considered energy range, this can have a substantial effect on the estimation of the spectral index. Following the calculation described in [28], where a weak source is considered with a reconstructed spectrum between the energies E_{min} and E_{max}, in the energy range $[E_{\mathrm{min}}, \sqrt{E_{\mathrm{min}}E_{max}}]$ the signal to background ratio is SBR_{LE} and in the range $[\sqrt{E_{\mathrm{min}}E_{max}}, E_{\mathrm{max}}]$ it is SBR_{HE}. The uncertainty on the spectral index α is then estimated to be

$$\Delta\alpha_{SBR} = 2 \times \frac{\sqrt{(1.4\%/SBR_{LE}) + (1.4\%/SBR_{HE})}}{\ln(E_{\mathrm{max}}/E_{\mathrm{min}})} \tag{5.9}$$

For a source with, e.g., $SBR_{\mathrm{LE}} = 5\%$ and SBR_{HE}=15% in the energy range 30-100 TeV, we obtain $\Delta\alpha = 0.21$. This would increase the total systematic uncertainty on the index from 0.15 to 0.26.

5.2.4.4 Atmospheric refraction

The effect described in Section 5.2.3.4 has a similar consequence as a residual mispointing, as it results in a loss of signal events due to an ill-defined source position. I have estimated the size of the effect by evaluating the variation in the event rate as a function of rotational angle ϕ in the camera, as shown in Figure 5.36. The figure shows the fraction of all the events that have been simulated within a source region of a given radius that is correctly reconstructed within the same source region for the zenith angle [75°, 80°]. Similar plots for the remaining zenith angles can be found in Section A.2. A clear trend of a higher fraction of events at $\phi \approx 270°$, corresponding to the bottom of the camera, can be seen. Each line in the plot represents a different size of the source region. By calculating the difference between the maximum and minimum value of each of these lines for all zenith angles, Figure 5.37 was obtained. It shows the decrease in variation of the event rate with larger radii of the source regions. At typical θ^2-cut values of below 0.02, the effect is around 3% below 70° and 6% above 70° and could potentially be decreased by loosening the θ^2-cut, however at the cost of accepting more background events in the source region. As for the background asymmetry described above, this is an effect that can be mitigated by using the wobble method and thereby frequently changing the source position in the camera. Nevertheless, this effect should be considered when estimating the total systematic uncertainty on the flux normalization.

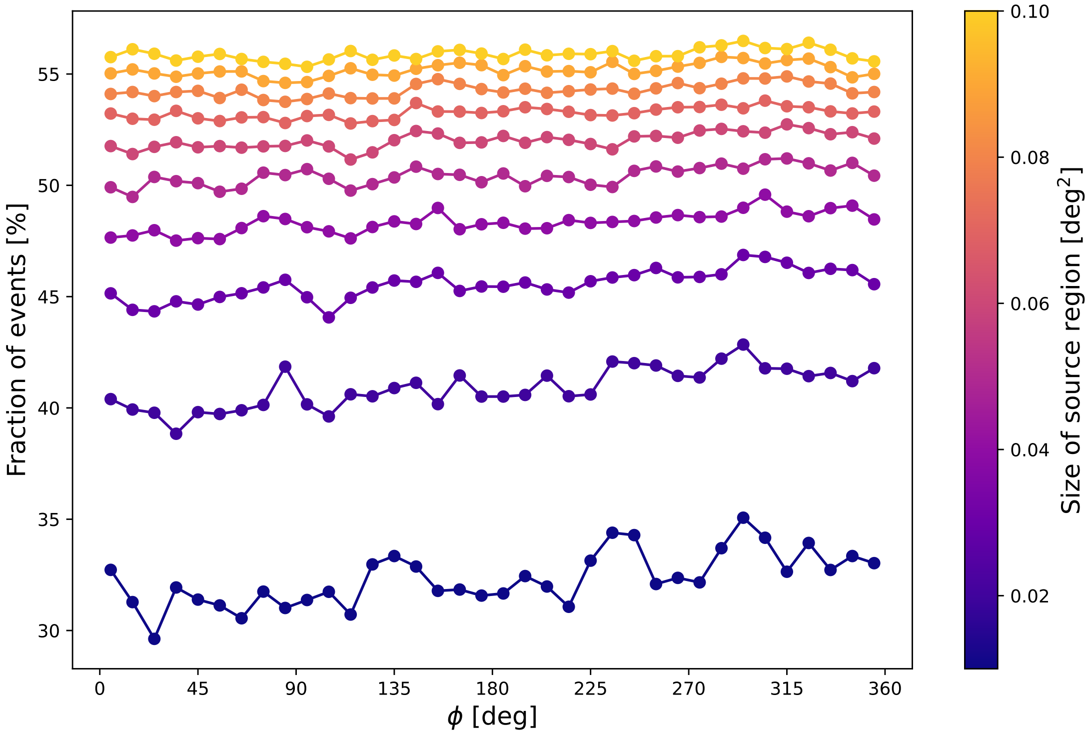

Figure 5.36: The fraction of simulated events simulated within a source region that is reconstructed within the same source region. The regions of varying radii and rotational angle ϕ in the camera are fixed at 0.4° distance from the camera center. This plot shows the figure for the zenith angle bin $[70^\circ, 75^\circ]$. Similar plots for the other zenith angle bins are shown in Section A.2.

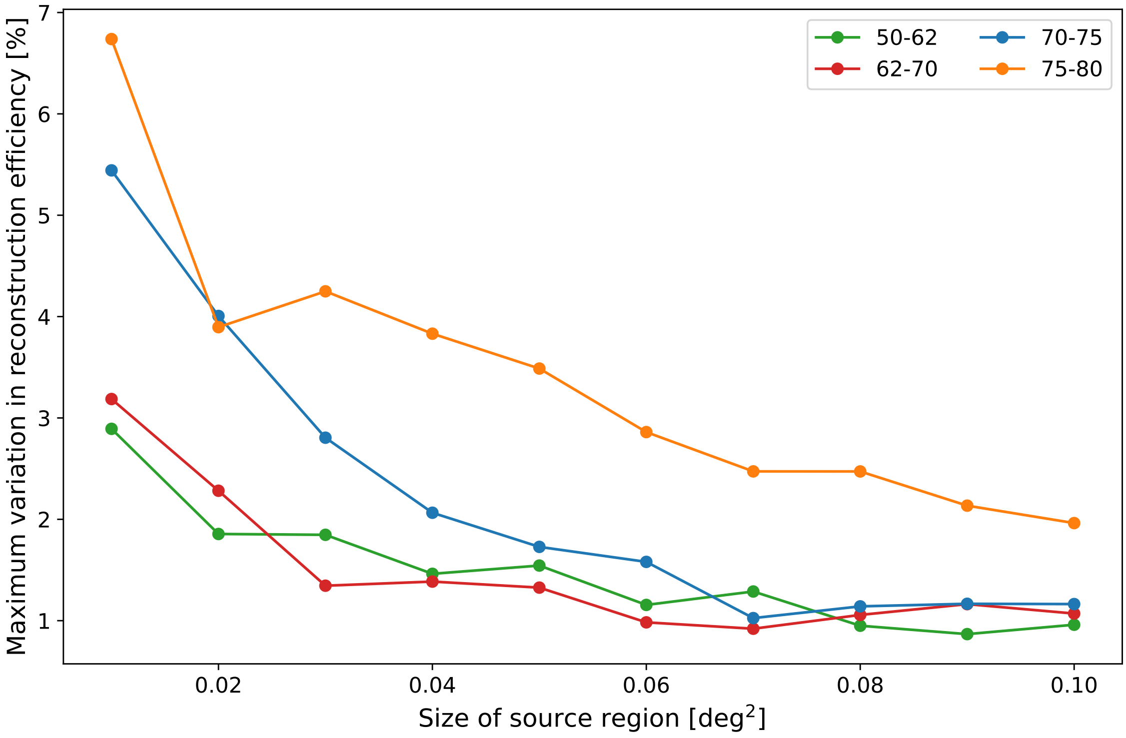

Figure 5.37: The difference between the maximum and minimum value of each line corresponding to a source region radius shown in Figure 5.36.

5.2.4.5 Total systematic uncertainties

A complete list of systematic uncertainties is given in Table 5.4. The main factors driving the systematic uncertainty on the energy scale are the F-Factor method and the atmospheric transmission. The flux normalization is most strongly affected by discrepancies in the Analysis and mismatches between MCs and real data. Adding the respective values for the energy scale and the flux normalization in quadrature results in an uncertainty of 18-20% for the energy scale for all zenith angles and 11-18% for the flux normalization below 50° and 12-20% above 50°.

Table 5.4: The values of the main sources of systematic uncertainties. They can affect the energy scale (ES), the flux normalization (FN), or the spectral slope (SL). All values that do not depend on the zenith angle and the values for Zd $< 50°$ are taken from [25, 28]. Values for Zd $> 50°$ have been taken from [140] or determined in this work. See the text for more explanations.

Systematic Effect	Uncertainty
F-Factor	10% ES
Mirror Reflectivity	8% ES
PMT electron collection efficiency	5% ES
Light collection in a Winston cone	5% ES
PMT quantum efficiency	4% ES
Signal extraction	3% ES
Temperature dependence of gains	2% ES
Charge flat-fielding	2–8% ES, FN
Analysis and MC discrepancies	<10–18% FN, SL
Broken channels/pixels	3% FN
NSB	1-4% FN
Trigger	1% FN
Unfolding of energy spectra	0.1 SL

	Zd $< 50°$	Zd $> 50°$
Atmospheric Transmission	< 10% ES	10% ES
Atmospheric Refraction	–	3-6% FN
Background subtraction	1% FN	1-2% FN
Mispointing	1-4% FN	4-8% FN

5.3 Study of the flux variability

In addition to the evaluation of the IRF and the flux sensitivity with related systematic uncertainties, I have carried out a study on the flux variability of the presented Crab Nebula data set. This study is interesting for two reasons. A stable flux estimation over a long timescale shows the stability of the system and the data processing, while small fluctuations between subsamples provide additional information on systematic uncertainties that are not stable in time. The latter is most prominently the case for atmospheric transmission, which exhibits night-by-night or even intra-night variability. This matter is discussed in the following Section 5.3.1. The fact that the source I study here is the Crab Nebula provides the second reason to lay an additional focus on the flux variability in the observations. As mentioned in Section 2.5.2, strong flares on short timescales have been observed in the HE band of the Crab Nebula emission. Since the emission in the Nebula is most likely due to

SSC (see Section 3.1.2), the same electron population that is responsible for these flares in HE, could also produce a flux enhancement in the VHE band. It is, therefore useful to search for any kind of variation in the observed data and to derive a sensitivity to the potential flares at energies of tens of TeV. I present the results of this second part of the variability study in the sections 5.3.2 and 5.3.3.

5.3.1 Stability of the observation

In order to study the stability of the system and to investigate the scale of variation of systematic uncertainties, I have estimated the integrated flux above a chosen E_{min} for the periods ST.03.06 and ST.03.07, which contain data across the entire zenith angle range between 50° and 80°. I combined all data subsets up to 75° Zd and divided them into subsamples chronologically in time. As before, when deriving the SED in Section 5.2.2.7, I have discarded the data taken in the zenith range [75°, 80°].

I applied two values of minimum energy $E_{\mathrm{min,LC}}$ and studied the stability for the resulting data respectively. In the case of $E_{\mathrm{min,LC}} = 1\,\mathrm{TeV}$, I produced bins of 1 day width. I removed bins from the sample which had an exposure of less than $600\,\mathrm{km}^2\,\mathrm{s}$, which corresponds to $\sim 30\,\mathrm{min}$ of observations for the average effective area across the entire sample of $\bar{A}_{\mathrm{eff}} \approx 0.3\,\mathrm{km}^2$. 74 bins remained, with effective observation times between 50 and 320 min and an average of $\bar{t}_{\mathrm{eff}} \approx 54\,\mathrm{min}$. Furthermore, samples in which the relative statistical error of the flux measurement was larger than 50% were also removed. This value is the limit at which, customarily, no flux points but only upper limits are calculated.

I followed a similar procedure as [28] and [25] to estimate the scale of fluctuations due to varying systematics. Figure 5.38 shows the resulting data samples as a function of sample number. The relative statistical error of all samples is below 19%; for roughly half, it is less than 10%. Fitting a constant flux to the set of samples results in a poor fit quality of $\chi^2/Ndf = 165/64$. The standard deviation of the flux points is $\sigma_{\mathrm{F}} \sim 17\%$, which leads to an estimate of the systematic uncertainty of $\sigma_{\mathrm{F}}/\sqrt{2} \approx 12\%$[3]. Notably, this value is of the same order as the estimated uncertainty on the atmospheric transmission, which is the most dominant factor influencing night-by-night fluctuations in the system. Adding this value in quadrature to the statistical uncertainties of the samples and repeating the fit results in a much better fit probability of $\sim 25\%$, with $\chi^2/Ndf = 71/64$. The fitted flux is $(1.68 \pm 0.03) \cdot 10^{-11}\,\mathrm{cm}^{-2}\,\mathrm{s}^{-1}$ and is shown in Figure 5.38. Above 10 TeV, the statistical errors are much larger when selecting samples of 1-day width and the number of excess counts is below 10 in most samples, making it difficult to treat the samples using Gaussian statistics. I therefore created samples of 7 days width, which resulted in a sufficient number of samples with a minimum of 10 Excess counts. The applied minimum values on the exposure are summarized in Table 5.5. The systematic uncertainty is $\sigma_{\mathrm{F}}/\sqrt{2} \approx 33\%/\sqrt{2} \approx 23\%$ in this case. The resulting flux values are shown in Figure 5.39. The constant fit has a $\chi^2/Ndf = 13/23$.

Applying a minimum energy larger than 10 TeV does not yield enough statistics to do a similar evaluation of the systematic uncertainties. Hence, I have focused my efforts on the two shown cases. I have studied the stability on various additional timescales, the details of which are summarized in Table 5.5.

Under the assumption that the intrinsic flux of the Crab Nebula is constant, this results in a night-by-night systematic uncertainty of $\sim 12\%$ of the integrated flux above 1 TeV. Above 10 TeV fluctuations due to varying systematic uncertainties of $\sim 23\%$ on a timescale of 3-days.

---

[3] The factor $\sqrt{2}$ results from the assumption that the observed deviation results from the same systematic uncertainty σ_{syst} that is effecting each sample independently. Comparing pairs of samples, to understand the sample-to-sample fluctuation, results in $\sigma_{\mathrm{F}}^2 = \sigma_{\mathrm{syst}} + \sigma_{\mathrm{syst}} = 2\sigma_{\mathrm{syst}}$. Therefore, $\sigma_{\mathrm{syst}} = \sigma_{\mathrm{F}}/\sqrt{(}2)$.

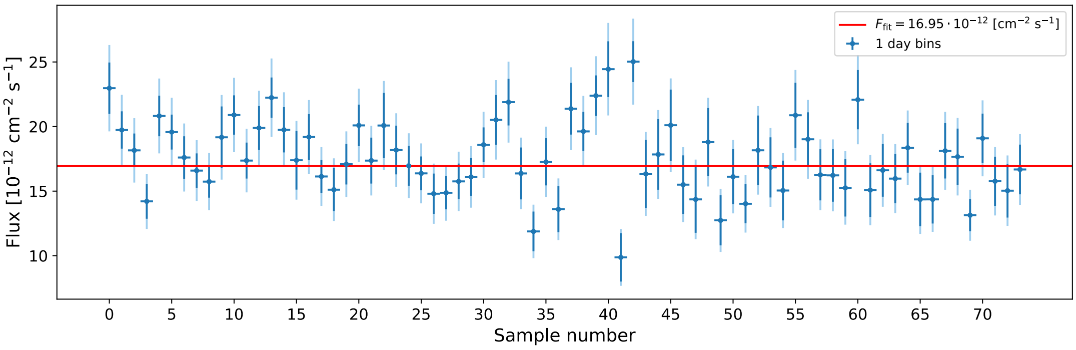

Figure 5.38: Integrated flux above $1\,\mathrm{TeV}$ for data samples with an average of $\sim\ 1\,\mathrm{h}$ effective observation time. Dark blue vertical error bars represent statistical uncertainties only; the light blue shaded extensions represent the total error with the estimated systematic uncertainty of 12% added in quadrature. The red line shows the constant fit to the flux values.

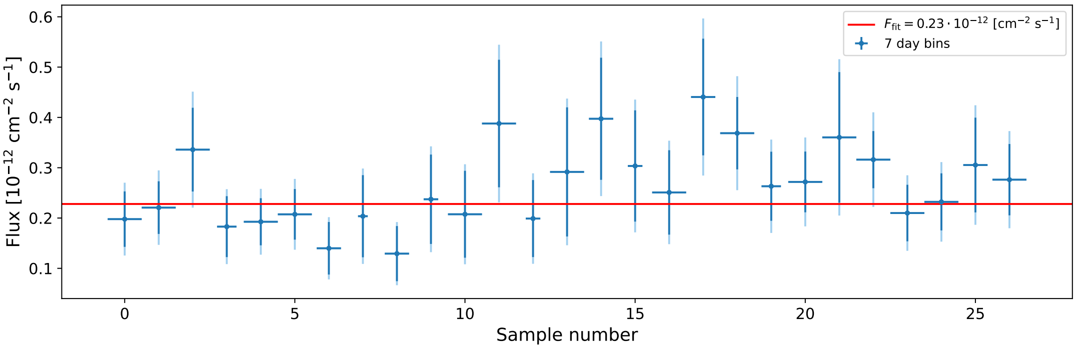

Figure 5.39: Integrated flux above $10\,\mathrm{TeV}$ for data samples with an average of $\sim\ 3\,\mathrm{h}$ effective observation time. Dark blue vertical error bars represent statistical uncertainties only; the light blue shaded extensions represent the total error with the estimated systematic uncertainty of 23% added in quadrature. The red line shows the constant fit to the flux values.

Table 5.5: Summary of the stability/variability study of the data set. For bins of 1 day, 7 days and 30 days width and minimum entries of $1\,\mathrm{TeV}$ and $10\,\mathrm{TeV}$, the average effective area and time per bin is shown, for all bins passing the criterium of the given minimum exposure. The number of all available bins selected according to this criterium is also given. $\bar{\sigma}_{\text{stat}}$ denotes the average statistical error of the individual samples, σ_{F} there standard deviation and σ_{stat} the resulting systematic error. The values of the fitted constant flux and the χ^2 of the fit are given, as well as the fractional variation assuming a global systematic uncertainty of 0.12 for all settings.

Binwidth	**1 day**	**7 days**		**30 days**	
E_{min}	**1 TeV**	**1 TeV**	**10 TeV**	**1 TeV**	**10 TeV**
$\bar{A}_{\text{eff}}\,[\mathrm{km}^2]$	0.3	0.3	1.0	0.3	0.98
$\bar{t}_{\text{eff, sel}}\,[\mathrm{h}]$	0.9	2.2	2.7	3.8	4.2
$\mathrm{Exp}_{\text{min}}\,[\mathrm{km}^2\,\mathrm{s}]$	600	600	3000	600	3000
$\mathrm{bins}_{\text{sel}}/\mathrm{bins}_{\text{all}}$	$74/143$	$38/47$	$27/44$	$23/26$	$19/23$
$\bar{\sigma}_{\text{stat}}$	0.11	0.10	0.31	0.07	0.27
σ_{F}	0.17	0.18	0.34	0.15	0.35
σ_{syst}	0.12	0.13	0.24	0.11	0.25
$F_{\text{fit}}\,[10^{-12}\,\mathrm{cm}^{-1}\,\mathrm{s}^{-1}]$	16.9 ± 0.3	16.6 ± 0.4	0.22 ± 0.02	16.9 ± 0.5	0.23 ± 0.02
χ^2/Ndf	$79/73$	$47/37$	$15/26$	$27/22$	$11/18$
F_{var}	0.02 ± 0.05	0.10 ± 0.03	undefined	0.06 ± 0.4	0.12 ± 0.1

5.3.2 Variability of the Crab Nebula flux

In the previous section, I assumed that the Crab Nebula flux is intrinsically stable and attributed all fluctuations in the light curve to statistical and systematic uncertainties. Under the hypothesis that the flux, especially at the highest energies, is not stable, it is possible to derive a measurement of this intrinsic flux variability or alternatively set an upper limit based on the observation. The fractional variation is a measure to quantify the intrinsic flux variability by subtracting the mean squared uncertainties of individual flux points from the overall variance of the measurements of a time series. It is defined as

$$F_{\mathrm{var}} = \frac{\sqrt{\sigma^2 - \delta^2}}{\langle f \rangle}, \tag{5.10}$$

where σ^2 is the variance and δ^2 the mean squared uncertainty of the flux measurements. $\langle f \rangle$ is the fitted constant flux. The uncertainty of F_{var} is defined as [180]

$$\delta F_{\mathrm{var}} = \sqrt{F_{\mathrm{var}}^2 + err(\sigma_{\mathrm{NXS}}^2)} - F_{\mathrm{var}} \tag{5.11}$$

with

$$err(\sigma_{\mathrm{NXS}}^2) = \sqrt{\left(\sqrt{\frac{2}{N}}\frac{\delta^2}{\langle f \rangle^2}\right)^2 + \left(\sqrt{\frac{\delta^2}{N}}\frac{2F_{\mathrm{var}}}{\langle f \rangle}\right)^2} \tag{5.12}$$

In the previous section, I derived a systematic night-by-night uncertainty of 12% of the average flux for a minimum energy of 1 TeV, where each night of measurements contains on average 1 h of observations. The scale of the uncertainty is the same as the one derived in [28] for the run-by-run uncertainty above 300 GeV where each run contains $\sim$ 20 min of data. Assuming that the same scale of uncertainty also applies to the light curves with a minimum energy of 10 TeV, which consist of 7-day (30-day) bins with an average observation time of 3 h (4 h), I have studied the scale of the flux variability in these data samples. For the 7-day binning, $\delta^2 > \sigma^2$ and F_{var} is therefore undefined. When considering only statistical uncertainties in the calculation, $F_{\mathrm{var}} = (0.13 \pm 0.09)$ is a value similar to the assumed systematic uncertainty, supporting my previous assumption. I have estimated upper limits on the intrinsic flux variability from simulations based on these observations. Using the flux value from the constant fit F_{fit} as a reference, for each bin in the simulated light curve, I have added an additional random fluctuation of $\pm\sigma_{\mathrm{syst}} \cdot F_{\mathrm{fit}}$ resulting in individual flux values F_i per bin. With the measured number of background events N_{off} in each bin, I have calculated the mean number of On counts N_{on} per bin i as

$$N_{\mathrm{on,i}} = F_i \cdot A_{\mathrm{eff,i}} \cdot t_{\mathrm{eff,i}} + N_{\mathrm{off,i}}. \tag{5.13}$$

For one simulated light curve, I created a set of simulated $N_{\mathrm{on,sim}}$ and $N_{\mathrm{off,sim}}$ events by pulling from a Poisson distribution with mean values $N_{\mathrm{on,i}}$ and $N_{\mathrm{off,i}}$ for each respective bin. The simulated flux value in each bin is then given by

$$F_{\mathrm{sim,i}} = (N_{\mathrm{on,sim,i}} - N_{\mathrm{off,sim,i}})/(A_{\mathrm{eff,i}} \cdot t_{\mathrm{eff,i}}) \tag{5.14}$$

and its statistical error by the usual error propagation. I have produced 10^5 such simulated lightcurves and calculated the fractional variation for each of them. Figure 5.40 shows the observed data from Figure 5.39 together with a subsample of 400 simulated light curves. The cumulative distribution of F_{var} from all simulated light curves is shown in Figure 5.41. As for the observed data set, most of the simulated light curves result in undefined values of F_{var}, set to zero in the plotted distribution. From the remaining values, it can be determined that a variability larger than 15% of the fitted flux on weekly timescales can be excluded at a 95% confidence level.

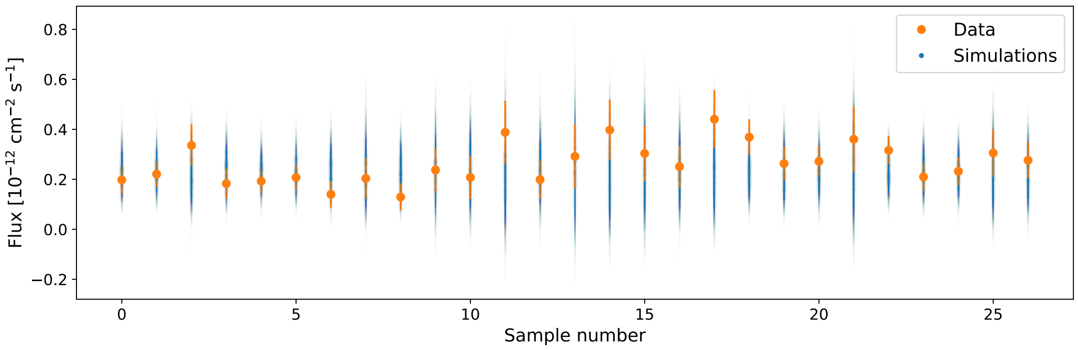

Figure 5.40: Observed light curve and a subsample of simulated light curves.

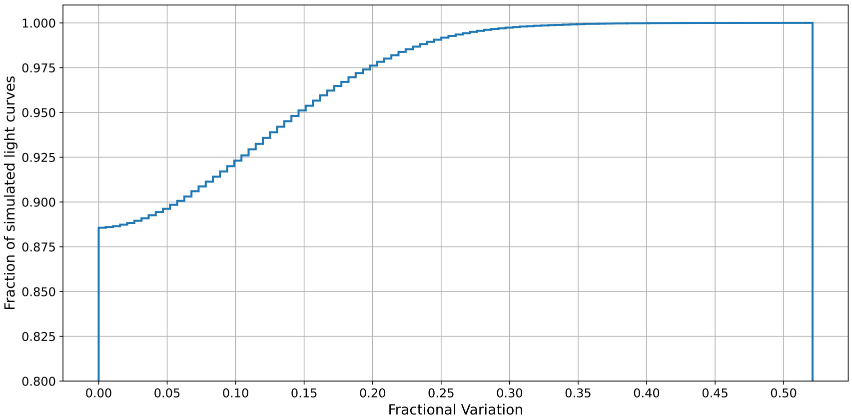

Figure 5.41: Cumulative distribution of the fractional variation calculated from the simulated light curves. Where F_{var} was ill-defined because $\delta^2 < \sigma^2$, F_{var} has been set to zero.

In the case of the 30-day binning, $F_{\text{var}} = (0.12 \pm 0.1)$. The significance of this value can be estimated from simulating light curves as described above. Based on the simulations, the probability of getting a value of F_{var} larger or equal to the observed one is $p = 0.07$, corresponding to a significance of 1.4σ, and therefore not significant. The 95% upper limit on the scale of variability on monthly timescales derived from the simulated light curves is 16% of the fitted constant flux, similar to the value derived for a weekly binning. The figures corresponding to Figure 5.40 and Figure 5.41 for the 30-day binning are shown in Section A.4.

5.3.3 Sensitivity to gamma-ray flares

Large sudden flares on the time scale of days with flux increases of several times the nominal flux have been observed at the high end of the synchrotron peak of the Crab Nebula by the Fermi and AGILE satellites (see Section 2.5.2). In the case of such flares translating to flux increases of similar duration in the VHE regime, it is important to understand how sensitive the observations are to such short-term flux enhancements. This can serve as a basis for triggering follow-up observations of flares reported by Fermi-LAT and for constraining parameters of theoretical models that try to explain the nature of the gamma-ray flares.

I have estimated the sensitivity of MAGIC to detect a potential flare in the VHE regime. By taking the weekly binned light curve above 10 TeV as a basis, I have assumed F_{Fit} as the “low state” Crab Nebula flux and have calculated a mean background flux by averaging the number of Off counts multiplied by the effective area and time across all bins. For a range of flare durations between 1 and 10 hours and for a range of flux increases between 1 and 3, I calculated a mean number of On and Off counts and created 10^4 samples drawing from Poisson distributions around these values. The flux for each of the 10^4 samples is then calculated according to Equation 5.14 using the respective flare duration as effective time, and the average effective area of 1 km^2 (see Table 5.5). This results in a distribution of possible flux values for each set of flare duration and flux increase. I then calculated the overlap of each of these distributions with the flux distribution of no flux increase and a duration of 3 hours, which is about the average effective time per bin of the observed lightcurve (see Table 5.5). The fraction of the overlap with respect to the "low state" distribution gives the probability of the measurement belonging to the flare distribution being attributed to the "low state" distribution. The smaller this probability is, the more likely such a measurement could be correctly identified as a flare rather than a statistical fluctuation.

Figure 5.42 shows the contours for such a correct identification of a flare as a function of flare duration and flux increase factor. With 95% confidence, a flare lasting more than 5 hours with a flux twice the nominal flux could be detected. The data set shown here is a realistic representation of the amount of data collected on average without a specific program of regular monitoring, accumulating around 3 hours of effective observation time on the Crab Nebula per week above 10 TeV. Using this sampling and the corresponding constant flux as a baseline for comparison, I found that a flare lasting around 5 hours would be detectable if its flux is roughly twice the nominal flux. In the case of a dedicated follow-up of a flaring alert received from Fermi-LAT, 1 h of observations per day would be more than reasonable. Assuming this average exposure as a baseline, a flux increase of 50% lasting 5 hours would already be detectable. This result should, therefore, serve as a basis for future efforts to follow-up observations of detected gamma-ray flares in HE regime. A sufficiently large accumulation of observations at zenith angles between 50° and 75° not only during the flare but also in the months preceding or following the flare should be planned in order to establish a solid baseline observation from which the potential flaring state could be distinguished.

5.4 Comparison with other instruments

I have shown in the previous sections that observations at large zenith angles provide a meaningful way of extending the observable energy range of MAGIC to higher energies. Below 75°, the performance remains stable and comparable to lower zenith angles. The community of VHE gamma-ray astronomy is actively growing, and new experiments have started data taking in recent years or are currently under construction. Specifically the air shower arrays HAWC and LHAASO (see Section 3.3.6) have changed the landscape at ultra-high (> 100 TeV) energies with the detection of emission beyond 100 TeV from multiple sources (see Chapter 2). The Cherenkov Telescope Array Observatory (CTAO), the next generation of IACTs, is currently under construction and will consist of telescope arrays in the Northern and Southern hemispheres. CTAO-South is optimized to be more sensitive at the highest energies than CTAO-North; the latter, however, is more advanced in its construction phase, with the first telescope already being operational and three more currently being built. To understand how MAGIC can contribute to observations at very-high and ultra-high energies within this changing landscape of VHE gamma-ray astronomy, it is important to compare its performance with other instruments.

Air shower arrays such as HAWC and LHAASO generally profit from their large detector areas and high duty cycles compared to IACTs when measuring the low fluxes of gamma-ray sources at the highest energies. Their angular and energy resolutions tend to be worse than for IACTs. The disadvantage of MAGIC in effective area can however largely be compensated when observing at zenith angles beyond 60°, where the effective area reaches

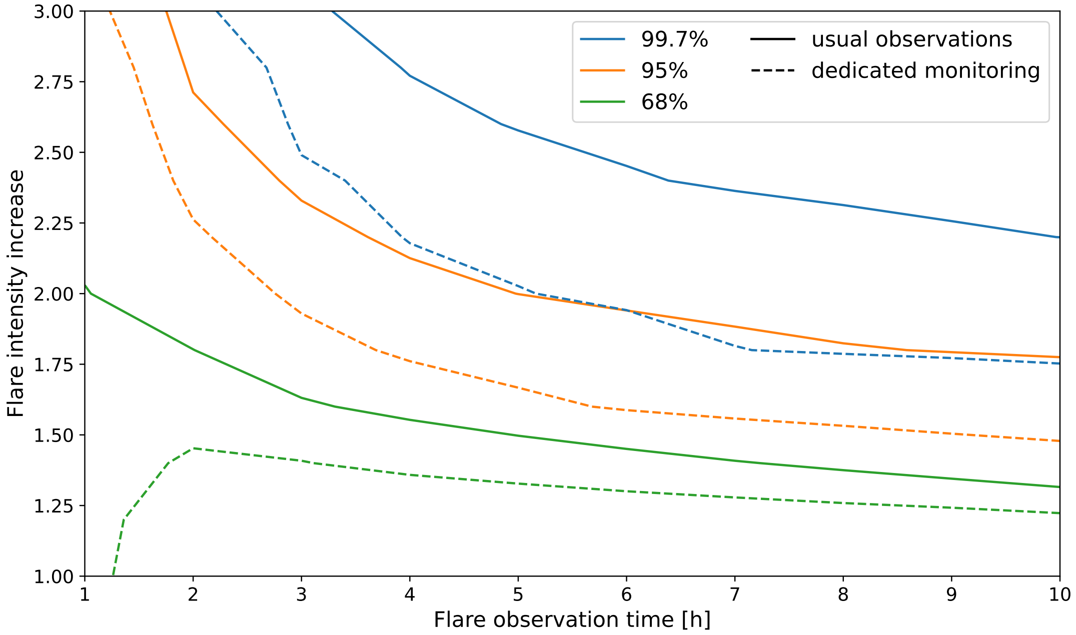

Figure 5.42: The sensitivity to potential gamma-ray flares above 10 TeV. The 68%, 95% and 99.7% contours are shown for two cases: using as a "low state" reference the average data sampling of the here analyzed data set (solid lines) or dedicated monitoring with daily 1 h observations (dashed lines). The x-axis refers to the amount of time in which the flare is observed, and its flux is increased by the factor given on the y-axis with respect to the nominal flux in the "low state".

more than 0.5 km^2 at few TeV and more than 1 km^2 at tens of TeV. LHAASO's KM2A detector has an effective area of 0.5-1 km^2 at tens of TeV and reach more than 1 km^2 beyond 100 TeV [137]. The water Cherenkov detectors of LHAASO (WCDA) and HAWC have an effective area of $78,000\,\mathrm{m}^2$ and $\sim 25,000\,\mathrm{m}^2$, respectively. The effective area of MAGIC at large zenith angles is also comparable to the effective area both CTAO arrays will achieve during standard observations [63].

The energy resolution of MAGIC at large zenith angles, as determined in Section 5.2.2.4, lies between 10-30% at tens of TeV while the energy bias is close to zero up to 100 TeV for zenith angles below 75°. These values are similar to the MAGIC performance at lower zenith angles [28]. For air shower arrays, the precise reconstruction of the energy is typically more challenging than for IACTs due to a less precise reconstruction of the shower properties.

The angular resolution determined in Section 5.2.2.5 lies below 0.06° for zenith angles up to 70° and between 0.06° and 0.08° for zenith angles between 70° and 75° which is roughly the same as for lower zenith angle observations with MAGIC [28]. CTAO will profit from a large number of telescopes resulting in a much better stereo reconstruction quality, achieving an angular resolution of below 0.05° at 1 TeV and 0.02° around 100 TeV [63]. In comparison with the existing air shower arrays, MAGIC performs significantly better in terms of angular resolution at TeV energies. Both LHAASO and HAWC achieve an angular resolution of only around 0.2° [137, 20], a factor of ~ 3 worse than the MAGIC angular resolution shown in this work.

The MAGIC sensitivity below 75° determined in Section 5.2.2.6 is shown in Figure 5.43 in comparison with the mentioned instruments and the MAGIC sensitivity at lower zenith angles from [28]. The sensitivity in the [50°, 62°] nicely connects to the previous MAGIC data. Close to 100 TeV, the VLZA MAGIC sensitivity reaches values comparable to the sensitivity of CTAO-North. All IACT sensitivities shown here are scaled to 50 h of observation time. For HAWC and LHAASO, the sensitivities are shown for 5 years and 1 year of data taking, respectively. HAWC can observe the Crab Nebula for an average of ~ 9 h

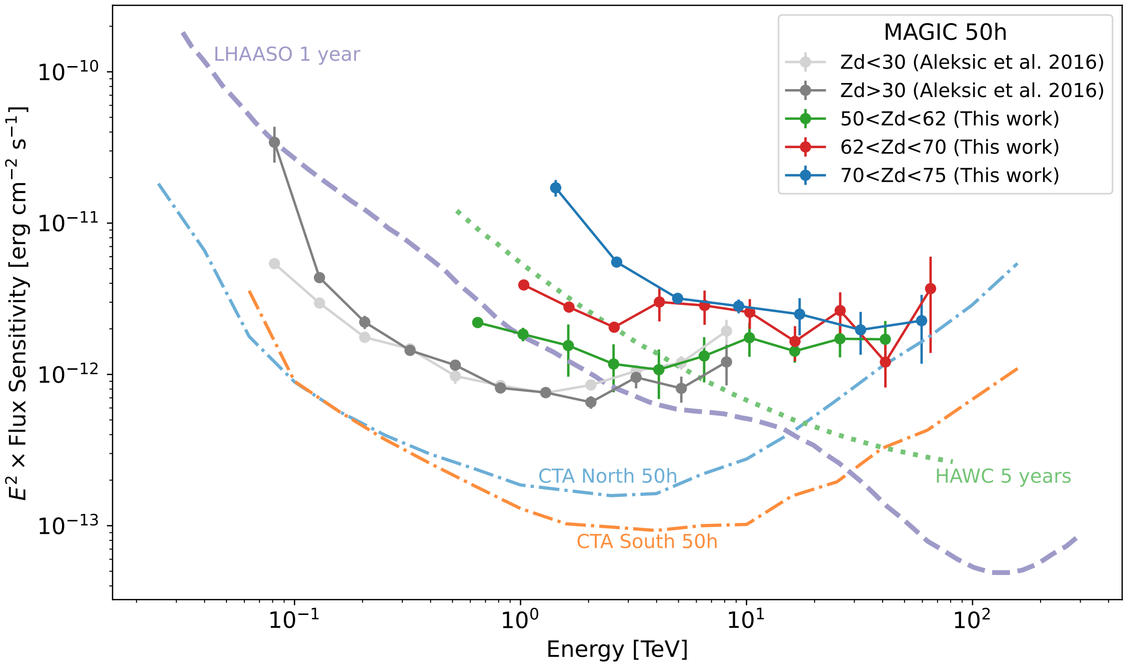

Figure 5.43: Comparison of MAGIC differential sensitivity above 50° with other instruments. The MAGIC sensitivity curves are shown in terms of estimated energy.

per day [5]. Five years consequently correspond to more than 16,000 h of Crab Nebula data. LHAASO observes the Crab Nebula for around 7.5 h per day [132] resulting in $\sim$ 2500 h of observations in one year. This remarkably large exposure over a time span in which an IACT can typically acquire the mentioned 50 h leads to the much better sensitivity of HAWC and LHAASO beyond tens of TeV as can be seen in Figure 5.43.

Figure 5.44 shows the Crab Nebula SED which I obtained in Section 5.2.2.7 in comparison in with measurements from other instruments. The spectra of the air shower arrays exhibit slightly higher fluxes than the spectrum obtained in this work; however, considering also systematic uncertainties, all measurements are consistent with each other.

5.5 Summary

In this chapter, I have presented the results of a detailed study of the performance of the MAGIC Telescope system during point-source observations at large zenith angles. The parameters that quantify the performance were introduced in Section 5.1, and their values at zenith angles below 50°, which have been obtained in [28], were presented. In Section 5.2.2 I have determined the performance quantities in four distinct zenith angle bins between 50° and 80° and, in the [70°–80°] range, additionally for two separate azimuth selections, dubbed *Rise* and *Set*, which represent the two observational settings in which the Crab Nebula is observed at these zenith angles. I split the MC data into the Rise and Set samples by two different approaches which are shown in Figure 5.9 and Figure 5.10: once tracing the azimuth angles of the Crab Nebula observation (*standard azimuth splitting*) and once selecting azimuth angles that correspond to the same range of effective baseline between the two MAGIC telescopes (*baseline azimuth splitting*). I evaluated all performance quantities for all four zenith angles, and the two azimuth angles in both selection approaches. No considerable difference arose between the Rise and Set samples or between the two azimuth splitting approaches. The only exception to this is the estimation of the angular resolution, where the Rise sample performs slightly better, and the standard azimuth splitting shows

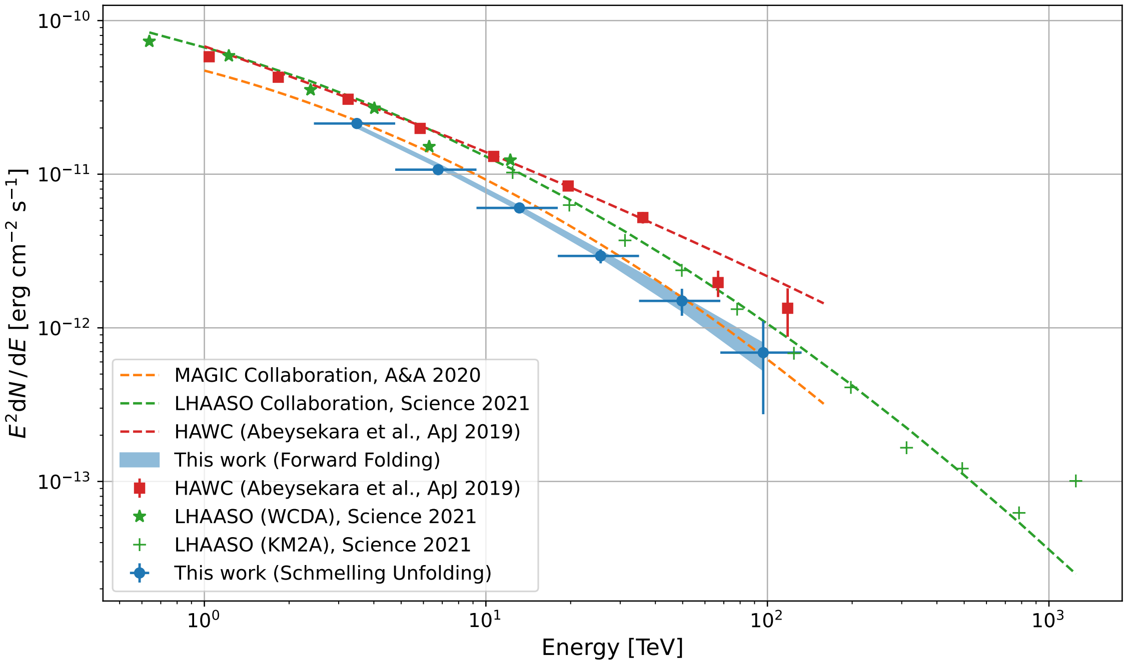

Figure 5.44: The unfolded flux points (blue data points) and forward folded SED (blue shaded region) obtained from the analyzed data set in comparison with other instruments. Green data points and the green line refer to the WCDA (stars), KM2A (crosses) and the best-fit spectrum (line) from LHAASO [132]. Red squares show data from HAWC [4]. The orange line shows the best-fit spectrum from [140].

much larger tales in the θ^2 distribution compared to the baseline azimuth splitting. I selected the latter as the more accurate analysis setting and used this in the estimation of the SED and the flux variability. From the results shown in Section 5.2.2 it has become clear that the performance of MAGIC remains quite stable up to zenith angles of 75°. The energy resolution has similar values to low and medium zenith angle observations, and the energy bias remains stable around zero up to a few tens of TeV for zenith angles up to 70° and up to 100 TeV zenith angles up to 75°. The angular resolution also remains comparable to lower zenith angles with the VLZA data providing resolutions below 0.08° even beyond 100 TeV. The major advantage of observations at large zenith angles is the dramatic rise in the effective area to a few km^2 with increasing zenith angles. The stable energy dispersion and angular resolution combined with the large effective area results in an overall IRF that has the potential to be as sensitive at energies of tens and hundreds of TeV as MAGIC observations at low and medium zenith angles are at GeV energies. The reason why the same sensitivity of $\lesssim 10\%$C.U. is not reached for zenith angles larger than 62°, as can be seen in Figure 5.23, is due to the degradation of the gamma-hadron separation at large zenith angles.

The spectral energy distribution obtained with the data set up to 75° Zd extends to 100 TeV (Figure 5.27) and matches well with previous measurements by MAGIC and other instruments. In Section 5.2.4, I summarize the systematic uncertainties of the observations. Several instrumental factors do not depend on the zenith angle, and their contribution to the systematic uncertainties can be taken from [28]. The precision of the atmospheric transmission measurements and the pointing accuracy of the telescopes do vary with the zenith angle. The corresponding systematic uncertainty in the [70°, 80°] range was already estimated in [140]. I have identified two additional sources of systematic uncertainties in this thesis. The effects of atmospheric refraction lead to a “squishing” effect of the recorded events, where events originating from larger zenith angles are reconstructed to slightly lower zenith angles. This effect starts to become noticeable above ∼ 60° (see Figure 5.33 and Figure 5.34) and causes an additional systematic uncertainty of 3-6% on the flux normalization. Another source of systematic uncertainty is the rapid increase of airmass across scales corresponding to the FOV of the MAGIC camera. This leads to different levels of LoNS brightness, translating into a variation of the camera acceptance across the FOV as shown in Figure 5.32. This effect needs to be considered during VLZA observations. While for point-source observations with the standard wobble offset, the effect is still minor, for extended sources observed at larger wobble distances, it should be taken into account.

By performing a detailed study on the flux variability in the analyzed data set on daily, weekly, and monthly timescales, I could confirm that the telescope system is stable over time and found that the part of systematic uncertainties that might vary over time do so on a scale of ∼ 12% above 1 TeV. Above 10 TeV this value increases to ∼ 25%. However, this could likely be an overestimation since the statistical errors of the data samples above 10 TeV are almost a factor of 3 larger than at lower energies, and the larger spread of the flux measurements, from which the systematic uncertainty is derived, might likely be dominated by statistical fluctuations. Under the assumption that the varying systematic uncertainty above 10 TeV is the same as for lower energies, I have evaluated the scale of variability in the observed data, which could be attributed to an intrinsic flux variability of the Crab Nebula itself. No significant variability was found, and I could place an upper limit on the flux variation of ∼ 15%. I have furthermore estimated the sensitivity of the observation towards potential gamma-ray flares. Given sufficient monitoring of the regular emission, a 50% increase of the flux, which lasts for 5 hours, would already be detectable at a 95% confidence level.

Figure 5.16 shows the performance of the gamma-hadron classification algorithm for all zenith and azimuth bins as a function of energy. At the lowest zenith angles, the classification still performs well and improves with higher energies. The latter behavior already starts to invert in the [62°,70°] zenith angle bin, where the classification becomes worse with increasing energy. The overall degradation of the gamma-hadron separation becomes most noticeable above 70°, where around 10% of the hadronic background survives cuts that select 95% of signal events, compared to the order of 1% of background surviving the same cut in the [50°,62°] range. Here, the classification suffers from the small numbers of pixels from the shower images due to the large distance between the EAS and the telescopes as explained in Section 5.2.3.2. The degradation of the background suppression at very large zenith angles provides the major limitation of this observational method. Considering the low rate of gamma rays at the highest energies, the large background poses a major challenge for signal extraction.

Observations in the range [75°, 80°] provide diminishing returns. All quantities that compose the IRF show a considerably worse performance compared to the [70°, 75°] range. The effective area of up to 4 km^2 could, in theory, provide a high sensitivity to the low fluxes of gamma rays beyond 100 TeV, but as Figure 5.16 shows, the gamma-hadron separation is the worst at these energies for this largest zenith angle range. Overall, this results in a differential flux sensitivity that can not compete with the performance achieved in a similar energy range at zenith angles between 50° and 75°. Therefore, while observations this close to the horizon are still possible and do provide meaningful results, more could be gained from focusing the data-taking at VLZA to below 75°.

5.6 Outlook

MAGIC observations at large zenith angles can provide valuable insight into the emission beyond tens of TeV of gamma-ray emitting sources. While air shower arrays are more sensitive at the highest energies and can detect this very-high to ultra-high energy emission more efficiently, they lack the superior energy and angular resolutions available to the IACT technique. Once CTAO is operational, it will provide unprecedented performance for the detailed study of this emission, but until then, MAGIC can provide competitive contributions to understanding the processes responsible for these gamma-ray signals by providing more details on the energy-dependent morphology of the sources in question. These are mostly extended sources spanning several degrees in diameter and typically have to be observed at larger wobble offsets than the standard 0.4°. In future observational campaigns at large zenith angles, special care needs to be taken to mitigate the effects of atmospheric refraction, which, as shown in Section 5.2.4.4, for point sources only adds a small systematic uncertainty, but for extended sources could potentially lead to a false reconstruction of their morphology. Since this effect is well-defined and consistent, if necessary, a method could be developed to correct it by applying a scale factor to the Y-coordinate of the reconstructed source position, which depends on the zenith angle and the corresponding size of atmospheric refraction. Furthermore, the background asymmetry described in Section 5.2.4.3 increases at larger wobble offsets, which are necessary to correctly reconstruct the large angular sizes of extended sources. This effect needs to be considered in the analysis. To gain valuable insight on the emission of PeVatron candidates at 100 TeV it would be desirable to further increase the sensitivity of MAGIC VLZA observations. The main obstacle here is the poor performance of the gamma-hadron classifier due to the use of a relatively large pixel size of 0.10° in the MAGIC cameras. While this is sufficient to resolve shower images from small to medium and large zenith angles, at VLZA this is not sufficient. Here, the images appear much smaller compared to lower zenith angle observations because the shower development happens at much greater distances from the telescopes. This could be improved by installing smaller PMTs, which would provide a higher resolution to the recorded images. This, however, would be a major effort and not worth it for an instrument as mature as MAGIC; it should be considered, however, if new instruments are being built that focus on observations at very large zenith angles. The existing observational setup can be approved by employing new methods to separate gamma-ray signals from a hadronic background. Efforts are ongoing to study how neural networks perform in this task. A large potential lies in the time profile of the recorded shower images. Hadronic air showers contain a large number of muons, which are expected to produce a short peaked signal prior to the main shower signal since they move faster than the speed of light of the Cherenkov photons produced in the shower. The larger the distance of the air shower from the telescopes, the larger this time separation becomes and could be detectable, provided the read-out window of the detector is large enough to contain both the muon and the main shower signal.

Even without these improvements, the current performance of the MAGIC Telescopes during observations above 50° Zd shows the great potential of contributing valuable insight into as-of-yet poorly understood sources. In the first catalog of gamma-ray sources published by the LHAASO collaboration [58], around one-third of the 90 sources do not have a known VHE source in their vicinity. Half of these are close to a HE source listed in the fourth catalog of the Fermi-LAT [40], eight are in the vicinity of a known pulsar or a SNR, and seven are "dark", meaning that no known potential gamma-ray emitter source is close by. Among the sources that are spatially coincident with or close to a known source in the TeVCat, the detection by LHAASO calls for further observations to resolve the emission region in greater detail in space and energy, especially since several of these sources show emission beyond 100 TeV, making them strong PeVatron candidates.

In the following, I present some examples to illustrate the potential of large and very large zenith angle observations with MAGIC in regard to these sources.

The source 1LHAASO J1814-1719u is detected by the WCDA and KM2A of LHAASO. In

the WCDA data, covering an energy range of 1 − 25 TeV, the region has an extension of 0.71°. In the KM2A data, which is analyzed in the energy range between 25 TeV and 1.6 PeV, the source is a point-source for LHAASO and is detected above 100 TeV with a TS value of 41. A second close-by source, 1LHAASO J1814-1636u, has been identified by LHAASO. It is detected by the KM2A with a TS value of 50 above 100 TeV. It has an extension of 0.68° [58]. Both of these sources can be associated with a point-source listed in the second HAWC catalog. 2HWC J1814-173 is at a distance of 0.16° and 0.72° from 1LHAASO J1814-1719u and 1LHAASO J1814-1636u, respectively. A potential further association could be a source HESS J1813-178 which was detected during the H.E.S.S. Galactic Plane Survey (HGPS) and identified as a composite SNR/PWN with a hard spectral index of ~ 1.64 [101]. The LHAASO collaboration further mentions two SNRs in the vicinity as well as an unidentified GeV source detected by Fermi-LAT (4FGL J1816.2-1654c).
Figure 5.45 shows the power law spectra for these two sources together with the MAGIC differential flux sensitivity obtained in Section 5.2.2.6 and the best-fit Crab Nebula spectrum from my analysis in Section 5.2.2.7. From this, it becomes clear that MAGIC could help to disentangle the two LHAASO sources from each other and the HAWC source with its superior angular resolution. A detailed reconstruction of the SED up to ~ 100 TeV is achievable within reasonable observation times of 50-100 h. MAGIC observations at large zenith angles could help pinpoint the origin of the emission beyond 100 TeV detected by LHAASO and provide valuable insight into this interesting PeVatron candidate.

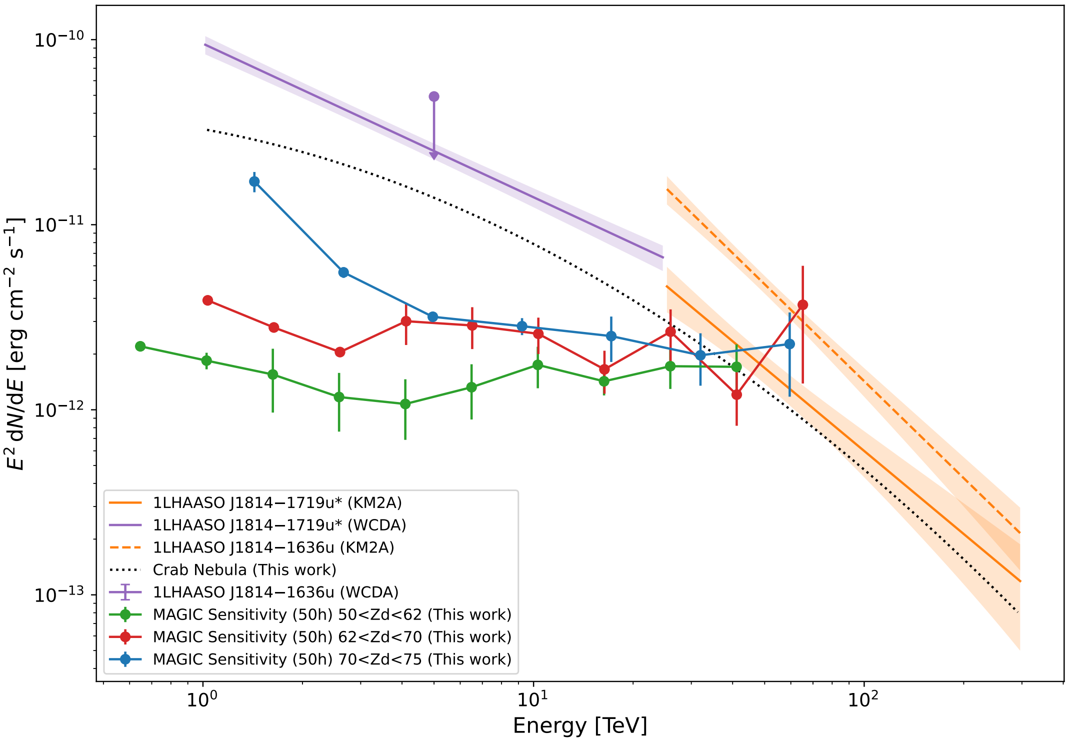

Figure 5.45: The SED of 1LHAASO J1814-1719u (solid lines) and 1LHAASO J1814-1636 (Upper Limit and dashed line) from the LHAASO catalog [58]. The spectral parameters observed by the WCDA are shown in purple, orange lines show the spectra observed by the KM2A. For comparison, the spectrum of the Crab Nebula with the best-fit parameters obtained in Section 5.2.2.7 is shown in black. The MAGIC differential flux sensitivity for 50 h of observations in the zenith angle ranges [50°,62°] (green), [62°,70°] (red), [70°,75°] (blue) which were obtained in Section 5.2.2.6 are shown.

1LHAASO J1843-0335u is another unidentified source in the LHAASO catalog, coincident with the HGPS source HESS J1843-033. In the KM2A data, the source shows a bright emission above 100 TeV with a TS value of 295. Its extension is 0.36° and 0.4° in the KM2A

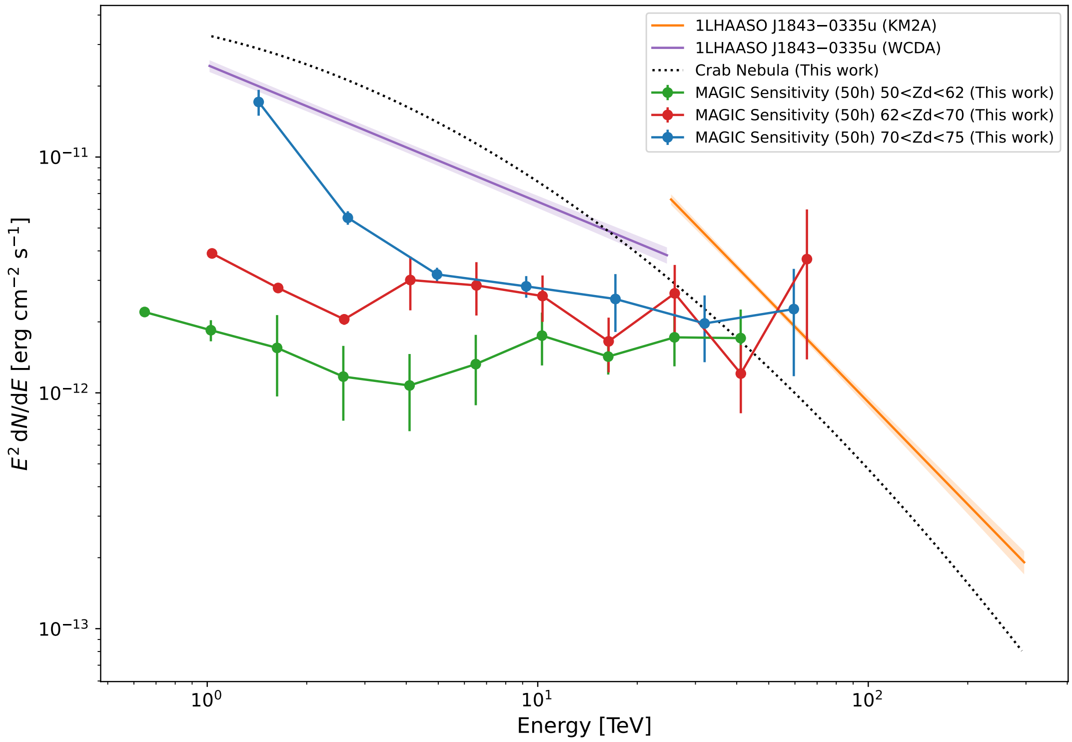

Figure 5.46: The SED of 1LHAASO J1843-0335u from the LHAASO catalog [58]. The spectral parameters observed by the WCDA are shown in purple, orange lines show the spectra observed by the KM2A. Crab Spectrum and MAGIC sensitivity curves are the same as in Figure 5.45.

and WCDA data, respectively. The nature of the observed emission is unclear. Figure 5.46 shows the spectra as listed in the LHAASO catalog together with the MAGIC sensitivity and the Crab Nebula spectrum obtained in previous sections. A mismatch between the two LHAASO components is evident. MAGIC observations at large zenith angles of this source could contribute to a more precise reconstruction of the emission at tens of TeV up to $\sim 100\,\text{TeV}$. A more detailed view of the morphology and SED at the highest energies would complement the existing data from H.E.S.S. and LHAASO and could help understand the origin of the emission of this bright PeVatron candidate.

Another interesting PeVatron candidate in the LHAASO catalog is 1LHAASO J1839-0548u. This source was already among the first 12 sources exhibiting emission beyond 100 TeV published by LHAASO in 2021 [59], where it was denoted as LHAASO J1839-0545 with a best-fit position 0.17° away from the position listed now in the catalog. 1LHAASO J1839-0548u has an extension of 0.22° in both WCDA and KM2A data and is detected above 100 TeV with a TS value of 127 by the KM2A. There is no other known counterpart in HE or VHE gamma rays. The pulsar PSR J1838-0537 lies at a distance of 0.2° from the source, and PSR J1837-0604 is 0.62° away from the original position of the source LHAASO J1839-0545. The potential of these two pulsars to power the gamma-ray emission observed by LHAASO has been discussed in [75]. An association of the gamma-ray emission with IC processes by electrons originating from either of the two pulsars is possible and would imply a maximum energy of the electrons of 2.8 PeV and 4.9 PeV for PSR J1837-0604 and PSR J1838-0537, respectively.

Figure 5.47 shows the two spectral components observed by LHAASO together with the MAGIC sensitivity as described above. The source can be studied from a few TeV to $\sim$ 100 TeV within 50-100 h of observations. Resolving the SED more precisely and gaining more detailed information on the spatial distribution of the emission profiting from MAGIC

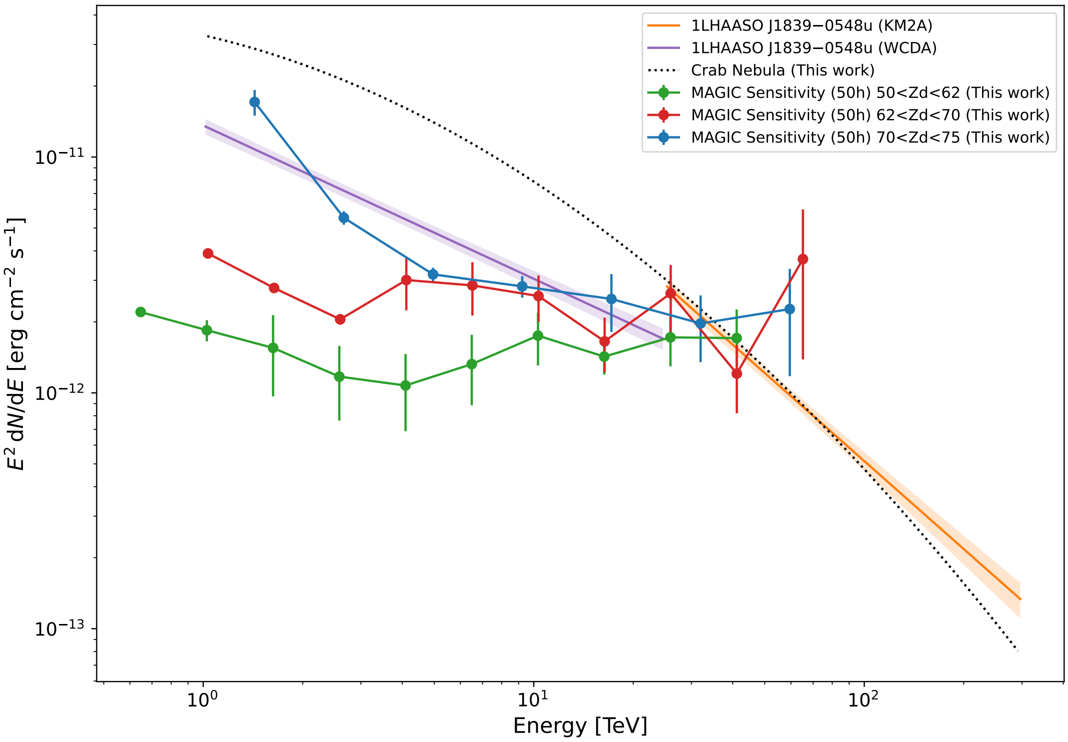

Figure 5.47: The SED of 1LHAASO J1839-0548u from the LHAASO catalog [58]. The spectral parameters observed by the WCDA are shown in purple, orange lines show the spectra observed by the KM2A. Crab Spectrum and MAGIC sensitivity curves are the same as in Figure 5.45.

observations at large zenith angles could help to confirm the hypotheses of a pulsar being responsible for the emission. This could give important insight into the contributions of PWN to the overall PeVatron population.

The examples given here illustrate how LHAASO has extended our view of the gamma-ray sky to energies beyond 100 TeV but also show the limitations of LHAASO observations. Due to the limited angular resolution of the instrument, it is difficult to disentangle partly overlapping emission regions or clearly connect them to previously observed sources. Especially at the highest energies, this is of utmost importance in the quest to find the sources that are capable of accelerating CRs to PeV energies. The capability of MAGIC to provide observations of high energy and spatial resolution up to 100 TeV provides an important tool to solve this pressing question in the pre-CTAO era.

Chapter 6

Conclusion

The origin of Cosmic Rays (CRs) is one of the most fundamental open questions in the field of astroparticle physics. The spectrum of CRs measured on Earth exhibits several distinct features attributed to changes in their source population and propagation. At least up to energies of the so-called *knee* at $\sim 3\,\mathrm{PeV}$, CRs are assumed to be produced within the Milky Way galaxy. Astrophysical sources which are capable of accelerating charged particles up to these energies are called *PeVatrons*. Supernova Remnants (SNRs) have long been the most popular type of source deemed to exhibit the conditions in which such efficient particle acceleration can take place, but the lack of observational evidence for such has motivated the community to increasingly look beyond this *Supernova Remnant Paradigm*. Active star-forming regions (SFRs) and superbubbles are such alternative PeVatron candidates as they can exhibit strong stellar winds and supernova explosions, creating multiple colliding shocks that are potentially capable of efficient CR acceleration. PWNe are other interesting candidates since it has been shown that large numbers of electron/positron pairs are produced in the pulsar magnetospheres and subsequently efficiently accelerated in the termination shock created by the interaction of the pulsar wind with the surrounding SNR. PWN are generally considered to be purely leptonic sources. The Crab Nebula stands out as the best-studied and most energetic PWN and the only undoubtedly confirmed PeVatron, shown by the detection of gamma-ray emission up to PeV energies. Gamma-ray astronomy plays a significant role in the identification of PeVatrons. Gamma rays are produced in the interactions of CRs and leptons with ambient magnetic or radiation fields and/or molecular gas. Unlike charged particles, gamma rays propagate to Earth undeflected by interstellar magnetic fields and allow us to identify the source of origin by reconstructing their incident direction. The study of the spectral energy distribution (SED) of the gamma rays observed from a given source can then enable us to deduct by which mechanism they have been produced. It can also reveal the maximum energy of the particle population that is responsible for the observed gamma-ray emission. If protons with PeV energies are present in the source, the observed gamma-ray spectrum should extend to energies of $100\,\mathrm{TeV}$ and beyond. If the underlying emission process is leptonic, the conversion between lepton energy and corresponding gamma-ray energy is closer to one, requiring the detection of a PeV gamma-ray signal to identify the source as a leptonic PeVatron. For the Crab Nebula, this has been achieved by the LHAASO collaboration, confirming the source to be accelerating electrons up to PeV. The LHAASO observatory has an unprecedented sensitivity for gamma-ray observations beyond $100\,\mathrm{TeV}$ and has presented a catalog of sources that were detected at these energies and which are, therefore, promising PeVatron candidates. It is, however, difficult to determine the precise nature of these sources and whether the emission is produced by leptons or hadronic CRs due to the limited angular and energy resolution air shower arrays such as LHAASO can provide. Imaging Atmospheric Cherenkov Telescopes (IACTs) detect gamma rays via the Cherenkov light, which is produced by charged particles created in the Extensive Air Showers (EAS) generated in the interaction of gamma rays with nuclei in the atmosphere. This detection technique yields higher precision in the directional and energy reconstruction of the primary gamma-ray compared to air shower detectors. The effective detection area of the current generation of telescope systems, which consist of only a small number of telescopes spread across a small area, is limited by the size of the surface on the ground illuminated by the Cherenkov light, which is $< 0.1\,\mathrm{km}^2$ for standard observations. This makes it difficult for IACTs to significantly detect the low gamma-ray fluxes at tens of TeV up to hundreds of TeV. The next generation of IACTs, the Cherenkov Telescope Array Observatory (CTAO), will mitigate this shortcoming by constructing large telescope arrays consisting of many telescopes spread across several square kilometers. With the currently operating MAGIC Telescopes, a system of two IACTs, a similar increase in the effective area can be achieved by extending the observation to large zenith angles. Under these conditions, the increased thickness of the atmosphere leads to a longer path length between the first interaction of the gamma-ray with the atmosphere and the ground. The EAS develops at larger distances from the telescopes and the area illuminated by Cherenkov light on the ground increases dramatically. Observations at large zenith angles thus increase the sensitivity of MAGIC at the highest energies.

In this thesis, I have performed the first complete study of the performance of the MAGIC Telescopes during point-source observations in the zenith angle range between 50° and 80°. I have determined the dependency of the energy threshold of the observations as a function of zenith angles, which differs from the previously derived function for lower zenith angles. I found that the IRF remains quite stable up to 75° and does not depend on the azimuth angle of the observations. The latter had been suspected since, especially at zenith angles beyond 70°, the differences in the effective baseline between the telescopes could affect the quality of the stereoscopic event reconstruction. I did, however, find that special care should be taken in this regard when matching the MCs used in the analysis with the observational data. Observations above 75° Zd provide diminishing returns, as I could show that the angular resolution and energy resolution are considerably worse for these zenith angles, and the large effective area can not make up for this worsened performance. The largest current limitation and, at the same time, the largest possibility for improvements to the sensitivity at large zenith angles is the gamma/hadron separation. Starting already noticeably at zenith angles beyond 62°, it worsens with increasing zenith angle and energy due to the progressively small geometrical sizes of the recorded shower images. There is potential in the analysis of the recorded shower images to improve the separation of gamma-ray signal from hadronic background. New classification methods based, for example, on neural networks or incorporating the timing information of the signal could lead to significant improvements in this regard. I have determined the differential sensitivity of MAGIC at observations above 50° Zd and have found that it is a continuation of MAGIC observations at low and medium zenith angles on similar scales and reaches values comparable to the future northern array of CTAO at tens of TeV. The measured spectral energy distribution extends to 100 TeV and matches previous observations by MAGIC and other instruments. I have studied the systematic errors of large zenith angles, identifying two aspects only arising at zenith angles above $\sim 60°$, and updated scales of the uncertainty on the energy scale and flux normalization. With a detailed study of the flux variability, I quantified the scale at which systematic errors might vary over time and provided upper limits on the intrinsic flux variability of the Crab Nebula. I have also determined the sensitivity of detecting gamma-ray flares above 10 TeV of various durations and sizes.

This thesis can be seen as a reference for the planning of future observations of PeVatron candidates with MAGIC. With the presented performance, it will be possible to predict the anticipated performance depending on the specific scientific goal of the observations, be it measuring the highest-energetic emission of a source or studying its energy-dependent morphology at tens of TeV in detail. Overall the presented performance at large zenith angles shows that MAGIC can contribute to the study of PeVatron candidates and help to shed light on their nature. Together with other existing gamma-ray observatories, MAGIC observations will help solve the mystery of the origin of cosmic rays.

Appendix A

Additional Material for Chapter 5

A.1 Data Quality Selection

This section provides additional information on the data quality selection described in Section 5.2.1. Table A.1 lists a summary of the selection cuts that have been applied on the VLZA data set.

Table A.1: Summary of the data quality selection cuts for the Crab Nebula data above 70° described in Section 5.2.1. The cuts are listed for all five analysis periods, separately for the Rise and Set sample, each of the two zenith bins and each of the two wobble positions. $T_{12\mathrm{km}}$ refers to the atmospheric transmission at an altitude of 12 km as measured by the LIDAR. The L3 Rate is the event rate passing the Level 3 Trigger (see Section 4.1.4). NumStars refers to the number of stars identified by the starguider camera (Section 4.1.5). The observation time in hours before and after applying these cuts is listed as well.

	Rise				Set			
	70-75		75-80		70-75		75-80	
	W1	W2	W1	W2	W1	W2	W1	W2
	ST.03.06							
$T_{12\mathrm{km}}$	-	-	-	-	0.6	0.6	0.6	0.6
L3 Rate [Hz]	-	-	-	-	40-400	40-400	20-300	20-300
NumStars	-	-	-	-	13	13	12	13
t_{obs} [h]	-	-	-	-	5.2	2.9	4.0	4.7
$t_{\mathrm{after\ cuts}}$ [h]	-	-	-	-	5.1	2.6	3.6	4.2
	ST.03.07/09							
$T_{12\mathrm{km}}$	0.6	0.6	0.6	0.6	0.6	0.6	0.6	0.6
L3 Rate [Hz]	60-700	50-600	20-600	20-600	60-250	60-250	20-200	20-200
NumStars	15	20	12	15	13	11	12	12
t_{obs} [h]	4.2	5.0	4.3	3.9	12.0	11.8	12.5	13.2
$t_{\mathrm{after\ cuts}}$ [h]	3.4	4.2	3.3	2.6	9.7	9.9	10.5	10.3
	ST.03.10							
$T_{12\mathrm{km}}$	0.5	0.6	0.5	0.5	-	-	-	-
L3 Rate [Hz]	40-220	40-220	40-220	40-220	-	-	-	-
NumStars	10	10	5	10	-	-	-	-
t_{obs} [h]	2.6	3.1	4.0	2.2	-	-	-	-
$t_{\mathrm{after\ cuts}}$ [h]	2.3	3.0	3.8	2.1	-	-	-	-
	ST.03.11							
$T_{12\mathrm{km}}$	0.6	0.5	0.5	0.6	0.6	0.5	0.6	0.5
L3 Rate [Hz]	40-180	40-250	20-180	20-180	20-250	80-220	20-180	20-180
NumStars	5	5	2	10	5	5	10	10
t_{obs} [h]	0.7	1.6	2.1	0.5	2.1	4.2	3.2	3.1
$t_{\mathrm{after\ cuts}}$ [h]	0.7	1.6	2.1	0.5	2.1	4.2	3.0	3.1
	ST.03.12							
$T_{12\mathrm{km}}$	0.5	0.6	0.5	0.5	0.6	0.5	0.6	0.6
L3 Rate [Hz]	20-250	10-250	20-120	20-180	50-250	20-250	10-120	10-250
NumStars	5	5	12	5	5	5	-	5
t_{obs} [h]	4.6	4.8	4.7	1.8	2.3	2.3	1.3	2.3
$t_{\mathrm{after\ cuts}}$ [h]	3.4	4.4	3.4	1.5	2.2	1.8	0.9	2.1

A.2 Angular Resolution

The following figures show the individual exponential fits to the θ^2-distributions in each energy bin for each zenith sample, and – for VLZA data – additionally for each azimuth sample both for the *standard azimuth splitting* (Figures A.3 to A.5) and the *baseline azimuth splitting* (Figures A.8 to A.9).

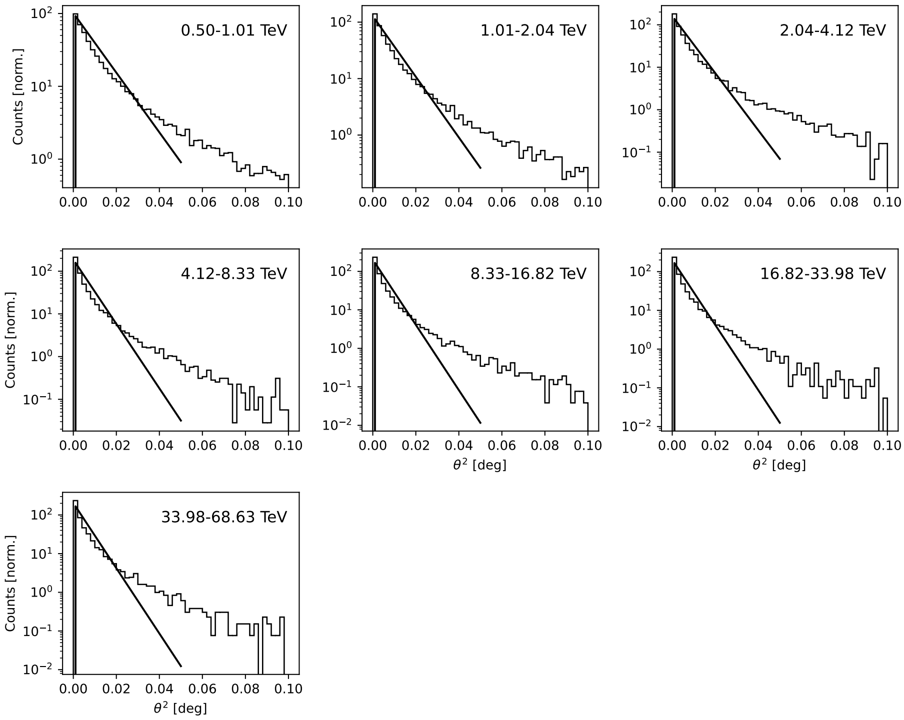

Figure A.1: Exponential fit to the θ^2 distribution in each energy bin of the [$50°$, $62°$] sample.

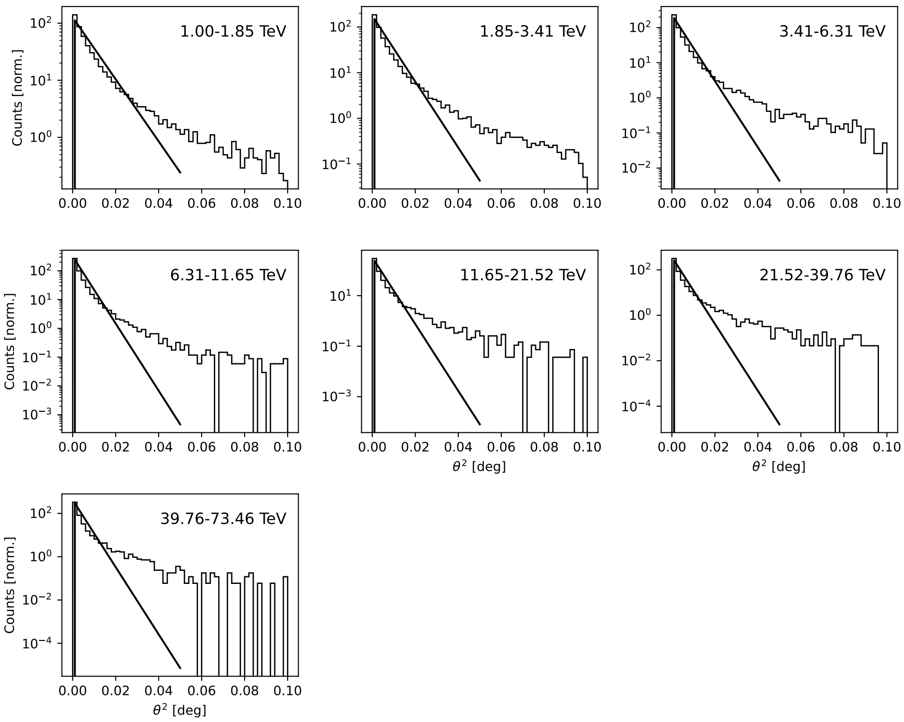

Figure A.2: Exponential fit to the θ^2 distribution in each energy bin of the $[62^\circ,\, 70^\circ]$ sample.

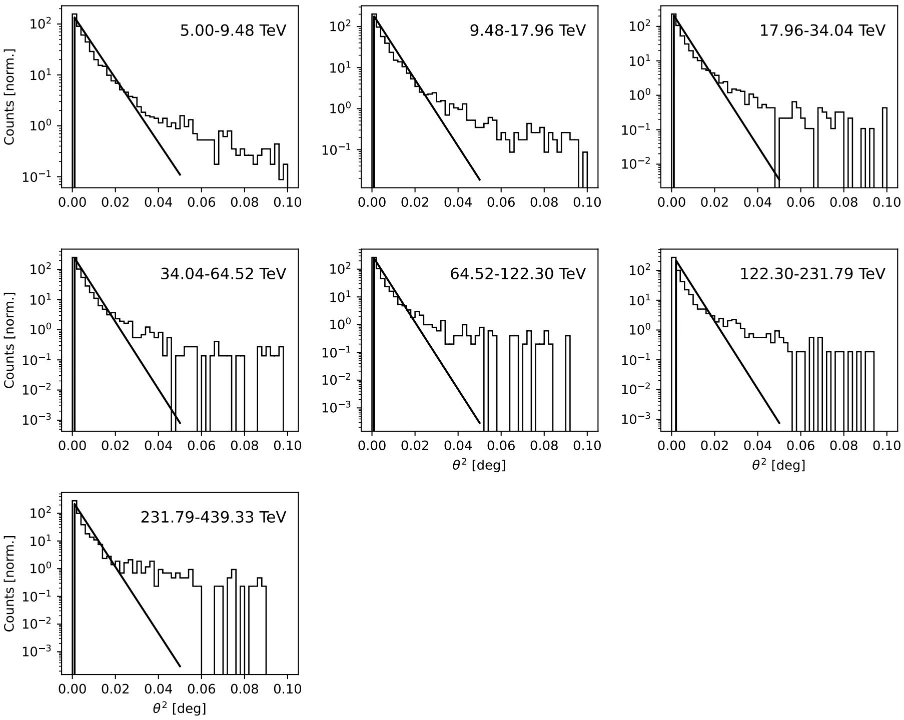

Figure A.3: Exponential fit to the θ^2 distribution in each energy bin of the $[70^\circ,\, 75^\circ]$ Rise sample *standard azimuth splitting*.

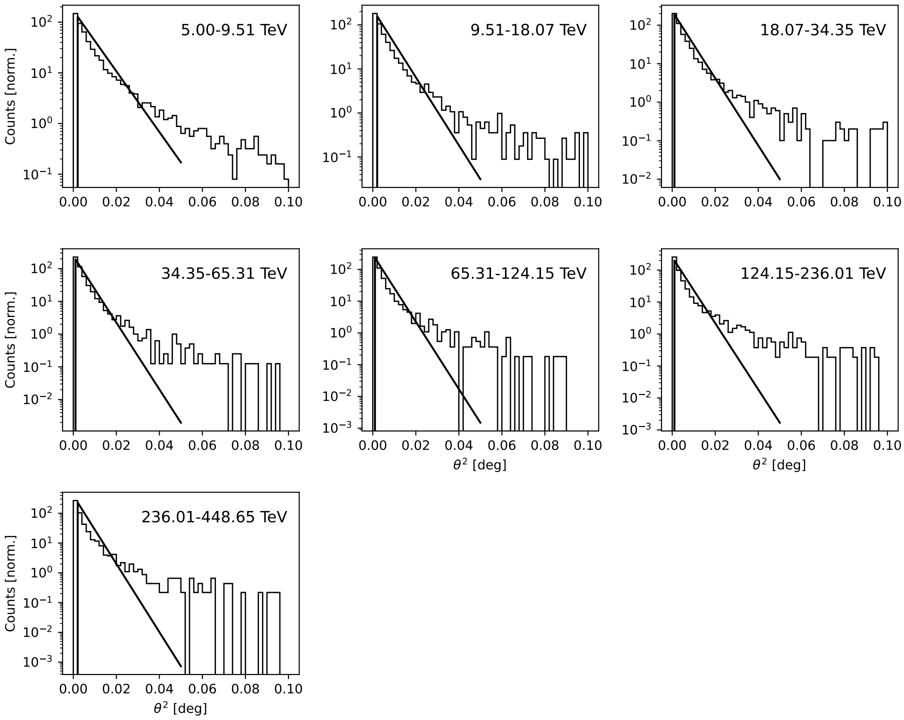

Figure A.4: Exponential fit to the θ^2 distribution in each energy bin of the $[70°,\ 75°]$ Set sample *standard azimuth splitting*.

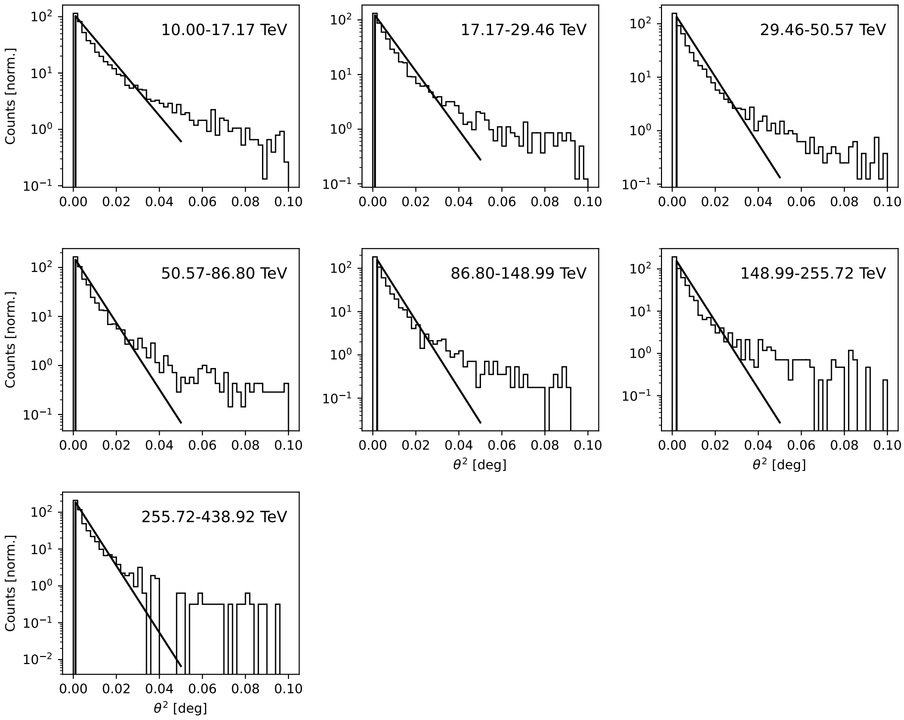

Figure A.5: Exponential fit to the θ^2 distribution in each energy bin of the $[75°,\ 80°]$ Rise sample *standard azimuth splitting*.

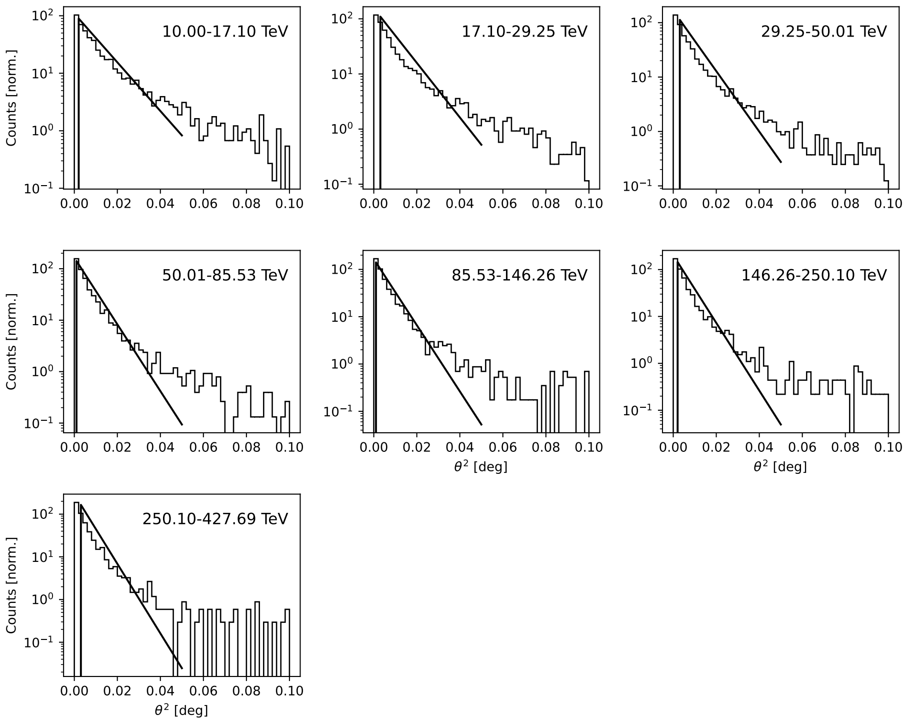

Figure A.6: Exponential fit to the θ^2 distribution in each energy bin of the $[75°,\ 80°]$ Set sample *standard azimuth splitting*.

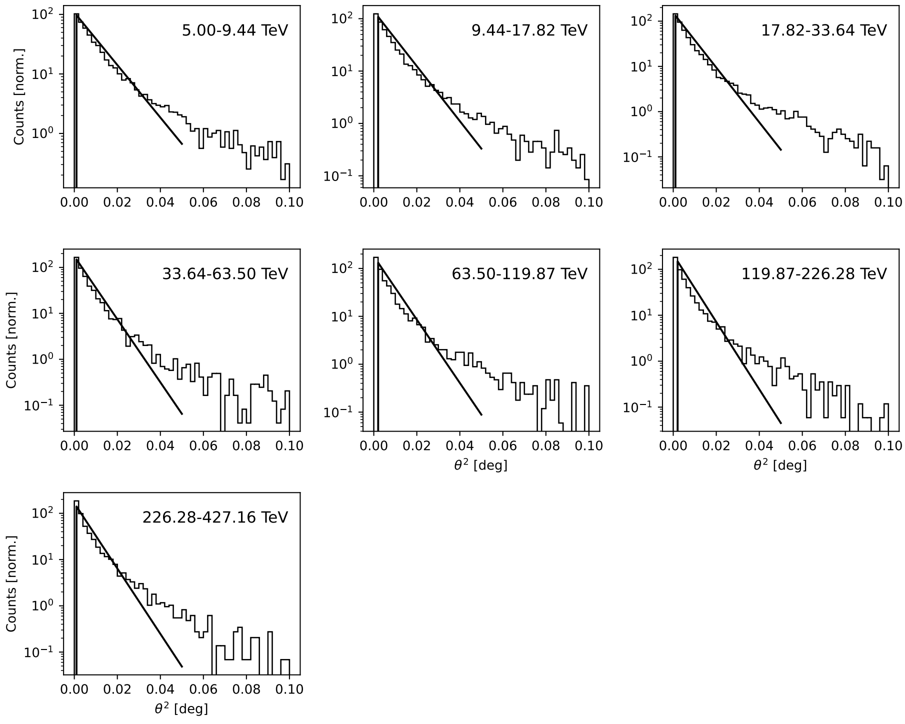

Figure A.7: Exponential fit to the θ^2 distribution in each energy bin of the $[70°,\ 75°]$ Rise sample and *baseline azimuth splitting*.

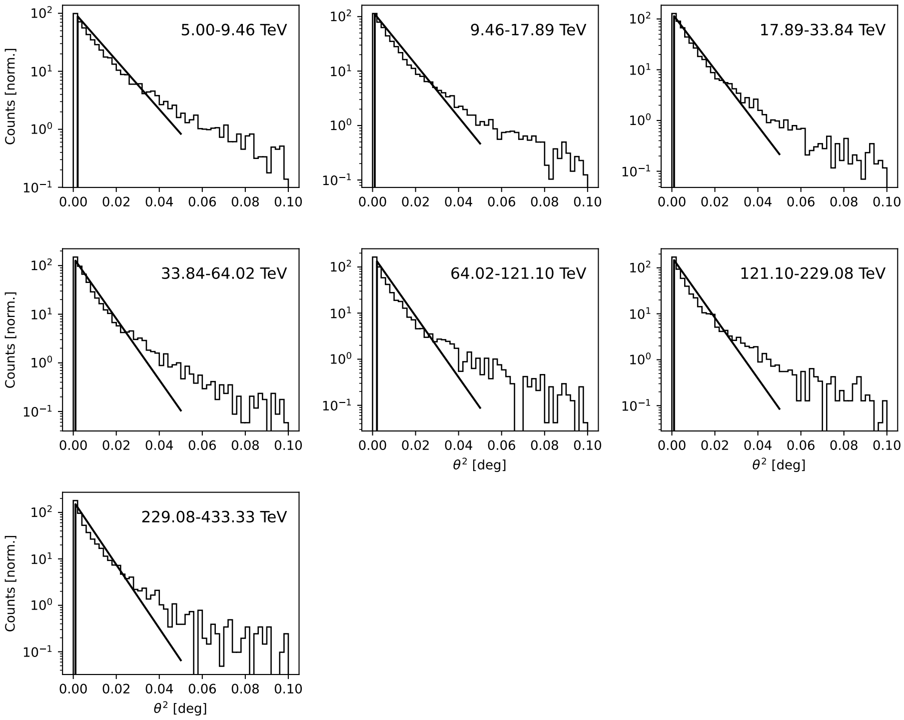

Figure A.8: Exponential fit to the θ^2 distribution in each energy bin of the $[70°,\ 75°]$ Set sample and *baseline azimuth splitting*.

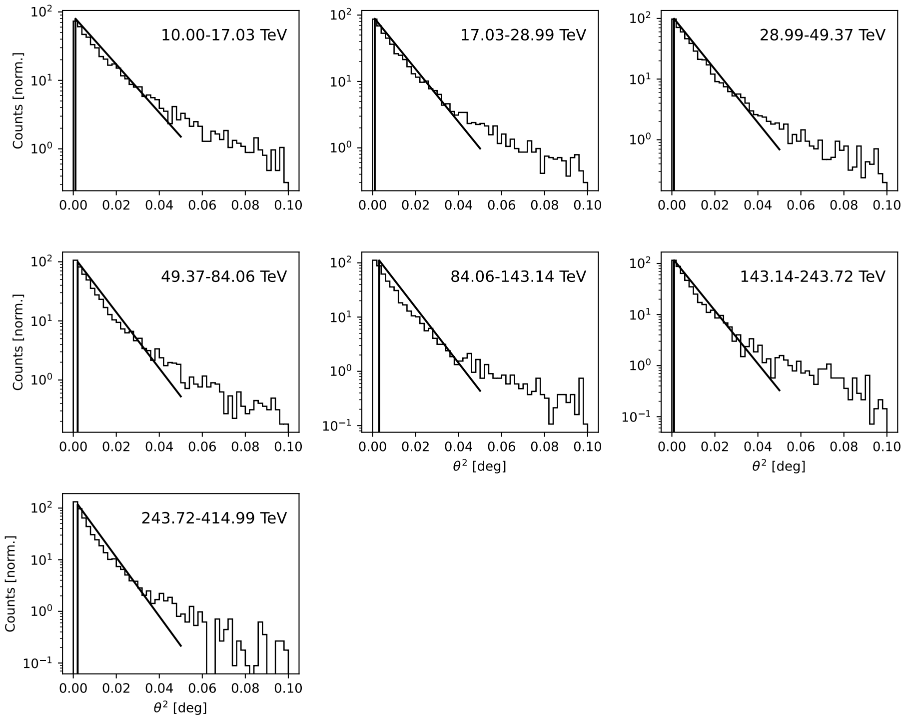

Figure A.9: Exponential fit to the θ^2 distribution in each energy bin of the $[75°,\ 80°]$ Rise sample and *baseline azimuth splitting*.

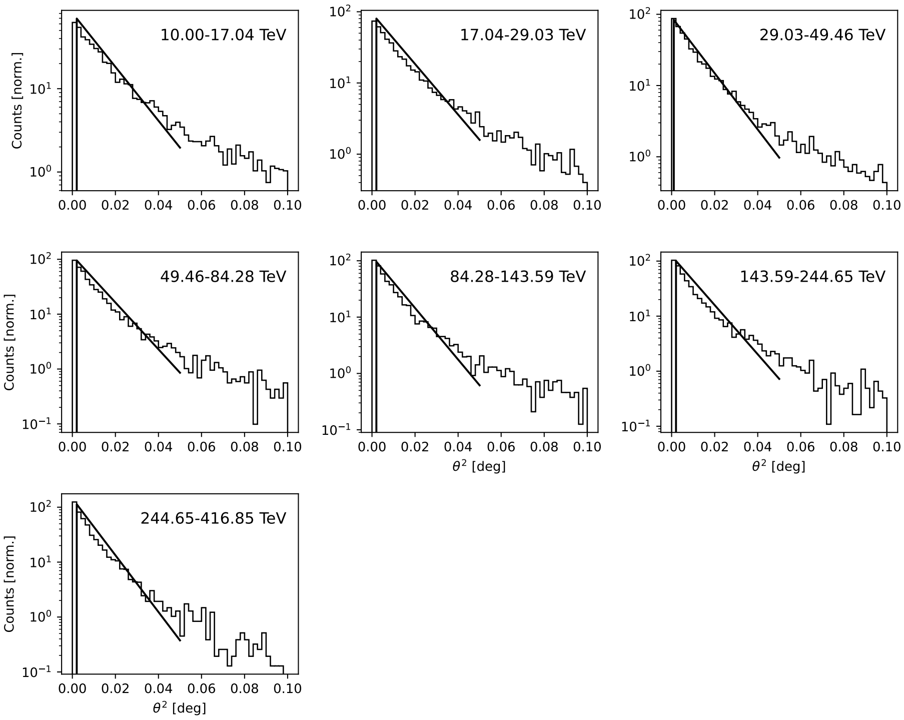

Figure A.10: Exponential fit to the θ^2 distribution in each energy bin of the $[75°, 80°]$ Set sample and *baseline azimuth splitting*.

A.3 Height of shower maximum

Figure A.11 complements the discussion of the distance between EAS and the telescopes described in Section 5.2.3.1. It shows the distributions of the reconstructed height of the shower maximum for different zenith angles and energy ranges. The figure shows that showers penetrate deeper into the atmosphere with increasing energy of the primary particle, which can be seen by comparing the distributions of one zenith angle bin between the different energy ranges. Within one energy range, the distributions of the shower maximum height of showers with incident directions at larger zenith angles are broader and extend to higher altitudes.

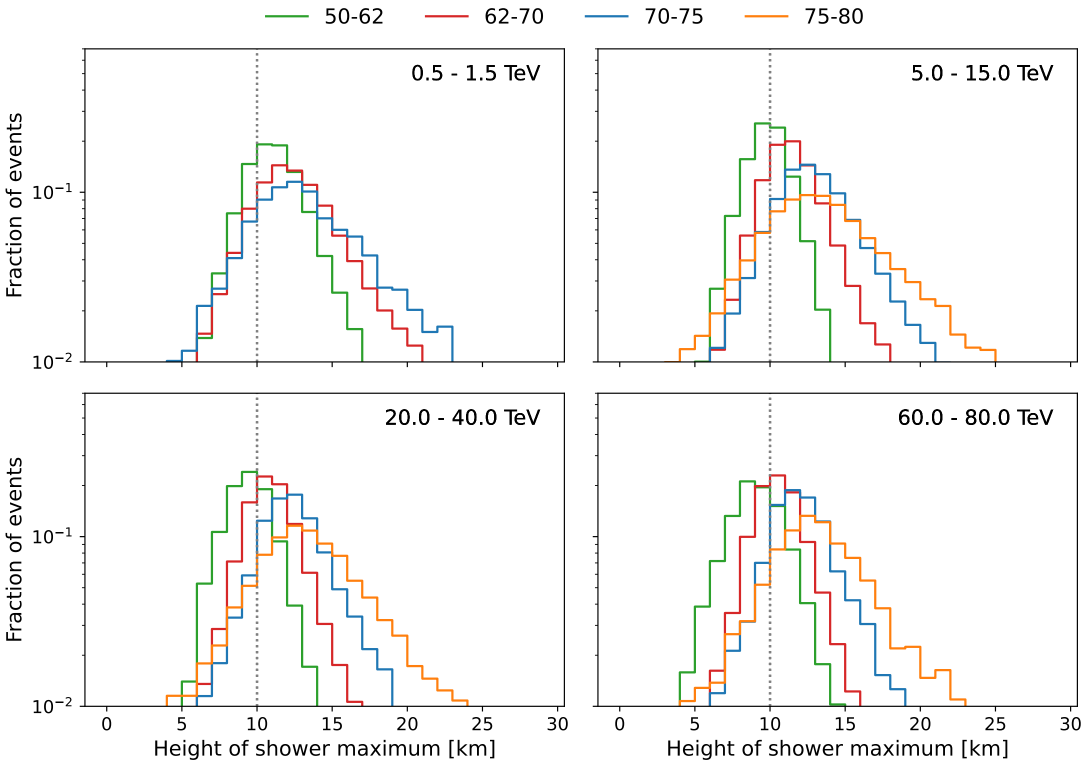

Figure A.11: The height of the shower maximum in selected energy bins for different zenith angles.

A.4 Variability

This section contains supplementary information on the variability study presented in Section 5.3. Figures A.12 to A.16 illustrate the bins that have been selected to produce the light curves of different minimum energy and bin widths. Each data point in these plots shows the effective area (y-axis) and effective time (x-axis) of the specific bin. Selected bins are shown as green points. Bins that have been deselected due to low exposure are shown as blue crosses, and bins for which only flux upper limits are calculated are shown as orange stars.
The figures A.17 to A.19 show the light curves that have been produced analogously to figures 5.38 and 5.39. The values quantifying the variability obtained from these lightcurves are listed in Table 5.5. Figure A.20 and Figure A.21 show the simulated light curves and fractional variation analogously to Figure 5.40 and Figure 5.41 but for 30-day bins.

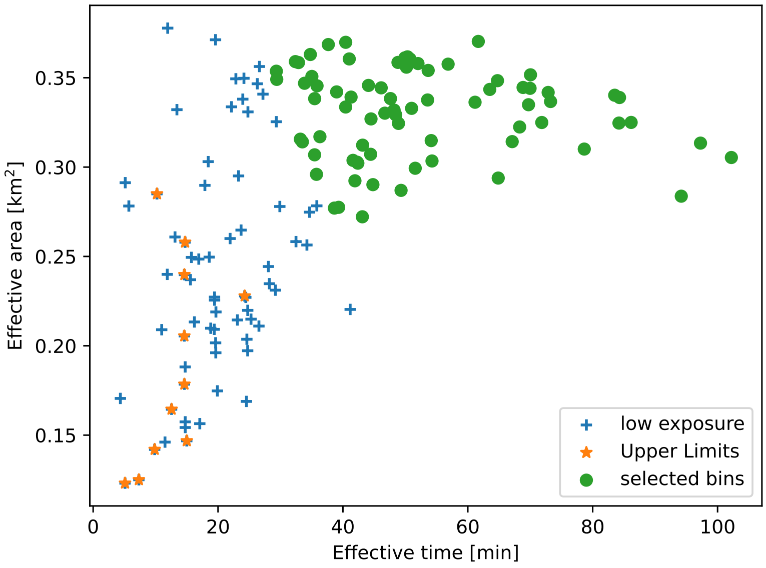

Figure A.12: Selection of bins for the Variability study based on the minimum required exposure for the 1-day binned light curve with $E_{\min} = 1\,\mathrm{TeV}$.

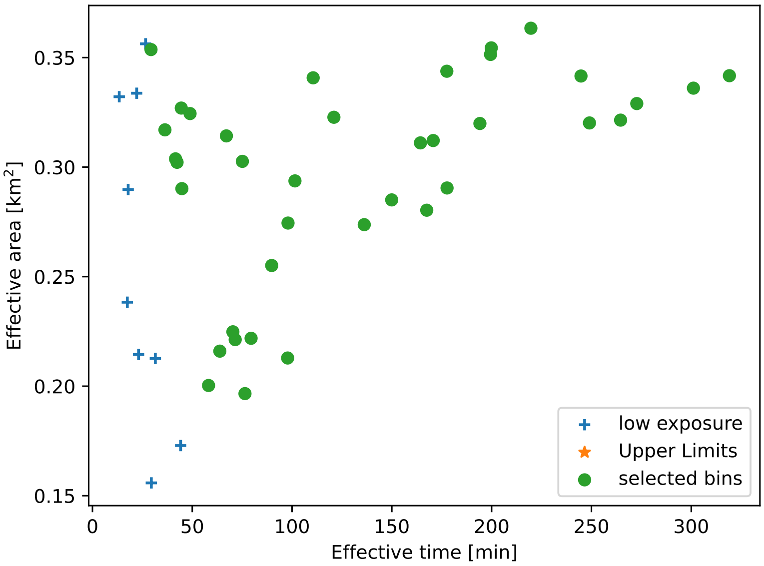

Figure A.13: Selection of bins for the Variability study based on the minimum required exposure for the 7-day binned light curve with $E_{\min} = 1\,\mathrm{TeV}$.

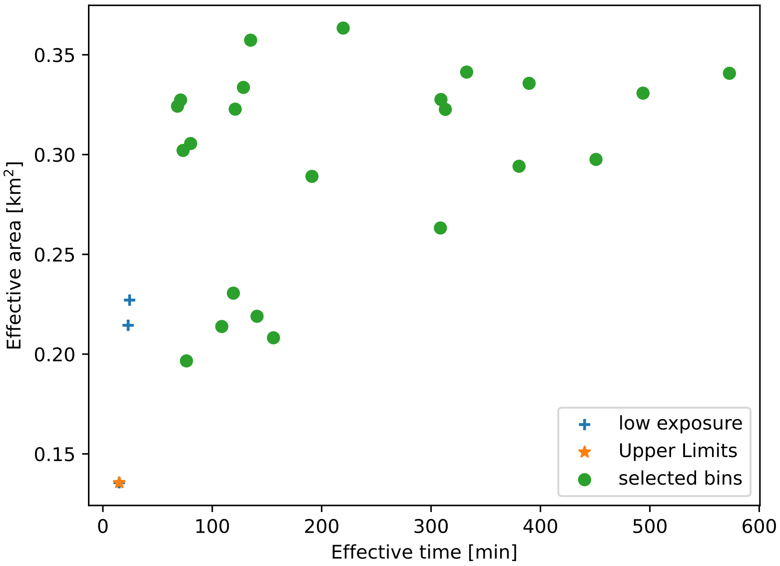

Figure A.14: Selection of bins for the Variability study based on the minimum required exposure for the 30-day binned light curve with $E_{\min} = 1\,\mathrm{TeV}$.

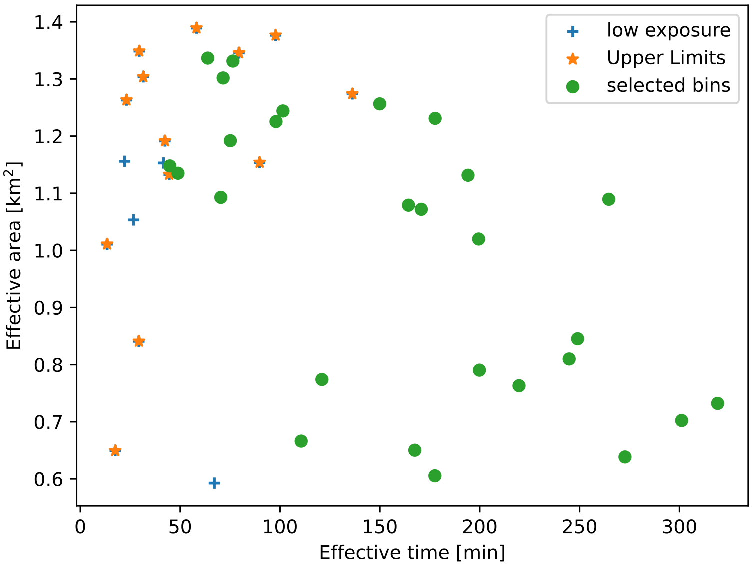

Figure A.15: Selection of bins for the Variability study based on the minimum required exposure for the 7-day binned light curve with $E_{\mathrm{min}} = 10\,\mathrm{TeV}$.

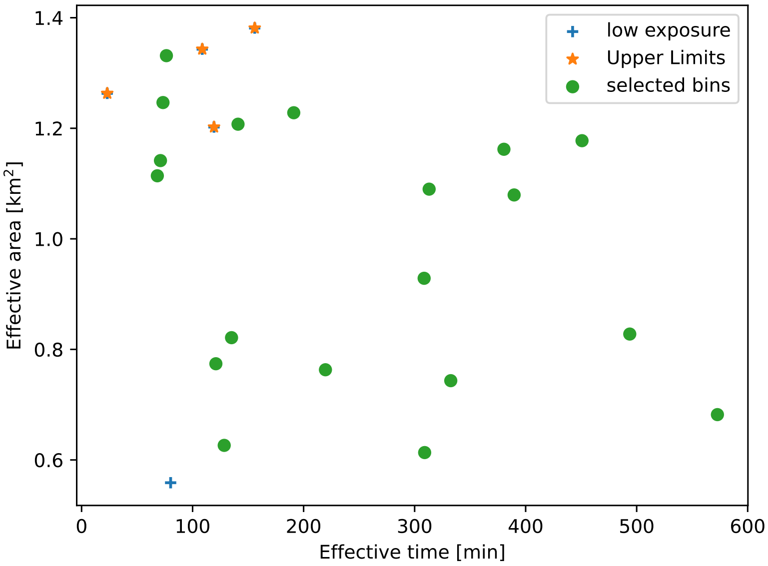

Figure A.16: Selection of bins for the Variability study based on the minimum required exposure for the 30-day binned light curve with $E_{\mathrm{min}} = 10\,\mathrm{TeV}$.

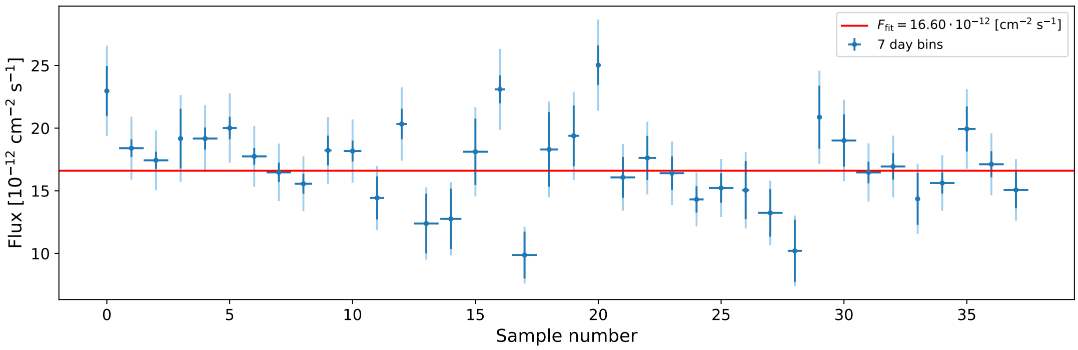

Figure A.17: Integrated flux above 1 TeV for data samples with an average of ~ 2.2 h effective observation time. Dark blue vertical error bars represent statistical uncertainties only; the light blue shaded extensions represent the total error with the estimated systematic uncertainty of 13% added in quadrature. The red line shows the constant fit to the flux values.

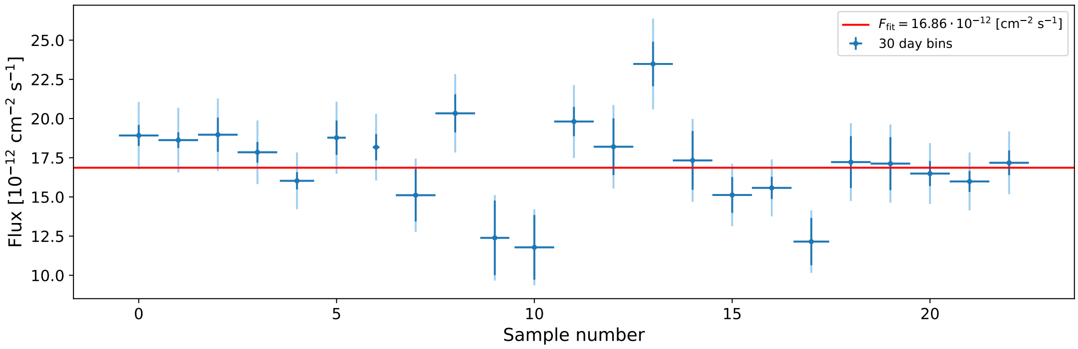

Figure A.18: Integrated flux above 1 TeV for data samples with an average of ~ 4 h effective observation time. Dark blue vertical error bars represent statistical uncertainties only; the light blue shaded extensions represent the total error with the estimated systematic uncertainty of 11% added in quadrature. The red line shows the constant fit to the flux values.

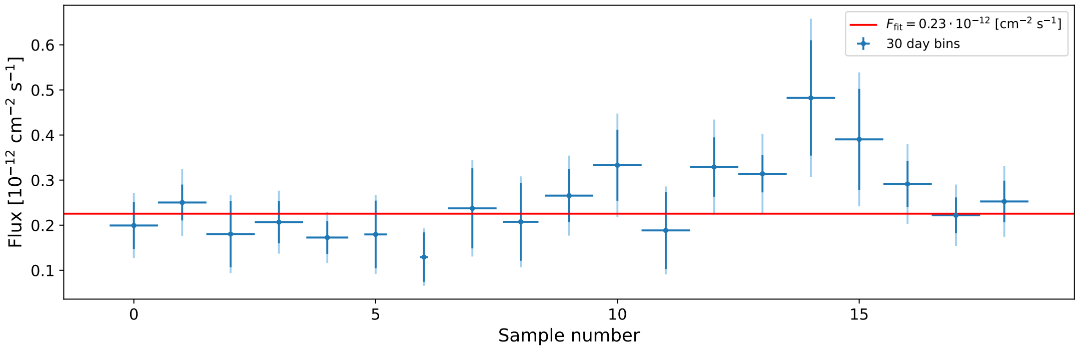

Figure A.19: Integrated flux above 10 TeV for data samples with an average of ~ 4 h effective observation time. Dark blue vertical error bars represent statistical uncertainties only; the light blue shaded extensions represent the total error with the estimated systematic uncertainty of 25% added in quadrature. The red line shows the constant fit to the flux values.

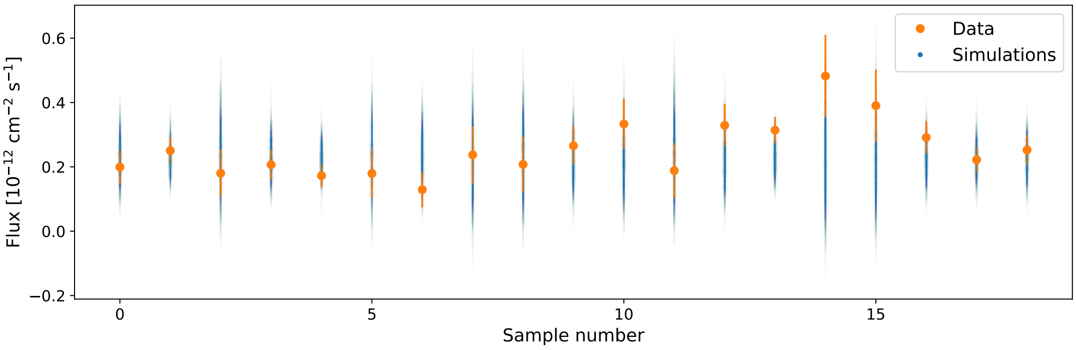

Figure A.20: Observed light curve and a subsample of simulated light curves for 30-day binning.

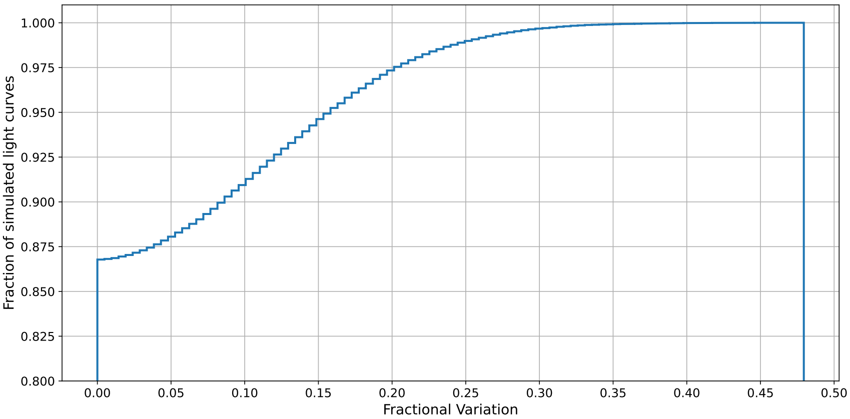

Figure A.21: Cumulative distribution of the fractional variation calculated from the simulated light curves for 30-day binning. Where F_{var} was ill-defined because $\delta^2 < \sigma^2$, F_{var} has been set to zero.

A.5 Differential Flux Sensitivity

This section provides supplementary information to the sensitivity curves derived in Section 5.2.2.6. The tables below list the precise values of the sensitivity curves shown in figures 5.23 and 5.43.

Table A.2: The MAGIC differential flux sensitivity in the zenith angle range [50°, 62°] as shown in Figures 5.23 and 5.43. The Sensitivity is given in percent of the Crab Nebula flux (C.U.) and in units of energy flux.

E_{min} [TeV]	E_{max} [TeV]	Sensitivity [% C.U.]	Sensitivity $[10^{-12}\,\text{erg}\,\text{cm}^{-2}\,\text{s}^{-1}]$
0.50	0.79	3.92 ± 0.15	2.20 ± 0.08
0.79	1.26	3.94 ± 0.40	1.84 ± 0.19
1.26	1.99	4.16 ± 1.57	1.55 ± 0.58
1.99	3.16	4.12 ± 1.44	1.17 ± 0.41
3.16	5.02	5.15 ± 1.85	1.07 ± 0.39
5.02	7.96	9.05 ± 2.99	1.32 ± 0.44
7.96	12.63	17.77 ± 4.49	1.75 ± 0.44
12.63	20.04	22.47 ± 3.62	1.42 ± 0.23
20.04	31.79	43.89 ± 10.82	1.72 ± 0.42
31.79	50.43	73.60 ± 23.67	1.70 ± 0.55

Table A.3: The MAGIC differential flux sensitivity in the zenith angle range [62°, 70°] as shown in Figures 5.23 and 5.43. The Sensitivity is given in percent of the Crab Nebula flux (C.U.) and in units of energy flux.

E_{min} [TeV]	E_{max} [TeV]	Sensitivity [% C.U.]	Sensitivity $[10^{-12}\,\text{erg}\,\text{cm}^{-2}\,\text{s}^{-1}]$
0.80	1.27	8.38 ± 0.35	3.90 ± 0.16
1.27	2.01	7.50 ± 0.31	2.78 ± 0.11
2.01	3.18	7.23 ± 0.37	2.05 ± 0.11
3.18	5.05	14.49 ± 3.71	3.01 ± 0.77
5.05	7.99	19.59 ± 4.99	2.85 ± 0.72
7.99	12.68	26.24 ± 5.84	2.57 ± 0.57
12.68	20.09	26.14 ± 6.82	1.65 ± 0.43
20.09	31.84	67.59 ± 21.62	2.64 ± 0.84
31.84	50.46	52.12 ± 16.73	1.21 ± 0.38
50.46	79.98	280.64 ± 175.24	3.69 ± 2.30

Table A.4: The MAGIC differential flux sensitivity in the zenith angle range [70°, 75°] as shown in Figures 5.23 and 5.43. The Sensitivity is given in percent of the Crab Nebula flux (C.U.) and in units of energy flux.

E_{min} [TeV]	E_{max} [TeV]	Sensitivity [% C.U.]	Sensitivity [$10^{-12}\,\mathrm{erg\,cm^{-2}\,s^{-1}}$]
1.00	1.86	42.95 ± 5.39	17.12 ± 2.15
1.86	3.46	19.80 ± 1.30	5.53 ± 0.36
3.46	6.45	17.58 ± 1.17	3.18 ± 0.21
6.45	12.01	26.06 ± 2.75	2.83 ± 0.30
12.01	22.35	41.46 ± 11.41	2.50 ± 0.69
22.35	41.60	63.50 ± 20.00	1.97 ± 0.62
41.60	77.44	153.46 ± 73.79	2.26 ± 1.09

Table A.5: The MAGIC differential flux sensitivity in the zenith angle range [75°, 80°] as shown in Figures 5.23 and 5.43. The Sensitivity is given in percent of the Crab Nebula flux (C.U.) and in units of energy flux.

E_{min} [TeV]	E_{max} [TeV]	Sensitivity [% C.U.]	Sensitivity [$10^{-12}\,\mathrm{erg\,cm^{-2}\,s^{-1}}$]
1.00	1.86	431.18 ± 477.72	120.33 ± 133.32
1.86	3.46	56.75 ± 9.46	10.27 ± 1.71
3.46	6.45	53.81 ± 8.79	5.84 ± 0.95
6.45	12.01	128.26 ± 45.58	7.73 ± 2.75
12.01	22.35	340.80 ± 310.26	10.57 ± 9.62
22.35	41.60	591.80 ± 864.95	8.74 ± 12.77
41.60	77.44	1038.42 ± 2522.08	6.76 ± 16.42

Bibliography

[1] Abdo, A. A. et al. "THE FIRST FERMI LARGE AREA TELESCOPE CATALOG OF GAMMA-RAY PULSARS". In: *The Astrophysical Journal Supplement Series* 187.2 (2010), p. 460. DOI: `10.1088/0067-0049/187/2/460`. URL: `https://dx.doi.org/10.1088/0067-0049/187/2/460`.

[2] Abdo, A. A. et al. "THE SECOND FERMI LARGE AREA TELESCOPE CATALOG OF GAMMA-RAY PULSARS". In: *The Astrophysical Journal Supplement Series* 208.2 (2013), p. 17. DOI: `10.1088/0067-0049/208/2/17`. URL: `https://dx.doi.org/10.1088/0067-0049/208/2/17`.

[3] Abeysekara, A. U. et al. "HAWC observations of the acceleration of very-high-energy cosmic rays in the Cygnus Cocoon". In: *Nature Astronomy* 5 (May 2021), pp. 465–471. DOI: `10.1038/s41550-021-01318-y`. arXiv: `2103.06820 [astro-ph.HE]`.

[4] Abeysekara, A. U. et al. "Measurement of the Crab Nebula Spectrum Past 100 TeV with HAWC". In: 881.2, 134 (Aug. 2019), p. 134. DOI: `10.3847/1538-4357/ab2f7d`. arXiv: `1905.12518 [astro-ph.HE]`.

[5] Abeysekara, A. U. et al. "Observation of the Crab Nebula with the HAWC Gamma-Ray Observatory". In: 843.1, 39 (July 2017), p. 39. DOI: `10.3847/1538-4357/aa7555`. arXiv: `1701.01778 [astro-ph.HE]`.

[6] Acciari, V. A. et al. "Teraelectronvolt emission from the gamma-ray burst GRB 190114C". In: *Nature* 575.7783 (Nov. 2019), pp. 455–458. ISSN: 1476-4687. DOI: `10.1038/s41586-019-1750-x`. URL: `https://doi.org/10.1038/s41586-019-1750-x`.

[7] Acero, F. et al. "First detection of VHE γ-rays from SN 1006 by HESS". In: 516, A62 (June 2010), A62. DOI: `10.1051/0004-6361/200913916`. arXiv: `1004.2124 [astro-ph.HE]`.

[8] Ackermann, M. et al. "A Cocoon of Freshly Accelerated Cosmic Rays Detected by Fermi in the Cygnus Superbubble". In: *Science* 334.6059 (Nov. 2011), p. 1103. DOI: `10.1126/science.1210311`.

[9] Ackermann, M. et al. "Detection of the Characteristic Pion-Decay Signature in Supernova Remnants". In: *Science* 339.6121 (Feb. 2013), pp. 807–811. DOI: `10.1126/science.1231160`. arXiv: `1302.3307 [astro-ph.HE]`.

[10] Aharonian, F. et al. "Observations of Mkn 421 in 2004 with HESS at large zenith angles". In: 437.1 (July 2005), pp. 95–99. DOI: `10.1051/0004-6361:20053050`. arXiv: `astro-ph/0506319 [astro-ph]`.

[11] Aharonian, F. A. and Atoyan, A. M. "Does the inverse Compton mechanism alone explain the GeV/TeV gamma-ray emission from the Crab Nebula?" In: *Astroparticle Physics* 3.3 (May 1995), pp. 275–282. DOI: `10.1016/0927-6505(95)00006-3`.

[12] Aharonian, F. A. et al. "Optimizing the angular resolution of the HEGRA telescope system to study the emission region of VHE gamma rays in the Crab Nebula". In: 361 (Sept. 2000), pp. 1073–1078.

[13] Aharonian, F. A. et al. "The Energy Spectrum of TEV Gamma Rays from the Crab Nebula as Measured by the HEGRA System of Imaging Air Cerenkov Telescopes". In: 539.1 (Aug. 2000), pp. 317–324. DOI: `10.1086/309225`. arXiv: `astro-ph/0003182 [astro-ph]`.

[14] Aharonian, F. *Very High Energy Cosmic Gamma Radiation.* World Scientific Publishing Co. Pte. Ltd., 2004.

[15] Aharonian, F., Yang, R., and de Oña Wilhelmi, E. "Massive stars as major factories of Galactic cosmic rays". In: *Nature Astronomy* 3 (Mar. 2019), pp. 561–567. DOI: `10.1038/s41550-019-0724-0`. arXiv: `1804.02331 [astro-ph.HE]`.

[16] Ahnen, M. L. et al. "Performance of the MAGIC telescopes under moonlight". In: *Astroparticle Physics* 94 (Sept. 2017), pp. 29–41. DOI: `10.1016/j.astropartphys.2017.08.001`. arXiv: `1704.00906 [astro-ph.IM]`.

[17] Albert, A. et al. "3HWC: The Third HAWC Catalog of Very-high-energy Gamma-Ray Sources". In: 905.1, 76 (Dec. 2020), p. 76. DOI: `10.3847/1538-4357/abc2d8`. arXiv: `2007.08582 [astro-ph.HE]`.

[18] Albert, A. et al. "HAWC J2227+610 and Its Association with G106.3+2.7, a New Potential Galactic PeVatron". In: 896.2, L29 (June 2020), p. L29. DOI: `10.3847/2041-8213/ab96cc`. arXiv: `2005.13699 [astro-ph.HE]`.

[19] Albert, A. et al. "Observation of the Galactic Center PeVatron beyond 100 TeV with HAWC". In: 973.1, L34 (Sept. 2024), p. L34. DOI: `10.3847/2041-8213/ad772e`. arXiv: `2407.03682 [astro-ph.HE]`.

[20] Albert, A et al. "Performance of the HAWC Observatory and TeV Gamma-Ray Measurements of the Crab Nebula with Improved Extensive Air Shower Reconstruction Algorithms". In: *arXiv e-prints*, arXiv:2405.06050 (May 2024), arXiv:2405.06050. DOI: `10.48550/arXiv.2405.06050`. arXiv: `2405.06050 [astro-ph.HE]`.

[21] Albert, J. et al. "FADC signal reconstruction for the MAGIC telescope". In: *Nuclear Instruments and Methods in Physics Research A* 594.3 (Sept. 2008), pp. 407–419. DOI: `10.1016/j.nima.2008.06.043`. arXiv: `astro-ph/0612385 [astro-ph]`.

[22] Albert, J. et al. "Implementation of the Random Forest method for the Imaging Atmospheric Cherenkov Telescope MAGIC". In: *Nuclear Instruments and Methods in Physics Research A* 588.3 (Apr. 2008), pp. 424–432. DOI: `10.1016/j.nima.2007.11.068`. arXiv: `0709.3719 [astro-ph]`.

[23] Albert, J. et al. "Unfolding of differential energy spectra in the MAGIC experiment". In: *Nuclear Instruments and Methods in Physics Research A* 583.2-3 (Dec. 2007), pp. 494–506. DOI: `10.1016/j.nima.2007.09.048`. arXiv: `0707.2453 [astro-ph]`.

[24] Aleksić, J. et al. "Observations of the Crab Pulsar between 25 and 100 GeV with the MAGIC I Telescope". In: 742.1, 43 (Nov. 2011), p. 43. DOI: `10.1088/0004-637X/742/1/43`. arXiv: `1108.5391 [astro-ph.HE]`.

[25] Aleksić, J. et al. "Performance of the MAGIC stereo system obtained with Crab Nebula data". In: *Astroparticle Physics* 35.7 (Feb. 2012), pp. 435–448. DOI: `10.1016/j.astropartphys.2011.11.007`. arXiv: `1108.1477 [astro-ph.IM]`.

[26] Aleksić, J et al. "Phase-resolved energy spectra of the Crab pulsar in the range of 50–400 GeV measured with the MAGIC telescopes". In: *Astron. Astrophys.* 540 (Apr. 2012), A69. DOI: `10.1051/0004-6361/201118166`.

[27] Aleksić, J. et al. "The major upgrade of the MAGIC telescopes, Part I: The hardware improvements and the commissioning of the system". In: *Astroparticle Physics* 72 (Jan. 2016), pp. 61–75. DOI: `10.1016/j.astropartphys.2015.04.004`. arXiv: `1409.6073 [astro-ph.IM]`.

[28] Aleksić, J. et al. "The major upgrade of the MAGIC telescopes, Part II: A performance study using observations of the Crab Nebula". In: *Astroparticle Physics* 72 (Jan. 2016), pp. 76–94. DOI: `10.1016/j.astropartphys.2015.02.005`. arXiv: `1409.5594 [astro-ph.IM]`.

[29] Aliu, E. et al. “Observation of Pulsed gamma-Rays Above 25 GeV from the Crab Pulsar with MAGIC”. In: *Science* 322.5905 (2008), pp. 1221–1224. DOI: `10.1126/science.1164718`. eprint: `https://www.science.org/doi/pdf/10.1126/science.1164718`. URL: `https://www.science.org/doi/abs/10.1126/science.1164718`.

[30] Aliu, E. et al. “Observation of Pulsed gamma-Rays Above 25 GeV from the Crab Pulsar with MAGIC”. In: *Science* 322.5905 (2008), pp. 1221–1224. DOI: `10.1126/science.1164718`. eprint: `https://www.science.org/doi/pdf/10.1126/science.1164718`. URL: `https://www.science.org/doi/abs/10.1126/science.1164718`.

[31] Amato, E. and Olmi, B. “The Crab Pulsar and Nebula as Seen in Gamma-Rays”. In: *Universe* 7.11 (Nov. 2021), p. 448. DOI: `10.3390/universe7110448`. arXiv: `2111.07712 [astro-ph.HE]`.

[32] Ansoldi, S. et al. “Teraelectronvolt pulsed emission from the Crab Pulsar detected by MAGIC”. In: *A&A* 585 (2016), A133. DOI: `10.1051/0004-6361/201526853`. URL: `https://doi.org/10.1051/0004-6361/201526853`.

[33] Arbeletche, L. B. and de Souza, V. “Parametrization of the angular distribution of Cherenkov light in air showers”. In: *European Physical Journal C* 81.2, 195 (Feb. 2021), p. 195. DOI: `10.1140/epjc/s10052-021-08971-7`. arXiv: `2007.13812 [astro-ph.HE]`.

[34] Archer, A. et al. “Very-high Energy Observations of the Galactic Center Region by VERITAS in 2010-2012”. In: 790.2, 149 (Aug. 2014), p. 149. DOI: `10.1088/0004-637X/790/2/149`. arXiv: `1406.6383 [astro-ph.HE]`.

[35] Astiasarain, X. et al. “Multiple emission components in the Cygnus cocoon detected from Fermi-LAT observations”. In: 671, A47 (Mar. 2023), A47. DOI: `10.1051/0004-6361/202245573`. arXiv: `2301.04504 [astro-ph.HE]`.

[36] Atoyan, A. M. and Aharonian, F. A. “On the fluxes of inverse Compton gamma-rays expected from the Crab Nebula.” In: 120 (Dec. 1996), pp. 453–456.

[37] Atoyan, A. M. and Aharonian, F. A. “On the mechanisms of gamma radiation in the Crab Nebula”. In: 278.2 (Jan. 1996), pp. 525–541. DOI: `10.1093/mnras/278.2.525`.

[38] Atwood, W. B. et al. “The Large Area Telescope on the Fermi Gamma-Ray Space Telescope Mission”. In: 697.2 (June 2009), pp. 1071–1102. DOI: `10.1088/0004-637X/697/2/1071`. arXiv: `0902.1089 [astro-ph.IM]`.

[39] Baade, W and Zwicky, F. “Cosmic rays from super-novae”. en. In: *Proc. Natl. Acad. Sci. U. S. A.* 20.5 (May 1934), pp. 259–263.

[40] Ballet, J. et al. “Fermi Large Area Telescope Fourth Source Catalog Data Release 4 (4FGL-DR4)”. In: *arXiv e-prints*, arXiv:2307.12546 (July 2023), arXiv:2307.12546. DOI: `10.48550/arXiv.2307.12546`. arXiv: `2307.12546 [astro-ph.HE]`.

[41] Bandiera, R et al. “Reverberation of pulsar wind nebulae (I): impact of the medium properties and other parameters upon the extent of the compression”. en. In: *Monthly Notices of the Royal Astronomical Society* 499.2 (Oct. 2020), pp. 2051–2062. ISSN: 0035-8711, 1365-2966. DOI: `10.1093/mnras/staa2956`. URL: `https://academic.oup.com/mnras/article/499/2/2051/5912462` (visited on 07/07/2022).

[42] Bandiera, R. et al. *Reverberation of pulsar wind nebulae (II): Anatomy of the "thin-shell” evolution.* arXiv:2301.04056 [astro-ph]. Jan. 2023. DOI: `10.48550/arXiv.2301.04056`. URL: `http://arxiv.org/abs/2301.04056` (visited on 01/11/2023).

[43] Bandiera, R. et al. *Reverberation of pulsar wind nebulae (III): Modelling of the plasma interface empowering a long term radiative evolution.* arXiv:2307.13491 [astro-ph]. July 2023. URL: `http://arxiv.org/abs/2307.13491` (visited on 08/03/2023).

[44] Becker Tjus, J. and Merten, L. “Closing in on the origin of Galactic cosmic rays using multimessenger information”. In: *Physics Reports* 872 (2020). Closing in on the origin of Galactic cosmic rays using multimessenger information, pp. 1–98. ISSN: 0370-1573. DOI: `https://doi.org/10.1016/j.physrep.2020.05.002`. URL: `https://www.sciencedirect.com/science/article/pii/S0370157320301927`.

[45] Bednarek, W. and Idec, W. “On the variability of the GeV and multi-TeV gamma-ray emission from the Crab nebula”. In: 414.3 (July 2011), pp. 2229–2234. DOI: `10.1111/j.1365-2966.2011.18539.x`. arXiv: `1011.4176 [astro-ph.HE]`.

[46] Bell, A. R. “Turbulent amplification of magnetic field and diffusive shock acceleration of cosmic rays”. In: 353.2 (Sept. 2004), pp. 550–558. DOI: `10.1111/j.1365-2966.2004.08097.x`.

[47] Bietenholz, M. F., Frail, D. A., and Hester, J. J. “The Crab Nebula’s Moving Wisps in Radio”. In: 560.1 (Oct. 2001), pp. 254–260. DOI: `10.1086/322244`. arXiv: `astro-ph/0106339 [astro-ph]`.

[48] Blasi, P. “The origin of galactic cosmic rays”. In: 21, 70 (Nov. 2013), p. 70. DOI: `10.1007/s00159-013-0070-7`. arXiv: `1311.7346 [astro-ph.HE]`.

[49] Bowyer, S. et al. “Lunar Occultation of X-ray Emission from the Crab Nebula”. In: *Science* 146.3646 (Nov. 1964), pp. 912–917. DOI: `10.1126/science.146.3646.912`.

[50] Bowyer, S. et al. “X-ray Sources in the Galaxy”. In: 201.4926 (Mar. 1964), pp. 1307–1308. DOI: `10.1038/2011307a0`.

[51] Bradt, H. *Astrophysics Processes*. Cambridge University Press, 2008.

[52] Bretz, T. et al. “The drive system of the major atmospheric gamma-ray imaging Cherenkov telescope”. In: *Astroparticle Physics* 31.2 (Mar. 2009), pp. 92–101. DOI: `10.1016/j.astropartphys.2008.12.001`. arXiv: `0810.4593 [astro-ph]`.

[53] Bühler, R. and Blandford, R. “The surprising Crab pulsar and its nebula: a review”. In: *Reports on Progress in Physics* 77.6, 066901 (June 2014), p. 066901. DOI: `10.1088/0034-4885/77/6/066901`. arXiv: `1309.7046 [astro-ph.HE]`.

[54] Bykov, A. M. et al. “Twinkling pulsar wind nebulae in the synchrotron cut-off regime and the γ-ray flares in the Crab Nebula”. In: 421.1 (Mar. 2012), pp. L67–L71. DOI: `10.1111/j.1745-3933.2011.01208.x`. arXiv: `1112.3114 [astro-ph.HE]`.

[55] Bykov, A. M. et al. “High-Energy Particles and Radiation in Star-Forming Regions”. In: 216.3, 42 (Apr. 2020), p. 42. DOI: `10.1007/s11214-020-00663-0`. arXiv: `2003.11534 [astro-ph.HE]`.

[56] Cao, Z. et al. “Introduction to Large High Altitude Air Shower Observatory (LHAASO)”. In: *Chinese Astronomy and Astrophysics* 43.4 (2019), pp. 457–478. ISSN: 0275-1062. DOI: `https://doi.org/10.1016/j.chinastron.2019.11.001`. URL: `https://www.sciencedirect.com/science/article/pii/S0275106219300773`.

[57] Cao, Z. et al. “Optimization of performance of the KM2A full array using the Crab Nebula”. In: *Chinese Physics C* 48.6, 065001 (June 2024), p. 065001. DOI: `10.1088/1674-1137/ad2e82`. arXiv: `2401.01038 [astro-ph.IM]`.

[58] Cao, Z. et al. “The First LHAASO Catalog of Gamma-Ray Sources”. In: 271.1, 25 (Mar. 2024), p. 25. DOI: `10.3847/1538-4365/acfd29`. arXiv: `2305.17030 [astro-ph.HE]`.

[59] Cao, Z. et al. “Ultrahigh-energy photons up to 1.4 petaelectronvolts from 12 γ-ray Galactic sources”. In: 594.7861 (June 2021), pp. 33–36. DOI: `10.1038/s41586-021-03498-z`.

[60] Cerutti, B. et al. “Simulations of Particle Acceleration beyond the Classical Synchrotron Burnoff Limit in Magnetic Reconnection: An Explanation of the Crab Flares”. In: 770.2, 147 (June 2013), p. 147. DOI: `10.1088/0004-637X/770/2/147`. arXiv: `1302.6247 [astro-ph.HE]`.

[61] Chapman, S. “The absorption and dissociative or ionizing effect of monochromatic radiation in an atmosphere on a rotating earth part II. Grazing incidence”. In: *Proceedings of the Physical Society* 43.5 (Sept. 1931), pp. 483–501. DOI: `10.1088/0959-5309/43/5/302`.

[62] Cherenkov, P. A. “Visible luminescence of pure liquids under the influence of γ-radiation”. In: *Dokl. Akad. Nauk SSSR* 2.8 (1934), pp. 451–454. DOI: `10.3367/UFNr.0093.196710n.0385`.

[63] Cherenkov Telescope Array Observatory and Cherenkov Telescope Array Consortium. *CTAO Instrument Response Functions - prod5 version v0.1*. Version v0.1. Sept. 2021. DOI: `10.5281/zenodo.5499840`. URL: `https://doi.org/10.5281/zenodo.5499840`.

[64] Chiu, H. Y. “Supernovae, neutrinos, and neutron stars”. In: *Annals of Physics* 26.3 (Feb. 1964), pp. 364–410. DOI: `10.1016/0003-4916(64)90256-8`.

[65] COCKE, W. J., DISNEY, M. J., and TAYLOR, D. J. “Discovery of Optical Signals from Pulsar NP 0532”. In: *Nature* 221.5180 (Feb. 1969), pp. 525–527. ISSN: 1476-4687. DOI: `10.1038/221525a0`. URL: `https://doi.org/10.1038/221525a0`.

[66] Commichau, S. C. et al. “Monte Carlo studies of geomagnetic field effects on the imaging air Cherenkov technique for the MAGIC telescope site”. In: *Nuclear Instruments and Methods in Physics Research A* 595.3 (Oct. 2008), pp. 572–586. DOI: `10.1016/j.nima.2008.07.144`. arXiv: `0802.2551 [astro-ph]`.

[67] Coroniti, F. V. “Magnetically Striped Relativistic Magnetohydrodynamic Winds: The Crab Nebula Revisited”. In: 349 (Feb. 1990), p. 538. DOI: `10.1086/168340`.

[68] Cristofari, P. “The Hunt for Pevatrons: The Case of Supernova Remnants”. In: *Universe* 7.9, 324 (Aug. 2021), p. 324. DOI: `10.3390/universe7090324`. arXiv: `2110.07956 [astro-ph.HE]`.

[69] Cristofari, P., Blasi, P., and Amato, E. “The low rate of Galactic pevatrons”. In: *Astroparticle Physics* 123, 102492 (Dec. 2020), p. 102492. DOI: `10.1016/j.astropartphys.2020.102492`. arXiv: `2007.04294 [astro-ph.HE]`.

[70] Da Vela, P. et al. “Study of the IACT angular acceptance and Point Spread Function”. In: *Astroparticle Physics* 98 (Mar. 2018), pp. 1–8. DOI: `10.1016/j.astropartphys.2018.01.002`.

[71] Daugherty, J. K. and Harding, A. K. “Gamma-ray pulsars: Emission from extended polar CAP cascades”. en. In: *Astrophys. J.* 458 (Feb. 1996), p. 278. DOI: `10.1086/176811`.

[72] de Jager, O. C. and Harding, A. K. “The Expected High-Energy to Ultra–High-Energy Gamma-Ray Spectrum of the Crab Nebula”. In: 396 (Sept. 1992), p. 161. DOI: `10.1086/171706`.

[73] de Jager, O. C. et al. “Gamma-Ray Observations of the Crab Nebula: A Study of the Synchro-Compton Spectrum”. In: 457 (Jan. 1996), p. 253. DOI: `10.1086/176726`.

[74] de Naurois, M. and Mazin, D. “Ground-based detectors in very-high-energy gamma-ray astronomy”. In: *Comptes Rendus Physique* 16.6-7 (Aug. 2015), pp. 610–627. DOI: `10.1016/j.crhy.2015.08.011`. arXiv: `1511.00463 [astro-ph.IM]`.

[75] de Oña Wilhelmi, E. et al. "On the Potential of Bright, Young Pulsars to Power Ultrahigh Gamma-Ray Sources". In: 930.1, L2 (May 2022), p. L2. DOI: `10.3847/2041-8213/ac66cf`. arXiv: `2204.09440 [astro-ph.HE]`.

[76] de Oña Wilhelmi, E. et al. "The hunt for PeVatrons as the origin of the most energetic photons observed in the Galaxy". In: *Nature Astronomy* 8 (Apr. 2024), pp. 425–431. DOI: `10.1038/s41550-024-02224-9`. arXiv: `2404.16591 [astro-ph.HE]`.

[77] Del Zanna, L. and Olmi, B. "Multidimensional Relativistic MHD Simulations of Pulsar Wind Nebulae: Dynamics and Emission". In: *Modelling Pulsar Wind Nebulae.* Ed. by Torres, D. F. Cham: Springer International Publishing, 2017, pp. 215–246. ISBN: 978-3-319-63031-1. DOI: `10.1007/978-3-319-63031-1_10`. URL: `https://doi.org/10.1007/978-3-319-63031-1_10`.

[78] Dirson, L. and Horns, D. "Phenomenological modelling of the Crab Nebula's broadband energy spectrum and its apparent extension". In: 671, A67 (Mar. 2023), A67. DOI: `10.1051/0004-6361/202243578`. arXiv: `2203.11502 [astro-ph.HE]`.

[79] Emmering, R. T. and Chevalier, R. A. "Shocked Relativistic Magnetohydrodynamic Flows with Application to Pulsar Winds". In: 321 (Oct. 1987), p. 334. DOI: `10.1086/165632`.

[80] Fabian Schmidt, U. L. *CORSIKA Shower Images — www-zeuthen.desy.de.* `https://www-zeuthen.desy.de/~jknapp/fs/photon-showers.html`. [Accessed 13-08-2024].

[81] Fabian Schmidt, U. L. *CORSIKA Shower Images — www-zeuthen.desy.de.* `https://www-zeuthen.desy.de/~jknapp/fs/proton-showers.html`. [Accessed 13-08-2024].

[82] Fermi, E. "On the Origin of the Cosmic Radiation". In: *Physical Review* 75.8 (Apr. 1949), pp. 1169–1174. DOI: `10.1103/PhysRev.75.1169`.

[83] Fermi-LAT collaboration. *Fermitools-Cicerone: Overview of the LAT.* `https://fermi.gsfc.nasa.gov/ssc/data/analysis/documentation/Cicerone/Cicerone_Introduction/LAT_overview.html`. [Accessed 01-11-2024].

[84] Fomin, V. P. et al. "New methods of atmospheric Cherenkov imaging for gamma-ray astronomy. I. The false source method". In: *Astroparticle Physics* 2.2 (May 1994), pp. 137–150. DOI: `10.1016/0927-6505(94)90036-1`.

[85] Fritz, G. et al. "X-ray Pulsar in the Crab Nebula". In: *Science* 164.3880 (1969), pp. 709–712. DOI: `10.1126/science.164.3880.709`. eprint: `https://www.science.org/doi/pdf/10.1126/science.164.3880.709`. URL: `https://www.science.org/doi/abs/10.1126/science.164.3880.709`.

[86] Fruck, C. et al. "Characterizing the aerosol atmosphere above the Observatorio del Roque de los Muchachos by analysing seven years of data taken with an GaAsP HPD-readout, absolutely calibrated elastic LIDAR". In: 515.3 (Sept. 2022), pp. 4520–4550. DOI: `10.1093/mnras/stac1563`. arXiv: `2202.09561 [astro-ph.IM]`.

[87] Gabici, S. and Aharonian, F. A. "Searching for Galactic Cosmic-Ray Pevatrons with Multi-TeV Gamma Rays and Neutrinos". In: 665.2 (Aug. 2007), pp. L131–L134. DOI: `10.1086/521047`. arXiv: `0705.3011 [astro-ph]`.

[88] Gabici, S. et al. "The origin of Galactic cosmic rays: Challenges to the standard paradigm". In: *International Journal of Modern Physics D* 28.15, 1930022-339 (Jan. 2019), pp. 1930022–339. DOI: `10.1142/S0218271819300222`. arXiv: `1903.11584 [astro-ph.HE]`.

[89] Gaisser, T. K., Engel, R., and Resconi, E. “Cosmic Rays and Particle Physics”. In: Cambridge University Press, 2016. Chap. Electromagnetic cascades, 302–312.

[90] Galbraith, W. and Jelley, J. V. “Light Pulses from the Night Sky associated with Cosmic Rays”. In: 171.4347 (Feb. 1953), pp. 349–350. DOI: `10.1038/171349a0`.

[91] Goldreich, P. and Julian, W. H. “Pulsar electrodynamics”. en. In: *Astrophys. J.* 157 (Aug. 1969), p. 869.

[92] Gorbar, E. V. and Shovkovy, I. A. “Chiral anomalous processes in magnetospheres of pulsars and black holes”. In: *The European Physical Journal C* 82.7 (July 2022), p. 625. ISSN: 1434-6052. DOI: `10.1140/epjc/s10052-022-10604-6`. URL: `https://doi.org/10.1140/epjc/s10052-022-10604-6`.

[93] Greisen, K. “Cosmic Ray Showers”. In: *Annual Review of Nuclear and Particle Science* 10.Volume 10, (1960), pp. 63–108. ISSN: 1545-4134. DOI: `https://doi.org/10.1146/annurev.ns.10.120160.000431`. URL: `https://www.annualreviews.org/content/journals/10.1146/annurev.ns.10.120160.000431`.

[94] Grenier, I. A. and Harding, A. K. “Gamma-ray pulsars: A gold mine”. en. In: *Comptes Rendus. Physique* 16.6-7 (2015), pp. 641–660. DOI: `10.1016/j.crhy.2015.08.013`.

[95] Grieder, P. K. F. “Extensive Air Showers”. In: 2010. Chap. Electromagnetic Interactions and Photon-Electron Cascades, pp. 147–204. DOI: `10.1007/978-3-540-76941-5`.

[96] Guelfand, M. et al. “Particle content of very inclined air showers for radio signal modeling”. In: 2024.5, 055 (May 2024), p. 055. DOI: `10.1088/1475-7516/2024/05/055`. arXiv: `2310.19612 [astro-ph.HE]`.

[97] H. E. S. S. Collaboration. “A new SNR with TeV shell-type morphology: HESS J1731-347”. In: 531, A81 (July 2011), A81. DOI: `10.1051/0004-6361/201016425`. arXiv: `1105.3206 [astro-ph.HE]`.

[98] H. E. S. S. Collaboration. “Acceleration of petaelectronvolt protons in the Galactic Centre”. In: 531.7595 (Mar. 2016), pp. 476–479. DOI: `10.1038/nature17147`. arXiv: `1603.07730 [astro-ph.HE]`.

[99] H. E. S. S. Collaboration. “H.E.S.S. observations of RX J1713.7-3946 with improved angular and spectral resolution: Evidence for gamma-ray emission extending beyond the X-ray emitting shell”. In: 612, A6 (Apr. 2018), A6. DOI: `10.1051/0004-6361/201629790`. arXiv: `1609.08671 [astro-ph.HE]`.

[100] H. E. S. S. Collaboration. “Resolving the Crab pulsar wind nebula at teraelectronvolt energies”. In: *Nature Astronomy* 4 (Feb. 2020), pp. 167–173. DOI: `10.1038/s41550-019-0910-0`. arXiv: `1909.09494 [astro-ph.HE]`.

[101] H. E. S. S. Collaboration. “The H.E.S.S. Galactic plane survey”. In: 612, A1 (Apr. 2018), A1. DOI: `10.1051/0004-6361/201732098`. arXiv: `1804.02432 [astro-ph.HE]`.

[102] Hahn, A. et al. “Direct comparison of SiPM and PMT sensor performances in a large-size imaging air Cherenkov telescope”. In: *Nuclear Instruments and Methods in Physics Research A* 1064, 169350 (July 2024), p. 169350. DOI: `10.1016/j.nima.2024.169350`. arXiv: `2404.14346 [astro-ph.IM]`.

[103] Harding, A. K. et al. “Multi-TeV Emission from the Vela Pulsar”. In: *The Astrophysical Journal Letters* 869.1 (2018), p. L18. DOI: `10.3847/2041-8213/aaf3b2`. URL: `https://dx.doi.org/10.3847/2041-8213/aaf3b2`.

[104] Haymes, R. C. et al. “Observation of Gamma Radiation from the Crab Nebula”. In: 151 (Jan. 1968), p. L9. DOI: `10.1086/180129`.

[105] Heck, D. et al. *CORSIKA: a Monte Carlo code to simulate extensive air showers.* Tech. rep. Forschungszentrum Karlsruhe, 1998.

[106] Heitler, W. *The Quantum Theory Of Radiation.* Second. London: Oxford University Press, 1944.

[107] Hester, J. J. et al. "Hubble Space Telescope and Chandra Monitoring of the Crab Synchrotron Nebula". In: 577.1 (Sept. 2002), pp. L49–L52. DOI: `10.1086/344132`.

[108] Hester, J. J. et al. "WFPC2 Studies of the Crab Nebula. I. HST and ROSAT Imaging of the Synchrotron Nebula". In: 448 (July 1995), p. 240. DOI: `10.1086/175956`.

[109] HEWISH, A. et al. "Observation of a Rapidly Pulsating Radio Source". In: *Nature* 217.5130 (Feb. 1968), pp. 709–713. ISSN: 1476-4687. DOI: `10.1038/217709a0`. URL: `https://doi.org/10.1038/217709a0`.

[110] Hillas, A. M. "Cerenkov Light Images of EAS Produced by Primary Gamma Rays and by Nuclei". In: *19th International Cosmic Ray Conference (ICRC19), Volume 3.* Ed. by Jones, F. C. Vol. 3. International Cosmic Ray Conference. Aug. 1985, p. 445.

[111] Hillas, A. M. "The Origin of Ultra-High-Energy Cosmic Rays". In: 22 (Jan. 1984), pp. 425–444. DOI: `10.1146/annurev.aa.22.090184.002233`.

[112] Hose, J. "Measurement of the total atmospheric transmittance for the correction of data of the imaging Cherenkov telescope MAGIC". MA thesis. Fernuniversität Hagen, 2017.

[113] Icecube Collaboration. "Observation of high-energy neutrinos from the Galactic plane". In: *Science* 380.6652 (June 2023), pp. 1338–1343. DOI: `10.1126/science.adc9818`. arXiv: `2307.04427 [astro-ph.HE]`.

[114] IceCube Collaboration et al. "Evidence for neutrino emission from the nearby active galaxy NGC 1068". In: *Science* 378.6619 (Nov. 2022), pp. 538–543. DOI: `10.1126/science.abg3395`. arXiv: `2211.09972 [astro-ph.HE]`.

[115] IceCube Collaboration et al. "Multimessenger observations of a flaring blazar coincident with high-energy neutrino IceCube-170922A". In: *Science* 361.6398, eaat1378 (July 2018), eaat1378. DOI: `10.1126/science.aat1378`. arXiv: `1807.08816 [astro-ph.HE]`.

[116] IceCube Collaboration et al. "Neutrino emission from the direction of the blazar TXS 0506+056 prior to the IceCube-170922A alert". In: *Science* 361.6398 (July 2018), pp. 147–151. DOI: `10.1126/science.aat2890`. arXiv: `1807.08794 [astro-ph.HE]`.

[117] Ishio, K. "Improvement in the -ray energy reconstruction of MAGIC and impact on the spectral analysis of the first Gamma Ray Burst detected at TeV energies". PhD thesis. Ludwig-Maximilians University of Munich, Germany, Sept. 2020.

[118] Ishio, K. and Paneque, D. "A novel energy reconstruction method for the MAGIC stereoscopic observation". In: *Astroparticle Physics* 158, 102937 (June 2024), p. 102937. DOI: `10.1016/j.astropartphys.2024.102937`. arXiv: `2212.03592 [astro-ph.IM]`.

[119] Kamata, K. and Nishimura, J. "The Lateral and the Angular Structure Functions of Electron Showers". In: *Progress of Theoretical Physics Supplement* 6 (Jan. 1958), pp. 93–155. DOI: `10.1143/PTPS.6.93`.

[120] Kaplan, D. L. et al. "A Precise Proper Motion for the Crab Pulsar, and the Difficulty of Testing Spin-Kick Alignment for Young Neutron Stars". In: 677.2 (Apr. 2008), pp. 1201–1215. DOI: `10.1086/529026`. arXiv: `0801.1142 [astro-ph]`.

[121] Kasten, F. and Young, A. T. "Revised optical air mass tables and approximation formula". In: *Appl. Opt.* 28.22 (1989), pp. 4735–4738. DOI: `10.1364/AO.28.004735`. URL: `https://opg.optica.org/ao/abstract.cfm?URI=ao-28-22-4735`.

[122] Kennel, C. F. and Coroniti, F. V. "Confinement of the Crab pulsar's wind by its supernova remnant." In: 283 (Aug. 1984), pp. 694–709. DOI: `10.1086/162356`.

[123] Kennel, C. F. and Coroniti, F. V. "Magnetohydrodynamic model of Crab nebula radiation." In: 283 (Aug. 1984), pp. 710–730. DOI: `10.1086/162357`.

[124] Khangulyan, D., Aharonian, F., and Taylor, A. M. "On the Properties of Inverse Compton Spectra Generated by Upscattering a Power-law Distribution of Target Photons". In: 954.2, 186 (Sept. 2023), p. 186. DOI: `10.3847/1538-4357/acea5d`. arXiv: `2307.12467 [astro-ph.HE]`.

[125] Komissarov, S. S. and Lyutikov, M. "On the origin of variable gamma-ray emission from the Crab nebula". In: 414.3 (July 2011), pp. 2017–2028. DOI: `10.1111/j.1365-2966.2011.18516.x`. arXiv: `1011.1800 [astro-ph.HE]`.

[126] Konopelko, A. et al. "Effectiveness of TeV γ-ray observations at large zenith angles with a stereoscopic system of imaging atmospheric Cerenkov telescopes". In: *Journal of Physics G Nuclear Physics* 25.9 (Sept. 1999), pp. 1989–2000. DOI: `10.1088/0954-3899/25/9/316`. arXiv: `astro-ph/9906405 [astro-ph]`.

[127] Kostunin, D. et al. "Detection of J2019+368: a case study of very-large-zenith angle observations with H.E.S.S." In: *PoS* Gamma2022 (2024), p. 136. DOI: `10.22323/1.417.0136`.

[128] Lafferty, G. D. and Wyatt, T. R. "Where to stick your data points: The treatment of measurements within wide bins". In: *Nuclear Instruments and Methods in Physics Research A* 355.2 (Feb. 1995), pp. 541–547. DOI: `10.1016/0168-9002(94)01112-5`.

[129] Lampland, C. O. "OBSERVED CHANGES IN THE STRUCTURE OF THE "CRAB" NEBULA (N. G. C. 1952)". In: *Publications of the Astronomical Society of the Pacific* 33.192 (1921), p. 79. DOI: `10.1086/123039`. URL: `https://dx.doi.org/10.1086/123039`.

[130] Lessard, R. W. et al. "A new analysis method for reconstructing the arrival direction of TeV gamma rays using a single imaging atmospheric Cherenkov telescope". In: *Astroparticle Physics* 15.1 (Mar. 2001), pp. 1–18. DOI: `10.1016/S0927-6505(00)00133-X`. arXiv: `astro-ph/0005468 [astro-ph]`.

[131] LHAASO Collaboration. "An ultrahigh-energy γ -ray bubble powered by a super PeVatron". In: *Science Bulletin* 69.4 (Feb. 2024), pp. 449–457. DOI: `10.1016/j.scib.2023.12.040`. arXiv: `2310.10100 [astro-ph.HE]`.

[132] LHAASO Collaboration. "Peta-electron volt gamma-ray emission from the Crab Nebula". In: *Science* 373 (July 2021), pp. 425–430. DOI: `10.1126/science.abg5137`. arXiv: `2111.06545 [astro-ph.HE]`.

[133] LHAASO Collaboration. *The bird view of LHAASO(2022.7)*. `http://english.ihep.cas.cn/lhaaso/gy/pt/202209/t20220927_320816.html`. [Accessed 01-09-2024].

[134] Li, T. P. and Ma, Y. Q. "Analysis methods for results in gamma-ray astronomy." In: 272 (Sept. 1983), pp. 317–324. DOI: `10.1086/161295`.

[135] Lyubarsky, Y. E. "Highly magnetized region in pulsar wind nebulae and origin of the Crab gamma-ray flares". In: 427.2 (Dec. 2012), pp. 1497–1502. DOI: `10.1111/j.1365-2966.2012.22097.x`. arXiv: `1209.1589 [astro-ph.HE]`.

[136] Lyutikov, M., Balsara, D., and Matthews, C. "Crab GeV flares from the corrugated termination shock". In: 422.4 (June 2012), pp. 3118–3129. DOI: `10.1111/j.1365-2966.2012.20831.x`. arXiv: `1109.1204 [astro-ph.HE]`.

[137] Ma, X.-H. et al. “Chapter 1 LHAASO Instruments and Detector technology *”. In: *Chinese Physics C* 46.3 (2022), p. 030001. DOI: `10.1088/1674-1137/ac3fa6`. URL: `https://dx.doi.org/10.1088/1674-1137/ac3fa6`.

[138] MAGIC Collaboration. “MAGIC observations of the diffuse γ-ray emission in the vicinity of the Galactic center”. In: 642, A190 (Oct. 2020), A190. DOI: `10.1051/0004-6361/201936896`. arXiv: `2006.00623 [astro-ph.HE]`.

[139] MAGIC Collaboration. “MAGIC observations provide compelling evidence of hadronic multi-TeV emission from the putative PeVatron SNR G106.3+2.7”. In: 671, A12 (Mar. 2023), A12. DOI: `10.1051/0004-6361/202244931`. arXiv: `2211.15321 [astro-ph.HE]`.

[140] MAGIC Collaboration. “MAGIC very large zenith angle observations of the Crab Nebula up to 100 TeV”. In: 635, A158 (Mar. 2020), A158. DOI: `10.1051/0004-6361/201936899`. arXiv: `2001.09566 [astro-ph.HE]`.

[141] Majumdar, P. et al. “Monte Carlo simulation for the MAGIC telescope”. In: *29th International Cosmic Ray Conference (ICRC29), Volume 5*. Ed. by Acharya, B. S. et al. Vol. 5. International Cosmic Ray Conference. Jan. 2005, p. 203.

[142] Matthews, J. “A Heitler model of extensive air showers”. In: *Astroparticle Physics* 22.5-6 (Jan. 2005), pp. 387–397. DOI: `10.1016/j.astropartphys.2004.09.003`.

[143] Matthews, J. “Modeling Energy Flow in Air Showers”. In: *International Cosmic Ray Conference*. Vol. 1. International Cosmic Ray Conference. Jan. 2001, p. 261.

[144] Mirzoyan, R. “On the Calibration Accuracy of Light Sensors in Atmospheric Cherenkov Fluorescence and Neutrino Experiments”. In: *International Cosmic Ray Conference*. Vol. 7. International Cosmic Ray Conference. Jan. 1997, p. 265.

[145] Mirzoyan, R. “The Development of Ground-Based Gamma-Ray Astronomy: A Historical Overview of the Pioneering Experiments”. In: *Handbook of X-ray and Gamma-ray Astrophysics*. Ed. by Bambi, C. and Santangelo, A. Singapore: Springer Nature Singapore, 2024, pp. 2521–2546. ISBN: 978-981-19696-0-7. DOI: `10.1007/978-981-19-6960-7_62`. URL: `https://doi.org/10.1007/978-981-19-6960-7_62`.

[146] Mirzoyan, R. et al. “Extending the observation limits of Imaging Air Cherenkov Telescopes toward horizon”. In: *Nuclear Instruments and Methods in Physics Research A* 952, 161587 (Feb. 2020), p. 161587. DOI: `10.1016/j.nima.2018.11.046`. arXiv: `1903.04989 [astro-ph.IM]`.

[147] Mochol, I. and Pétri, J. “Very high energy emission as a probe of relativistic magnetic reconnection in pulsar winds”. In: *Monthly Notices of the Royal Astronomical Society: Letters* 449.1 (Mar. 2015), pp. L51–L55. ISSN: 1745-3925. DOI: `10.1093/mnrasl/slv018`. eprint: `https://academic.oup.com/mnrasl/article-pdf/449/1/L51/54653083/mnrasl\_449\_1\_l51.pdf`. URL: `https://doi.org/10.1093/mnrasl/slv018`.

[148] NATHER, R. E., WARNER, B., and MACFARLANE, M. “Optical Pulsations in the Crab Nebula Pulsar”. In: *Nature* 221.5180 (Feb. 1969), pp. 527–529. ISSN: 1476-4687. DOI: `10.1038/221527a0`. URL: `https://doi.org/10.1038/221527a0`.

[149] Nishimura, J. “Theory of Cascade Showers”. In: *Handbuch der Physik* 46.2 (Jan. 1967), pp. 1–114. DOI: `10.1007/978-3-642-46079-1_1`.

[150] Novick, R. et al. “Detection of X-Ray Polarization of the Crab Nebula”. In: 174 (May 1972), p. L1. DOI: `10.1086/180938`.

[151] Oda, M. et al. “The Size and Position of the X-Ray Source in the Crab Nebula”. In: 148 (Apr. 1967), p. L5. DOI: `10.1086/180002`.

[152] Olmi, B. et al. “Constraints on particle acceleration sites in the Crab nebula from relativistic magnetohydrodynamic simulations”. In: 449.3 (May 2015), pp. 3149–3159. DOI: `10.1093/mnras/stv498`. arXiv: `1502.06394 [astro-ph.HE]`.

[153] Olmi, B. and Bucciantini, N. “The Dawes Review 11: From young to old: The evolutionary path of Pulsar Wind Nebulae”. en. In: *Publications of the Astronomical Society of Australia* 40 (2023), e007. ISSN: 1323-3580, 1448-6083. DOI: `10.1017/pasa.2023.5`. URL: `https://www.cambridge.org/core/product/identifier/S132335802300005X/type/journal_article` (visited on 04/12/2024).

[154] Ormes, J. and Freier, P. “On the propagation of cosmic rays in the Galaxy.” In: 222 (June 1978), pp. 471–483. DOI: `10.1086/156160`.

[155] Osmanov, Z. and Rieger, F. M. “Pulsed VHE emission from the Crab Pulsar in the context of magnetocentrifugal particle acceleration”. In: *Monthly Notices of the Royal Astronomical Society* 464.2 (Sept. 2016), pp. 1347–1352. ISSN: 0035-8711. DOI: `10.1093/mnras/stw2408`. eprint: `https://academic.oup.com/mnras/article-pdf/464/2/1347/8334691/stw2408.pdf`. URL: `https://doi.org/10.1093/mnras/stw2408`.

[156] Pacini, F. “Energy emission from a neutron star”. en. In: *Nature* 216.5115 (Nov. 1967), pp. 567–568.

[157] Peresano, M. “MAGIC telescopes observations at Very Large Zenith angles and the first neutrino-gamma association”. PhD Thesis. Universit‘a degli Studi di Udine, 2018.

[158] Rees, M. J. and Gunn, J. E. “The Origin of the Magnetic Field and Relativistic Particles in the Crab Nebula”. In: *Monthly Notices of the Royal Astronomical Society* 167.1 (Apr. 1974), pp. 1–12. ISSN: 0035-8711. DOI: `10.1093/mnras/167.1.1`. eprint: `https://academic.oup.com/mnras/article-pdf/167/1/1/8079729/mnras167-0001.pdf`. URL: `https://doi.org/10.1093/mnras/167.1.1`.

[159] Rolke, W. A., López, A. M., and Conrad, J. “Limits and confidence intervals in the presence of nuisance parameters”. In: *Nuclear Instruments and Methods in Physics Research A* 551.2-3 (Oct. 2005), pp. 493–503. DOI: `10.1016/j.nima.2005.05.068`. arXiv: `physics/0403059 [physics.data-an]`.

[160] Rossi, B. and Greisen, K. “Cosmic-Ray Theory”. In: *Rev. Mod. Phys.* 13 (4 1941), pp. 240–309. DOI: `10.1103/RevModPhys.13.240`. URL: `https://link.aps.org/doi/10.1103/RevModPhys.13.240`.

[161] Rosswog, S. and Brüggen, M. *Introduction to High-Energy Astrophysics*. Cambridge University Press, 2011.

[162] Rozenberg, G. V. *Twilight - A study in atmospheric optics*. Plenum Press New York, 1966.

[163] Ruderman, M. A. and Sutherland, P. G. “Theory of pulsars - Polar caps, sparks, and coherent microwave radiation”. In: *Astrophys. J.* 196 (Feb. 1975), p. 51. DOI: `10.1086/153393`.

[164] Scargle, J. D. “Activity in the Crab Nebula”. In: 156 (May 1969), p. 401. DOI: `10.1086/149978`.

[165] Schmuckermaier, F. et al. “Correcting Imaging Atmospheric Cherenkov Telescope data with atmospheric profiles obtained with an elastic light detecting and ranging system”. In: 673, A2 (May 2023), A2. DOI: `10.1051/0004-6361/202245787`. arXiv: `2302.12072 [astro-ph.IM]`.

[166] Schoenfelder, V. et al. “Instrument Description and Performance of the Imaging Gamma-Ray Telescope COMPTEL aboard the Compton Gamma-Ray Observatory”. In: 86 (June 1993), p. 657. DOI: `10.1086/191794`.

[167] Schweizer, T. et al. "Characterization of the optical and X-ray properties of the north-western wisps in the Crab nebula". In: 433.4 (Aug. 2013), pp. 3325–3335. DOI: `10.1093/mnras/stt995`. arXiv: `1301.1321 [astro-ph.HE]`.

[168] Shayduk, M. et al. "A New Image Cleaning Method for the MAGIC Telescope". In: *29th International Cosmic Ray Conference (ICRC29), Volume 5*. Ed. by Acharya, B. S. et al. Vol. 5. International Cosmic Ray Conference. Jan. 2005, p. 223.

[169] Shklovskii, I. S. "On the Nature of the Optical Emission from the Crab Nebula." In: 1 (Oct. 1957), p. 690.

[170] Shklovskii, I. S. "Remarks on the Synchrotron-Radiation Spectrum of the Crab Nebula". In: 10 (Aug. 1966), p. 6.

[171] Smith, D. A. et al. "The Third Fermi Large Area Telescope Catalog of Gamma-Ray Pulsars". In: *The Astrophysical Journal* 958.2 (2023), p. 191. DOI: `10.3847/1538-4357/acee67`. URL: `https://dx.doi.org/10.3847/1538-4357/acee67`.

[172] Staelin, D. H. and Reifenstein, E. C. "Pulsating Radio Sources near the Crab Nebula". In: *Science* 162.3861 (1968), pp. 1481–1483. DOI: `10.1126/science.162.3861.1481`. eprint: `https://www.science.org/doi/pdf/10.1126/science.162.3861.1481`. URL: `https://www.science.org/doi/abs/10.1126/science.162.3861.1481`.

[173] Strzys, M. C. "Deciphering the γ-ray sky: study of the γ-Cygni SNR using a novel likelihood analysis technique for the MAGIC telescopes". PhD thesis. Ludwig-Maximilians University of Munich, Germany, Jan. 2020.

[174] Tanimori, T. et al. "Detection of Gamma Rays of up to 50 TeV from the Crab Nebula". In: 492.1 (Jan. 1998), pp. L33–L36. DOI: `10.1086/311077`. arXiv: `astro-ph/9710272 [astro-ph]`.

[175] Tibet ASγ Collaboration. "Potential PeVatron supernova remnant G106.3+2.7 seen in the highest-energy gamma rays". In: *Nature Astronomy* 5 (Jan. 2021), pp. 460–464. DOI: `10.1038/s41550-020-01294-9`. arXiv: `2109.02898 [astro-ph.HE]`.

[176] Trimble, V. "The Distance to the Crab Nebula and NP 0532". In: 85.507 (Oct. 1973), p. 579. DOI: `10.1086/129507`.

[177] Tsai, Y.-S. "Pair production and bremsstrahlung of charged leptons". In: *Rev. Mod. Phys.* 46 (4 1974), pp. 815–851. DOI: `10.1103/RevModPhys.46.815`. URL: `https://link.aps.org/doi/10.1103/RevModPhys.46.815`.

[178] Vacanti, G. et al. "Gamma-Ray Observations of the Crab Nebula at TeV Energies". In: 377 (Aug. 1991), p. 467. DOI: `10.1086/170376`.

[179] VASSEUR, J. et al. "Possible Pulsed Gamma Ray Emission above 50 MeV from the Crab Pulsar". In: *Nature* 226.5245 (May 1970), pp. 534–535. ISSN: 1476-4687. DOI: `10.1038/226534a0`. URL: `https://doi.org/10.1038/226534a0`.

[180] Vaughan, S. et al. "On characterizing the variability properties of X-ray light curves from active galaxies". In: 345.4 (Nov. 2003), pp. 1271–1284. DOI: `10.1046/j.1365-2966.2003.07042.x`. arXiv: `astro-ph/0307420 [astro-ph]`.

[181] VERITAS Collaboration. "Detection of Pulsed Gamma Rays Above 100 GeV from the Crab Pulsar". In: *Science* 334.6052 (2011), pp. 69–72. DOI: `10.1126/science.1208192`. eprint: `https://www.science.org/doi/pdf/10.1126/science.1208192`. URL: `https://www.science.org/doi/abs/10.1126/science.1208192`.

[182] Vink, J. *Physics and Evolution of Supernova Remnants*. Springer Cham, 2020. DOI: `10.1007/978-3-030-55231-2`.

[183] Wakely, S. P. and Horan, D. "TeVCat: An online catalog for Very High Energy Gamma-Ray Astronomy". In: *International Cosmic Ray Conference* 3 (2008), pp. 1341–1344.

[184] Weekes, T. C. et al. "Observation of TeV Gamma Rays from the Crab Nebula Using the Atmospheric Cerenkov Imaging Technique". In: 342 (July 1989), p. 379. DOI: `10.1086/167599`.

[185] Will, M. "Atmospheric Monitoring at the Site of the MAGIC Telescopes". In: *European Physical Journal Web of Conferences*. Vol. 144. European Physical Journal Web of Conferences. Jan. 2017, 01002, p. 01002. DOI: `10.1051/epjconf/201714401002`.

[186] Woltjer, L. "X-Rays and Type i Supernova Remnants". en. In: *Astrophys. J.* 140 (Oct. 1964), p. 1309.

[187] Woltjer, L. "X-Rays and Type I Supernova Remnants." In: 140 (Oct. 1964), pp. 1309–1313. DOI: `10.1086/148028`.

[188] Workman, R. L. et al. "Review of Particle Physics". In: *PTEP* 2022 (2022), p. 083C01. DOI: `10.1093/ptep/ptac097`.

[189] Young, A. T. "Air mass and refraction". In: *Appl. Opt.* 33.6 (1994), pp. 1108–1110. DOI: `10.1364/AO.33.001108`. URL: `https://opg.optica.org/ao/abstract.cfm?URI=ao-33-6-1108`.

[190] Zanin, R. et al. "MARS, The MAGIC Analysis and Reconstruction Software". In: *International Cosmic Ray Conference*. Vol. 33. International Cosmic Ray Conference. Jan. 2013, p. 2937.

The MAGIC Collaboration is acknowledged for allowing the use of proprietary observational data. MAGIC results presented in this thesis have not undergone the internal review procedure of MAGIC publications

Acknowledgments

These last few years were not always the easiest, and I would not have made it here without the support of many people. I would like to thank Razmik Mirzoyan and Masahiro Teshima not only for accepting me into the group back in 2017 and for letting me continue my work in the group for my PhD. I am also tremendously grateful for their support and understanding during the times when I was struggling. Thank you for giving me the time and space that I needed to finish this thesis. A huge thank you goes to David Green for his unwavering support. He was always available if I had questions and taught me so much, but most importantly, with his invaluable pep talks, he made me feel good about my work and myself when I was having doubts. I am very grateful to Susanne Mertens for agreeing to act as my official supervisor. I also want to thank Elisa Resconi, the first female professor I encountered during my physics studies at TUM. She accepted me into her group for my bachelor's thesis, and she has been somehow involved in my entire scientific journey. I am happy that she is also part of this final step by acting as the second referee.

I can not stress enough how grateful I am to have had such fantastic colleagues. Even on difficult days, it was always worth coming to the office just to hang out with the wonderful, kind, and funny people of the MAGIC group at MPP. Special thanks to my office roommate Alex, a fountain of knowledge on all MAGICal things, who always made time to help me. And thank you, Lea, for being a partner in crime in fighting for more DEI and for always being available for a good rant when I needed it.

MAGIC is an exceptional collaboration. I consider myself extremely lucky to have met so many smart, interesting, funny, and joyful people. Thank you for all the great times at meetings, conferences, and on shift. I have made friends for life in MAGIC and at MPP, and that is worth a million times more than being allowed to write a "Dr." in front of my name.

I could not have gotten through the last years without being surrounded by amazing people outside of work. Thank you to my Ensemble Fenice ladies, my TUM/CCG choir friends Alex, Lena, Martin, Bernhard, and the incredible people from Opera Incognita for filling my life with music. Thank you to my shred buddies, Andy, Gabriel, Saskia, Suska, Tom, and all my other winter friends, for taking my mind far away from physics most weekends of the year.

I am forever grateful to my parents for their unconditional love and support and for sharing their down-to-earth, factual, unagitated views on life with me. I don't want to imagine my life without my wonderful sister Cornelia. Thank you for saying, "Maybe you just need to take a break," exactly when I needed to hear it almost 4 years ago. Martin, finding you was, without a doubt, the best thing to have come out of all of this. You give me all of the above and so much more.

Last but not least - to say it in the words of Snoop Dog - I want to thank me! This was not easy, and I wanted to quit a thousand times, but I have shown strength, resilience, and discipline. I saw it through. I did it! And I am damn proud of that.